# Sailing through fluid mud
## Verification and Validation of a CFD model for simulations of ships sailing in muddy areas

Lovato, S.

**DOI**
10.4233/uuid:b2156264-39f4-4a8d-a34d-35e5a21d38e9

**Publication date**
2023

**Document Version**
Final published version

**Citation (APA)**
Lovato, S. (2023). *Sailing through fluid mud: Verification and Validation of a CFD model for simulations of ships sailing in muddy areas*. [Dissertation (TU Delft), Delft University of Technology]. https://doi.org/10.4233/uuid:b2156264-39f4-4a8d-a34d-35e5a21d38e9

# Sailing through fluid mud

## Verification and Validation of a CFD model for simulations of ships sailing in muddy areas

Stefano Lovato

# SAILING THROUGH FLUID MUD

## VERIFICATION AND VALIDATION OF A CFD MODEL FOR SIMULATIONS OF SHIPS SAILING IN MUDDY AREAS

# SAILING THROUGH FLUID MUD

## VERIFICATION AND VALIDATION OF A CFD MODEL FOR SIMULATIONS OF SHIPS SAILING IN MUDDY AREAS

**Dissertation**

for the purpose of obtaining the degree of doctor
at Delft University of Technology
by the authority of the Rector Magnificus prof.dr.ir. T.H.J.J. van der Hagen,
chair of the Board for Doctorates
to be defended publicly on
Thursday 23 February 2023 at 10:00 o'clock

by

**Stefano LOVATO**

Laurea Magistrale in Ingegneria Navale,
Università di Genova, Italy,
born in Turin, Italy.

This dissertation has been approved by the promotors.

Composition of the doctoral committee:

| | |
|---|---|
| Rector Magnificus, | chairperson |
| Prof.dr.ir. C. van Rhee, | Delft University of Technology, promotor |
| Dr.ir. G.H. Keetels, | Delft University of Technology, copromotor |
| | |
| *Independent members:* | |
| Prof.dr.ir. E.A. Toorman, | Katholieke Universiteit Leuven (Belgium) |
| Prof.dr.ir. C. Vuik, | Delft University of Technology |
| Prof.dr. G.D. Weymouth, | Delft University of Technology |
| Dr.ir. A.M. Talmon, | Delft University of Technology |
| Prof.dr.ir. B.J. Boersma, | Delft University of Technology, reserve member |
| | |
| *Other member:* | |
| Dr.ir. S.L. Toxopeus, | Maritime Research Institute Netherlands (MARIN) |

This research is funded by the Netherlands Organization for Scientific Research (NWO).The experimental part is funded by Topconsortium voor Kennis en Innovatie (TKI) Deltatechnologie, Port of Rotterdam and Hamburg Port Authority. Calculations were performed on the Marclus4 (MARIN) cluster. This research was carried out within the framework of the MUDNET academic network.

*Keywords:* CFD, Ship, Mud, Numerical Modelling, Non-Newtonian, Code Verification, Validation
*Printed by:* Ridderprint | www.ridderprint.nl

*Front & Back:* A ship sailing through mud (by Fabio Del Regno)

ISBN 978-94-6458-954-2

An electronic version of this dissertation is available at
doi:10.4233/uuid:b2156264-39f4-4a8d-a34d-35e5a21d38e9

*To my parents,*
*to Coccolino, Yoshi and Nala*

# CONTENTS

# SUMMARY

The increasing size of today's ships is a major concern for navigation in confined waters. In order to ensure safe manoeuvres, port authorities prescribe, among others, a minimum under-keel clearance that must be maintained by the ships during navigation. However, the seabed of ports situated at the estuaries or along rivers is often covered by mud as a result of sedimentation. Hence, while the position of a solid bottom is clearly defined and can be easily detected by sonar techniques, the presence of deposited sediments makes the definition of "bottom" and "depth" less clear. This also poses some questions on the optimal dredging strategy to adopt to minimise maintenance costs while ensuring the required safety.

For practical reasons, port authorities define the (nautical) bottom as the level where the mud reaches either a critical density or a critical yield stress (i.e. the shear stress below which the fluid behaves as a solid-like material). However, an optimal choice that minimises dredging activities while preserving the required safety shall also take into account the behaviour of ships. As the understanding of the link between mud rheology and ships' controllability and manoeuvrability with muddy seabeds is rather limited, this research project was started. With the rapidly increasing power of today's computers, Computational Fluid Dynamics (CFD) has become a viable option to study this problem.

The CFD code selected for this research is a multi-phase viscous-flow solver developed, verified and validated exclusively for maritime applications. As such, it was originally developed for Newtonian fluids only. Since mud exhibits a non-Newtonian rheology, the 'step zero' of this research was to implement the Herschel-Bulkley model, which allows to numerically simulate two important flow features of mud, i.e. its shear-thinning and viscoplastic behaviour. Other rheological characteristics, such as thixotropy, were not considered in this study as they are deemed of minor importance at this stage.

The next step was concerned with ensuring that the modification of the flow solver to account for the non-Newtonian rheology of mud was correct. This was done by using the Method of Manufactured Solutions (MMS), which allows to rigorously verify the code against user-defined exact solutions. The verification exercises showed that the code performs as intended for both single- and two-phase flows of Herschel–Bulkley fluids. The illustrated procedure can be readily adapted to verify the correct implementation of other rheological models that may be implemented in the future.

In this case, it is recommended to examine, in addition to the grid convergence of velocity and pressure, also the grid convergence of the apparent viscosity as the latter is particularly sensitive to coding mistakes related to the implementation of the new rheological model.

While code verification ensured that the Herschel–Bulkley model was correctly implemented, obtaining fully-converged solutions for realistic non-Newtonian problems may still be difficult. The non-Newtonian solver has thus been tested on the laminar flow of Herschel-Bulkley fluids around a sphere, as the latter is the simplest three-dimensional flow exhibiting features that are typical of the flow around ships, such as boundary layer development and flow separation. Although obtaining a fully-converged solutions was indeed challenging, it was possible to replicate data from the literature with good accuracy. This provided confidence to employ the CFD code to simulate ships sailing through fluid mud.

The verification of the CFD code was followed by validation of the mathematical model. The problem of a ship sailing through fluid mud was simplified into a simpler one, i.e. a plate moving through homogeneous mud as to mimic a portion of the hull penetrating the mud layer. The objective was to investigate the accuracy of the (regularised) Bingham model (which is a special case of Herschel-Bulkley) to predict the frictional forces on a plate moving through mud. The comparison between experimental and numerical data showed that the ideal Bingham model well captures the relative increase in the resistance due to the increase in the mud concentration but, at low speed, it tends to over-predict the resistance. On the other hand, choosing a lower regularisation parameters seem more favourable, both from the numerical and physical perspective. In fact, this research showed that better predictions at low speed were achieved by using lower regularisation parameters that were determined from the first points in the mud flow curves. It should be noted, however, that the thixotropy of mud and possible deflections of the plate during the experiments may prevent drawing definitive conclusions.

Finally, one question arising when simulating a ship sailing through a non-Newtonian fluid is how accurate are standard Reynolds-Averaged Navier-Stokes (RANS) models, which are developed for Newtonian fluids, when applied to non-Newtonian flows. In the last step of this dissertation, the accuracy of three RANS models was assessed against published Direct Numerical Simulations (DNS) data for pipe flows. From this study it was concluded that, among the three tested Newtonian RANS models, the SST model produced the best predictions and it is reasonably accurate for weakly non-Newtonian fluids and for high Reynolds numbers. In addition, a new RANS model, labelled SST-HB, has been developed. The new model showed good agreement with DNS of pipe flows in the mean velocity, average viscosity, mean shear stress budget and friction factors. However, the new RANS model was calibrated and tested for pipe flows only, a relatively simple internal-flow problem.

Hence, the applicability of the new model to complex external flows, such as the flow around a ship, still requires further investigations. Furthermore, RANS simulations with some realistic mud conditions predicted laminar flow in the mud layer. In this case, the use of the standard SST model is recommended.

The developed and tested CFD code, together with other insights provided by this research, can be used in the future to both numerically investigate the effect of mud on ships and to obtain the hydrodynamic coefficients for manoeuvring models. These models could then be used in real- and fast-time simulators for research and commercial purposes, but also for pilots training.

# LIST OF SYMBOLS

## Abbreviations

| | |
|---|---|
| CFD | Computational Fluid Dynamics |
| CFL | Courant–Friedrichs–Lewy |
| DNS | Direct Numerical Simulations |
| GN | Generalised Newtonian |
| GNF | Generalised Newtonian Fluid |
| KSKL | $k-\sqrt{k}L$ |
| LES | Large-Eddy Simulations |
| MARIN | Maritime Research Institute Netherlands |
| MMS | Method of Manufactured Solutions |
| PIANC | Permanent International Association of Navigation Congresses |
| RANS | Reynolds-Averaged Navier-Stokes |
| RHS, LHS | Right-Hand Side, Left-Hand Side |
| RMS | Root Mean Square |
| RPM | Revolutions per minute |
| SA | Spalart-Allmaras |
| SIMPLE | Semi-Implicit Method for Pressure Linked Equations |
| SST | Shear Stress Transport |
| TEU | Twenty-foot Equivalent Unit |

| | |
|---|---|
| TKE | Turbulent kinetic energy |
| TVD | Total Variation Diminishing |
| UKC | Under-Keel Clearance |
| VoF | Volume of Fluid |

**Greek letters**

| | | |
|---|---|---|
| $\alpha$ | Coefficient of the SST model | - |
| $\alpha$ | Constant in the formula of the discretisation error | same as $\phi$ |
| $\alpha_1$ | Coefficient of the SST model | - |
| $\alpha_2$ | Coefficient of the SST model | - |
| $\alpha_t$ | Constant in the formula of the discretisation error | same as $\phi$ |
| $\alpha_x$ | Constant in the formula of the discretisation error | same as $\phi$ |
| $\beta$ | Coefficient of the SST model | - |
| $\beta^*$ | Coefficient of the SST model | - |
| $\beta_1$ | Coefficient of the SST model | - |
| $\beta_2$ | Coefficient of the SST model | - |
| $\boldsymbol{\tau}$ | Deviatoric stress tensor | Pa |
| $\boldsymbol{\tau}^{nn} \equiv \tau_{ij}^{nn}$ | Non-Newtonian stress tensor | Pa |
| $\chi^{nn}$ | Mean shear turbulent viscous dissipation | $\mathrm{kg\,m^{-1}\,s^{-3}}$ |
| $\Delta f$ | Difference between friction factors | - |
| $\Delta t_i$ | i-th time step | s |
| $\delta$ | Difference between two values | % |
| $\delta_{ij}$ | Kronecker delta | - |
| $\delta_{model}$ | Modelling error | |
| $\dot{\gamma}$ | Shear rate (second invariant of $S_{ij}$) | $\mathrm{s^{-1}}$ |

| | | |
|---|---|---|
| $\dot{\gamma}_E$ | Shear rate on a cell centroid $E$ | $\mathrm{s}^{-1}$ |
| $\dot{\gamma}_e$ | Shear rate on a cell face centroid $e$ | $\mathrm{s}^{-1}$ |
| $\dot{\gamma}_P$ | Shear rate on a cell centroid $P$ | $\mathrm{s}^{-1}$ |
| $\dot{\gamma}_{max}$ | Maximum shear rate in the rheological characterisation | $\mathrm{s}^{-1}$ |
| $\epsilon$ | Viscous dissipation rate of turbulent kinetic energy | $\mathrm{m}^2\,\mathrm{s}^{-3}$ |
| $\hat{\phi}$ | Instantaneous generic flow quantity (e.g. $\hat{\boldsymbol{u}}, \hat{\mu}, \hat{S}_{ij}$) | |
| $\hat{\phi}_n$ | n-th observation of $\hat{\phi}$ | |
| $\lambda$ | Degree of structure in a thixotropic fluid model | - |
| $\lambda_i$ | i-th grid/time step size | |
| $\mu(\dot{\gamma})$ | Apparent viscosity | Pa s |
| $\mu$ | Plastic viscosity | Pa s |
| $\mu^{nn}$ | Turbulent non-Newtonian viscosity | Pa s |
| $\mu_1$ | Fitting parameter of the Tscheuschner model | Pa s |
| $\mu_1$ | Viscosity of fluid 1 | Pa s |
| $\mu_2$ | Fitting parameter of the Tscheuschner model | Pa $\mathrm{s}^n$ |
| $\mu_2$ | Viscosity of fluid 2 | Pa s |
| $\mu_B$ | Plastic viscosity | Pa s |
| $\mu_E$ | Apparent viscosity on a cell centroid $E$ | Pa s |
| $\mu_e$ | Apparent viscosity on a cell face centroid $e$ | Pa s |
| $\mu_P$ | Apparent viscosity on a cell centroid $P$ | Pa s |
| $\mu_t$ | Eddy (or turbulent) viscosity | Pa s |
| $\nu_w$ | Wall kinematic viscosity | $\mathrm{m}^2\,\mathrm{s}^{-1}$ |
| $\omega$ | Specific dissipation rate of turbulent kinetic energy | $\mathrm{s}^{-1}$ |
| $\overline{\hat{\phi}} \equiv \phi$ | Ensemble-averaged value of $\hat{\phi}$ (e.g. $\boldsymbol{u}, \mu, S_{ij}$) | |

| | | |
|---|---|---|
| $\phi'$ | Fluctuating part of $\hat{\phi}$ (e.g. $\boldsymbol{u}', \mu', S'_{ij}$) | |
| $\phi$ | Generic scalar quantity | |
| $\Pi$ | Pressure diffusion | $\mathrm{kg\,m^{-1}\,s^{-3}}$ |
| $\pi$ | Irrational constant equal to 3.14159 | |
| $\rho$ | Density | $\mathrm{kg\,m^{-3}}$ |
| $\rho_1$ | Density of fluid 1 | $\mathrm{kg\,m^{-3}}$ |
| $\rho_2$ | Density of fluid 2 | $\mathrm{kg\,m^{-3}}$ |
| $\sigma_k$ | Coefficient of the SST model | - |
| $\sigma_{\omega 1}$ | Coefficient of the SST model | - |
| $\sigma_{\omega 2}$ | Coefficient of the SST model | - |
| $\sigma_\omega$ | Coefficient of the SST model | - |
| $\sigma_{k1}$ | Coefficient of the SST model | - |
| $\sigma_{k2}$ | Coefficient of the SST model | - |
| $\tau$ | Shear stress (second invariant of $\tau_{ij}$) | Pa |
| $\tau^{nn+}$ | Non-dimensional non-Newtonian stress | - |
| $\tau^{nn}$ | Non-Newtonian stress | Pa |
| $\tau^{t+}$ | Non-dimensional turbulent stress | - |
| $\tau^{tot+}$ | Non-dimensional total mean shear stress in cylindrical coordinates | - |
| $\tau^t$ | Turbulent stress | Pa |
| $\tau^{v+}$ | Non-dimensional viscous stress | - |
| $\tau^v$ | Viscous stress | Pa |
| $\tau_0$ | Yield stress | Pa |
| $\tau_B$ | Bingham yield stress | Pa |
| $\tau_i$ | i-th time step | s |

| | | |
|---|---|---|
| $\tau_w$ | Wall shear stress | Pa |
| $\tau_{ij}$ | Deviatoric stress tensor | Pa |
| $\tau_{zr}^{tot} \equiv \tau^{tot}$ | Total mean shear stress in cylindrical coordinates | Pa |
| $\varepsilon$ | Inverse of $M$ | - |
| $\varepsilon$ | Small constant | |
| $\xi^{nn}$ | Mean shear turbulent viscous transport | $\mathrm{kg\,m^{-1}\,s^{-3}}$ |
| $\zeta$ | Wave elevation | m |

**Roman letters**

| | | |
|---|---|---|
| $\boldsymbol{F_f}$ | Frictional force vector | N |
| $\boldsymbol{F_p}$ | Pressure force vector | N |
| $\boldsymbol{g}$ | Acceleration of gravity vector | $\mathrm{m\,s^{-2}}$ |
| $\boldsymbol{n}$ | Unit normal vector | - |
| $\boldsymbol{S}$ | Deformation rate tensor | $\mathrm{s^{-1}}$ |
| $\boldsymbol{u}$ | Velocity vector | $\mathrm{m\,s^{-1}}$ |
| $\boldsymbol{x}$ | Cartesian reference frame (also equivalent to $(x, y, z)$ or $(x_1, x_2, x_3)$) | m |
| $\mathscr{D}$ | Mean viscous transport | $\mathrm{kg\,m^{-1}\,s^{-3}}$ |
| $\mathscr{D}^{nn}$ | Turbulent viscous transport | $\mathrm{kg\,m^{-1}\,s^{-3}}$ |
| $\overline{X_i}$ | Mean value of $X_i$ | |
| err | Small coding error in percentage of the apparent viscosity | % |
| $\tilde{P}_k$ | Production term of the SST model | $\mathrm{kg\,m^{-1}\,s^{-3}}$ |
| $b$ | Steepening parameter | - |
| $Bn20$ | Bingham case with $\tau_0/\tau_w = 20$ | – |
| $Bn$ | Bingham number | - |
| $Bn^*$ | Bingham number | - |

| | | |
|---|---|---|
| $C$ | Constant | - |
| $c$ | Volume fraction | - |
| $c$ | Wave celerity | $\mathrm{m\,s^{-1}}$ |
| $C_D$ | Drag coefficient | - |
| $C_p$ | Pressure coefficient | - |
| $C_S$ | Stokes coefficient | - |
| $C_\beta$ | Calibration coefficient of the SST-HB model | - |
| $C_\chi$ | Calibration coefficient of the SST-HB model | - |
| $C_\tau$ | Calibration coefficient of the SST-HB model | - |
| $C_\xi$ | Calibration coefficient of the SST-HB model | - |
| $C_{Df}$ | Frictional component of $C_D$ | - |
| $C_{Dp}$ | Pressure component of $C_D$ | - |
| $C_{E1}$ | Lower bound of $C_E$ | - |
| $C_{E2}$ | Upper bound of $C_E$ | - |
| $C_E$ | Calibration coefficient of the SST-HB model | - |
| $C'_{RF}$ | Modified formula for $C_{RF}$ | - |
| $C_{RF}$ | Frictional resistance coefficient | - |
| $C_{RP}$ | Pressure resistance coefficient | - |
| $C_{Sf}$ | Frictional component of $C_S$ | - |
| $C_{Sp}$ | Pressure component of $C_S$ | - |
| $D$ | Diameter and length of the cylindrical tube | m |
| $D$ | Experimental/literature data (for validation procedure) | |
| $D$ | Turbulent transport term | $\mathrm{kg\,m^{-1}\,s^{-3}}$ |
| $d$ | Distance from the wall | m |

| | | |
|---|---|---|
| $d$ | Pipe diameter | m |
| $d$ | Sphere diameter | m |
| $D_i$ | Tube diameter for the i-th domain | m |
| $dS$ | Infinitesimal surface element | $\mathrm{m}^2$ |
| $e(\phi)$ | Discretisation error for the quantity $\phi$ | same as $\phi$ |
| $E$ | Comparison error | |
| $E^{nn}$ | Non-Newtonian contribution of the $\omega$ equation | $\mathrm{kg\,m^{-3}\,s^{-2}}$ |
| $e_0$ | Extrapolated error for zero grid/time step size | same as $\phi$ |
| $f$ | Friction factor | - |
| $F_1$ | Blending function of the SST model | - |
| $F_2$ | Blending function of the SST model | - |
| $F_E(n)$ | Blending function of the SST-HB model | - |
| $f_j$ | j-th sampling force | N |
| $F_r$ | Froude number | - |
| $g$ | Acceleration of gravity | $\mathrm{m\,s^{-2}}$ |
| $h$ | Distance between free surface and solid bottom (channel depth) | m |
| $h$ | Thickness of the mud layer (or mud depth) | m |
| $H_e$ | Hedstrom number | - |
| $h_i$ | Grid (cell) size of the i-th grid | m |
| $h_w$ | Thickness of the first cell away from the wall | m |
| $HB10$ | Herschel-Bulkley case with $\tau_0/\tau_w = 10$ | – |
| $i$ | index/counter | - |
| $j$ | index/counter | - |
| $K$ | Consistency parameter | Pa $\mathrm{s}^n$ |

| | | |
|---|---|---|
| $k$ | Turbulent kinetic energy | $\mathrm{m^2\,s^{-2}}$ |
| $k$ | coverage factor | - |
| $k^+$ | Non-dimensional turbulent kinetic energy | - |
| $L$ | Characteristic length | m |
| $L$ | Plate's chord | m |
| $L$ | Ship's length | m |
| $L_q$ | $L^q$-norm $(q = 1,2,...,\infty)$ | same as $\phi$ |
| $M'$ | Non-dimensional regularisation parameter | - |
| $M$ | Non-dimensional regularisation parameter | - |
| $m$ | Regularisation parameter | s |
| $M_i$ | i-th non-dimensional regularisation parameter | - |
| $M_{down}$ | Non-dimensional regularisation parameter from the first point in the ramp-down flow curve | - |
| $M_{fit}$ | Non-dimensional regularisation parameter from fitting the regularised model to the ramp-down flow curve | - |
| $M_{up}$ | Non-dimensional regularisation parameter from the first point in the ramp-up flow curve | - |
| $N$ | Number of repeated observations | - |
| $N$ | Number of repeated tests | - |
| $n$ | Flow index | - |
| $n$ | Number of sampling data points | - |
| $n$ | index/counter | - |
| $N_i$ | Number of cells of the i-th grid | - |
| $N_{cells}$ | Total number of grid cells | - |
| $P$ | Production | $\mathrm{kg\,m^{-1}\,s^{-3}}$ |

| | | |
|---|---|---|
| $p$ | Observed order of grid/time convergence | - |
| $p$ | Pressure | Pa |
| $p^*$ | Observed order of grid/time convergence assuming $e_0 = 0$ | - |
| $p_{ls}$ | Observed order of grid/time convergence calculated in the least-square sense | - |
| $PL06$ | Power-law case with $n = 0.6$ | − |
| $R$ | Pipe radius | m |
| $r$ | Radial coordinate | m |
| $R_e^\mu$ | Viscous Reynolds number (used to obtain $R_e^e$) | - |
| $R_e^\tau$ | Yield stress Reynolds number (used to obtain $R_e^e$) | - |
| $R_e^e$ | Effective Reynolds number | - |
| $R_F$ | Frictional resistance | N |
| $R_P$ | Pressure resistance | N |
| $R_T$ | Total resistance (either experimental or numerical) | N |
| $R_{mean}$ | Mean of the $N$ time-average forces | N |
| $R_{t.a}^i$ | Time-average of the i-th force signal | N |
| $Re$ | Generalised Reynolds number | - |
| $Re$ | Reynolds number | - |
| $Re^*$ | Modified Reynolds number | - |
| $Re_w$ | Reynolds number based on $\nu_w$ | - |
| $Re_\tau$ | Friction Reynolds number | - |
| $Re_{MR}$ | Metzner-Reed Reynolds number | - |
| $S$ | Numerical data (for validation procedure) | |
| $S$ | Side surface area of the plate | $\mathrm{m}^2$ |
| $S$ | Strain rate | $\mathrm{s}^{-1}$ |

| | | |
|---|---|---|
| $S$ | Surface area | $\mathrm{m}^2$ |
| $s$ | Unbiased standard uncertainty | N |
| $S_f$ | Frontal surface area of the plate | $\mathrm{m}^2$ |
| $S_w$ | Total wetted surface of the plate | $\mathrm{m}^2$ |
| $S_{ij}$ | Deformation rate tensor | $\mathrm{s}^{-1}$ |
| $S_{mud}$ | Surface area of the ship hull in contact with mud | $\mathrm{m}^2$ |
| $T$ | Plate's draught | m |
| $T$ | Ship draught | m |
| $T$ | Turbulent transport | $\mathrm{kg\,m^{-1}\,s^{-3}}$ |
| $T$ | Wave period | s |
| $t$ | Plate's thickness | m |
| $t$ | Time | s |
| $U$ | Average velocity over a channel depth | $\mathrm{m\,s^{-1}}$ |
| $U$ | Characteristic velocity | $\mathrm{m\,s^{-1}}$ |
| $U$ | Inflow velocity | $\mathrm{m\,s^{-1}}$ |
| $u$ | Standard uncertainty | |
| $u^+$ | Non-dimensional velocity | - |
| $U_b$ | Bulk velocity | $\mathrm{m\,s^{-1}}$ |
| $u_i$ | Standard uncertainty of $X_i$ | |
| $u_\tau$ | Friction velocity | $\mathrm{m\,s^{-1}}$ |
| $U_{C_{Df}}$ | Discretisation uncertainty of $C_{Df}$ | % |
| $U_{C_{Dp}}$ | Discretisation uncertainty of $C_{Dp}$ | % |
| $U_{cal}$ | Calibration uncertainty | % |
| $U_{discr}$ | Uncertainty due to discretisation errors | % |

| | | |
|---|---|---|
| $U_{dom}$ | Uncertainty due to domain size | % |
| $U_d^F$ | Discretisation uncertainty in $R_F$ | % |
| $U_d^P$ | Discretisation uncertainty in $R_P$ | % |
| $U_d^T$ | Discretisation uncertainty in $R_T$ | % |
| $U_{exp}$ | Experimental uncertainty | |
| $U_{input}$ | Input parameter uncertainty | % |
| $u_{input}$ | Standard input uncertainty | N |
| $U_{input}^F$ | Input parameter uncertainty of $R_F$ | % |
| $U_{input}^P$ | Input parameter uncertainty of $R_P$ | % |
| $U_{input}^T$ | Input parameter uncertainty of $R_T$ | % |
| $U_{iter}$ | Uncertainty due to iterative errors | % |
| $U_{it}^F$ | Iterative uncertainty in $R_F$ | % |
| $U_{it}^P$ | Iterative uncertainty in $R_P$ | % |
| $U_{it}^T$ | Iterative uncertainty in $R_T$ | % |
| $U_{lit}$ | Uncertainty in the literature data | % |
| $U_{num}$ | Numerical uncertainty | % |
| $U_{reg}$ | Uncertainty due to regularisation parameter | % |
| $U_{rep}$ | Repeated tests uncertainty | % |
| $U_{val}$ | Validation uncertainty | % |
| $V$ | Inflow velocity | $\text{m s}^{-1}$ |
| $V$ | Plate's speed | $\text{m s}^{-1}$ |
| $X_i$ | i-th input parameter | |
| $y^+$ | Dimensionless wall distance | - |
| $y^+_{max}$ | Maximum $y^+$ at the first cell away from the wall | - |

# 1

# INTRODUCTION

*The increasing size of today's ships is a major concern for navigation in confined waters. In order to ensure safe manoeuvres, port authorities prescribe, among others, a minimum under-keel clearance that must be maintained by the ships during navigation. However, the seabed of ports situated at the estuaries or along rivers is often covered by mud as a result of sedimentation. For practical reasons, port authorities define the (nautical) bottom as the level where the mud reaches either a critical density or a critical yield stress. But an optimal choice that minimises dredging costs while preserving the required safety shall also take into account the behaviour of ships. The need for a better understanding of the link between mud rheology and the hydrodynamic behaviour of ships is the reason that motivated this dissertation.*
*This chapter gives an overview of past theoretical, experimental and numerical research on the behaviour of ships when sailing in shallow waters with muddy seabeds. With the rapidly increasing power of today's computers, Computational Fluid Dynamics (CFD) has become a viable option to investigate the ship-mud interaction. The focus of this research is on the verification of the CFD code and on the validation of the mathematical model for simplified problems related to navigation with muddy bottoms. This research is divided in four tasks, which are outlined at the end of this chapter.*

## 1.1. BACKGROUND

About 80% of the tonnes of goods traded between the European Union and the rest of the world is transported by ships [57]. Shipping is in fact the main mode of transportation for global trade because of the low cost of transport per unit of cargo. The raising demands for goods due to economic growth, combined with the fact that costs of transport drop even further with larger ships, led to a progressive increase in the sizes of ships over the past decades. As an example, the capacity of container ships, which currently account for the transport of about 90% of the non-bulk cargo worldwide, went from about 1000 TEU in the 1970s to nearly 28000 TEU in 2022.

But the cross-section of ports and waterways did not grow at the same pace. As a result, ships often navigate in very shallow waters, or very close to lateral boundaries. Moreover, as traffic has also increased over the years, ships may have to navigate close to each other. The vicinity of ships to solid boundaries means that possible contacts that can impair the integrity of the hull are more likely to occur. Furthermore, ships are usually designed and optimised for navigation in deep waters, where they spend most of their time. Therefore, when ships navigate in confined waters, they often operates in off-design conditions, meaning that their manoeuvring capacity is reduced and tug assistance is often required. In order to ensure safe navigation in shallow waters, port authorities prescribe, among others, a minimum under-keel clearance (UKC) that a ship must keep during navigation in the harbour. This implies that either deep-draught vessels cannot enter the harbour or the fairways need to be deepened.

To make things worse, some of the largest European ports are situated on estuaries (e.g. in Rotterdam, Antwerp) and along rivers (e.g. Hamburg). As these rivers typically widen in proximity of the harbours, the sediments transported by the stream lose their kinetic energy and eventually settle on the seabed. This results in the formation of mud layers, which further reduce the navigable depth (Fig. 1.1).

Thus, even if the solid bottom is low enough to allow safe access to large vessels, the presence of deposited sediments requires regular and costly dredging operations to maintain a minimum UKC. But how to define the UKC in case of a muddy seabed? In fact, while the position of a solid bottom is clearly defined and can be easily detected by sonar techniques, the presence of mud makes the definition of "bottom" and "depth" less clear. This also poses some questions about the optimal dredging strategy to adopt to minimise maintenance costs while ensuring the required safety.

As proposed by PIANC [109], a compromise between costs and safety can be better identified by introducing a new definition of "bottom" and "depth", which would be referred to as “nautical bottom” and “nautical depth”. PIANC [109] defines the nautical bottom as *“the level where physical characteristics of the bottom reach a critical limit beyond which contact with a ship’s keel causes either damage or unacceptable*

Figure 1.1: A container ship moving above (left) and through (right) a mud layer (snapshots from do] www.youtube.com/watch?v=LSbQhUJMBJw).

*effects on controllability and manoeuvrability*". The nautical depth is then simply the distance between the nautical bottom and the still water level. The definition of nautical bottom, however, still leaves room for interpretations as neither the physical characteristics nor the unacceptable effects are clearly defined.

For practical reasons, port authorities define the nautical bottom as the level where the mud reaches either a critical density or a critical yield stress (i.e. the shear stress below which the fluid behaves as a solid-like material), as shown in Table 1.1. These values usually correspond approximately to a depth where the mud undergoes a 'rheological transition', in which the density and strength of the mud increase rapidly over a short distance. Below such depth, the mud resembles more and more a solid bottom.

Table 1.1: Examples of nautical bottom criteria around the world (McAnally et al. [108]).

| Country | Port | Criterion | Value |
|---|---|---|---|
| The Netherlands | Rotterdam | Density | 1200 kg/m$^3$ |
| Belgium | Zeebrugge | Density | 1200 kg/m$^3$ |
| France | Nantes-Saint-Nazaire | Density | 1200 kg/m$^3$ |
| United Kingdom | Avonmouth | Density | 1200 kg/m$^3$ |
| China | Yangtze | Density | 1250 kg/m$^3$ |
| Surinam | Paramaribo | Density | 1230 kg/m$^3$ |
| Thailand | Bangkok | Density | 1200 kg/m$^3$ |
| Germany | Emden | Yield stress | 100 Pa |

But how do muddy seabeds affect ship navigation? An optimal implementation of the nautical bottom concept would indeed require, according to its definition, a good understanding of the effects of muddy bottoms on the ship's behaviour in order to identify what are the "unacceptable effects on controllability and manoeuvrability". The only documented case in which the ships' behaviour was taken into account in the definition of the nautical bottom is the port of Zeebrugge, where the nautical bottom is still density-based but the conditions for safe navigation with such criterion were assessed by means of real-time manoeuvring simulations (Vantorre et al. [170]). These conditions are however case-specific, thus they cannot be generalised to other ports.

The need for a better understanding of the influence of the mud rheology on the hydrodynamic behaviour of ships is the reason that motivated this dissertation. As we shall see in the next section, most of the previous studies have been experimental, whereas this work will tackle the problem using numerical simulations.

## 1.2. SHIP BEHAVIOUR WITH MUDDY BOTTOMS

### 1.2.1. SHALLOW WATER EFFECTS

Before describing what is known about the effect of mud on ships, it is useful to first briefly outline the effects of shallow waters with solid bottoms.

When a ship sails in a channel with limited depth, the water between the keel and the bottom of the channel moves faster than in deep waters. This is to maintain a constant mass flow rate at each cross-section of the channel, in fulfilment of the law of mass conservation. According to the Bernoulli's principle, the increase in the flow velocity induces a pressure drop (Fig. 1.2), which makes the ship to sink and trim (squat). Evidently, this increases the risk of contact between the hull and the bottom of the channel. The increasing flow speed also leads to an increase in the viscous and wave-making resistance. These effects are further magnified with narrower channels.

In terms of controllability, the restricted water depth tends, at least for full ship forms, to reduce the capacity to manoeuvre. For example, the turning ability of the ship is observed to decrease with reduced depth, which is reflected by larger and larger turning circles (Fig. 1.3). The yaw-checking ability in a standard zig-zag manoeuvre is also observed to increase for typical cargo ships, leading to more stable but slower manoeuvres.

### 1.2.2. EFFECTS OF MUDDY BOTTOMS

Previous research has shown that the shallow water effects tend to be enhanced by the presence of mud layers. In general, the force distribution acting on the hull is altered because of two main effects.

The first effect occurs when sailing with negative UKC relative to the mud-water

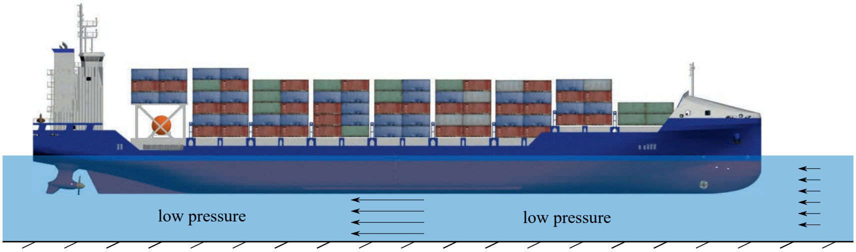

Figure 1.2: increase in flow speed (overspeed) and consequent pressure drop caused by the flow restriction under the ship.

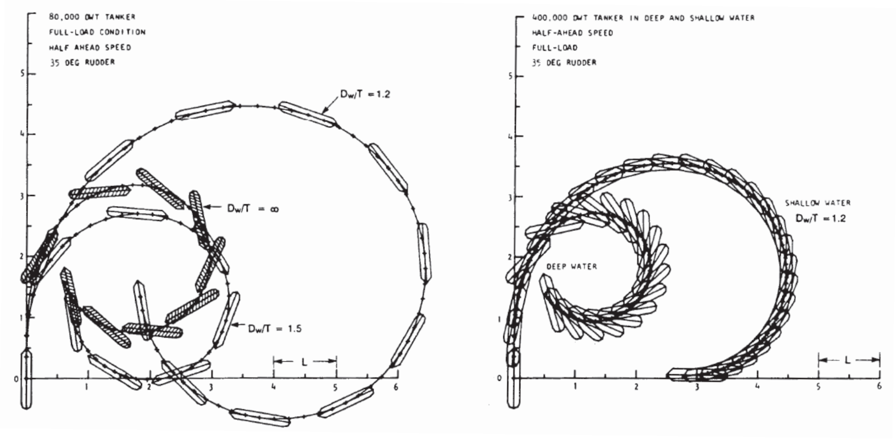

Figure 1.3: Effect of under-keel clearance on the turning circle, where $D_w$ is the water depth and $T$ is the ship's draught (picture from Eda et al. [53]).

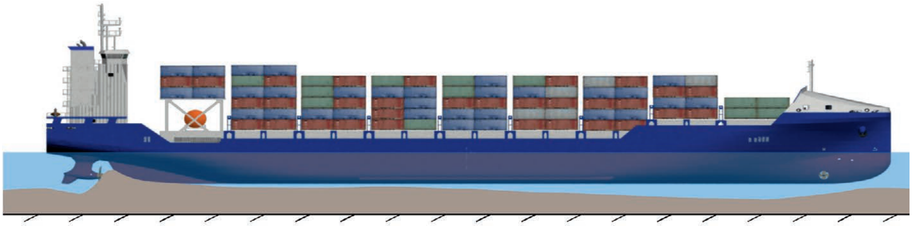

Figure 1.4: Mud undulation generated by a passing ship.

interface and it is due to the contact with a highly viscous fluid like mud. This leads to an increase in the shear stress (friction) in the portion of the hull in contact with mud.

The second effect, on the other hand, can occur with both negative and positive UKC, and stems from the generation of an undulation at the mud-water interface (Fig. 1.4). This occurs even when the Froude number, $F_r$, is sufficiently low to cause hardly any disturbance of the free surface (air-water interface). When ships sail at speeds close to a critical value associated with the celerity of the fastest internal waves, the mud undulation can cause a significant change in the pressure distribution around the hull and therefore in the manoeuvring and propulsion characteristics.

### THEORETICAL RESEARCH

The mud undulation has the same nature of the internal wave occurring at the interface between fluids of different salinity or temperature. The sudden increase in the resistance due to internal waves was firstly reported in 1893 by Nansen [123], after he had observed a sudden drop in the ship's speed during navigation in the Arctic ocean. Subsequently, in 1904, Ekman [54, 177] studied this phenomenon experimentally and named it “dead-water effect".

Zilman and Miloh [187] used a linearised theory based on potential flow to calculate the (internal) wave-making resistance of a parabolic strut and of a body of revolution moving through inviscid water above a thin Newtonian mud layer. A sharp peak was observed in the wave-making resistance when the object's speed matched a critical speed associated with the fastest internal waves, i.e when the densimetric Froude number was close to 1 (Fig. 1.5).

Interestingly, the peak of resistance significantly decreases with increasing mud viscosity (Fig. 1.5, left), most likely as a result of wave damping. However, at low speeds (subcritical range), the resistance seems larger with high viscosity. This can be explained by the fact that when the mud is more viscous, it is more resistant to deformation. As a result, the interface behaves more like a solid bottom, which leads to a net reduction in the channel depth and an increase in shallow water effects. The theoretical calculations of Doctors [42] support this explanation but further investigations are needed.

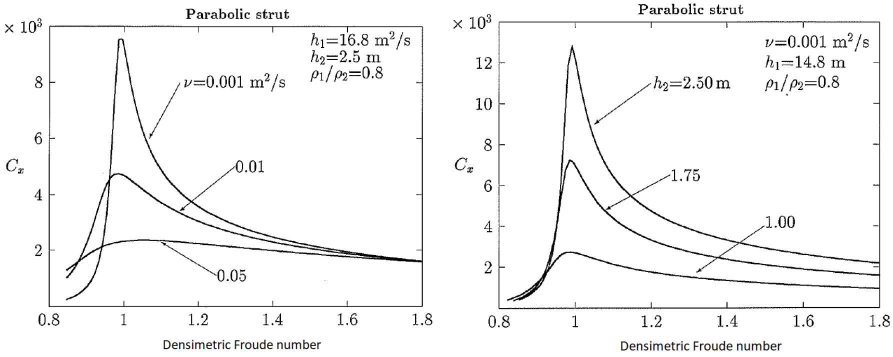

Figure 1.5: Mud-induced wave resistance coefficient on a parabolic strut (adapted from Zilman and Miloh [187]). The peak in the resistance occurs when the strut's speed is close to the critical speed of the internal wave generated at the mud-water interface.

### EXPERIMENTAL RESEARCH

The most substantial research on the ship-mud interaction has been experimental. The first reported model-scale experiments were conducted at the Netherlands Ship Model Basin (currently MARIN) in 1976 by Sellmeijer and Van Oortmerssen [145], who used a layer of chlorinated paraffin to mimic the presence of mud. The effect of the (simulated) mud on a model-scaled tanker was observed to be stronger when the ship's speed was close to the maximum (critical) speed of the internal wave (between 2 and 4 knots), whereas smaller effects were observed at higher speeds. This agrees with the theoretical research on the dead-water effect. In general, higher RPMs were required with a muddy bottom in order to maintain the same speed achieved without mud (see Fig. 1.6), even when no contact between the hull and the mud occurred.

Analogous observations were made by Vantorre and Coen [171] and Delefortrie et al. [38] at Flanders Hydraulics Research (Belgium), although the interface deformation and the change in the ship behaviour were attributed to an hydraulic jump rather than to an internal wave [169]. The internal wave was also observed at SOGREAH (France) (Brossard et al. [21]), where experiments have been conducted on a model-scaled tanker and using fluid mud with different concentrations and density gradients.

The influence of muddy bottoms on the manoeuvring and propulsion behaviour has also been investigated by means of full-scale trials, carried out in the harbour

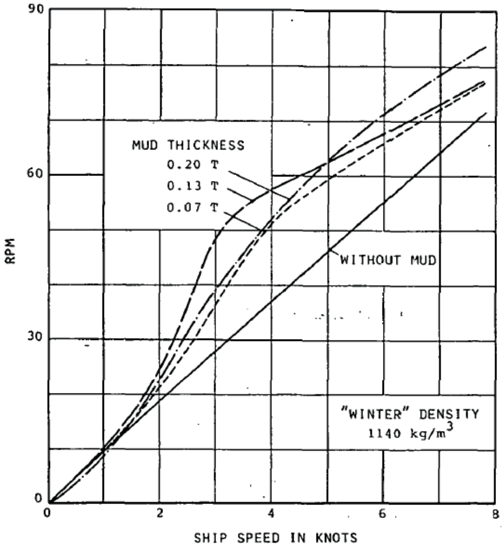

Figure 1.6: RPM versus speed with UKC= $0.2T$ relative to the solid bottom, where $T$ is the draught of the ship (picture adapted from [145]).

of Rotterdam (Netherlands, see Van Bochove and Nederlof [19]), Delfzijl (Netherlands, see Verwilligen et al. [175] and Barth et al. [10]) and Zeebrugge (Belgium, see Craenenbroeck et al. [34]).

Although it is not possible to generalise the previous experimental results for all ship geometries, speeds, channel/basin dimensions and mud characteristics, some recurring observations can be listed:

- The speed-RPM curve is approximately linear when navigating above solid bottoms. With muddy bottoms, on the other hand, higher RPMs are required to sail at the same speed as without mud. This can be due to both a reduction of the propulsive efficiency and an increase in the resistance.

- The ship's resistance tends to increase in presence of mud both because of the contact with a highly viscous fluid (in case of negative UKC) and because of the wave-making type of resistance associated with the energy required to generate the internal wave.

- In general, sinkage and trim tend to be smaller with mud than with a hard bottom, mainly because of buoyancy effects. However, at high speed and with negative UKC, the sinkage was observed to be larger than with solid bottoms.

- The undulation at the mud-water interface tends to obstruct the flow to the propeller, thus decreasing the propulsive efficiency.
- The internal wave amplitude is larger with thicker mud layer and lower density.
- The ship tends to be more sluggish as the UKC relative to the mud-water interface decreases. The presence of the mud layer is felt the most when the UKC is close to zero. With a further small decrease in the UKC (which becomes negative) the influence of the mud tends to reduce. This may be ascribed to near-field (or proximity) effects, i.e. to the stronger pressure disturbance caused by the hull when the latter is closer to the mud-water interface.

### NUMERICAL RESEARCH

The number of numerical studies on the effects of muddy bottoms on ships is rather limited, but it appears to be increasing in recent years. The earliest published Computational Fluid Dynamic (CFD) study that can be found in the literature is dated 2015 and it was carried out by Gao et al. [62], who used Ansys-Fluent 12.0 to simulate the flow around the Wigley hull. The rheology of mud was mathematically described by the Herschel-Bulkley model (see also Section 2.4.1), with a yield stress of approximately 7 Pa. Another CFD study was later published in 2020 by Kaidi et al. [78], who investigated the effect muddy bottoms on the resistance, sinkage and trim of a model-scaled container vessel using Ansys-Fluent 13.0. In their study, the mud layer was modelled as a Newtonian fluid, as little difference in the results was observed when a non-Newtonian model was used.

Neglecting the non-Newtonian rheology of mud was taken even further by Sano and Kunitake [143], who used a potential flow solver to compute the wave-making resistance of KLVCC2 moving above an inviscid mud layer. Their computed (internal) wave-making resistance is given in Fig. 1.7, which shows a large peak when the Froude number reaches a critical value. This critical Froude number was mathematically derived by Yeung and Nguyen [186] and it is a function of the density and thickness of both the water and mud layers. Interestingly, the speed corresponding to the critical Froude number in Fig. 1.7 is very close to the critical speed of the internal wave reported by Sellmeijer and Van Oortmerssen [145] and Zilman and Miloh [187], despite their different definitions.

In summary, it appears clear from previous research that the presence of an internal wave at the mud-water interface can significantly alter the forces distribution around the hull. Previous research suggests that even when the free-surface (air-water) waves can be neglected one should keep track of the ship's speed in relation to the critical (maximum) speed of the internal waves. The importance of this lies in the fact that varying a certain parameter can have opposite effects depending on

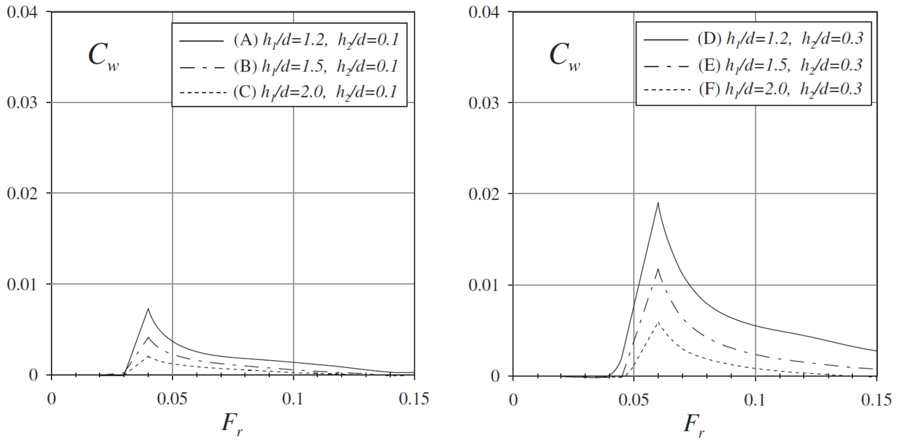

Thin lower layer

Thick lower layer

Figure 1.7: Wave-making resistance versus the Froude number, $F_r = U/\sqrt{gL}$, of KVLCC2; $h_1$ and $h_2$ are the upper (water) and lower (mud) layer thicknesses, respectively, whereas $d$ is the ship's draught. (picture adapted from [143])

whether the ship is moving faster (supercritical) or slower (subcritical) than such critical speed. As an example, with reference to the work of Sano and Kunitake [143], let's assume that a ship is sailing at the critical Froude number for a thin mud layer, i.e. $F_r \approx 0.04$ (Fig. 1.7, left). When the mud layer thickness, $h_2$, is increased (Fig. 1.7, right), the critical Froude number increases to about 0.06. Consequently, the ship would be now sailing in the subcritical range, thus with a much lower resistance. However, if the ship was initially sailing in the supercritical range, say at $F_r \approx 0.07$, an increase in the mud layer thickness would have brought the ship closer to the critical range, therefore increasing the resistance. In other words, the same event (i.e. increasing the mud layer thickness) led to opposite results depending on whether the ships was initially sailing in the subcritical or supercritical range.

### 1.2.3. KNOWLEDGE GAP AND LIMITATIONS OF PREVIOUS RESEARCH

The influence of muddy bottoms on ships has been studied theoretically, experimentally and numerically. Theoretical studies have helped, among other things, to identify some important parameters that influence the ship's resistance, such as the densimetric Froude number. However, the applicability of these theoretical studies is very limited because of the significant physical and geometrical simplifications. More realistic problems were addressed using CFD, but the current literature is still too limited to draw definitive conclusions about the influence of muddy seabeds on the hydrodynamic behaviour of ships.

The most insightful results come from model-scale experiments. However, results are difficult to generalise because of the large number of parameters involved such as UKC, mud layer thickness, mud properties, geometry and speed of the ship, and fairway cross-section. Furthermore, it is still not clear how and if these results can be reliably extrapolated to full scale. The main obstacle is the complex non-Newtonian rheology of mud, which precludes a straightforward application of standard extrapolation techniques typically used in ship model basins.

Issues related to scale effects and the mud rheology can be avoided by performing full-scale trials, which are certainly a useful way to qualitatively confirm or dismiss model-scale observations and to train pilots in realistic conditions. However, quantitative results are difficult to obtain as the trial conditions (e.g. ship's speed, wind, waves, currents, mud properties, etc.) are difficult to control and monitor. Other issues are related to the large costs involved, the accuracy of the measurements and the logistics (e.g., finding a large, muddy and low-traffic area to perform the manoeuvres). Furthermore, validation of the CFD model against full-scale trials would require to model the rudder and the propeller, with a substantial increase in the complexity and costs of the CFD simulations.

A question arising from the literature is how much the non-Newtonian properties of mud (e.g. yield stress) influence the ship's hydrodynamic behaviour. In fact, most model-scale experiments were carried out using mud-simulating materials which were more viscous than water but still with Newtonian-like properties. In the CFD studies, the effects of the non- Newtonian rheology of mud on the ship's resistance were either not discussed (Gao et al. [62]) or simply neglected (Sano and Kunitake [143] and Kaidi et al. [78]). It is indeed possible that, at least in some cases, the non-Newtonian properties of mud are of minor importance for navigation, but this has yet to be demonstrated.

## 1.3. AIM AND SCOPE OF THIS DISSERTATION

With the rapidly increasing power of today's computers, CFD has become a promising tool to study the the behaviour of ships sailing in muddy areas. The CFD code considered in this dissertation is REFRESCO (described in Section 2.5), a multiphase viscous-flow solver developed for maritime applications. As such, it has been originally developed for Newtonian fluids only.

This research project was initiated with the aim to implement, verify and validate non-Newtonian models in REFRESCO in order capture the non-Newtonian behaviour of fluid mud. The developed CFD model could then be used not only to numerically investigate the ship-mud interaction, but also to perform virtual cap-

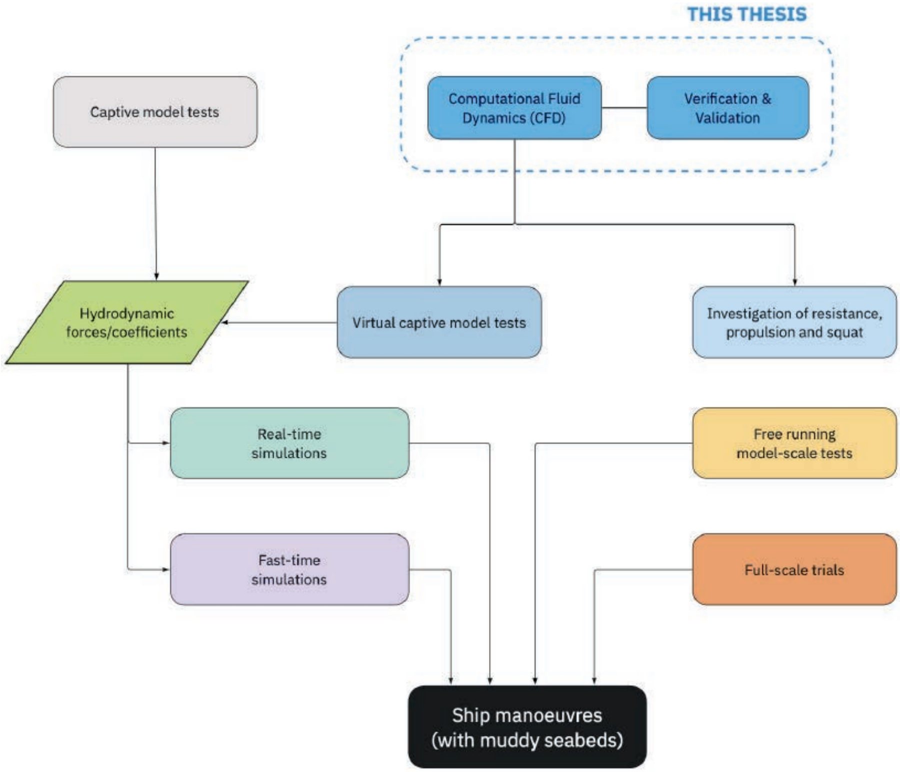

Figure 1.8: Schematic representation of the scope of this dissertation, within the context of ship navigation with muddy bottoms.

tive model tests to obtain the hydrodynamic coefficients for manoeuvring models (e.g. Toxopeus [165] and Hajivand and Mousavizadegan [70]). These manoeuvring models could then be used in real- and fast-time simulators to reproduce manoeuvres of ships both for research and commercial purposes, but also for pilots training (e.g. Delefortrie et al. [39]). The scope of this research is schematically illustrated in Fig. 1.8.

## 1.4. RESEARCH METHODOLOGY

The focus of this research is on the verification of the CFD code and on the validation of the mathematical model for simplified problems that can be related to navigation with muddy seabeds, with a specific emphasis on the non-Newtonian character of mud. The research methodology is thus divided into the following steps:

- Code verification of the newly implemented non-Newtonian solver.
- Application of the non-Newtonian solver to a benchmark problem.
- Validation of the numerical model for a plate moving through homogeneous mud.
- Assessment of standard Reynolds-Averaged Navier-Stokes (RANS) models when applied to specific non-Newtonian flows.

The first step is concerned with ensuring that the modification of REFRESCO to account for the non-Newtonian rheology of mud is correct. This is done by using the Method of Manufactured Solutions (MMS), which allows to rigorously verify the code against user-defined exact solutions.

A major aspect of the final CFD application is the calculation of the forces acting on the hull. In the second step, the code is applied to a typical three-dimensional benchmark flow for Newtonian and non-Newtonian fluids: the flow around a sphere. For non-Newtonian flows, the viscosity can vary by several orders of magnitude within the fluid domain, making the equations more difficult to solve. In this research step, it was checked whether literature data can be reproduced with good accuracy by the non-Newtonian solver of REFRESCO.

Another important challenge of CFD modelling for 'sailing-through-mud applications' is the lack of validation data. As full-scale trials are impractical for this purpose, the only alternative is model testing. However, a logistical and crucially difficult problem is to find ship model basins that allow to carry out experiments with fluids other than water, let alone mud or other highly viscous (and often toxic) mud-simulating materials. Thus, a simplified problem that can be studied experimentally with a smaller setup is considered. In this third step, an experimental and numerical study on the resistance of a thin plate moving through homogeneous mud in laminar regime is carried out.

Finally, one question would arise when simulating a ship sailing through a non-Newtonian fluid. How accurate are standard RANS models, which are developed for Newtonian fluids, when applied to wall-bounded non-Newtonian flows? In the last step of this dissertation, the accuracy of three RANS models are assessed against published DNS data for pipe flows and a new turbulence model is proposed.

## 1.5. THESIS OUTLINE

Chapter 2 describes the flow solver used in this work, the basic equations and the implemented rheological models. The code verification of non-Newtonian solver is discussed in Chapter 3, both for single- and two-phase flow simulations. The code is then applied in Chapter 4 to solve laminar non-Newtonian flows around a sphere, where issues related to the iterative convergence are discussed and results are compared with available literature data. Chapter 5 presents a validation exercise for a plate moving through fluid mud collected from the Port of Rotterdam area (Netherlands). The performance of the turbulence models are assessed in Chapter 6, where the modification of an existing model is also proposed. Finally, the conclusions and recommendations of this research are summarised in Chapter 7.

# 2

# MATHEMATICAL MODEL AND NUMERICAL METHODS

*...in which the governing equations, the flow solver and the implemented rheological models to simulate fluid mud are introduced. The flow is assumed to be isothermal, incompressible and turbulent. It is further assumed that water and mud are immiscible. Two of the rheological characteristics of mud (shear-thinning and yield stress behaviour) are modelled using the regularised Herschel-Bulkley model.*

## 2.1. PROBLEM FORMULATION

This research study is carried out having in mind a target situation to be simulated with CFD in which a displacement hull is sailing (not necessarily straight) above a flat solid bottom covered by a mud layer.

The flow is assumed to be isothermal, incompressible and turbulent (at least the water part). Another assumption made in this dissertation is that the disturbance of the air-water free surface can be neglected, which is especially true for deep-draught vessels navigating at low speeds in ports and waterways. Hence, the ship is assumed to be moving only through water and mud, as illustrated in Fig. 2.1.

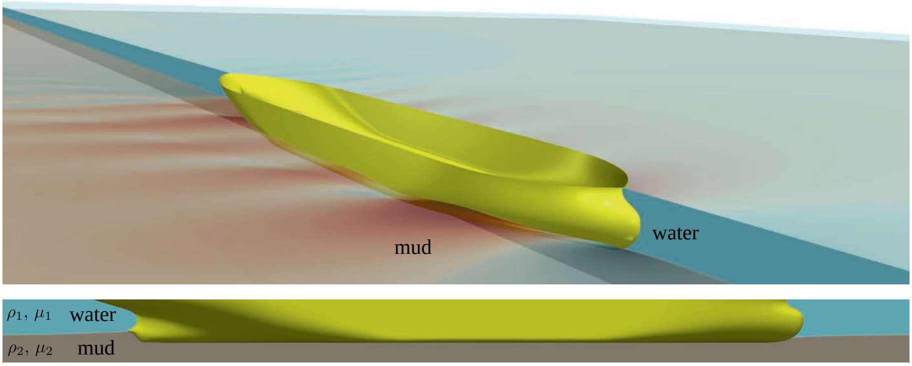

Figure 2.1: Example of a typical scenario simulated with CFD. The free-surface waves are neglected, while mud and water are assumed to be immiscible.

Furthermore, it is assumed that the high viscosity of mud combined with the stabilising effect of gravity reduces the turbulent mixing that may occur at the interface between mud and water. In other words, the two fluids are assumed to be immiscible. Previous model-scale experiments with natural mud (see Vantorre [169]) have shown that the interface between mud and water remains quite sharp during the passage of the ship. Mixing of mud and water was only observed at the higher speeds and, in any case, it occurred behind the stern of the ship so that the flow field around the hull was not affected. It is noticed, however, that if the propeller is included in the CFD simulation (e.g. using an actuator disk), the propeller-induced mixing may be strong enough to require more advanced modelling strategies in order to be accurately captured. In any case, as long as the mixing is mostly contained around the mud-water interface and astern of the ship, its effect on the force predictions for a large cargo ship can be reasonably neglected at this stage.

## 2.2. BASELINE GOVERNING EQUATIONS

The isothermal, multi-phase, turbulent and incompressible flow is modelled using the Reynolds-averaged Navier-Stokes (RANS) equations:

$$\nabla \cdot \boldsymbol{u} = 0\,, \tag{2.1}$$

$$\frac{\partial(\rho \boldsymbol{u})}{\partial t} + \nabla \cdot (\rho \boldsymbol{u}\boldsymbol{u}) = \nabla \cdot \left[ (\mu + \mu_t)(\nabla \boldsymbol{u} + \nabla \boldsymbol{u}^T) \right] - \nabla p + \rho \boldsymbol{g}\,, \tag{2.2}$$

where $\boldsymbol{u}(\boldsymbol{x}, t) \equiv (u_x, u_y, u_z)$ is the velocity vector in Cartesian coordinates as a function of the time $t$ and of the position vector $\boldsymbol{x}$; $p$ is the pressure and $\boldsymbol{g} = (0,0,g)$ the acceleration of gravity vector. The first element inside the brackets on the RHS of Eq. (2.2) is the deviatoric stress tensor, which reads:

$$\boldsymbol{\tau} = 2\mu \boldsymbol{S} \tag{2.3}$$

where $\boldsymbol{S} \equiv S_{ij} = \frac{1}{2}(\nabla \boldsymbol{u} + \nabla \boldsymbol{u}^T)$ is the deformation rate tensor and $\mu$ is the molecular viscosity of the fluid. The eddy (or turbulent) viscosity, $\mu_t$, accounts for the net turbulent diffusion of the mean momentum, in accordance with the Bousinnesq's hypothesis. The expression of $\mu_t$ will depend upon the turbulence model being used. The turbulence models considered in this work (and also typically used for maritime applications) are given in Appendices B.1 to B.3. Note that in the context of the RANS approach, all the field quantities such as velocity and pressure must be intended as Reynolds-averaged quantities (see also Section 6.2). More details about RANS modelling are given in dedicated textbooks (e.g. Wilcox [179] and Pope [135]).

The flow of two immiscible fluids is modelled in REFRESCO using the Volume-of-Fluid (VoF) method introduced by Hirt and Nichols [72], which considers a single continuum fluid having density $\rho$ and viscosity $\mu$ defined as

$$\rho = \rho_1(1-c) + \rho_2 c\,, \qquad \mu = \mu_1(1-c) + \mu_2 c\,, \tag{2.4}$$

where $c$ is the volume fraction that equals 0 and 1 in the fluid region occupied by fluid 1 (water) and 2 (mud), respectively. The interface is then assumed to be the locus of points where $c = 0.5$. The problem is closed by solving, in addition to the already-mentioned equations, the transport equation for $c$,

$$\frac{Dc}{Dt} \equiv \frac{\partial c}{\partial t} + \boldsymbol{u} \cdot \nabla c = 0\,, \tag{2.5}$$

which stems from the assumption that the volume fraction of a fluid element is constant and it is transported with the flow.

In the water region, we have that $\mu = \mu_1$, where $\mu_1$ is simply a constant corresponding to the molecular viscosity of water. In the mud region, on the other hand, $c = 1$ and so $\mu = \mu_2$. In this case, the viscosity $\mu_2$ is in general not a constant but rather a function of the fluid deformation, as we shall see in the next section.

## 2.3. MUD RHEOLOGY

In this section, a brief and general overview of the mud rheology is given. More details can be found in dedicated textbooks such as Coussot [33] and Mehta [110].

Mud is in general a cohesive material composed of water, clay, silt, sand and organic matter. At one particular location, layers of different concentrations can be found in the water column, as shown in Fig. 2.2. Nevertheless, in a first approximation, the mud is numerically modelled as one homogeneous layer. Hence, the mud layer shown in Fig. 2.1 can be seen as the top part, made of fluid mud and partly of the pre-consolidated sediments. The lower layer, made of consolidated sediment, could either be included in the homogeneous mud layer or assumed to be rigid enough to be modelled as a solid bottom.

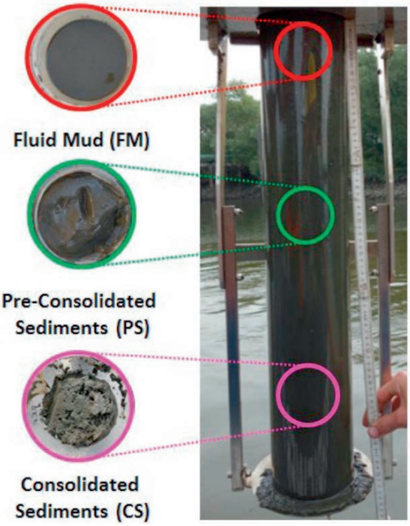

Figure 2.2: Mud at different consolidation states in a sample collector (picture adapted from Shakeel et al. [146]).

In any case, the main question is how to numerically describe the rheology of the homogenoeus (top) fluid mud layer. Generally speaking, mud displays a complex non-Newtonian rheology, with four main rheological characteristics:

1) Shear-thinning (pseudoplasticity): this effect is associated with the tendency of the flow to rearrange the microstructure of the mud in order to facilitate the shearing. As a result, the viscosity tends to decrease with increasing applied shear. The opposite behaviour is called shear-thickening (see Fig. 2.3).

2) Yield stress (viscoplasticity): mud starts to flow only when the shear stress level exceeds a threshold called yield stress, which is associated with the minimum force required to break the network formed by the particle bonds. Although the existence of an actual yield stress has been the subject of debates (Barnes and Walters [9]), its concept is still useful for modelling purposes. The yield stress is also used, in some cases, as nautical bottom criterion, as was shown in Table 1.1. Note that yield-stress fluids can be seen as particular case of shear-thinning materials, because once the structure is broken (yield stress is exceeded) the viscosity tends to decrease with increasing shear rate.

3) Thixotropy: this characteristic is associated with the fact that the rupture and recovery of the network responsible for the yield stress does not occur instantaneously. This means that, given a steady imposed shear, the viscosity will change over time until an equilibrium is reached. Hence, the relationship between deformation and applied forces is not unique but it rather depends on the shear history (see Fig. 2.3).

4) Viscoelasticity: this is the ability of the microstructure to store deformation energy. For applied stresses below the yield stress, the particle bonds are able to elastically deform and recover their original configuration once the applied forced is removed.

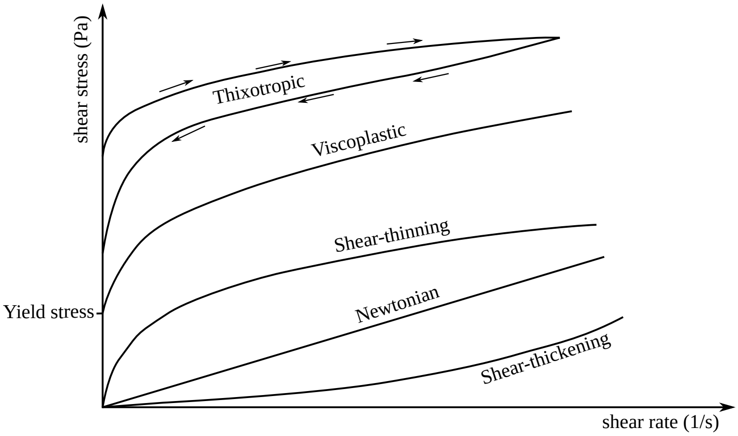

Figure 2.3: Example of flow curves for different rheological behaviours.

## 2.4. SELECTION OF THE RHEOLOGICAL MODEL

A number of options are available to mathematically describe the rheology of mud. In principle, it would be possible to elaborate a model that is advanced enough to take into account all the above mentioned rheological characteristics. The obvious advantage of using such advanced model is that a thorough description of the mud rheology would be achieved. Hence, in principle, more accurate numerical predictions would be achieved. However, at the present stage, there are a number of reasons to prefer simpler models.

First, such complex model would be computationally expensive because viscoelasticity and thixotropy would require to solve additional transport equations, which would be coupled to the already mentioned continuity, momentum, volume-fraction and turbulence equations. Second, the non-linearity of the problem would increase significantly, making more difficult the convergence of the iterative solver. Third, even assuming that this hypothetical model works perfectly, i.e. it gives the perfect representation of the flowing behaviour of mud, the parameters of the model would still rely on measurement data, which are inevitably affected by errors. Fourth, even with no measurement errors, the numerical solution would still be affected by other approximations. For example, in reality mud is not actually homogeneous because its properties can vary both vertically and horizontally. In other words, such a complex model would not be in line with the level of approximation adopted for the other physical aspects of the problem. Fifth, a complete description of the mud rheology may require more than 10 parameters. However, on a more practical level, a feasible implementation of the nautical bottom approach shall require to monitor no more than two or three mud properties, such as, for example, density, (Bingham) yield-stress and dynamic viscosity. Thus, the results obtained with such an advanced model should eventually be reduced and associated to a simpler model containing only a few parameters.

On the other side of the complexity spectrum shown in Fig. 2.4, mud could be assumed to be an inviscid fluid, as done by Sano and Kunitake [143]. While this could still be a reasonable assumption to study the wave-making resistance due to the mud undulation, it is a too crude approximation to study the manoeuvring behaviour of ships, where viscous effects cannot be entirely neglected. This would be especially true when sailing through mud, as the increase in friction due to contact with mud is not negligible. Modelling mud as a viscous Newtonian fluid, on the other hand, would certainly be an improvement with respect to the inviscid assumption, however it is not clear which value for the constant viscosity should be used.

A further step beyond the Newtonian model is to model mud as an inelastic, non-thixotropic (time-independent), yield-stress (viscoplastic) material, which is the choice adopted in this dissertation. In fact, even though the mud rheology can

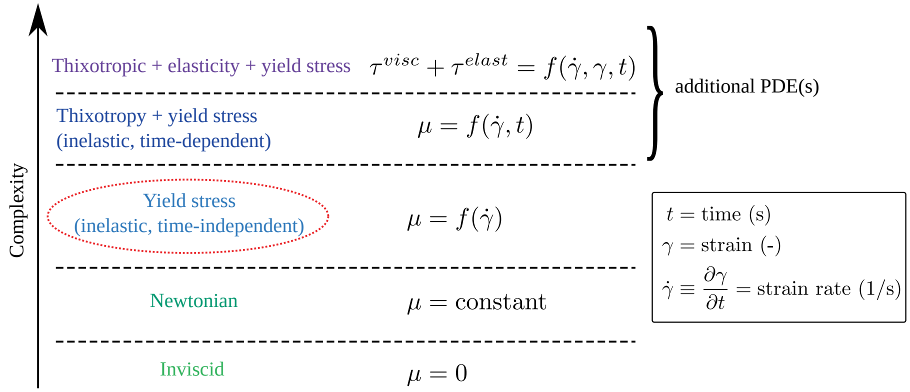

Figure 2.4: Examples of different levels of modelling complexity for the mud rheology.

vary significantly depending on the composition, a rheological characteristic that is typically observed in mud samples across different locations around the world is the yield stress. At the current state of knowledge, investigating the effect of yield stress on the ships' behaviour would be already an important step towards a better understanding of the link between mud rheology and the hydrodynamic forces acting on ships. Other effects such as thixotropy could be investigated, when deemed important, at a later stage.

### 2.4.1. THE HERSCHEL-BULKLEY MODEL

Inelastic and time-independent fluids are also classified as Generalised Newtonian Fluids (GNF), for which the stress tensor can be expressed as

$$\boldsymbol{\tau} = 2\,\mu(\dot{\gamma})\,\boldsymbol{S}, \tag{2.6}$$

where $\mu(\dot{\gamma})$ is the so-called *apparent viscosity*. For GN fluids, the apparent viscosity is uniquely determined by the local shear rate $\dot{\gamma} = 2\sqrt{S_{ij}S_{ij}/2}$, hence there is no dependency on the shear history.

Several options are available to model the yield-stress behaviour; the simplest is the Bingham model [16]. In this work, however, a more generalised version of the Bingham model is adopted. Such generalised model was proposed by Herschel and Bulkley [71], and it has already been used in the past to describe the rheology of mud (Coussot and Piau [32], Wurpts [185], and Gao et al. [62]).

The expression of the apparent viscosity for the Herschel-Bulkley model reads:

$$\begin{cases} \mu = \frac{\tau_0 + K\dot{\gamma}^n}{\dot{\gamma}}, & \tau_0 \leq \tau, \\ \mu = \infty, & \tau < \tau_0, \end{cases} \tag{2.7}$$

where $\tau_0$ (Pa) is the yield stress; $\tau = \sqrt{\tau_{ij}\tau_{ij}/2}$ (Pa) is the second invariant of $\boldsymbol{\tau}$; $n$ is a non-dimensional flow index, which determines the degree of shear-thinning ($n < 1$) or shear-thickening ($n > 1$) behaviour; $K$ (Pa s$^n$) is the consistency parameter, which has dimensions of a viscosity when $n = 1$. The infinite viscosity means that the fluid does not deform ($\boldsymbol{S} = 0$) when the stress level is below the yield stress. The Herschel–Bulkley model reduces to the Bingham model when $n = 1$, to the power-law model when $\tau_0 = 0$, and to the Newtonian model ($\mu = K$) when both $n = 1$ and $\tau_0 = 0$. For an overview and classification of different rheological models, the reader is referred to specialised textbooks (e.g. Irgens [76] and Chhabra and Richardson [30]).

### 2.4.2. REGULARISATION

The issue associated with the infinite viscosity in Eq. (2.7) is typical of viscoplastic models and it can be avoided using regularisation methods (see e.g. Saramito and Wachs [144] and Mitsoulis and Tsamopoulos [120]). These methods consist in approximating the non-differentiable constitutive equation with a smoother and differentiable equation that is valid in the whole domain, regardless of the level of shear stress. Over the years, several regularisation methods have been proposed. In REFRESCO, the Bingham model has been modified using the popular Papanastasiou regularisation [130]:

$$\mu(\dot{\gamma}) = \frac{\tau_0(1 - e^{-m\dot{\gamma}}) + K\dot{\gamma}}{\dot{\gamma}}, \tag{2.8}$$

where $m$ (s) is the regularisation parameter that is sometimes expressed in a non-dimensional form as

$$M = \frac{mU}{L}, \tag{2.9}$$

where $U$ and $L$ are the characteristic velocity and length of a particular problem. For Herschel–Bulkley fluids, the Papanastasiou regularisation would still produce an infinite viscosity for $\dot{\gamma} \to 0$ when $n < 1$. This is avoided using the modification proposed by Souza Mendes and Dutra [156]:

$$\mu(\dot{\gamma}) = \frac{\tau_0 + K\dot{\gamma}^n}{\dot{\gamma}}(1 - e^{-m\dot{\gamma}}). \tag{2.10}$$

In the limit of $m \to \infty$, both regularised models tend to the ideal (non-regularised) models. The effect of the regularisation on the Bingham flow curve is illustrated in

Fig. 2.5 as an example. Note that thanks to the regularisation parameter, the implementation of Herschel-Bulkley model in an existing CFD solver becomes relatively straightforward, although at the cost of introducing a new and somewhat arbitrary parameter.

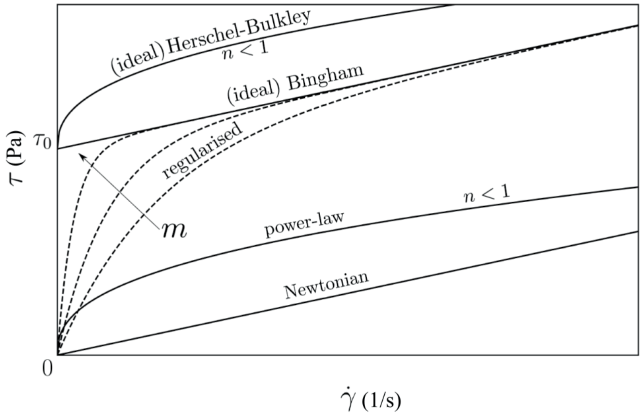

Figure 2.5: Shear stress versus shear rate for the Newtonian, power-law, Bingham and Herschel-Bulkley model. The dashed lines show the effect of the regularisation on the Bingham model. The axes are in linear scales.

## 2.5. FLOW SOLVER

As already mentioned in Chapter 1, the CFD code used for the present work is REFRESCO (Vaz et al. [172]), a viscous-flow code currently being developed and verified for maritime purposes by MARIN in collaboration with several non-profit organisations around the world. The code solves multi-phase (unsteady) incompressible flows using momentum, continuity and volume-fraction transport equations. A number of other features such as deforming grids and cavitation models are also included, however they are not considered in this dissertation.

The equations are discretised in strong-conservation form with the finite-volume method for unstructured meshes with cell-centred co-located variables. Spurious pressure oscillations arising from the co-located arrangement are prevented using the pressure-weighted interpolation method (Miller and Schmidt [118]). Mass conservation is ensured with a pressure-correction equation based on the SIMPLE algorithm (Klaij and Vuik [86]). Details about the above mentioned numerical techniques can be found in a number of textbooks (see for instance Ferziger et al. [59]), hence they are not further discussed. Other numerical settings that may vary from one simulation to another will be progressively reported in the rest of this dissertation.

# 3

# CODE VERIFICATION OF THE NON-NEWTONIAN FLUID SOLVER

*...in which the non-Newtonian solver of* REFRESCO *is verified for simulations of Herschel–Bulkley flows to ensure that the code is free of mistakes and numerical algorithm deficiencies. The code verification is performed using the method of manufactured solutions (MMS) and it comprehends three exercises: (Case 1) steady single-phase flow; (Case 2) unsteady two-phase flow with a smooth and continuous interface; (Case 3) unsteady two-phase flow with a free surface.*

---

The work in this chapter is based on the published article “Lovato, S., Toxopeus, S. L., Settels, J. W., Keetels, G. H. and Vaz, G. (2021). Code verification of non-Newtonian fluid solvers for single-and two-phase laminar flows. *Journal of Verification, Validation and Uncertainty Quantification*, 6(2)" [101].

## 3.1. INTRODUCTION

It is important that the implementation of new features is followed by code verification (Roache [140] and Oberkampf and Roy [127]) to ensure that the code is free of mistakes and numerical algorithm deficiencies. The most rigorous code verification exercise is the order-of-accuracy test, which consists of demonstrating that the rate of convergence of the discretisation error tends to the theoretical/expected order of accuracy with grid/time step refinement.

A typical way to verify a code is to numerical solve a simple problem for which the analytical solution is known. However, analytical solutions for non-Newtonian fluid flows are rather scarce, thus performing code verification tends to be more challenging than for Newtonian flows. When analytical solutions exist, such as Poiseuille/channel flow of Herschel-Bulkley fluids (see e.g. Wu et al. [184] and Grasinger et al. [68]), they are often rather simple and thus they exercise only few terms of the governing equations, giving more chances to coding mistakes to go undetected.

Furthermore, non-Newtonian models are sometimes modified by regularisation methods, as in the present work (Section 2.4.2), making analytical solutions (that are valid for non-regularised models) inadequate for code verification purposes. A possibility to perform code verification for regularised models is to generate a very accurate numerical solution of the governing equations using a very large number of grid points, typically for a simple problem. Then, this ‘quasi-exact’ solution can be used as reference for the estimation of the discretisation errors. Such procedure has been applied, for instance, in Lovato et al. [100] for 2D Poiseuille flows of Herschel-Bulkley fluids.

A more rigorous alternative is offered by the method of manufactured solutions (MMS) [139, 127]. The method consists of adding source terms to the right-hand side of the governing equations in such a way that a previously chosen (manufactured) solution is the exact solution of the modified equations. Examples of code verification of Newtonian fluid solvers based on MMS can be found in Turgeon and Pelletier [167], Knupp [88], Eça et al. [52], Veluri et al. [173], Blais and Bertrand [18], Choudhary et al. [31], and Eça et al. [51] and in the references therein. On the other hand, in the context of non-Newtonian fluids, formal code verification studies based on MMS have started to appear only recently in the literature (Venkatesan and Ganesan [174], Kim and Reddy [83], Carrozza et al. [27], and Kim and Park [82]).

This chapter illustrates a code verification study based on MMS on three test cases of increasing complexity using the Herschel–Bulkley model: (Case 1) steady single-phase flow (Section 3.5); (Case 2) unsteady two-phase flow with a smooth and continuous interface (Section 3.6); (Case 3) unsteady two-phase flow with a free surface (Section 3.7).

Note that although only the verification with Herschel–Bulkley is discussed in this chapter, the code has been verified also for power-law and Bingham.

## 3.2. GOVERNING EQUATIONS

The governing equations considered for the verification of single-phase flows are:

$$\nabla \cdot \boldsymbol{u} = 0\,, \tag{3.1}$$

$$\frac{\partial(\rho \boldsymbol{u})}{\partial t} + \nabla \cdot (\rho \boldsymbol{u}\,\boldsymbol{u}) = \nabla \cdot \boldsymbol{\tau} - \nabla p + \rho \boldsymbol{g}\,. \tag{3.2}$$

For the two-phase flow cases, the density $\rho$ and viscosity $\mu$ becomes

$$\rho = \rho_1(1-c) + \rho_2 c\,, \qquad \mu = \mu_1(1-c) + \mu_2 c\,, \tag{3.3}$$

where $c$ is the volume fraction, which is equal to 0 and 1 in the fluid region occupied by fluid 1 and 2, respectively. Note that, if fluid 1 is an Herschel–Bulkley fluid, the viscosity $\mu_1$ is not simply a constant but rather a function of the shear rate by virtue of Eqs. (2.8) and (2.10). The problem is closed by solving, in addition to the continuity and the momentum equations, the transport equation for $c$,

$$\frac{\partial c}{\partial t} + \boldsymbol{u} \cdot \nabla c = 0\,. \tag{3.4}$$

## 3.3. VERIFICATION PROCEDURE

### 3.3.1. THE METHOD OF MANUFACTURED SOLUTIONS

The MMS is a powerful tool to generate analytical solutions for code verification purposes. A complete description of the MMS can be found, for example, in Roache [139] and Oberkampf and Roy [127]. In brief, an arbitrary (manufactured) solution is chosen and substituted in the governing equations; the remaining terms are then considered as source terms. In other words, the manufactured solution is the solution of a new set of equations that differs from the original one by additional source terms. Such source terms can be obtained with the aid of computer algebra systems. For the present study, the expressions of the source terms were obtained with the free software Maxima [107]. The scripts used to generate the source terms are reported in [101].

### 3.3.2. DISCRETISATION ERROR AND ORDER OF ACCURACY

It is generally accepted to divide numerical errors into three components: the round-off error, the iterative error and the discretisation error [1]. Code verification requires

---

[1] For periodic flows, there is also the contribution of statistical errors (Eça et al. [50]), which are out of the scope of this article.

the evaluation of the discretisation error, therefore the other two components must be reduced to negligible levels.

Round-off errors are due to the finite precision of computers and, for the calculations in this article, they can be safely neglected using double-precision number format. On the other hand, iterative errors arise from the use of iterative methods to solve the non-linear system of equations. Their contribution can be neglected by reducing the residuals to machine accuracy, although for practical applications less strict criteria are often sufficient. For the present work, we ensured that the convergence tolerances adopted for the residuals were sufficiently strict to avoid contamination of discretisation errors by iterative errors. This was done by systematically reducing the convergence tolerance until numerical errors were no longer influenced by the choice of the convergence tolerance [2]. Therefore, in the remainder, it can be safely assumed that the contributions of iterative and round-off errors are both negligible compared to the contribution of the discretisation error.

Discretisation errors stem from discretisation of space and time derivatives in the governing equations. The standard approach is to assume that the discretisation error $e(\phi)$ of any local or functional quantity $\phi$ follows a truncated power-series behaviour (Roache [138] and Eça et al. [51]). Thus, for steady calculations, the discretisation reads:

$$e(\phi_i) = \phi_i - \phi_{exact} = e_0 + \alpha\left(\frac{h_i}{h_1}\right)^p, \tag{3.5}$$

where $\phi_{exact}$ is the exact solution of the mathematical model, $\phi_i$ is the computed solution on a grid having cell size $h_i$ ($i = 1$ corresponds to the finest grid), $\alpha$ is a constant, $e_0$ is the extrapolated error for cell size zero ($h_i = 0$) and $p$ is the observed order of grid convergence. The three constants $e_0$, $\alpha$ and $p$ can be determined knowing the error on at least three grids. In this paper, the three selected grids cover a refinement ratio of about 2.

In Eq. (3.5) it is implicitly assumed that the grid refinement is constant for the whole grid, allowing the use of one parameter (cell size in this case) as representative of the grid resolution. In other words, the grids are assumed to be geometrically similar. The consequences of using unsimilar grids in code verification are discussed in Eça et al. [51].

For unsteady calculations, the error is a function of both the grid size $h_i$ and the time step $\tau_i = \Delta t_i$,

$$e(\phi_i) = \phi_i - \phi_{exact} = e_0 + \alpha_x\left(\frac{h_i}{h_1}\right)^{p_x} + \alpha_t\left(\frac{\tau_i}{\tau_1}\right)^{p_t}, \tag{3.6}$$

where $\tau_1$ is the smallest time step. By writing the grid refinement as a function of the

---

[2] We also made sure that residuals did not stagnate.

time step or vice versa,

$$\left(\frac{h_i}{h_1}\right) = \left(\frac{\tau_i}{\tau_1}\right)^{\frac{p_t}{p_x}} \quad or \quad \left(\frac{\tau_i}{\tau_1}\right) = \left(\frac{h_i}{h_1}\right)^{\frac{p_x}{p_t}}, \tag{3.7}$$

the form of Eq. (3.5) is retrieved:

$$e(\phi_i) = \phi_i - \phi_{exact} = e_0 + \alpha\left(\frac{\lambda_i}{\lambda_1}\right)^p, \tag{3.8}$$

where

$$\frac{\lambda_i}{\lambda_1} = \frac{h_i}{h_1} = \left(\frac{\tau_i}{\tau_1}\right)^{\frac{p_t}{p_x}}, \tag{3.9}$$

and $e_0$, $\alpha$ and $p$ have the same meaning as in Eq. (3.5). In this work, Eqs. (3.5) and (3.8) are used to estimate $e_0$, $\alpha$ and $p$ for steady and unsteady simulations, respectively. The use of Eq. (3.6) is discussed in Eça et al. [50].

While errors are evaluated at every grid cell, the convergence properties of $\phi$ will be evaluated based on the $L_1$, $L_2$ and $L_\infty$ error norms:

$$L_q[e(\phi)] = \left(\frac{1}{N_{cells}}\sum_{i}^{N_{\text{cells}}} |\phi_i - \phi_{exact}|^q\right)^{\frac{1}{q}} \quad \text{with} \quad q = 1, 2 \quad , \tag{3.10}$$

$$L_\infty[e(\phi)] = \max|\phi_i - \phi_{exact}| \quad \text{for} \quad 1 < i < N_{\text{cells}} \quad , \tag{3.11}$$

with $N_{cells}$ being the total number of grid cells.

The goal of code verification is to demonstrate the correctness of the code by showing that $e_0 = 0$ and that the observed rate of convergence $p$ matches the theoretical order of accuracy. However, some remarks should be made:

- Correct application of Eqs. (3.5) and (3.8) requires sufficiently fine grids/time steps to have the numerical solution in the asymptotic range, i.e. in the range of space/time discretisation such that the observed order $p$ is nearly constant.
- $e_0$ includes the contribution of high order terms that were neglected in Eqs. (3.5) and (3.8). Thus, at best, we can expect $e_0$ to decrease with refinement (if the code is correct) but, in any case, it cannot drop below round-off and iterative errors (Eça et al. [51]).
- The theoretical order for velocity and pressure is unknown due to the non-linearity of the system (Wesseling [176]), therefore it is common practice to replace the theoretical order with the expected order of the discretisation techniques adopted. For the present solver, we expect second-order accuracy for velocity, pressure and volume fraction, unless stated otherwise.

- In code verification one usually examines the grid/time convergence of only dependent variables. The dependent variables for the present work are velocity, pressure and volume fraction. However, as the implementation of GNF models is done by modifying the viscosity, which is a derived quantity and not a dependent variable, it is intuitive that the examination of the grid/time convergence properties of the viscosity also plays an important role for code verification of non-Newtonian fluid solvers. Unfortunately, neither the theoretical nor the expected order of accuracy of viscosity is known, thus the correctness of the viscosity will be verified by ensuring that discretisation ($e(\phi)$) and extrapolated ($e_0$) errors decrease with grid/time step refinement.

## 3.4. NUMERICAL SETTINGS

The convective flux in the momentum equation is linearised with the Picard's method and it is discretised with the Total Variation Diminishing (TVD) Harmonic scheme (Leer [93]). Other information about REFRESCO are given in Section 2.5. After each SIMPLE (outer) iteration, the computed velocity is used to evaluate first the shear rate $\dot{\gamma}$ and then the apparent viscosity $\mu(\dot{\gamma})$, by virtue of Eq. (2.10). The viscosity is then updated in the momentum equation for the next SIMPLE iteration. For the unsteady two-phase flow simulations in this chapter, time integration is performed implicitly with the second-order backward scheme (BDF2). At each implicit time step, the linearised system for velocity and pressure is solved using the SIMPLE algorithm. After each outer iteration, the calculated velocity is then used to solve the volume-fraction equation and to calculate the apparent viscosity.

It is anticipated that for Case 3 (Section 3.7), where the chosen manufactured solution has a sharp (discontinuous) interface between the fluids, the convective flux of the volume-fraction equation is discretised with an interface-capturing scheme (Klaij et al. [85]), a blend of compressive and high-resolution interpolation schemes. This scheme prevents both the smearing of the interface due to the numerical diffusion and the appearance of spurious oscillations of the volume fraction. However, for Case 2 (Section 3.6), where the interface between the fluids is not sharp, the interface-capturing scheme is not suitable. In fact, in this case the interface-capturing scheme would tend to sharpen the interface, causing large numerical errors in the volume fraction. For this reason, the convective flux of the volume-fraction equation for Case 2 is discretised with the TVD Harmonic scheme.

## 3.5. CASE 1: STEADY SINGLE-PHASE FLOW

### 3.5.1. TEST CASE SET-UP

The first code verification exercise assesses the correctness of the implementation of the Herschel–Bulkley model for laminar single-phase flows using the manufactured solution from Salari and Knupp [142], Knupp [88], and Eça et al. [51]:

$$\begin{aligned} u_x(x,y) &= \sin(x^2+y^2)+\varepsilon\,, \\ u_y(x,y) &= \cos(x^2+y^2)+\varepsilon\,, \\ p(x,y) &= \sin(x^2+y^2)+\varepsilon\,, \end{aligned} \tag{3.12}$$

where $\varepsilon = 0.001$ is a small constant added to avoid symmetry in the solution. Note that the manufactured solution is not divergence-free, therefore the term $-2/3(\nabla\cdot\boldsymbol{u})\,\delta_{ij}$ must be included in the stress tensor, with $\delta_{ij}$ being the Kronecker delta. With this manufactured solution, pressure is expected to be first-order accurate at the boundaries for the reasons explained in Eça et al. [51].

In order to obtain asymptotic grid convergence without excessive grid resolution, large viscosity gradients should be avoided. This is achieved (a) by selecting low values for both the yield stress and the regularisation parameter (thus limiting the maximum viscosity) and (b) by moving the computational domain away from the axes origin. The latter stems from the fact that $\dot{\gamma}(0,0) = 0$ and so the viscosity variation is steeper around the origin. This results in a relatively small variation of the viscosity within the domain (Fig. 3.1), especially when compared with realistic flow conditions in which the viscosity in low-deformation regions can be thousands times larger than the viscosity in high-deformation regions (e.g. in boundary-layer flows). We recall however that code verification is purely a mathematical exercise, therefore physical realism is not required (Roache [139]).

On the other hand, a convenient choice of the fluid density should ensure a dominant contribution of the viscous term in the momentum equations. By doing so, there are more chances that anomalies in the viscous term will be detected from the convergence properties of velocity and pressure. With the current choice of fluid properties, convective and pressure terms in the momentum equations have about the same order of magnitude, whereas the diffusive term is about one order of magnitude larger (Fig. 3.2).

The domain is discretised with 21 two-dimensional uniform Cartesian grids, the finest grid having 640 × 640 cells. Dirichlet conditions based on the manufactured velocity are applied to all boundaries together with Neumann conditions for pressure. Since no pressure boundaries are used, a reference pressure is imposed in one point using the exact pressure. Furthermore, pressure and viscosity are both linearly extrapolated to the boundaries using the gradient from the previous outer iteration.

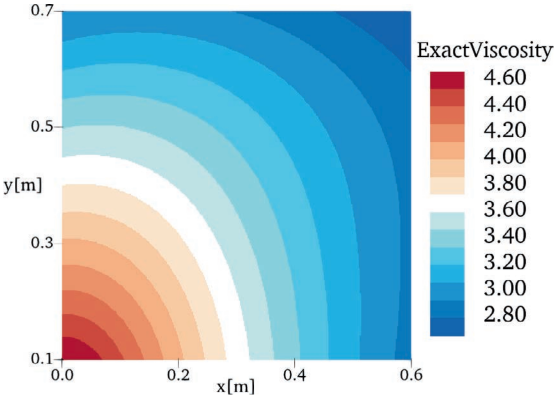

Figure 3.1: Exact viscosity $\mu(x, y)$ [Pa s] of the regularised Herschel–Bulkley model for Case 1.

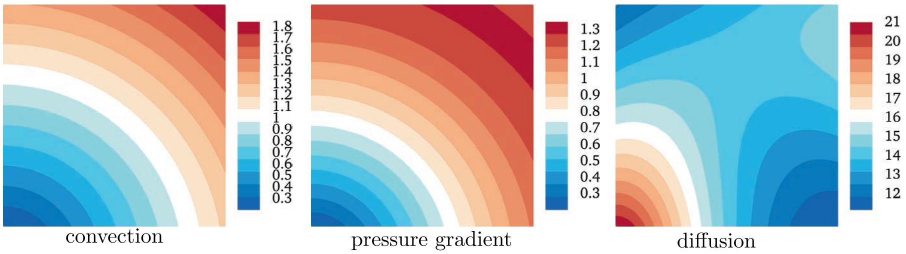

Figure 3.2: Magnitude of convection, pressure and diffusion terms [N m$^{-3}$] corresponding to the manufactured solution of Case 1.

The parameters used for the calculations are given in Table A.3 in the appendix.

### 3.5.2. Results and Discussion

The $L_2$ and $L_\infty$ error norms and the observed order of convergence $p$ are reported in Table 3.1 as function of grid refinement. All quantities appear to be in the asymptotic range for about $h_i/h_1 < 4$, where $p$ is nearly constant. Velocity matches the expected second-order both for the $L_2$ and the $L_\infty$ error norms, whereas the pressure coefficient, $C_p = p/(0.5\rho U_{ref}^2)$, exhibits first-order accuracy in the $L_\infty$ error norm. The largest errors were found near the boundaries, with the maximum error on the top left corner. This confirms that pressure is first-order accurate at the boundaries, as expected. As a result of the first-order behaviour at the boundaries and second-order on interior cells, the $L_2$ error norm of $C_p$ converges with $p \approx 1.9$. It is also remarkable that the grid convergence properties of velocity and pressure with the Herschel–Bulkley model are very similar to those of the verification exercise in Eça et al. [51] with the same manufactured solution and Newtonian fluids.

Table 3.1: $L_2$ and $L_\infty$ error norms and observed order of convergence $p$ for velocity, pressure coefficient and viscosity for Case 1.

| $h_i/h_1$ | $L_2[e(u)]$ | $p$ | $L_2[e(C_p)]$ | $p$ | $L_2[e(\mu)]$ | $p$ | $L_\infty[e(u)]$ | $p$ | $L_\infty[e(C_p)]$ | $p$ | $L_\infty[e(\mu)]$ | $p$ |
|---|---|---|---|---|---|---|---|---|---|---|---|---|
| 16.00 | 1.23E-05 | 2.00 | 5.27E-04 | 1.86 | 8.06E-05 | 1.77 | 1.03E-04 | 1.99 | 4.71E-02 | 0.70 | 7.16E-03 | 0.98 |
| 13.33 | 8.55E-06 | 2.00 | 3.78E-04 | 1.78 | 5.76E-05 | 1.79 | 7.20E-05 | 1.99 | 3.99E-02 | 0.78 | 5.97E-03 | 0.98 |
| 11.23 | 6.06E-06 | 2.00 | 2.78E-04 | 1.81 | 4.19E-05 | 1.81 | 5.12E-05 | 1.99 | 3.39E-02 | 0.81 | 5.03E-03 | 0.98 |
| 9.28 | 4.14E-06 | 2.00 | 1.96E-04 | 1.88 | 2.93E-05 | 1.82 | 3.50E-05 | 1.98 | 2.84E-02 | 0.81 | 4.16E-03 | 0.99 |
| 8.00 | 3.08E-06 | 2.00 | 1.49E-04 | 1.77 | 2.23E-05 | 1.83 | 2.61E-05 | 1.98 | 2.47E-02 | 0.88 | 3.59E-03 | 0.99 |
| 6.53 | 2.05E-06 | 2.00 | 1.03E-04 | 1.77 | 1.52E-05 | 1.84 | 1.74E-05 | 1.98 | 2.03E-02 | 0.90 | 2.93E-03 | 0.99 |
| 5.47 | 1.44E-06 | 2.00 | 7.40E-05 | 1.83 | 1.09E-05 | 1.85 | 1.22E-05 | 1.99 | 1.71E-02 | 0.90 | 2.46E-03 | 0.99 |
| 4.60 | 1.02E-06 | 2.00 | 5.38E-05 | 1.83 | 7.88E-06 | 1.86 | 8.71E-06 | 1.99 | 1.45E-02 | 0.92 | 2.07E-03 | 0.99 |
| 4.00 | 7.69E-07 | 2.00 | 4.15E-05 | 1.84 | 6.04E-06 | 1.87 | 6.59E-06 | 1.99 | 1.27E-02 | 0.93 | 1.80E-03 | 0.99 |
| 3.23 | 5.02E-07 | 2.00 | 2.79E-05 | 1.84 | 4.03E-06 | 1.87 | 4.32E-06 | 1.98 | 1.03E-02 | 0.94 | 1.45E-03 | 1.00 |
| 2.71 | 3.54E-07 | 2.00 | 2.01E-05 | 1.84 | 2.89E-06 | 1.88 | 3.05E-06 | 1.98 | 8.66E-03 | 0.95 | 1.22E-03 | 1.00 |
| 2.28 | 2.49E-07 | 2.00 | 1.45E-05 | 1.85 | 2.07E-06 | 1.88 | 2.15E-06 | 1.98 | 7.29E-03 | 0.96 | 1.03E-03 | 1.00 |
| 2.00 | 1.92E-07 | 2.00 | 1.14E-05 | 1.85 | 1.62E-06 | 1.89 | 1.66E-06 | 1.98 | 6.42E-03 | 0.96 | 9.01E-04 | 1.00 |
| 1.61 | 1.24E-07 | 2.00 | 7.54E-06 | 1.86 | 1.07E-06 | 1.89 | 1.08E-06 | 1.98 | 5.17E-03 | 0.97 | 7.24E-04 | 1.00 |
| 1.35 | 8.80E-08 | 2.00 | 5.45E-06 | 1.86 | 7.68E-07 | 1.90 | 7.64E-07 | 1.99 | 4.36E-03 | 0.97 | 6.10E-04 | 1.00 |
| 1.14 | 6.21E-08 | 2.00 | 3.92E-06 | 1.87 | 5.51E-07 | 1.90 | 5.40E-07 | 1.99 | 3.67E-03 | 0.98 | 5.12E-04 | 1.00 |
| 1.00 | 4.81E-08 | 2.00 | 3.08E-06 | 1.87 | 4.31E-07 | 1.90 | 4.18E-07 | 1.99 | 3.23E-03 | 0.98 | 4.51E-04 | 1.00 |

The grid convergence properties of $\mu$ are very similar to $C_p$, with a rate of convergence about 1.9 for the $L_2$ norm and with first-order for the $L_\infty$ norm. The maximum error was found on the top boundary, where also the maximum error of the tangential velocity derivative is located. It was observed that velocity derivatives converged with first-order accuracy at the boundaries [3]. Thus, it appears that the first-order accuracy of velocity derivatives leads to first-order accuracy of the viscosity, as a result of their dependency (Eq. (2.10)).

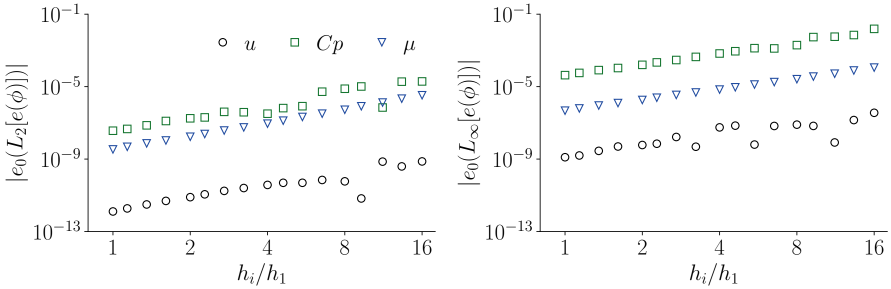

Figure 3.3: Extrapolated error for cell size zero $e_0$ for the $L_2$ and $L_\infty$ error norms as function of grid refinement for Case 1.

The examination of the extrapolated error for cell size zero $e_0$ is convenient when $p$ does not match the theoretical (expected) order of grid convergence or when the asymptotic order of convergence is hard to determine (Eça et al. [51]). For the present exercise, this is the case of viscosity and pressure. Nonetheless, $e_0$ decreases upon grid refinement for all quantities and for both norms (Fig. 3.3), providing convincing evidence about the correctness of the code.

Larger values of the yield stress and regularisation parameter were also tested, and results were virtually identical to those reported in Table 3.1, except for marginally larger discretisation errors for all quantities. Larger errors are in fact expected for larger yield stress and regularisation parameters because of the increased viscosity gradient (Syrakos et al. [159]). We mention, however, that increasing the regularisation parameter to very large values, as normally required by practical applications, is neither necessary nor convenient for code verification. In fact, using large regularisation parameters will likely cause stagnation of residuals[4] and consequent contamination of numerical errors by iterative errors. Moreover, even when residuals converge, asymptotic grid convergence may be difficult to achieve. In any case, it is shown in Appendix A.1 that, with the adopted choice of yield stress and regularisation parameter, this exercise is very sensitive to coding mistakes in the rheological model.

In conclusion, for all quantities, the observed orders matched the expected or-

---

[3] This is because the velocity derivatives are computed with the Gauss's theorem, which is a second-order method but it reduces to first order at the boundary, even on Cartesian grids (Syrakos et al. [162]).

[4] Stagnation of residuals for large regularisation parameters is a known issue for SIMPLE-type solvers (Syrakos et al. [159]). The robustness of the code will be addressed in Chapter 4 on a benchmark problems.

ders, and the extrapolated errors $e_0$ tend to zero upon grid/time step refinement. Furthermore, the grid convergence properties of velocity and pressure are analogous to the verification with Newtonian fluids in Eça et al. [51]. The code can thus be considered verified for laminar single-phase flow of Herschel–Bulkley fluids.

## 3.6. CASE 2: UNSTEADY TWO-PHASE FLOW WITH A CONTINUOUS INTERFACE

### 3.6.1. TEST CASE SET-UP

This exercise verifies that laminar flows of Herschel–Bulkley fluids are correctly solved also for two-phase flows. The manufactured solution is taken from Klaij et al. [85] and it represents a sinusoidal wave moving at speed $c$ on deep water from potential flow theory (Larsson and Raven [91]):

$$u_x(x,z,t) = \frac{g}{c} A \exp\left(\frac{gz}{c^2}\right) \cos\left(\frac{gx}{c^2} - \frac{gt}{c}\right), \tag{3.13}$$

$$u_z(x,z,t) = \frac{g}{c} A \exp\left(\frac{gz}{c^2}\right) \sin\left(\frac{gx}{c^2} - \frac{gt}{c}\right), \tag{3.14}$$

$$p(x,z,t) = \rho g \Big(\zeta(x,z,t) - z\Big), \tag{3.15}$$

$$c(x,z,t) = \frac{1}{2}\left(1 + \operatorname{erf}(b(z - \zeta(x,z,t)))\right), \tag{3.16}$$

where $\zeta$ is the wave elevation,

$$\zeta(x,z,t) = A \exp\left(\frac{gz}{c^2}\right) \cos\left(\frac{gx}{c^2} - \frac{gt}{c}\right). \tag{3.17}$$

The pressure is assumed to be zero at the free surface, i.e. at $z = \zeta$. We recall that the above solution describes the circular motion of fluid particles for $z \le \zeta$. However, for code verification purposes, the above solution is applied also for $z > \zeta$.

The parameter $b$ in the error function erf in Eq. (3.16) determines how steeply the volume fraction (and fluid properties) varies around $z = \zeta$. The error function assumes values from 0 to 1 over a distance of about $2/b$. Thus, if $2/b$ is less than the cell size, the volume fraction is discontinuous at the discrete level. Verification with a discontinuous solution is more challenging because the asymptotic grid/time convergence is extremely hard to achieve, thus we postpone it to Section 3.7. For the present test case we considered $b = 12$, which produces a smooth and continuous variation of the volume fraction from one fluid to the other (Fig. 3.4). Note that the viscosity of fluid 1 (right plot in Fig. 3.4) varies in space not only because of the volume fraction but also because fluid 1 is non-Newtonian.

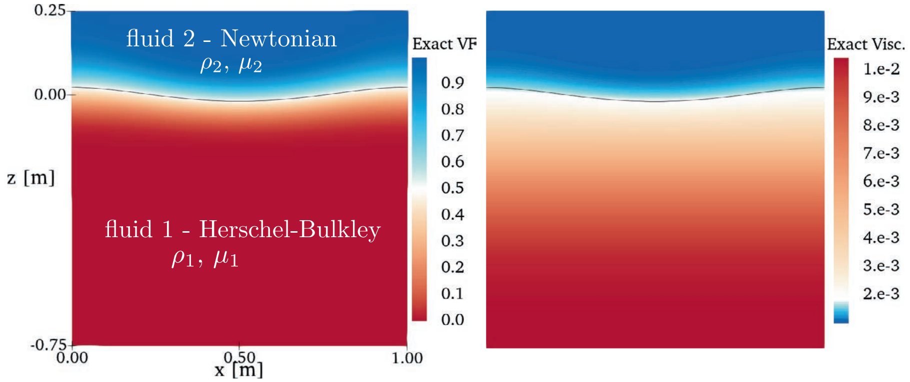

Figure 3.4: Exact volume fraction (left) and viscosity [Pa s] (right) for Case 2 at $t = 0$ with steepening parameter $b = 12$. The black isoline corresponds to $c = 0.5$.

Considering a smooth interface increases the chances of achieving asymptotic grid/time convergence with reasonable grid/time resolution. The drawback is that special treatments for discontinuities may not be fully exercised by the verification. Therefore, a successful outcome from this exercise can be seen as a necessary but not sufficient condition to ensure that the code works correctly for free-surface calculations with Herschel–Bulkley fluids. On the other hand, this test case well represents those applications where the interface between two liquids (e.g. between water and mud suspensions) is not as sharp as a gas-liquid interface. For such applications, one might sometimes avoid the use of interface-capturing schemes, thus allowing smearing of the interface by diffusion (molecular, turbulent and/or numerical). In light of the above considerations, liquid-like properties are assigned to both fluids to justify the use of a smooth interface between the fluids.

The computational domain is a square with sides of 1.0 m, discretised with 21 two-dimensional uniform Cartesian grids, the finest grid having 640 × 640 cells. Dirichlet boundary conditions based on the manufactured velocity and volume fraction are applied to all boundaries together with Neumann conditions for pressure. As for Case 1, pressure and viscosity are both linearly extrapolated to the boundaries using their gradients from the previous outer iteration.

Calculations are initialised with the manufactured solution and are carried out for one wave period $T$. The time steps are chosen such that the CFL numbers are less than 1/6 to ensure that the BDF2 scheme is TVD (Duraisamy et al. [43] and Klaij et al. [85]), and the time step for the finest grid is $\tau_1 = T/4800$. Time steps are refined using the same ratio as the grid refinement, i.e. $h_i/h_1 = \tau_i/\tau_1 = \lambda_i/\lambda_1$. The parameters used for the computations are summarised in Table A.3 in the appendix.

Table 3.2: $L_1$ and $L_2$ error norms and observed order of convergence $p$ for Case 2.

| $\lambda_i/\lambda_1$ | $L_1[e(u)]$ | $p$ | $L_1[e(C_p)]$ | $p$ | $L_1[e(c)]$ | $p$ | $L_1[e(\mu)]$ | $p$ | $L_2[e(u)]$ | $p$ | $L_2[e(C_p)]$ | $p$ | $L_2[e(c)]$ | $p$ | $L_2[e(\mu)]$ | $p$ |
|---|---|---|---|---|---|---|---|---|---|---|---|---|---|---|---|---|
| 16.00 | 1.12E-03 | 2.08 | 1.32E-02 | 2.15 | 4.18E-03 | 2.42 | 3.00E-02 | 2.00 | 1.70E-03 | 2.08 | 2.09E-02 | 2.18 | 8.41E-03 | 2.35 | 3.87E-02 | 1.92 |
| 13.33 | 7.73E-04 | 2.04 | 8.98E-03 | 2.08 | 2.66E-03 | 2.59 | 2.09E-02 | 2.00 | 1.16E-03 | 2.13 | 1.41E-02 | 2.17 | 5.44E-03 | 2.49 | 2.74E-02 | 1.92 |
| 11.23 | 5.44E-04 | 2.03 | 6.55E-03 | 2.05 | 1.79E-03 | 2.68 | 1.53E-02 | 2.00 | 8.12E-04 | 2.12 | 1.01E-02 | 2.14 | 3.71E-03 | 2.58 | 2.04E-02 | 1.90 |
| 9.28 | 3.70E-04 | 2.05 | 4.67E-03 | 2.04 | 1.16E-03 | 2.70 | 1.10E-02 | 2.00 | 5.46E-04 | 2.12 | 7.12E-03 | 2.12 | 2.45E-03 | 2.61 | 1.50E-02 | 1.88 |
| 8.00 | 2.74E-04 | 2.04 | 3.16E-03 | 2.05 | 6.99E-04 | 2.69 | 7.52E-03 | 2.00 | 4.02E-04 | 2.10 | 4.75E-03 | 2.13 | 1.50E-03 | 2.59 | 1.05E-02 | 1.86 |
| 6.53 | 1.82E-04 | 2.04 | 2.18E-03 | 2.04 | 4.34E-04 | 2.64 | 5.23E-03 | 2.00 | 2.65E-04 | 2.09 | 3.23E-03 | 2.12 | 9.49E-04 | 2.53 | 7.50E-03 | 1.85 |
| 5.47 | 1.28E-04 | 2.03 | 1.53E-03 | 2.03 | 2.80E-04 | 2.56 | 3.71E-03 | 1.99 | 1.84E-04 | 2.09 | 2.25E-03 | 2.09 | 6.22E-04 | 2.46 | 5.48E-03 | 1.85 |
| 4.60 | 9.03E-05 | 2.02 | 1.04E-03 | 2.03 | 1.74E-04 | 2.46 | 2.54E-03 | 1.98 | 1.29E-04 | 2.08 | 1.51E-03 | 2.08 | 3.94E-04 | 2.37 | 3.87E-03 | 1.84 |
| 4.00 | 6.81E-05 | 2.02 | 7.72E-04 | 2.03 | 1.22E-04 | 2.39 | 1.90E-03 | 1.98 | 9.70E-05 | 2.07 | 1.11E-03 | 2.08 | 2.80E-04 | 2.31 | 2.96E-03 | 1.84 |
| 3.23 | 4.44E-05 | 2.01 | 5.12E-04 | 2.03 | 7.63E-05 | 2.30 | 1.27E-03 | 1.97 | 6.28E-05 | 2.06 | 7.33E-04 | 2.08 | 1.77E-04 | 2.23 | 2.05E-03 | 1.84 |
| 2.71 | 3.13E-05 | 2.01 | 3.57E-04 | 2.02 | 5.12E-05 | 2.24 | 8.97E-04 | 1.97 | 4.39E-05 | 2.06 | 5.08E-04 | 2.06 | 1.20E-04 | 2.18 | 1.50E-03 | 1.84 |
| 2.28 | 2.20E-05 | 2.01 | 2.52E-04 | 2.02 | 3.52E-05 | 2.18 | 6.40E-04 | 1.97 | 3.08E-05 | 2.05 | 3.57E-04 | 2.05 | 8.33E-05 | 2.13 | 1.11E-03 | 1.81 |
| 2.00 | 1.70E-05 | 2.00 | 1.90E-04 | 2.02 | 2.60E-05 | 2.13 | 4.86E-04 | 1.97 | 2.37E-05 | 2.04 | 2.68E-04 | 2.05 | 6.19E-05 | 2.10 | 8.70E-04 | 1.78 |
| 1.61 | 1.10E-05 | 2.00 | 1.23E-04 | 2.02 | 1.66E-05 | 2.08 | 3.21E-04 | 1.96 | 1.52E-05 | 2.04 | 1.73E-04 | 2.04 | 3.98E-05 | 2.06 | 6.08E-04 | 1.72 |
| 1.35 | 7.77E-06 | 2.00 | 8.66E-05 | 2.02 | 1.15E-05 | 2.06 | 2.28E-04 | 1.94 | 1.07E-05 | 2.03 | 1.21E-04 | 2.03 | 2.78E-05 | 2.05 | 4.56E-04 | 1.65 |
| 1.14 | 5.48E-06 | 2.00 | 6.09E-05 | 2.01 | 8.08E-06 | 2.06 | 1.62E-04 | 1.92 | 7.56E-06 | 2.03 | 8.51E-05 | 2.03 | 1.95E-05 | 2.04 | 3.46E-04 | 1.56 |
| 1.00 | 4.24E-06 | 2.00 | 4.69E-05 | 2.01 | 6.20E-06 | 2.04 | 1.26E-04 | 1.92 | 5.84E-06 | 2.03 | 6.55E-05 | 2.02 | 1.50E-05 | 2.03 | 2.83E-04 | 1.50 |

### 3.6.2. RESULTS AND DISCUSSION

The order of convergence $p$ and the $L_1$ and $L_2$ error norms are given in Table 3.2. It is immediately evident that errors in the velocity, pressure coefficient and volume fraction converge asymptotically with the expected second-order accuracy. The first goal of code verification is thus fulfilled for the dependent variables. The convergence of the viscosity does not appear asymptotic, with rates of convergence ranging between 1 and 2. The largest viscosity errors were found on the side and bottom boundaries, where also the largest errors of velocity derivatives are located. This suggests that local grid refinement at the boundaries is needed to reduce such errors and to achieve asymptotic convergence for the viscosity without a significant increase in the computational costs. However, local refinement, which requires the use of unstructured/non-uniform grids, is out of the scope of this chapter and it should be investigated in future studies. Another option may be to improve the discretisation of the gradients at the boundaries, but for solvers that use unstructured-grid assumptions this option is not straightforward and therefore outside of the scope of the present study. At least, the present exercise proves its usefulness by demonstrating the expected convergence behaviour for the dependent variables, while also detecting inconsistencies in the solution that went unnoticed in Case 1.

In any case, the extrapolated error $e_0$ for cell size/time step zero clearly decreases upon grid/time step refinement for all quantities (Fig. 3.5). This, combined with the second-order accuracy of the dependent variables and with the results of Case 1, provides compelling evidence that the code performs correctly also for two-phase laminar flows of Herschel–Bulkley fluids with a smooth interface.

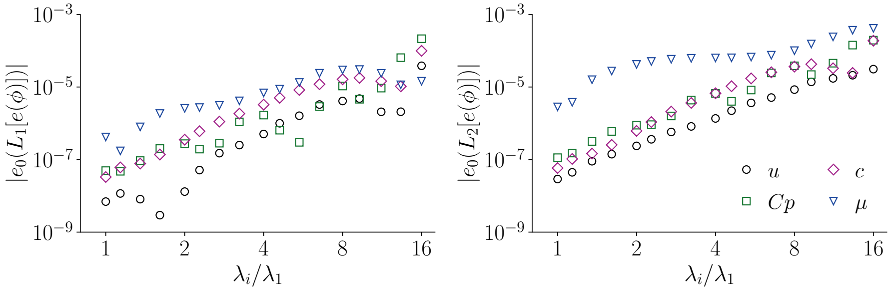

Figure 3.5: Extrapolated error for grid size/time step zero $e_0$ for the $L_1$ and $L_2$ error norms as a function of the refinement factor for Case 2.

## 3.7. CASE 3: UNSTEADY TWO-PHASE FLOW WITH A FREE SURFACE

### 3.7.1. TEST CASE SET-UP

In the previous test case we have shown that by considering a smooth interface between the fluids rigorous code verification is possible also for two-phase flows. However, for applications in which the top fluid is a gas, one usually wants to keep the interface as sharp as possible to accurately capture the free surface. It can be the case, for example, of mud slurries in an open channel or dip-coating processes (Filali et al. [60]). But it is also the case of ship sailing with muddy seabeds, where the mud-water interface is assumed to be sharp (see also Section 2.1).

In this case study we test the code on free-surface calculations by increasing the steepening parameter in the manufactured volume fraction (Eq. (3.16)) from 12 to 1200. Now the volume fraction varies between 0 and 1 over a distance about the cell size of our finest grid, hence the volume fraction is discontinuous at the discrete level, as shown in Fig. 3.6. Moreover, the convective fluxes of the volume-fraction equation are now discretised with an interface-capturing scheme, as was anticipated in Section 3.4. The grids and all the other parameters are the same as Case 2, except for fluid 2, which now has the density and viscosity of air (see Table A.3 in Appendix A.2).

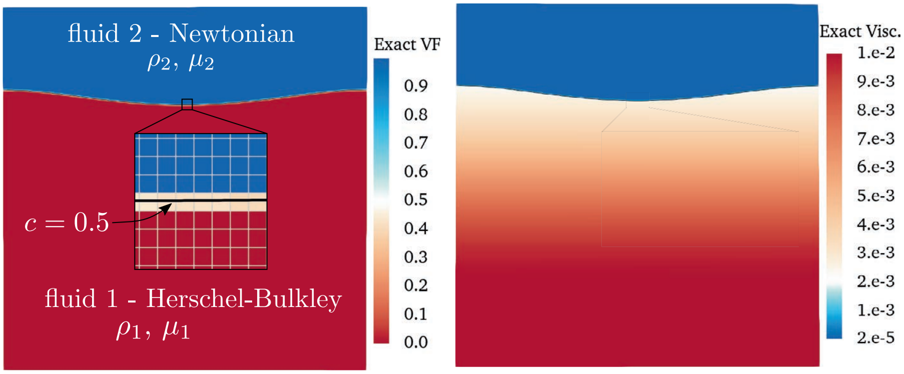

Figure 3.6: Exact volume fraction (left) and viscosity [Pa s] (right) for Case 3 at $t = 0$ with steepening parameter $b = 1200$. The black isoline corresponds to $c = 0.5$.

### 3.7.2. RESULTS AND DISCUSSION

The oscillatory convergence due to the presence of a discontinuity (free surface) is clearly noticeable from the convergence of the $L_1$ and $L_2$ error norms in Fig. 3.7, with discretisation errors that sometimes increase upon grid/time step refinement. For this reason we have estimated $\alpha$, $e_0$ and $p$ in the least-square sense by fitting Eq. (3.8) to the data on the 10 finest grids. The observed order of accuracy is thus indicated in Fig. 3.7 with $p_{ls}$.

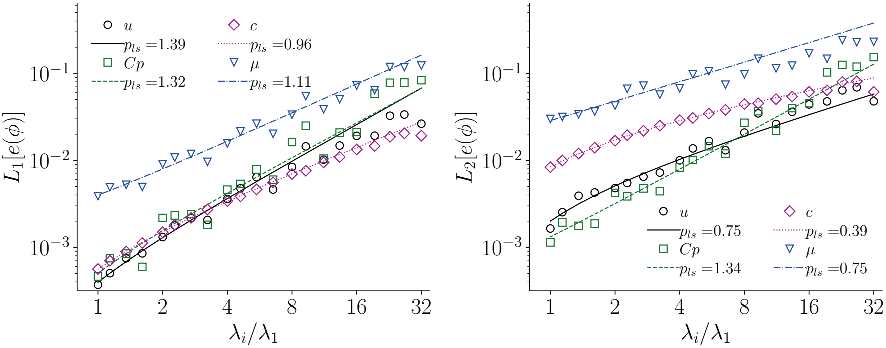

Figure 3.7: $L_1$ error norms as function of the refinement factor. $p_{ls}$ is obtained from the best weighted least-square fitting of Eq. (3.8) to data on the 10 finest grids.

A close look at the velocity errors in Fig. 3.8 reveals the presence of the well-known ‘spurious velocities’ (Klaij et al. [85]) for free-surface calculations with the VoF model. These are caused by the density-weighted interpolation scheme for pressure (Miller and Schmidt [118]), which assumes that the free surface coincides with the cell boundaries. When the free surface is not aligned with the cells boundaries, an imbalance occurs in the discretisation of the pressure gradient, which acts as a source/sink of momentum. Since $\rho\boldsymbol{u}$ is conserved across the free surface, errors in the velocity are amplified in the low-density fluid (Fig. 3.8). For this reason they are often called ‘spurious air velocities’. This explains the oscillatory convergence of pressure and velocity, and it is reassuring that, overall, there is a clear decreasing trend as the grid/time step is refined.

We remark that artefacts in the velocity have nothing to do with the use of non-Newtonian fluids. However, when non-Newtonian fluids are used, additional artefacts are generated. In fact, spurious velocities cause large errors in the shear rate $\dot{\gamma}$, as shown in the top panel of Fig. 3.9. In turn, such large errors in the shear rate produce ‘spurious viscosities’ in the non-Newtonian fluid near the free surface (bottom panel in Fig. 3.9), hence explaining the oscillatory convergence of the viscosity.

On the other hand, the convergence of the volume fraction is monotonic and exhibits a rate of convergence $p_{ls}$ for the $L_1$ error norm close to 1.0, whereas for the $L_2$ error norm $p_{ls}$ is roughly halved. These results agree with the verification of the

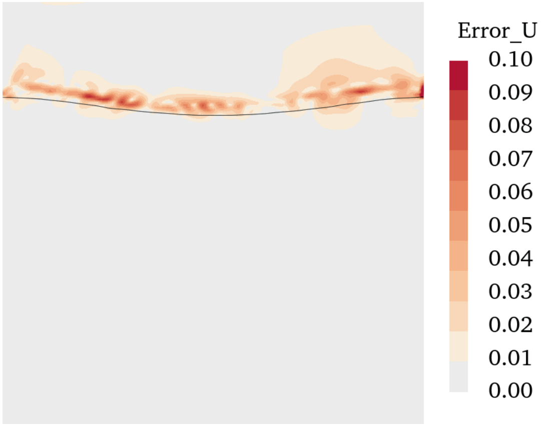

Figure 3.8: Velocity errors on the grid with $160^2$ cells. The black isoline corresponds to $c = 0.5$.

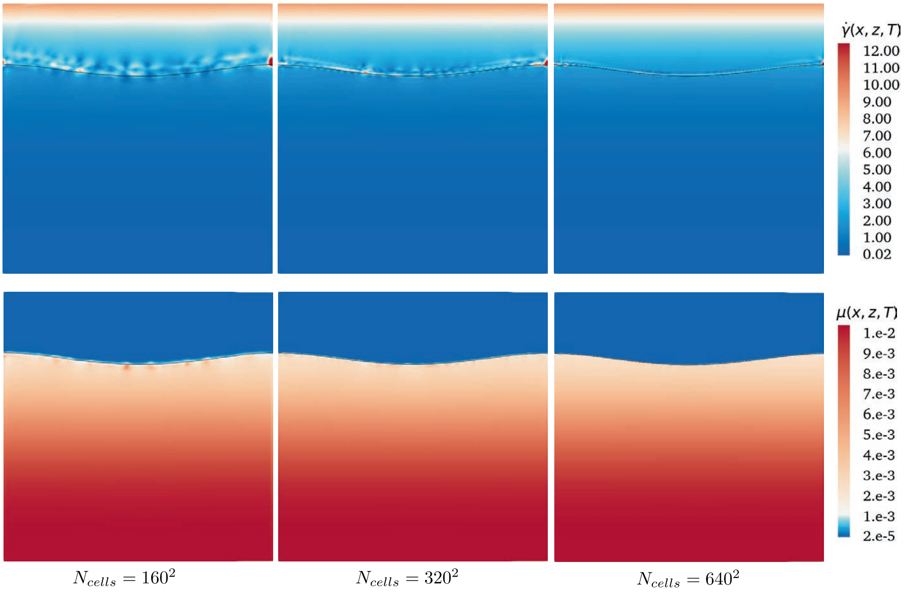

Figure 3.9: Contour plots of the shear rate $\dot{\gamma}$ [s$^{-1}$] (top panel) and the viscosity $\mu(\dot{\gamma})$ [Pa s] (bottom panel) for different refinement levels at computational time $t = T$. The artefacts caused by spurious velocities are clearly visible near the free surface on the grid with $160^2$ cells.

stand-alone volume-fraction equation with a discontinuous initial solution in Klaij et al. [85].

A common practice in code verification is to assume $e_0 = 0$ in Eqs. (3.5) and (3.8) (see e.g. Salari and Knupp [142], Veluri et al. [173], Blais and Bertrand [18], and Klaij et al. [85]). The implications of making such assumption are discussed in detail in Eça et al. [51]. The main advantage is that the observed order can be simply determined from data on grid doublets as

$$p^* [e(\phi_i)] = \frac{\log\left(e(\phi_{i-1})/e(\phi_i)\right)}{\log(2)}, \tag{3.18}$$

where, in this case, the selected grids cover a refinement ratio of 2.

For the present exercise we assumed $e_0 = 0$ for two reasons. First, solving a non-linear system of three equations to determine $e_0$, $\alpha$ and $p$ was not possible because of the oscillatory grid/time convergence caused by the above-mentioned spurious velocities. Second, the present results can be more easily compared with the work of Klaij et al. [85], where the order of convergence was also determined assuming $e_0 = 0$. With this in mind, the discretisation error and order of convergence $p^*$ are reported in Table 3.3.

The convergence of the $L_1$ error of pressure and volume fraction is similar to Klaij et al. [85]: pressure errors converge with order oscillating between 1 and 2, whereas the volume fraction is well-behaved and its order of convergence reaches 1.4. On the other hand, our velocity errors appear to be reaching second-order accuracy, in contrast with the order close to 2/3 in Klaij et al. [85]. Such difference is due to the different boundary conditions applied on the bottom boundary. In Klaij et al. [85] a Dirichlet condition for pressure was imposed on the bottom using the exact pressure at $t = 0$, whereas in the present work we imposed a Dirichlet condition for velocity using the exact velocity at each time step. This, combined with the slightly finer grids of the present work, produced a better convergence of the velocity error compared to (Klaij et al. [85]).

To summarise, while results of this code verification exercise are less conclusive than Case 2, errors of all quantities have a clear decreasing trend upon grid/time step refinement, and the order $p^*$ compares favourably with an earlier verification exercise performed with only Newtonian fluids (Klaij et al. [85]). We have also shown that the oscillatory convergence is due to the presence of spurious velocities, a known issue for many free-surface calculations performed using the VOF method and the density-weighted interpolation scheme.

Finally, the exercise revealed that spurious velocities produce artefacts in the viscosity of the non-Newtonian fluid, but it was just shown that such artefacts tend to disappear with grid/time step refinement. For practical applications where high

Table 3.3: $L_1$ and $L_2$ error norms and observed order of convergence $p^*$ (Eq. (3.18)) for Case 3.

| $\lambda_i/\lambda_1$ | $L_1[e(u)]$ | $p^*$ | $L_1[e(C_p)]$ | $p^*$ | $L_1[e(c)]$ | $p^*$ | $L_1[e(\mu)]$ | $p^*$ | $L_2[e(u)]$ | $p^*$ | $L_2[e(C_p)]$ | $p^*$ | $L_2[e(c)]$ | $p^*$ | $L_2[e(\mu)]$ | $p^*$ |
|---|---|---|---|---|---|---|---|---|---|---|---|---|---|---|---|---|
| 32 | 2.64E-02 | - | 8.37E-02 | - | 1.92E-02 | - | 1.23E-01 | - | 4.78E-02 | - | 1.54E-01 | - | 6.13E-02 | - | 2.30E-01 | - |
| 16 | 1.91E-02 | 0.46 | 2.12E-02 | 1.98 | 1.34E-02 | 0.53 | 7.24E-02 | 0.76 | 4.40E-02 | 0.12 | 4.55E-02 | 1.76 | 6.14E-02 | 0.00 | 1.71E-01 | 0.43 |
| 8 | 8.40E-03 | 1.19 | 1.63E-02 | 0.38 | 6.97E-03 | 0.94 | 3.35E-02 | 1.11 | 2.09E-02 | 1.08 | 2.70E-02 | 0.75 | 4.45E-02 | 0.47 | 9.77E-02 | 0.80 |
| 4 | 3.60E-03 | 1.22 | 4.60E-03 | 1.82 | 3.40E-03 | 1.04 | 1.57E-02 | 1.10 | 1.00E-02 | 1.06 | 8.29E-03 | 1.71 | 2.90E-02 | 0.62 | 6.74E-02 | 0.54 |
| 2 | 1.31E-03 | 1.46 | 2.18E-03 | 1.08 | 1.49E-03 | 1.19 | 9.03E-03 | 0.79 | 4.80E-03 | 1.06 | 4.22E-03 | 0.97 | 1.68E-02 | 0.79 | 4.26E-02 | 0.66 |
| 1 | 3.71E-04 | 1.82 | 4.63E-04 | 2.23 | 5.63E-04 | 1.40 | 3.87E-03 | 1.22 | 1.65E-03 | 1.54 | 1.14E-03 | 1.89 | 8.35E-03 | 1.01 | 3.00E-02 | 0.51 |

grid resolution around the free surface is too expensive, spurious viscosities in the non-Newtonian fluid might be even visible to the naked eye. Fortunately, spurious velocities mainly occur in low density fluids, which are typically Newtonian, thus the viscosity of the non-Newtonian fluid is only moderately affected. Furthermore, the impact of these spurious viscosities on the flow field depends on how large the viscous forces are in comparison with other forces, and this varies from application to application.

## 3.8. CONCLUSIONS

In this chapter, code verification of REFRESCO for laminar Herschel–Bulkley flows has been performed and discussed through three exercises with increasing complexity: steady single-phase flow (Case 1), unsteady two-phase flow with a smooth interface (Case 2) and with a free surface (Case 3).

For Case 1 and 2, the two goals of code verification are achieved: the observed order of convergence matches the expected order and the extrapolated error to cell size/time step zero tends to zero with grid/time step refinement. Therefore, the code performs as intended for both single- and two-phase laminar flows of Herschel–Bulkley fluids. Code verification in Case 3 is less conclusive due to the lack of asymptotic grid/time convergence. Nevertheless, this test case can be used as an extension of Case 2 to check that, in presence of a free surface, errors of all quantities have at least an overall decreasing trend with grid/time step refinement. Furthermore, the exercise revealed that the well-known ‘spurious velocities’ typical of free-surface calculations with the VoF model induce ‘spurious viscosities’ in the non-Newtonian fluid. We have however demonstrated that these artefacts disappear with grid/time step refinement.

Additionally, it is shown in Appendix A.1 that examining the convergence properties of the viscosity is a valuable tool for detecting coding mistakes in the rheological model, especially for Case 2 and Case 3, where viscous effects have little influence on the convergence properties of the dependent variables.

The procedure shown in this chapter can be applied to any GNF model. For instance, if another GNF model is implemented, code verification can be performed using the same manufactured solutions but adapting the scripts used to generate the source terms. The scripts used for work in this chapter are reported in [101].

# 4

# SOLUTION OF A 3D BENCHMARK PROBLEM FOR NON-NEWTONIAN FLUIDS: THE FLOW AROUND A SPHERE

*...in which the accuracy and robustness of the solution approach is tested, as a stepping stone towards more practical applications, on a classic benchmark problem in non-Newtonian fluid mechanics: the laminar flow around a sphere. The aim is to test the performance of the non-Newtonian solver before applying it to the more complex scenarios. Flow simulations are carried out at low Reynolds numbers in order to compare our results with numerical data from the literature. Results agree well with literature both qualitatively and quantitatively. When combined with the previous code verification exercises, these results suggest that the non-Newtonian solver works as intended. The reported numerical data could also be used as reference for future testing.*

---

The work in this chapter is based on the published article "Lovato, S., Toxopeus, S., Settels, J. and Keetels, G. (2022). Application of a maritime CFD code to a benchmark problem for non-Newtonian fluids: the flow around a sphere. *International Shipbuilding Progress*, 1-25" [102].

## 4.1. INTRODUCTION

The code verification in Chapter 3 ensured that the Herschel–Bulkley model was correctly implemented. However, even if the code is correct, fully-converged solutions for realistic non-Newtonian problems may still be difficult to obtain. In fact, REFRESCO is optimised and verified exclusively for maritime applications, which are typically concerned with Newtonian fluids such as air and water. The code also presents features that are common in general commercial CFD codes, such as the finite-volume method (FVM) and SIMPLE-type solution algorithms. While these features are standard for maritime applications, they are less common to simulate non-Newtonian flows. The latter are characterised by a shear-dependent viscosity that makes the equations stiffer and thus more difficult to solve.

### 4.1.1. RESEARCH QUESTION AND AIM OF THE CHAPTER

Can the newly developed non-Newtonian solver of REFRESCO reproduce numerical data from the literature?

In this chapter, the question is answered for 3D simulations of laminar flows of power-law, Bingham and Herschel–Bulkley fluids around a sphere, which is a classic problem in non-Newtonian fluid mechanics. This problem has been also been extensively studied in the past decades, both experimentally (e.g. [168, 4, 89, 8, 20, 7, 163, 5]) and numerically (e.g. [37, 15, 166, 67, 17, 14, 119, 41, 126, 125, 63]), because of its interest for industrial processes such as sediment transport, sedimentation and fluidisation (the reader is also referred to the book of Chhabra [29] for an exhaustive survey on the topic).

Furthermore, while it is probably the simplest three-dimensional flow, it also exhibits features that are typical of the flow around ships, such as boundary layer development and flow separation. Hence, the availability of literature data and its flow features make the flow around a sphere a useful benchmark problem to test the non-Newtonian solver of ReFRESCO as a stepping stone towards practical applications.

## 4.2. PROBLEM FORMULATION AND GOVERNING EQUATIONS

The problem of a sphere $d$ moving in an infinite medium is modelled as a sphere fixed at the centre of a cylindrical tube with a uniform inflow $U$ (Fig. 4.1). The tube has both diameter and length equal to $D$. The origin of the Cartesian reference frame is placed at the sphere centre with the $z$-axis aligned with flow direction.

The laminar, steady, isothermal and single-phase flow of an incompressible fluid around the sphere is governed by the following continuity and momentum equations (in Cartesian coordinates):

$$\nabla\cdot\boldsymbol{u}=0, \quad \rho\boldsymbol{u}\cdot\nabla\boldsymbol{u}=\nabla\cdot\boldsymbol{\tau}-\nabla p, \tag{4.1}$$

where $\boldsymbol{\tau}$ is the deviatoric stress tensor already defined in Eq. (2.6). For Bingham fluids, the apparent viscosity is calculated using Eq. (2.8), whereas Eq. (2.10) is used for Herschel–Bulkley fluids.

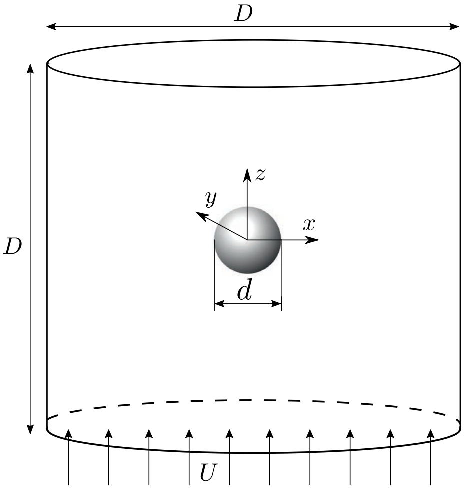

Figure 4.1: Schematic representation of the problem.

## 4.3. NON-DIMENSIONAL NUMBERS AND TEST CASES

The Herschel–Bulkley flow around a sphere is characterised by two non-dimensional numbers: the generalised Reynolds number

$$Re=\frac{\rho U^2}{K(U/d)^n}\quad\left(\sim\frac{\text{inertia}}{\text{viscous stress}}\right), \tag{4.2}$$

and the Bingham number

$$Bn=\frac{\tau_0}{K(U/d)^n}\quad\left(\sim\frac{\text{yield stress}}{\text{viscous stress}}\right). \tag{4.3}$$

For power-law and Newtonian fluids the Bingham number is zero, whereas when $n=1$ the Reynolds number reduces to the canonical $Re=\rho Ud/K$.

The non-dimensional friction, pressure and drag coefficients are calculated respectively as

$$C_{Df} = \frac{(\boldsymbol{F_f})_z}{1/8\rho\pi d^2 U^2}\,, \quad C_{Dp} = \frac{(\boldsymbol{F_p})_z}{1/8\rho\pi d^2 U^2}\,, \quad C_D = C_{Df} + C_{Dp}\,, \tag{4.4}$$

$$\boldsymbol{F_p} = -\int_S p\,\boldsymbol{n}\,dS\,, \qquad \boldsymbol{F_f} = \int_S \boldsymbol{\tau}\cdot\boldsymbol{n}\,dS\,, \tag{4.5}$$

where $S$ is the sphere surface having $\boldsymbol{n}$ as its outward normal vector, $(\boldsymbol{F_p})_z$ and $(\boldsymbol{F_f})_z$ are the $z$-component of the pressure and frictional force vectors, respectively.

Throughout the chapter, the regularisation parameter $m$ will be expressed in the following non-dimensional form

$$M = \frac{mU}{d}\,. \tag{4.6}$$

Numerical simulations are performed for all the combinations of $n = 1$, 0.8 and 0.6, $Bn = 10$ and 100 and $Re = 10$ and 100. This choice is made to maximise the number of considered cases for which there is published CFD data in the literature while also running a feasible number of simulations.

Additional simulations are performed for creep flow ($Re < 1$) of Bingham fluids for two reasons. First, under the latter flow regime, obtaining a fully converged solution with a SIMPLE-type solver can be challenging (if not impossible in some cases) because of the very low shear rate and consequently very large viscosity. Second, literature data for Bingham creep flow are in excellent agreement with each other, contrary to data for $Re = 10$ and 100. These two reasons make the Bingham creep flow an interesting case to test the accuracy and robustness of the solution approach, even though it may be far from the typical flow conditions encountered in maritime applications.

For Bingham creep flow, however, the drag coefficient as defined in Eq. (4.4) becomes extremely large. The reason is that inertia is virtually zero for creep flows, hence $1/2\rho U^2$ is no longer a suitable factor to non-dimensionalise the forces. Since viscous effects are dominant, a better alternative could be to use $KU/d$. Nonetheless, we have adopted the more common practice of using the Stokes coefficient (Beris et al. [15]), defined as

$$C_S = \frac{C_D}{(24/Re)}\,. \tag{4.7}$$

The Stokes coefficient is thus a measure of how large is the drag force compared to the exact drag coefficient for Newtonian creep flow, the latter being equal to $24/Re$ according to the Stokes' law [158].

## 4.4. NUMERICAL METHODS AND SETUP

### 4.4.1. FLOW SOLVER

The CFD settings are the same as for the single-phase flow case in Chapter 3, except for the convective term in the momentum equation, which is now discretised with a central difference scheme instead of the TVD Harmonic scheme.

### 4.4.2. BOUNDARY CONDITIONS

The boundary conditions are set as follows. A uniform inflow $u_z = U$ is imposed at the inlet $(z = -D/2)$, whereas outflow conditions $(\partial u_z/\partial z = 0)$ are imposed at the outlet boundary $(z = D/2)$. The no-slip/no-permeability conditions $(\boldsymbol{u} = 0)$ are set at the sphere surface together with the free-slip conditions $(u_n = 0, \partial u_z/\partial n = 0)$ on the outer cylindrical tube. For the pressure field, Neumann conditions $(\partial p/\partial n = 0)$ are applied to all the boundaries, thus a pressure reference is imposed in one point at the inlet boundary.

### 4.4.3. DOMAIN SIZE

In order to mimic a sphere settling in an infinite domain, the outer cylindrical tube diameter must be sufficiently large compared to the sphere diameter. The influence of the tube-to-sphere diameter ratio, $D/d$, was assessed by computing the drag coefficients on four grids having size $D = 25d$, $50d$, $100d$ and $200d$ respectively, with the grid $50d$ having the second finest refinement shown in Table 4.1 (Section 4.4.4) and the regularisation parameters in Table 4.3 (Section 4.4.5).

The uncertainty in the solution due to the finite domain size has been estimated with the method of Eça and Hoekstra [46] by replacing the grid size with the tube diameter $D$. Since this method was designed to estimate the discretisation uncertainties, we have checked the validity of this procedure by performing additional calculations for Newtonian creep flow, whose exact solution for the unbounded domain is $C_S = 1$ by virtue of Eq. (4.7). With the adopted procedure the extrapolated $C_S$ for $d/D = 0$ was found to be 0.99995 (Fig. 4.2, left), thus the procedure is deemed reliable for the present calculations. Note that the 4% uncertainty shown in Fig. 4.2 is irrelevant in this work as the Newtonian creep flow will not be considered further.

The uncertainties were then estimated for all the test cases, and the two largest values obtained with $D = 50d$ were 0.12% and 0.09%, which corresponded to the Newtonian and power-law cases $(Bn = 0)$ for $Re = 10$, respectively (Fig. 4.2, right). This is not surprising since the strongest disturbance to the flow field occurs for such test cases (see also Fig. 4.7 in Section 4.5.1). For $Bn > 0$, the domain size uncertainties were found to be less than 0.005%. Therefore all subsequent calculations were performed with $D = 50d$. In conclusion, the maximum domain-size uncertainty for Newtonian and power-law fluid is about 0.1%, whereas for all the other test cases the influence of the domain size can be safely neglected.

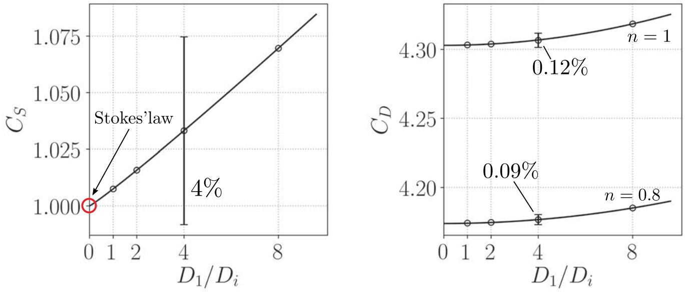

Figure 4.2: Convergence of the Stokes/drag coefficients with $D_1/D_i$ ($D_i = 200d, 100d, 50d, 25d$) for Newtonian creep flow ($Re = 0.01$) (left) and Newtonian and power-law flows ($Bn = 0$) at $Re = 10$ (right). The percentages indicate the domain uncertainty for the case with $D_1 = 50d$.

### 4.4.4. DOMAIN DISCRETISATION

The domain was discretised with two series of three-dimensional multi-block structured grids, with the layout as sketched in Fig. 4.3. Four geometrically similar grids were generated for each series in order to estimate the discretisation uncertainties. The number of grid cells and the size of the first cells away from the sphere surface are reported in Table 4.1. One series was generated for $Re = 0.01$ (creep flow) of Bingham fluids and the other for the higher Reynolds numbers ($Re = 10$ and 100). Note that the series used for creep flow calculations has higher resolution in order to better capture the steep velocity gradient near the sphere walls occurring for large $Bn$.

The discretisation uncertainties on the force coefficients are given in Table 4.2 and they were estimated with the method of Eça and Hoekstra [46]. All the calculations were carried out using the regularisation parameters discussed in the following section. Except for the two cases with $Bn = 100$ and $n = 0.6$, all the uncertainties are below 1%. The larger uncertainties observed in $C_{Df}$ for $Bn = 100$ and $n = 0.6$ can be explained by the decrease in the apparent viscosity at the sphere surface (high-shear region) when $n$ is decreased. In fact, the already steep velocity profile at the sphere walls for $Bn = 100$ (see also Fig. 4.10 in Section 4.5.1) becomes even steeper when the viscosity is reduced, which would thus require a finer grid to be more accurately captured.

### 4.4.5. REGULARISATION METHODS

The use of regularisation methods produces regularisation errors, which are defined as the difference between the solution obtained with the regularised and non-

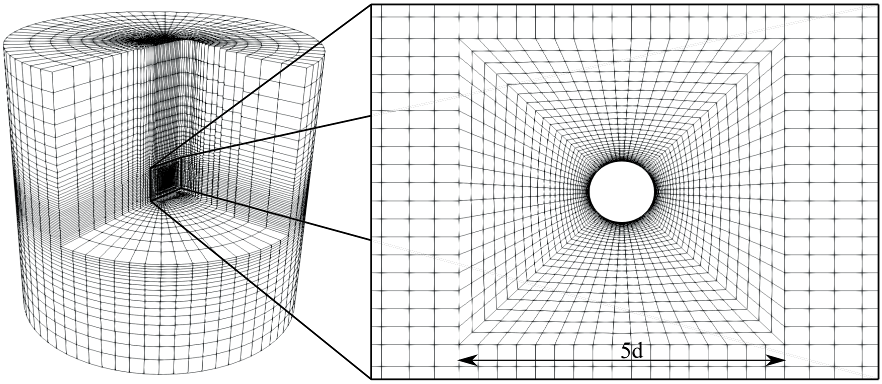

Figure 4.3: Illustration of the coarsest grid of Series 1.

Table 4.1: Grid size ratio, number of cells $N_i$ and thickness $h_w$ of the first cell away from the sphere surface.

| | Series 1<br>$Re = 10$ and $100$ | | | Series 2<br>$Re = 0.01$ | | |
|---|---|---|---|---|---|---|
| $i$ | $\sqrt[3]{N_1/N_i}$ | $N_i$ | $h_w/d$ | $\sqrt[3]{N_1/N_i}$ | $N_i$ | $h_w/d$ |
| 4 | 2.59 | 129 064 | 0.00800 | 2.60 | 156 808 | 0.00200 |
| 3 | 1.90 | 324 070 | 0.00571 | 1.91 | 397 072 | 0.00143 |
| 2 | 1.38 | 857 600 | 0.00408 | 1.38 | 1 054 208 | 0.00102 |
| 1 | 1.00 | 2 238 368 | 0.00292 | 1.00 | 2 761 088 | 0.00073 |

Table 4.2: Discretisation uncertainties in percentage of the corresponding drag component for the pressure, frictional and total drag on the finest grid.

| | | $Bn = 0$ | | | $Bn = 10$ | | | $Bn = 100$ | | | $Re = 0.01$ | | | |
|---|---|---|---|---|---|---|---|---|---|---|---|---|---|---|
| $Re$ | $n$ | $U_{C_{Dp}}$ | $U_{C_{Df}}$ | $U_{C_D}$ | $U_{C_{Dp}}$ | $U_{C_{Df}}$ | $U_{C_D}$ | $U_{C_{Dp}}$ | $U_{C_{Df}}$ | $U_{C_D}$ | $Bn$ | $U_{C_{Dp}}$ | $U_{C_{Df}}$ | $U_{C_D}$ |
| 10 | 1 | 0.03 | 0.12 | 0.09 | 0.88 | 0.17 | 0.25 | 0.40 | 0.38 | 0.36 | 2.299 | 0.61 | 0.25 | 0.36 |
| 10 | 0.8 | 0.02 | 0.11 | 0.08 | 0.34 | 0.10 | 0.57 | 0.34 | 0.94 | 0.38 | 8.047 | 0.56 | 0.39 | 0.43 |
| 10 | 0.6 | 0.02 | 0.09 | 0.05 | 0.31 | 0.18 | 0.26 | 0.33 | 3.34 | 0.76 | 59.59 | 0.28 | 0.21 | 0.20 |
| 100 | 1 | 0.10 | 0.05 | 0.07 | 0.28 | 0.10 | 0.17 | 0.32 | 0.30 | 0.30 | 340.7 | 0.49 | 0.12 | 0.42 |
| 100 | 0.8 | 0.18 | 0.11 | 0.15 | 0.33 | 0.09 | 0.24 | 0.30 | 0.88 | 0.39 | 497.5 | 0.24 | 0.15 | 0.22 |
| 100 | 0.6 | 0.38 | 0.23 | 0.31 | 0.19 | 0.17 | 0.25 | 0.66 | 3.26 | 0.69 | 544.6 | 0.24 | 0.21 | 0.23 |

regularised rheological models. Large regularisation parameters are needed to minimise these errors, but this may lead to very slow or even stagnating convergence of the residuals in the iterative solver, as as will be shown in Section 4.4.6.

For practical applications, however, low regularisation parameters may be acceptable since the rheology of many real fluids is better captured by regularised models (e.g. Dzuy and Boger [45] and Ellwood et al. [56]). On the other hand, for the purpose of comparison with literature data it is important to minimise these errors, also to avoid possible cancellation of regularisation and discretisation errors that can cause a spurious agreement with literature data. Figure 4.4 shows an example in which $C_S$ on an a very coarse grid with $M = 20$ is nearly identical to the $C_S$ on a fine grid with $M = 200$. Despite the latter case is numerically more accurate, both $C_S$ are very close to literature data (cf. also with Table 4.7) as a result of errors cancellation.

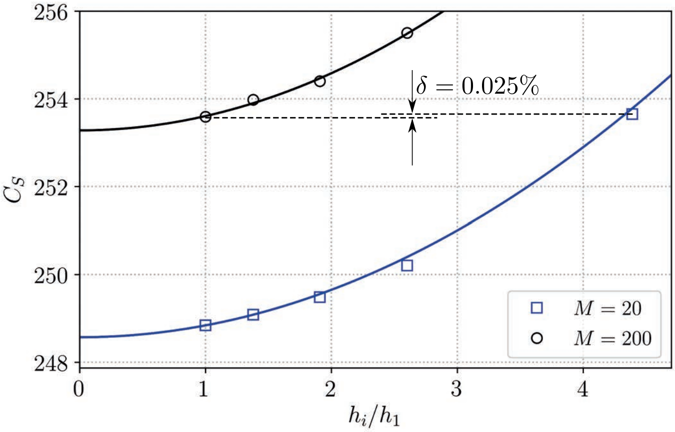

Figure 4.4: Grid convergence of the Stokes coefficient for $Bn = 197.5$ using $M = 20$ and 200. The difference $\delta$ is between $C_S$ on an a very coarse grid with $M = 20$ and on a fine grid with $M = 200$.

The choice of the proper regularisation parameter is found to be problem-dependent. With regard to the laminar flow around a sphere, previous numerical studies used very different values, both dimensional and non-dimensional. For instance, Blackery and Mitsoulis [17] used $m = 200$ s, whereas Beaulne and Mitsoulis [14] suggest to keep the product $M\,Bn$ equal to $10^3$. On the other hand, Gavrilov et al. [63] and Nirmalkar et al. [126, 125] have used $M = 10^3$ and $m = 10^6$ s, respectively.

For the current work, the regularisation parameter for each test case has been gradually increased until the regularisation uncertainty became less than 1%. The remaining question, however, is how to estimate the regularisation uncertainty.

Frigaard and Nouar [61] showed that, for typical Bingham shear flows, the Papanastasiou regularisation errors tend to zero with first order as $1/M \rightarrow 0$. As a first approximation, it is thus reasonable to estimate the regularisation uncertainty with the same method used for the discretisation uncertainty, with the grid spacing replaced by $1/M$ (Fig. 4.5). The final selected values of $M$ that ensured a regularisation uncertainty below 1% are reported in Table 4.3. We found that the maximum and average regularisation uncertainties in percentage of the drag coefficient are 0.77% and 0.2%, respectively.

Finally, we remark that the values reported in Table 4.3 may still be too low to accurately capture the so-called yielded surface, i.e. the locus of points where $\tau = \tau_0$ (see e.g. [25, 96]). This aspect is however beyond the scope of this work, hence it is no further discussed.

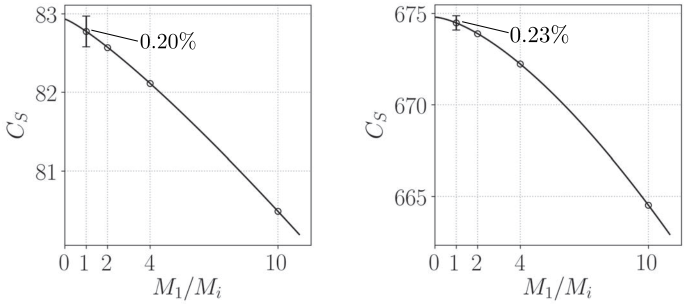

Figure 4.5: Convergence of the Stokes coefficient with $M_1/M_i$ ($M_i = 200, 100, 50, 20$) for $Re = 0.01$ with $Bn = 59.59$ (left) and $Bn = 544.6$ (right). The percentages indicate the regularisation uncertainty relative to $C_S$ obtained with $M_1 = 200$.

Table 4.3: Selected non-dimensional regularisation parameter $M = mU/d$ for each test case.

| | $Re = 10$ | | $Re = 100$ | | Creep flow, $Re < 1$ | | | | | |
|---|---|---|---|---|---|---|---|---|---|---|
| Bn | 10 | 100 | 10 | 100 | 2.299 | 8.047 | 59.59 | 197.5 | 340.7 | 544.6 |
| $n = 1$ | 500 | 200 | 1000 | 200 | 2000 | 2000 | 200 | 200 | 200 | 200 |
| $n = 0.8$ | 500 | 200 | 1000 | 200 | - | - | - | - | - | - |
| $n = 0.6$ | 500 | 200 | 500 | 200 | - | - | - | - | - | - |

### 4.4.6. ITERATIVE CONVERGENCE AND VISCOSITY INTERPOLATION SCHEME

As mentioned in the previous section, iterative convergence can become difficult when using large regularisation parameters. This issue seems rather common when using SIMPLE-like algorithms (see e.g. Syrakos et al. [160, 159]). In this work, we found that the rate of convergence of the residuals is significantly influenced by the choice of the interpolation scheme for the viscosity.

Within the finite-volume method, the diffusive term in Eq. (4.1) requires the evaluation of the apparent viscosity, $\mu$, at the cell faces. Since in REFRESCO the computational node coincides with the cells' centroid, the face value must be obtained by interpolation. Assuming for simplicity that a cell face $e$ is halfway between two Cartesian grid cells $P$ and $E$, the simplest second-order interpolation scheme to calculate $\mu_e$ reads

$$\mu_e = \frac{\mu_P(\dot{\gamma}_P) + \mu_E(\dot{\gamma}_E)}{2} . \tag{4.8}$$

Another simple alternative is to first evaluate $\dot{\gamma}_e$ from linear interpolation of $\dot{\gamma}_P$ and $\dot{\gamma}_E$ and then to calculate the viscosity at the face $e$, i.e.

$$\dot{\gamma}_e = \frac{\dot{\gamma}_P + \dot{\gamma}_E}{2} , \quad \mu_e = \mu(\dot{\gamma}_e) . \tag{4.9}$$

The two schemes have the same computational cost, thus, in principle, there is no reason to prefer one scheme to the other. Furthermore, when we performed a code verification exercise (not shown here) similar to that in Lovato et al. [101], the two schemes exhibited the same accuracy and rate of convergence of the residuals. However, on the present problem, the first scheme (Eq. (4.8)) turned out to be more robust as it was possible to obtain a fully converged solution using relatively large regularisation parameters[1] up to $M = 200$, as shown in Fig. 4.6.

With the second scheme (Eq. (4.9)), on the other hand, the residuals were stagnating already with $M = 50$. Therefore, an interpolation scheme that uses the cell centre values of the apparent viscosity was eventually adopted in REFRESCO.

For this work and with the setup described above, the iterative convergence criterion was set to $L_\infty < 10^{-8}$ and the iterative uncertainties were estimated with the method of Eça and Hoekstra [47]. For all the test cases we found that the iterative uncertainties were virtually zero ($< 0.0005\%$).

### 4.4.7. TOTAL NUMERICAL UNCERTAINTY

The final numerical uncertainty in the computed drag coefficient was calculated assuming that all the uncertainty components are dependent on each other, i.e.

$$U_{num} = U_{dom} + U_{discr} + U_{reg} + U_{iter} , \tag{4.10}$$

---

[1] Sufficiently large, at least, to keep the regularisation uncertainty below 1%.

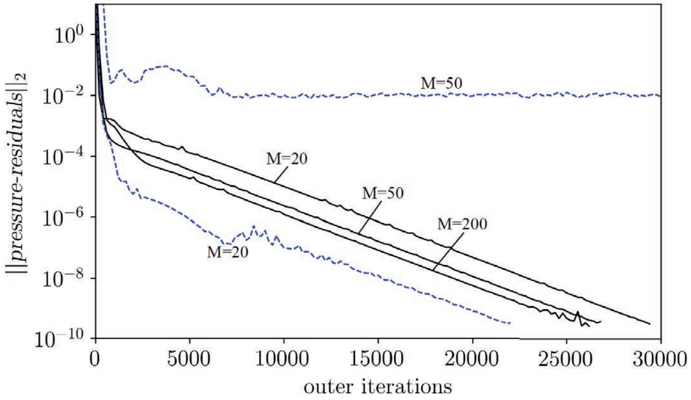

Figure 4.6: Effect of the two viscosity interpolation schemes on the iterative convergence of the pressure residuals. Test case: $Re = 0.01$, $Bn = 59.59$. Black line corresponds to Equation (4.8), whereas the blue dashed line to Eq. (4.9).

where $U_{dom}$, $U_{dis}$ , $U_{reg}$ and $U_{it}$ are the uncertainties produced by the finite domain size, the domain discretisation, the regularisation parameter and the iterative method, respectively. The total numerical uncertainties are reported in Table 4.4 and, for all the test cases, they do not exceed 1%.

Table 4.4: Total numerical uncertainties, $U_{num}$, in percentage of the computed drag coefficient.

| | | $Bn = 0$ | $Bn = 10$ | $Bn = 100$ | $Re = 0.01$ | |
|---|---|---|---|---|---|---|
| $Re$ | $n$ | $U_{C_D}$ | $U_{C_D}$ | $U_{C_D}$ | $Bn$ | $U_{C_D}$ |
| 10 | 1 | 0.21 | 0.63 | 0.55 | 2.299 | 0.55 |
| 10 | 0.8 | 0.16 | 0.85 | 0.50 | 8.047 | 0.53 |
| 10 | 0.6 | 0.10 | 0.45 | 0.83 | 59.59 | 0.44 |
| 100 | 1 | 0.19 | 0.94 | 0.55 | 340.7 | 0.52 |
| 100 | 0.8 | 0.24 | 0.85 | 0.56 | 497.5 | 0.30 |
| 100 | 0.6 | 0.38 | 1.02 | 0.80 | 544.6 | 0.29 |

## 4.5. RESULTS AND DISCUSSION

### 4.5.1. FLOW FIELD

Some features of the computed flow field are now discussed. More detailed descriptions have been already discussed by other authors [15, 126, 125, 63], thus they will not be completely repeated here. The contours of the velocity, shear rate and viscosity for $Re = 10$ and 100 are shown in Figs. 4.7 to 4.9, respectively. Note that flow field for Bingham creep flow ($Re = 0.01$) is not shown as it is very similar to the the case with $Re = 10$ and $Bn = 100$.

For Newtonian and power-law fluids ($Bn = 0$), the flow is attached to the sphere for $Re = 10$, whereas at $Re = 100$ the flow is separated and exhibits the characteristic toroidal eddy behind the sphere (Fig. 4.7, top). The effect of decreasing $n$ is less evident. When $n < 1$, the apparent viscosity becomes lower than the Newtonian viscosity, $K$, in the region where $\dot{\gamma} > 1$ (i.e. the region within the black isoline in Fig. 4.8, top). This leads to a thinner boundary layer for $n < 1$ compared to Newtonian fluids. Another effect of reducing $n$ is the smaller wake eddy. The latter observation agrees qualitatively with the results of Dhole et al. [41] for power-law fluids.

For yield stress fluids ($Bn > 0$), the viscosity increases significantly, especially in the undisturbed flow region away from the sphere (Fig. 4.9, middle and bottom panels). The large viscosity damps advection, leading to the disappearance of the toroidal eddy behind the sphere. The fore-aft symmetry typical of creep flow is thus restored. For $Bn = 100$, the flow appears symmetrical with respect to the equatorial plane ($z = 0$), both for $Re = 10$ and 100 (Fig. 4.7, bottom).

When $Bn > 0$, the fluid far upstream is undeformed with very high viscosity, i.e. it behaves as a solid-like material ($\tau < \tau_0$). The fluid is then deformed as it encounters the sphere and the viscosity is reduced ($\tau > \tau_0$). The black isoline in the middle and bottom plots of Fig. 4.8 identifies the computed yielded surface, i.e. the locus of points where $\tau = \tau_0$. This surface shrinks with increasing $Bn$ and decreasing $n$, whereas it grows with higher $Re$. These observations are in line with those of Nirmalkar et al. [125]. Furthermore, small unyielded regions are observed near the stagnation points. These regions are usually referred to as 'polar caps' [15, 17].

As $Bn$ increases, the solid-like region (uniform undisturbed flow) tends to expand towards the sphere, thus 'squeezing' the fluid close to the sphere. As a result, the fluid has to increase its velocity in order to keep the flow rate constant along the tube cross-sections. Another way to see this is that the streamlines become denser near the sphere.

Furthermore, for yield stress fluids, the velocity in the equatorial plane exhibits a local maximum, which leads to a local viscosity maximum[2] (Fig. 4.9), as also observed by Nirmalkar et al. [126] and Gavrilov et al. [63]. Such steep variation of viscosity over a relative short distance was a major cause for the difficult iterative convergence. We found in fact that the largest residuals were always near this local viscosity maximum.

For ideal (i.e. non-regularised) Bingham and Herschel–Bulkley fluids, the fluid region far from the sphere would have an infinite viscosity and zero shear rate. The

---

[2] Note that, in three dimensions, this local maximum is actually a circle around the sphere

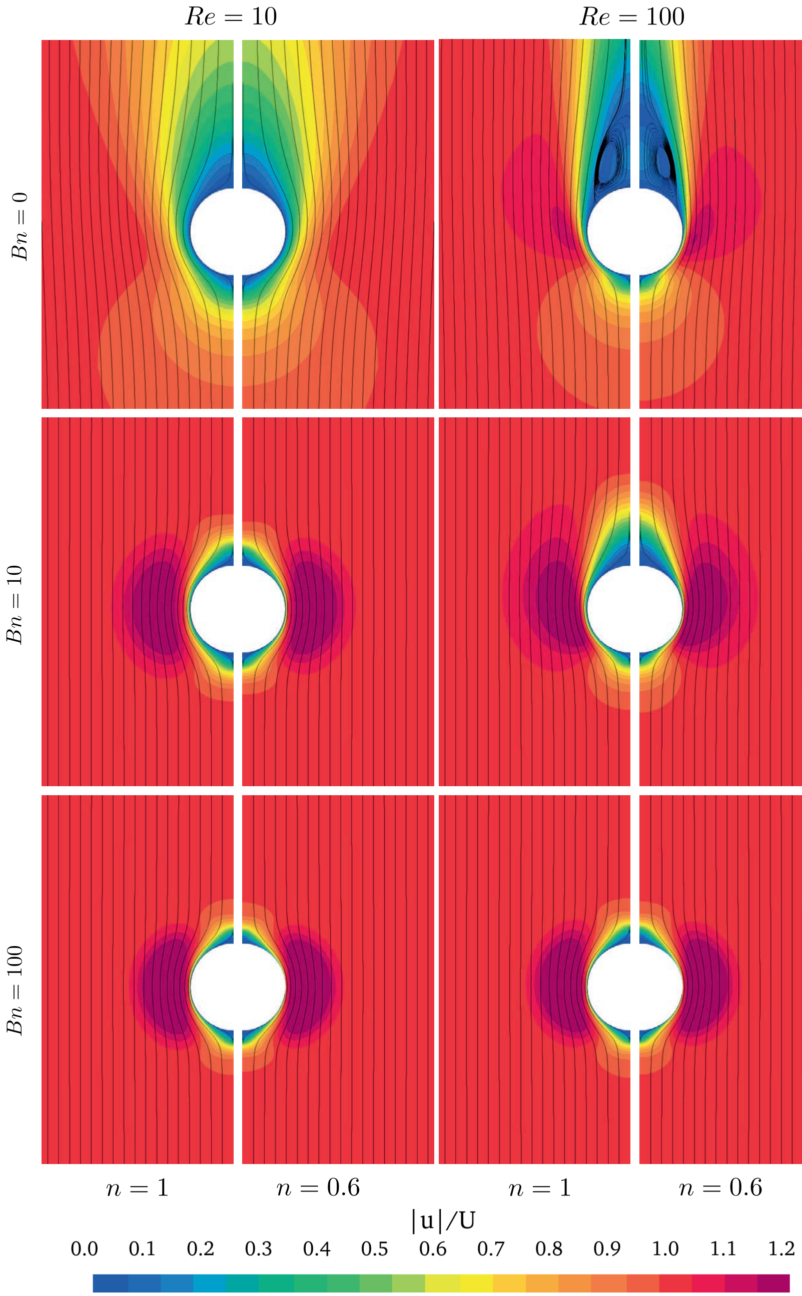

Figure 4.7: Velocity contour and streamlines. The flow is from bottom to top.

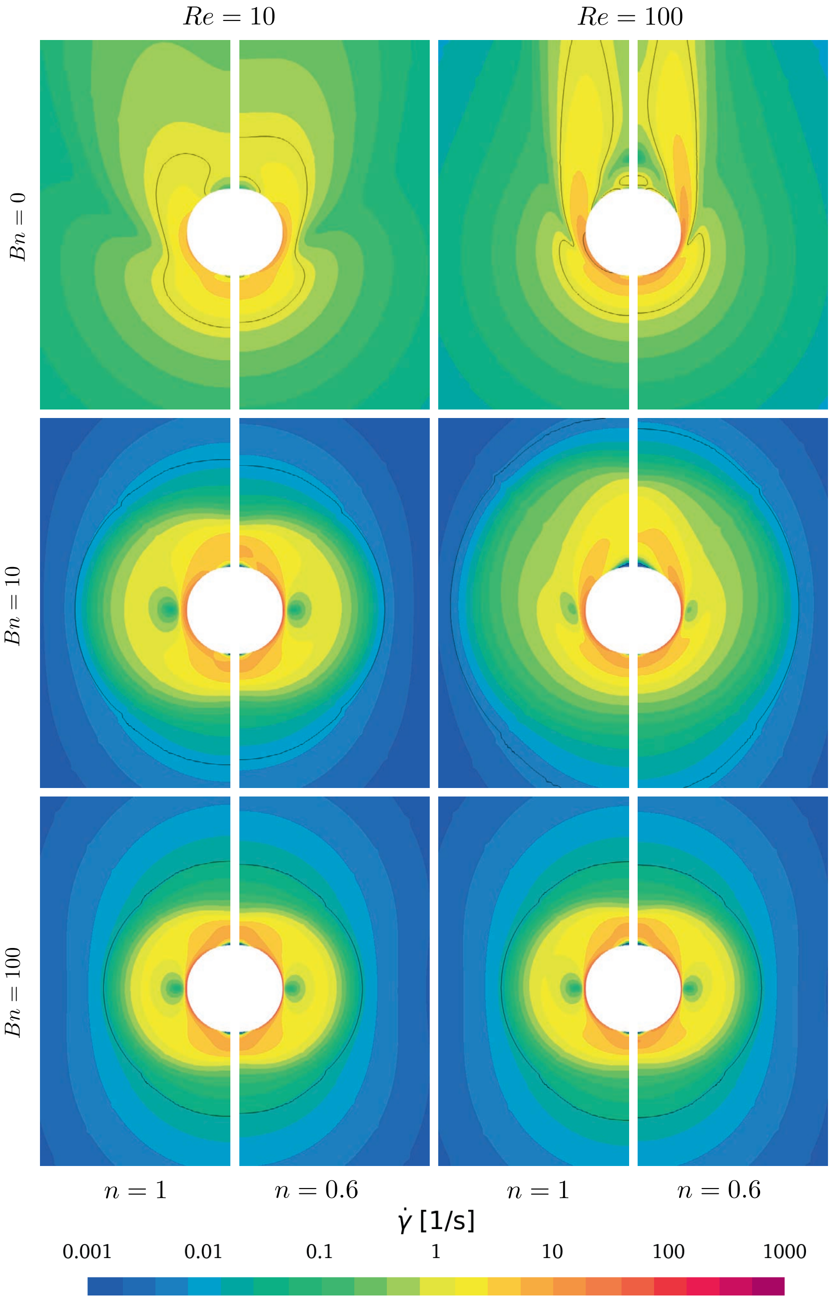

Figure 4.8: Contour plot of the shear rate $\dot{\gamma}$. The black isoline corresponds to $\dot{\gamma} = 1\ \mathrm{s}^{-1}$ for $Bn = 0$, whereas it corresponds to $\tau = \tau_0$ for $Bn = 10, 100$.

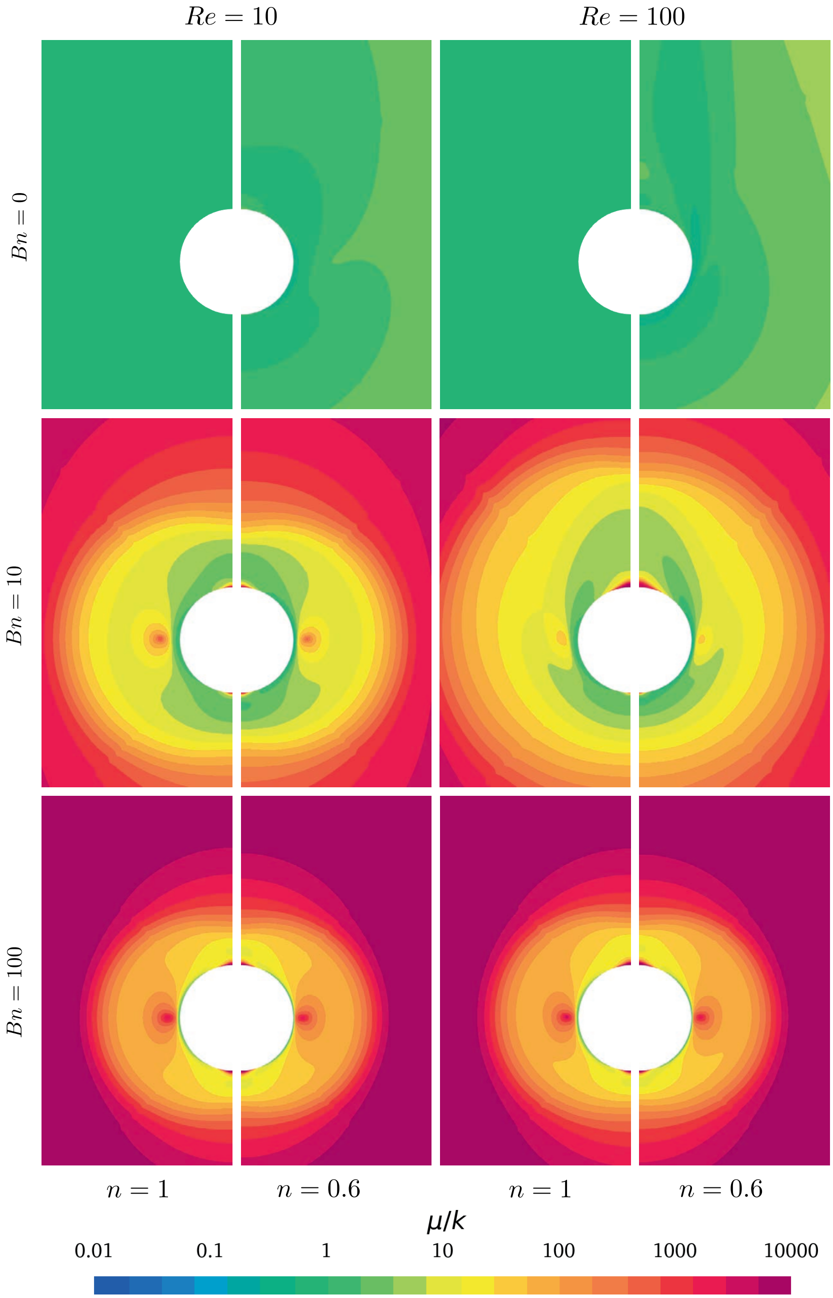

Figure 4.9: Contour plot of $\mu(\dot{\gamma})/K$, which is equal to 1 for Newtonian fluids.

effect of the regularisation is evident in Figs. 4.8 and 4.9: the shear rate is very low (but not zero) and the viscosity is very large (but not infinite).

Finally, the velocity profiles for Bingham fluids at $Re = 100$ are plotted in Fig. 4.10 and compared with the available literature data of Gavrilov et al. [63] and Nirmalkar et al. [126]. The above mentioned disappearance of the recirculation region with increasing $Bn$ is clearly visible in Fig. 4.10 (b). Overall, our results agree fairly well with literature data, especially with those of Gavrilov et al. Some visible discrepancies are observed in Fig. 4.10 (a) for $Bn = 100$, which probably stem from the different settings (e.g. grids, regularisation parameters, domain size, etc.) used in this work and in the work of Nirmalkar et al. [126].

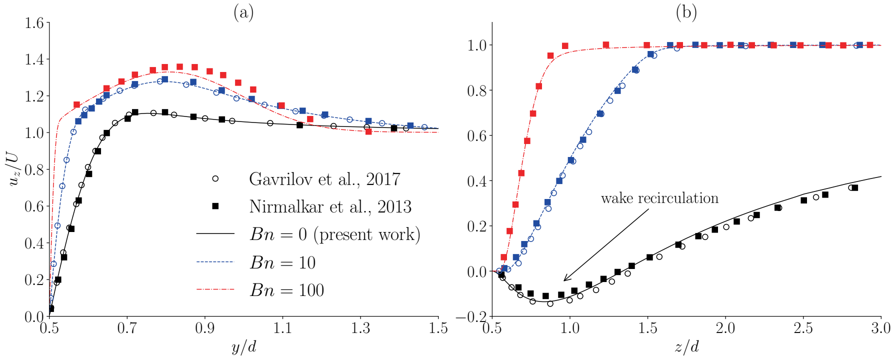

Figure 4.10: Axial velocity profiles for Bingham fluids ($n = 1$) at $Re = 100$; (a) along $y$ on the plane $z = 0$; (b) along the centreline ($x = y = 0$) near the rear stagnation point.

In conclusion, the flow field is qualitatively in line with previous studies from the literature, and it quantitatively agrees with the results of Gavrilov et al. and Nirmalkar et al.

### 4.5.2. DRAG COEFFICIENTS AND COMPARISON WITH LITERATURE

The drag coefficient is often the only quantity of interest in many engineering applications. It is therefore a meaningful quantity to assess whether REFRESCO can reproduce the results from the literature.

The drag coefficients and its components are reported in Table 4.5. The ratio $C_{D_p}/C_{D_f}$ is observed to increase with the non-Newtonian character of the fluid (i.e. with higher $Bn$ or lower $n$). This observation is consistent with the previous numerical studies of Dhole et al. [41], Nirmalkar et al. [126], and Gavrilov et al. [63]. Furthermore, $C_D$ decreases with $n$, which is due to the shear-thinning effect the reduces the viscosity in the high-shear region near the sphere. A direct comparison of $C_D$ with the literature data is given in Tables 4.6 and 4.7.

Note that performing a rigorous validation is not possible because the numerical uncertainties for the literature data are not known. Nevertheless, we have applied the validation procedure proposed by ASME [6] by replacing experimental data with numerical data from the literature. According to the procedure, the modelling error, $\delta_{model}$, is estimated by comparing two quantities: the (expanded) validation uncertainty,

$$U_{val} = \sqrt{U_{num}^2 + U_{lit}^2 + U_{input}^2}, \tag{4.11}$$

and the comparison error,

$$E = S - D, \tag{4.12}$$

where $S$ is our numerical solution value and $D$ is the literature data. $U_{input}$ is the uncertainty due to the input parameters, which is zero for the present work. $U_{num}$ is the uncertainty in our numerical data, and it is reported in Table 4.4. $U_{lit}$ is the uncertainty in the literature data. Since this is unknown, it was assumed $U_{lit} = 1\%$.

$E$ and $U_{val}$ define an interval within which $\delta_{model}$ falls, i.e.

$$E - U_{val} \leq \delta_{model} \leq E + U_{val}. \tag{4.13}$$

It is however remarked that, since the comparison is made with numerical data instead of experiments, the modelling errors are expected to be zero. A successful validation with literature data must thus yield $|E| \leq U_{val}$. The comparison errors and the validation uncertainties are plotted in Fig. 4.11, from which the following observations are made:

- For power-law fluids ($Bn = 0$), the maximum $|E|$ with Dhole et al. [41] and Tripathi et al. [166] is about 7%, which is well outside the uncertainty range. We found that the difference with respect to Dhole et al. lies in the pressure component, where $|E|$ reaches about 20% relative to our data. The reasons for such difference are however not known. It is possible that the uncertainty in the literature data is actually greater than 1%, therefore assuming $U_{lit} = 1\%$ might have led to an underestimation of the validation uncertainty. Nevertheless, the agreement with the more recent results of Gavrilov et al. [63] is better, with comparison errors that are either within or very close to $U_{val}$.

- For Bingham and Herschel–Bulkley fluids ($Bn > 0$) at $Re = 10$ and 100, the larger discrepancies are found with respect to the data of Gavrilov et al., with $|E| > U_{val}$ for all cases. On the other hand, the agreement with Nirmalkar et al. [126, 125] is excellent, with differences that are well within the validation uncertainties.

Table 4.5: Pressure, frictional and total drag coefficients for $Re = 10$ and 100.

| | | $Bn = 0$ | | | $Bn = 10$ | | | $Bn = 100$ | | | $Re < 1$ | | | |
|---|---|---|---|---|---|---|---|---|---|---|---|---|---|---|
| $Re$ | $n$ | $C_{D_p}$ | $C_{D_f}$ | $C_D$ | $C_{D_p}$ | $C_{D_f}$ | $C_D$ | $C_{D_p}$ | $C_{D_f}$ | $C_D$ | $Bn$ | $C_{S_p}$ | $C_{S_f}$ | $C_S$ |
| 10 | 1 | 1.528 | 2.781 | 4.308 | 25.10 | 18.30 | 43.39 | 223.1 | 97.62 | 320.8 | 2.299 | 3.071 | 3.325 | 6.395 |
| 10 | 0.8 | 1.641 | 2.537 | 4.178 | 25.00 | 15.22 | 40.22 | 222.9 | 86.25 | 309.2 | 8.047 | 8.599 | 6.668 | 15.27 |
| 10 | 0.6 | 1.799 | 2.222 | 4.021 | 24.86 | 12.45 | 37.31 | 222.6 | 77.99 | 300.6 | 59.59 | 55.93 | 26.85 | 82.78 |
| 100 | 1 | 0.512 | 0.577 | 1.089 | 2.789 | 1.915 | 4.704 | 22.41 | 9.775 | 32.18 | 340.7 | 181.9 | 71.71 | 253.6 |
| 100 | 0.8 | 0.494 | 0.446 | 0.940 | 2.764 | 1.570 | 4.334 | 22.39 | 8.632 | 31.02 | 497.5 | 312.7 | 115.3 | 428.0 |
| 100 | 0.6 | 0.471 | 0.320 | 0.790 | 2.722 | 1.261 | 3.983 | 22.36 | 7.802 | 30.16 | 544.6 | 499.0 | 175.5 | 674.5 |

Table 4.6: Drag coefficient, $C_D$, from the present calculations and the literature. All the literature data is from numerical simulations and not from the correlations proposed in the respective articles.

| | | $Re = 10$ | | | $Re = 100$ | | |
|---|---|---|---|---|---|---|---|
| | Data from | $n = 1$ | $n = 0.8$ | $n = 0.6$ | $n = 1$ | $n = 0.8$ | $n = 0.6$ |
| $Bn = 0$ | present work | 4.308 | 4.178 | 4.021 | 1.089 | 0.940 | 0.790 |
| | Dhole [41] | 4.281 | 4.086 | 3.769 | 1.062 | 0.921 | 0.759 |
| | Tripathi [166] | 4.31 | 4.17 | 3.76 | 1.02 | 0.920 | 0.780 |
| | Gavrilov [63] | 4.334 | 4.167 | 3.969 | 1.095 | 0.941 | 0.787 |
| $Bn = 10$ | present work | 43.39 | 40.22 | 37.31 | 4.704 | 4.334 | 3.983 |
| | Gavrilov [63] | 42.15 | 38.90 | 35.91 | 4.587 | 4.217 | 3.880 |
| | Nirmalkar [126, 125] | 43.63 | 40.40 | 37.43 | 4.743 | 4.363 | 4.015 |
| $Bn = 100$ | present work | 320.8 | 309.2 | 300.6 | 32.18 | 31.02 | 30.16 |
| | Gavrilov [63] | 307.9 | 295.4 | 284.7 | 30.95 | 29.69 | 28.61 |

Table 4.7: Stokes coefficients, $C_S$, for Bingham creep flow from the present calculations and the literature.

| | $Re = 0.01$ | | | | | |
|---|---|---|---|---|---|---|
| Data from | $Bn = 2.299$ | 8.047 | 59.59 | 197.5 | 340.7 | 544.6 |
| present work | 6.395 | 15.27 | 82.78 | 253.6 | 428.0 | 674.5 |
| Beris [15] | 6.39 | 15.24 | 82.77 | 252.2 | 426.9 | 669.7 |
| Liu [96] | 6.38 | 15.21 | 82.67 | 253.6 | 426.0 | 671.9 |
| Nirmalkar [126] | - | 15.25 | 82.83 | - | 427.5 | 673.5 |

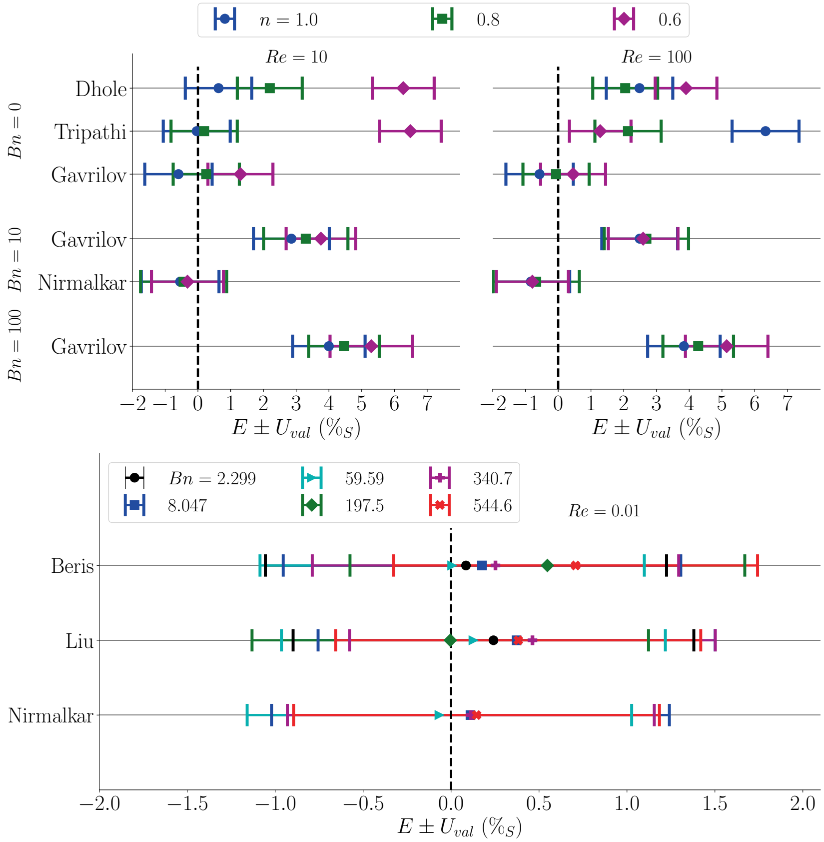

Figure 4.11: Comparison error (± validation uncertainty) for the drag coefficient in percentage of our data for $Re = 10$ and 100 (top) and for $Re = 0.01$ (bottom).

- The best agreement with literature data is achieved for Bingham creep flow ($Re = 0.01$), with all the comparison errors being within the validation uncertainties.

- Our results tend to be on the overpredicting side, i.e. $E$ leans towards the right side of Fig. 4.11. We observed that $C_D$ tends to decrease with grid refinement and to increase with higher regularisation parameters. It is thus possible that the other authors have used finer grids and/or lower regularisation parameters. Another possible reason for a systematic increase in the sphere drag may be expected from the effect of the tube-to-sphere diameter ratio [29]. However, it was found in Section 4.4.3 that the uncertainty in $C_D$ due to the finite domain size was between 0.05% and 0.12% for power-law fluids and below 0.001% for the other non-Newtonian cases. Thus, the reasons for the over-predicting trend remain unclear.

## 4.6. CONCLUSIONS

The non-Newtonian solver of REFRESCO has been tested on the laminar non-Newtonian flow around a sphere as a stepping stone towards more practical maritime applications.

Some difficulties were encountered when using large regularisation parameters, which led to stagnating residuals and thus large iterative errors. A determining factor turned out to be the choice of the viscosity interpolation scheme. Although obtaining a fully converged solutions remained challenging, the improved iterative convergence provided a significant reduction of the iterative and regularisation errors. This allowed a more compelling comparison with literature.

The flow field around the sphere exhibited the expected behaviour for the considered test cases and it is both qualitatively and quantitatively consistent with previous numerical studies. The maximum difference in drag coefficient between the calculated values and the values from the literature reached 7% (i.e. outside the validation uncertainty range) for power-law fluids, whereas it was insignificant for Bingham creep flow. Overall, the agreement with previous studies is good, with discrepancies that are, in most cases, close or within the validation uncertainties.

Combining the evidence from the code verification exercises in the previous chapter and the results of this work, it is concluded that the power-law, Bingham and Herschel–Bulkley models are implemented correctly and that the code is capable of reproducing literature data with good accuracy despite the high non-linearity introduced by the non-Newtonian viscosity. This provides confidence to employ REFRESCO for more complex applications such as a ship sailing through fluid mud.

# 5

# VALIDATION OF THE RESISTANCE OF A PLATE MOVING THROUGH MUD: CFD MODELLING AND TOWING TANK EXPERIMENTS

*...in which the accuracy of the Bingham model is investigated for numerical predictions of the resistance on a plate moving through fluid mud in laminar regime. The aim is to provide some information about the accuracy of the Bingham model for the prediction of the viscous resistance of a ship sailing through fluid mud. This chapter presents a comparison of experimental and numerical data on the resistance of a plate moving through fluid mud from the Europoort area (Netherlands). Results suggest that the regularised Bingham model can be a reasonable compromise between simplicity and accuracy, although attention must be paid to the choice of the regularisation parameter.*

---

The work in this chapter is based on the published article "Lovato, S., Kirichek, A., Toxopeus, S. L., Settels, J. W. and Keetels, G. H. (2022). Validation of the resistance of a plate moving through mud: CFD modelling and towing tank experiments. *Ocean Engineering*, 258, 111632" [99].

## 5.1. INTRODUCTION

The verification of the code performed in the previous chapters is now followed by the validation of the CFD model. This chapter focuses on the validation of the rheological model. As was already anticipated in Section 2.4, one of the open questions for CFD simulations of mud flows is which constitutive equation adequately describes the complex non-Newtonian flow behaviour of mud. Clearly, this will depend on the application.

The more complex models are typically utilised in rheological studies as their objective is to reproduce the rheology of mud as precisely as possible. Coussot and Piau [32] showed that mud suspensions can be well described by the Herschel–Bulkley model, which has also been used to characterise the mud from the Port of Emden (Germany) [185] and it is recommended by PIANC [109]. Wright and Krone [183] used a more complex model that is parametrised with the solid content. Continuing with higher level of complexity, Toorman [164] proposed a five-parameter thixotropic model that is an extension of the Moore [122] and Worrall-Tuliani [182] models. Van Kessel and Blom [81] used the Toorman model for a comparison of the rheological properties of artificial and natural mud from the Port of Rotterdam (Netherlands). Recently, Shakeel et al. [149] proposed a two-step yielding model containing six fitting parameters that was based on the rheological analysis of mud from the Port of Hamburg (Germany) [146, 147].

Such complex rheological models may be unnecessary for large-scale processes, where in fact simpler models have found their own field of applicability. For example, the wave-induced motions of muddy beds have been studied assimilating the mud to a Bingham fluid (Mei and Liu [112], Liu and Mei [97], Ko-Fei and Mei [58], and Chan and Liu [28]) or a Newtonian fluid (Jiang and Mehta [77] and Winterwerp et al. [181]). As a counterexample, however, Knoch and Malcherek [87] used a modified version of the Worrall-Tuliani model for numerical simulations of stratified mud flows in coastal and estuarine environments.

Simple rheological models seem preferred also to study the effect of muddy seabeds on marine vessels. The Newtonian model was used by Zilman and Miloh [187] whereas Sano and Kunitake [143] even assumed inviscid mud. These strong simplifications could be justified by the fact that viscosity plays a minor role in gravity waves. Recently, Gao et al. [62] and Kaidi et al. [78] have performed CFD simulations to study the influence of muddy seabeds on ships. The former modelled the mud as an Herschel–Bulkley fluid, whereas the latter used the Newtonian model as they observed little difference in the computed resistance when the Bingham model was used.

### 5.1.1. RESEARCH QUESTION AND AIM OF THE CHAPTER

To summarise, a broad range of rheological models for mud were used in previous studies. For ‘sailing-through mud applications’, it is hypothesised that the Bingham model is a good starting point to study the effect of yield stress on the frictional resistance. This chapter tests this hypothesis on a simplified problem: a thin plate moving through mud in laminar regime. In the context of ships sailing through mud, the plate can be locally regarded as a part of the flat bottom of a typical ship hull, although the displacement effects due to the hull form are not accounted.

An analysis and comparison of experimental and numerical data is presented. The experiments consist of towing a plate in a towing tank filled with mud from the Europoort area (Rotterdam, Netherlands) and diluted with sea water from the same location. Three mud conditions are considered, all with density below or equal to 1200 kg/m$^3$, in line with the nautical bottom criterion applied in several harbours across the world [109, 84]. The Bingham yield stress of the considered mud conditions ranges between 10 and 23 Pa. Finally, CFD results have been compared with predictions from simple analytical formulas.

## 5.2. EXPERIMENTAL DATA

### 5.2.1. FACILITY AND SETUP

The experimental data were obtained in the ‘Water and Soil Flume’ at Deltares (Netherlands) [40]. In the remainder, the flume will be referred to as ‘towing tank’ as the latter better describes how it was used in this work.

The towing tank is 30 m long and 2.4 m wide. The experiments consisted in towing a smooth plywood plate through the mud in the tank. The plate was attached to a carriage through a load cell (Fig. 5.1), which enabled force measurements in the towing direction. The nominal towing speed of the carriage was varied between 0.25 and 1.0 m/s and, for each speed, the tests were repeated eight times in order to estimate the random scatter of the mean force. The plywood plate has a chord of 0.8 m and it is 0.012 m thick. For the tests with the most dense mud (Mud_23 in Table 5.2) the plate was submerged by 0.96 m, whereas for all other cases it was 1.0 m. The plate has been reinforced with vertical and horizontal wooden beams to increase its stiffness and to reduce possible bending. The main information about the experimental setup is summarised in Table 5.1.

To make an analogy with a ship, the aforementioned dimensions correspond to $h/T = 2$, where $h$ and $T$ are the mud depth and the ship’s draught, respectively. This depth-to-draught ratio is considered to be shallow enough to influence the forces acting on a sailing ship. However, the relative width of the plate is an order of magnitude lower than expected for typical ships, which practically eliminates the blockage and the subsequent shallow water effects.

Table 5.1: Main information about the experiments.

| Plate | | Towing tank | |
|---|---|---|---|
| Chord, $L$ (m) | 0.8 | Length (m) | 30.0 |
| Thickness, $t$ (m) | 0.012 | Width (m) | 2.4 |
| Draught, $T$ (m) | 0.96, 1.0 | Mud level, $h$ (m) | 1.96, 2.0 |
| Speed, V (m/s) | 0.27, 0.52, 0.77, 1.02 | | |
| $F_r = V/\sqrt{gL}$ | 0.10, 0.19, 0.27, 0.36 | | |
| $F_{rh} = V/\sqrt{gh}$ | 0.06, 0.12, 0.17, 0.23 | | |

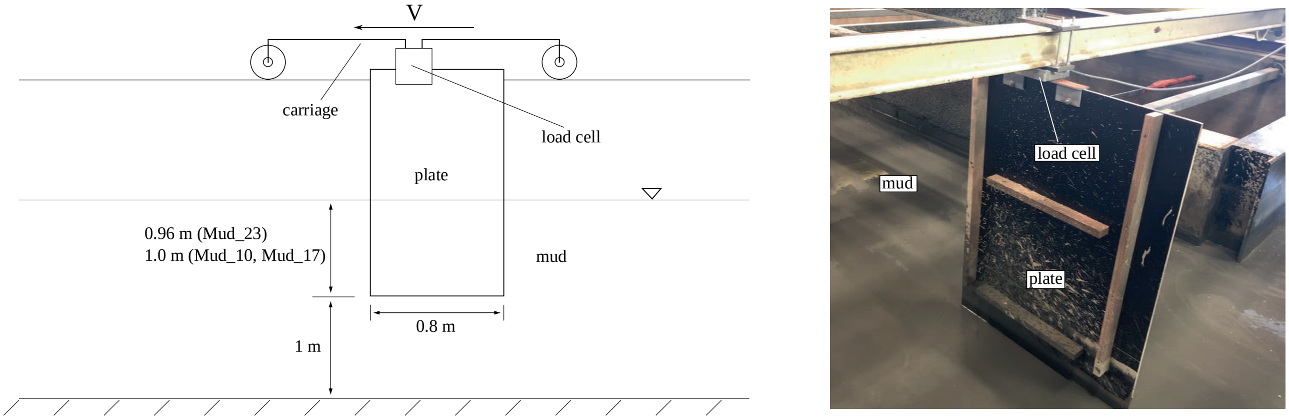

Figure 5.1: Schematic representation of the experiments (left) and picture of the plate immersed in mud (right).

### 5.2.2. MUD PREPARATION

The mud was collected from the Calandkanaal (Europoort, Netherlands) and transported to the towing tank. In order to perform the validation for different mud conditions, the mud was diluted with sea water (having the same salinity as the natural system) to obtain three densities that correspond to target yield stress values of approximately 10, 20 and 30 Pa.

To ensure homogeneous mud, the latter was stirred using a rotating mixer (Fig. 5.2), which has been towed three times back-and-forth prior the start of the experiments with each mud. After the homogenisation, samples of mud were collected twice (before the start of the experiments and after about six hours) at three specific locations along the towing tank. Thus, six samples for each mud were analysed to obtain the density and the rheology properties.

Figure 5.2: The rotating mixer used to homogenise the mud. The right panel shows the mixer in action.

### 5.2.3. MUD DENSITY AND RHEOLOGY

The bulk densities of the mud samples were determined by a portable density meter (Anton Paar, DMA 35). The mud rheology was analysed using the HAAKE MARS I rheometer with a concentric cylinder geometry (CC25) having a gap width of 1 mm. A Peltier controller system was utilised to maintain the temperature at 20 °C during each experiment, which was the average temperature in the towing tank.

The flow curves of the mud samples were obtained in controlled shear rate mode with the following protocol: (i) shear rate ramp-up from 0 to 300 $\mathrm{s}^{-1}$ in 180 s, (ii) constant shear rate of 300 $\mathrm{s}^{-1}$ for 60 s, and (iii) shear rate ramp-down from 300 to 0 $\mathrm{s}^{-1}$ in 180 s. This protocol is proven to be quite fast and repeatable to obtain the yield stress of remoulded samples [149]. Then, the ramp-down[1] flow curves between 200 and 300 $\mathrm{s}^{-1}$ were used for the least-squares fitting of the Bingham model (Fig. 5.3).

For simple shear flow, the Bingham model reads

$$\tau = \tau_B + \mu_B \dot{\gamma}\,, \tag{5.1}$$

where $\tau$ (Pa) is the shear stress, $\dot{\gamma}$ ($\mathrm{s}^{-1}$) is the shear rate, $\tau_B$ (Pa) is the Bingham yield stress and $\mu_B$ (Pa s) is the Bingham (or plastic) viscosity. The mean density and the mean Bingham parameters (over the six samples) of each mud are reported in Table 5.2, together with the standard uncertainties that will be used for the estimation of the input parameter uncertainties in the numerical simulations.

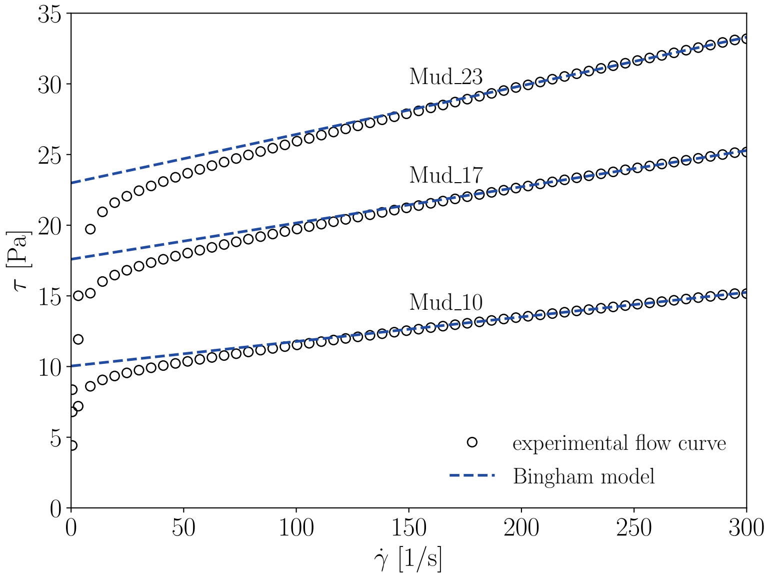

Figure 5.3: Ramp-down flow curves and Bingham fits for one of the six samples of each mud.

---

[1] The ramp-down curves were used because, after the mixing, the mud is assumed to be in a remoulded state.

Table 5.2: Mean values (± standard uncertainty) of density and Bingham parameters for the three mud dilutions. The mean values are calculated over the six samples of each mud.

| Mud case | $\rho$ (kg/m$^3$) | $\tau_B$ (Pa) | $\mu_B$ (Pa s) |
|---|---|---|---|
| Mud_10 | $1171 \pm 0.08\%$ | $9.96 \pm 0.46\%$ | $0.0172 \pm 0.67\%$ |
| Mud_17 | $1190 \pm 0.03\%$ | $17.3 \pm 0.99\%$ | $0.0249 \pm 0.63\%$ |
| Mud_23 | $1200 \pm 0.05\%$ | $23.0 \pm 1.76\%$ | $0.0344 \pm 2.56\%$ |

### 5.2.4. ANALYSIS OF EXPERIMENTAL DATA

#### CALIBRATION UNCERTAINTY

The experimental uncertainties were estimated following the procedure in the ISO-GUM [75]. The first source of experimental uncertainty originates from the calibration of the load cell, $U_{cal}$. The calibration is needed to find the coefficients that ensure the correct conversion of the measured signal from Volt to Newton. This was done by attaching a thread to the plate, and then pulling it in the flow direction with a dynamometer that was previously calibrated using weights. The force was increased from 4 to 24 N by constant increments of 2 N, and the calibration coefficients were obtained from linear curve fitting. Thereafter, the load cell was tested again using the found coefficients, and the maximum observed discrepancy against the dynamometer was about 3.5%. One possible explanation for such rather large discrepancy is that the load cell, which is capable of measuring up to 1000 N, is working in a low range of forces. In fact, the discrepancies between the load cell and the dynamometer were lower when the applied forces were larger. Another reason can be attributed to the non-perfect rigidity of the system composed by the load cell and the plate. Eventually, it was decided to adopt $U_{cal} = 4\%$ as a 'Type B' uncertainty.

#### REPEATED TESTS UNCERTAINTY

The uncertainty in the mean force due to the repeated tests can be estimated by statistical methods ('Type A' uncertainty). For a given mud concentration and a given speed, tests were repeated eight times. In order to determine the time window in which the force signal is stationary (see Fig. 5.4), the Transient Scanning Technique (TST) of Brouwer et al. [22] was applied using an open source code [95]. Some force signals had to be discarded because it was not possible to find any time window in which the signal appeared to be statistically steady. This means that the actual number of repetitions may be eventually equal or less than eight.

After having established the time interval in which the force signal is stationary,

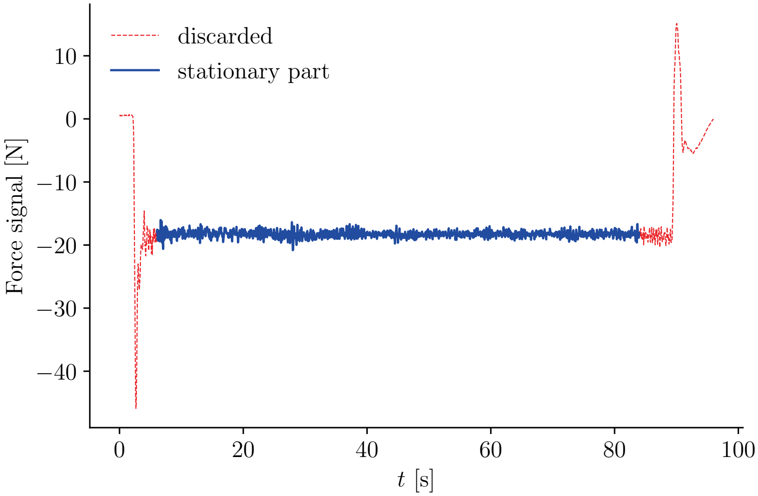

Figure 5.4: Instance of one of the force signals obtained at 0.27 m/s with Mud_10. Only the steady part highlighted in the plot was used in Eq. (5.2).

the time-average force $R^i_{t.a.}$ was obtained from each i-th signal as

$$R^i_{t.a.} = \frac{1}{n}\sum_{j=1}^{n} f_j\,, \tag{5.2}$$

where $n$ is the number of sampling data points in the stationary time interval and $f_j$ is the j-th sampling force.

The final measured force is the mean of the time-average forces, i.e.

$$R_T \equiv R_{mean} = \frac{1}{N}\sum_{i=1}^{N} R^i_{t.a.}\,, \tag{5.3}$$

where $N \leq 8$ is the number of repetitions. Then, the (unbiased) standard deviation of the repeated tests reads

$$s = \sqrt{\frac{1}{N-1}\sum_{i=1}^{N}(R_{mean} - R^i_{t.a.})^2}\,, \tag{5.4}$$

whereas the standard uncertainty is

$$u = \frac{s}{\sqrt{N}}\,. \tag{5.5}$$

Finally, the expanded uncertainty of the repeated tests is

$$U_{rep} = k\,u, \tag{5.6}$$

where $k$ is the coverage factor. Assuming that the mean force follows the Student's t-distribution, $k = 2.306$ ensures a 95% confidence level with eight repetitions (degrees of freedom). For the cases where some signals had to be discarded, larger coverage factors were used.

### OTHER UNCERTAINTIES

Other uncertainties such as those due to manufacture tolerances and precision of the measuring devices were assumed to be negligible compared to the calibration and repeated tests uncertainties, therefore they were not considered. Another important source of uncertainty originates from the experimental setup. A way to account for this is to repeat the tests after having disassembled and reassembled the plate, the load cell and the steel beam to which the load cell is attached. In this way, the possible variability in the setup, such as that due to small misalignments of the plate with the carriage direction, would be included in the uncertainties of the repeated tests. However, this was not done as the time required would have been incompatible with the time window available to complete the experiments. As will be shown in Section 5.4.5, even small rotations of the plate can visibly increase the resistance, thus the experimental uncertainties might have been somewhat underestimated.

### TOTAL EXPERIMENTAL UNCERTAINTY AND MEAN FORCES

Finally, the experimental uncertainties $U_{exp}$ relative to the mean resistance of the plate were obtained as RMS of $U_{cal}$ and $U_{rep}$, and are reported in Table 5.3 together with the mean experimental resistance $R_T$. As expected, the total resistance increases with speed and it is larger for the higher mud concentrations.

It is also worth noticing that $R_T \neq 0$ as $V \to 0$, contrary to what would be expected in Newtonian fluids such as air and water. This is because of the mud yield stress, which approximately increases the resistance by $\tau_B S$, where $S = 2LT$, with $L$ and $T$ being the plate chord and draught, respectively. In fact, a good estimate of the Bingham yield stress can be obtained by extrapolation to $V = 0$ of $R_T/S$ with a second-order polynomial (Fig. 5.5). These estimates are within 3% of the Bingham yield stress for the three muds. This is a first indication that, for this application, the rheology of mud is reasonably well captured by the Bingham model.

## 5.3. CFD SETUP

The experimental data reported in the previous section have been compared with the predictions obtained with REFRESCO. This section presents the governing equa-

Table 5.3: Mean experimental resistance and relative percentage uncertainty.

| $V$ (m/s) | $R_T$ (N) | $U_{exp}$ | $R_T$ (N) | $U_{exp}$ | $R_T$ (N) | $U_{exp}$ |
|---|---|---|---|---|---|---|
| | Mud_10 | | Mud_17 | | Mud_23 | |
| 0.27 | 18.0 | 5.4 | 30.0 | 5.3 | 39.2 | 4.7 |
| 0.52 | 20.4 | 4.2 | 34.2 | 4.3 | 44.7 | 6.2 |
| 0.77 | 23.8 | 4.2 | 38.9 | 4.0 | 49.0 | 4.6 |
| 1.02 | 28.3 | 5.0 | 45.1 | 4.6 | 55.2 | 4.5 |

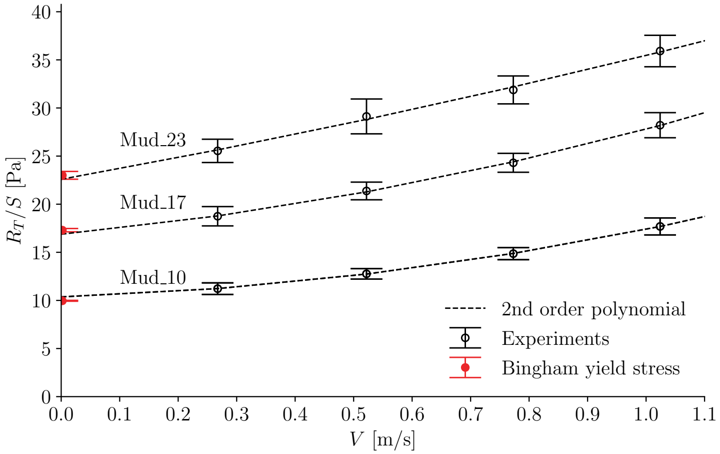

Figure 5.5: Extrapolation to $V = 0$ of the experimental resistance (divided by the side surface of the plate) using a second-order polynomial. The Bingham yield stresses are plotted with their standard uncertainties.

tions, the computational domain and the boundary conditions. Finally, the numerical and input parameters uncertainties are discussed.

### 5.3.1. GOVERNING EQUATIONS

An important decision that will have significant impact on the computing costs is whether the free surface must be modelled or not.

In a first crude approximation, the plate can be regarded as a marine vessel and the resistance can be divided into a viscous component and a wave component. The latter can be reasonably considered to be a function of only the Froude number, $F_r = V/\sqrt{gL}$, where $V$ is the speed, $g$ is acceleration of gravity and $L$ is the plate length. The maximum $F_r$ for the plate is 0.36, a value that is typical of fishing vessels. For these type of vessels the wave resistance is roughly 60% of the total resistance (Larsson and Raven [91]). However, it is possible to identify at least two reasons to neglect the wave resistance for the case of a plate moving in mud.

First, with the given dimensions, the plate has a wetted surface that is roughly ten times that of a fishing vessel, thus the viscous resistance component is also roughly ten times larger. This already reduces the wave resistance from 60% to about 15% of the total resistance. Second, even neglecting the yield stress, the least viscous mud (Mud_10) has a viscosity that is about twenty times that of water. Since in laminar regime the drag on a flat plate scales with $\sqrt{\mu_B}$, the viscous resistance in mud is at least four times larger than in water. This brings the wave resistance for the highest speed down to only a few percent of the total resistance, meaning that the effect of the free surface could be neglected.

To further validate this assumption, preliminary calculations were performed including the free surface, which was modelled using the VOF method (see Chapter 2). Simulations were run in unsteady mode and the time integration was performed implicitly with a first-order backwards Euler scheme. The convective flux of the volume-fraction equation was discretised with an interface-capturing scheme [85] and the grid was refined around the initial mud level. Figure 5.6 shows that double-body (without free surface) and free-surface calculations produce virtually the same pressure resistance. In terms of the total resistance, the average and maximum difference in percentage of the double-body results are 0.3% and 0.9%, respectively.

In light of the above considerations, the contribution of the wave resistance can be neglected, thus double-body calculations are performed unless stated otherwise.

The equations being solved are the incompressible continuity and momentum equations (in Cartesian coordinates):

$$\nabla \cdot \boldsymbol{u} = 0\,, \qquad \frac{\partial \rho \boldsymbol{u}}{\partial t} + \nabla \cdot (\rho \boldsymbol{u}\,\boldsymbol{u}) = \nabla \cdot \boldsymbol{\tau} - \nabla p\,. \tag{5.7}$$

The flow behaviour of mud has been described by the regularised Bingham constitu-

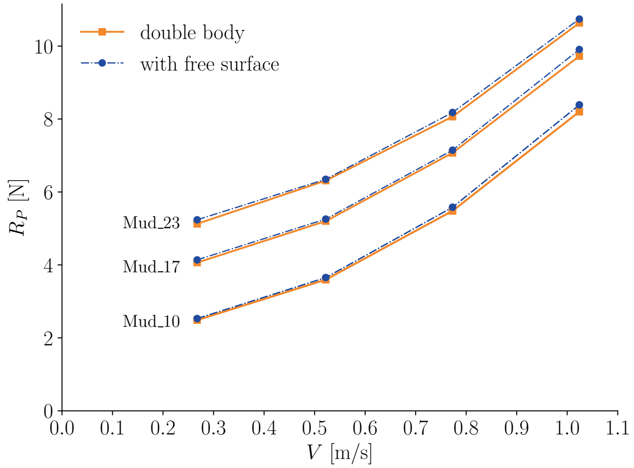

Figure 5.6: Pressure resistance computed with and without the free surface ($M = 12000$, see Section 5.3.4).

tive equation (see also Section 2.4.2), for which the deviatoric stress tensor reads

$$\tau_{ij} = 2\left[\frac{\tau_B(1-e^{-m\dot{\gamma}})}{\dot{\gamma}} + \mu_B\right] S_{ij}\,. \tag{5.8}$$

For this problem, the non-dimensional regularisation parameter is expressed as $M = m\tau_B/\mu_B$, which represents the ratio of maximum-to-minimum viscosity attainable by the fluid (analogous to $M'$ defined in Section 4.3). The uncertainties originating from the use of the regularisation are discussed in Section 5.3.4.

### 5.3.2. FORCE CALCULATIONS

One of the advantages of numerical methods over the experiments is the possibility to distinguish between the frictional and the pressure resistance. These components are calculated respectively as:

$$R_F = \left(\int_{S_w} \boldsymbol{\tau}\cdot\boldsymbol{n}ds\right)_x, \quad R_P = \left(\int_{S_w} -p\cdot\boldsymbol{n}\right)_x ds, \tag{5.9}$$

where $S_w$ is the total wetted surface of the plate, $\boldsymbol{n}$ is the unit normal vector of the plate pointing outwards and the subscript $x$ indicates the x-component (flow direction). The total plate resistance, $R_T$, is simply the arithmetic summation of $R_P$ and $R_F$.

### 5.3.3. COMPUTATIONAL SETTINGS, DOMAIN AND BOUNDARY CONDITIONS

The numerical settings are the same as described in Section 3.4 for steady calculations.

Although experiments at the higher speed may have been affected by small deflections of the plate, calculations will be initially performed with a plate perfectly aligned with the flow direction. The effect of possible rotations will be investigated in Section 5.4.5. Due to symmetry considerations, only the starboard side of the domain containing the plate was modelled. The computational domain has been discretised with H-type grids (Fig. 5.7). In order to reproduce the experimental setup, two series of grids were generated: one where the plate is immersed in the mud up to 1.0 meter (used for Mud_10 and Mud_17), and another where the plate is immersed up to 0.96 meter (used for Mud_23). For both series, the finest grid is made of about 1.77 million cells and the size of the first cell away from the plate surface is $2 \times 10^{-4}$, yielding the maximum $y^+$ between 0.6 and 2.4 among all calculations.

For the boundary conditions, the inflow velocity (towing carriage's speed) was applied at the inlet boundary, whereas the no-slip/non-permeability condition was applied to the plate surface (Fig. 5.7). At the outlet, a Dirichlet condition was imposed for the pressure while symmetry conditions were applied to the top and symmetry plane. The side and bottom boundaries were set as impermeable walls moving at the same velocity of the inflow.

The inlet and outlet boundaries were placed at a distance equal to 2.5 and 5.25 plate lengths, respectively. Calculations performed with twice the distance showed a maximum difference lower than 0.1% in the plate's drag, confirming that the domain is sufficiently long to neglect the influence of the inlet and outlet boundaries.

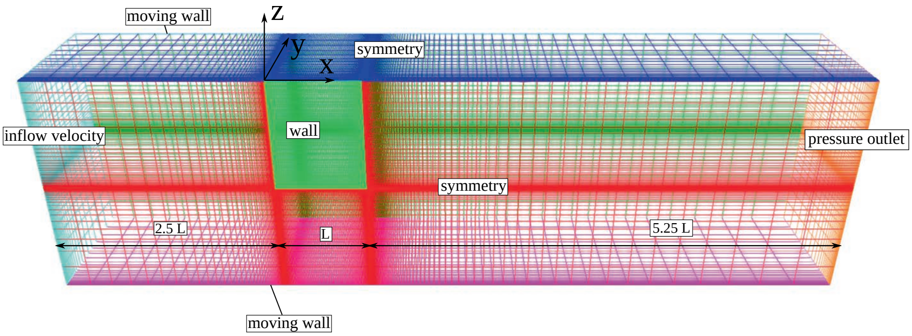

Figure 5.7: Computational domain (finest grid) and boundary conditions.

### 5.3.4. NUMERICAL UNCERTAINTIES

For steady flows, numerical errors are usually divided into three components: round-off, iterative and discretisation errors. However, the use of the regularisation for the Bingham model produces additional errors, hereafter labelled as regularisation errors. Present calculations were performed on a double-precision machine, therefore round-off errors are neglected and not further discussed.

#### ITERATIVE AND DISCRETISATION UNCERTAINTIES

Iterative errors stem from the use of iterative methods to find the solution of the discretised equations. For this work, the iterative convergence criterion was set to $L_\infty < 10^{-7}$. However, this convergence tolerance was actually hardly met; thus, in practice, iterations were stopped when the maximum number of iterations was reached. As a result, iterative errors could not be neglected and the uncertainties, $U_{it}$, were estimated using the method of Eça and Hoekstra [47].

Discretisation errors arise from the use of grids with a finite number of points, and from the use of finite differences instead of partial derivatives. The discretisation uncertainties, $U_d$, were estimated with the method of Eça and Hoekstra [46] using four geometrically similar grids. Figure 5.8 shows an example of the grid sensitivity of $R_T$ for Mud_23 and $V = 0.27$ m/s.

The iterative and discretisation uncertainties are reported in Table 5.4 for the pressure, friction and total resistance. Simulations were carried out using $M = 12000$ (the sensitivity to $M$ is discussed in the next sub-section). The larger percentage uncertainties are found in the pressure component, especially at low speed, with a maximum $U_{it}^P + U_d^P$ of about 16% for Mud_23. For the frictional component, on the other hand, the uncertainties are much lower and do not exhibit a clear trend. Overall, $U_{it}^T + U_d^T$ never exceeds 2.4%.

#### REGULARISATION UNCERTAINTY

As already mentioned in Section 4.4.5, the use of regularisation methods produces an additional error component, the regularisation error, which is the difference between the solution obtained with the regularised and the ideal (non-regularised) model. This error can be minimised by using very large regularisation parameters, although this often leads to slow or stagnating iterative convergence. Furthermore, large regularisation parameters produce stronger viscosity gradients and consequent larger discretisation errors. Because of this interdependency, the final numerical uncertainty was estimated as

$$U_{num} = U_{it} + U_d + U_{reg}\,, \tag{5.10}$$

where $U_{reg}$ is the regularisation uncertainty.

5

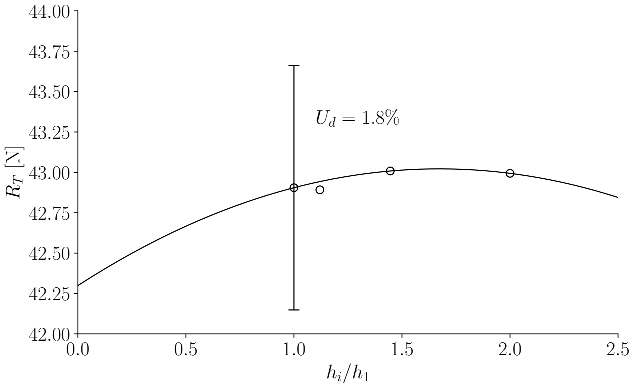

Figure 5.8: Grid sensitivity of $R_T$ for Mud_23, $V = 0.27$ m/s. The grid refinement ratios are $h_i/h_1 = 1$, 1.12, 1.45, 2, which correspond to grids having 1.77, 1.26, 0.59, 0.22 millions cells, respectively,.

Table 5.4: Iterative and discretisation uncertainties in percentage of the corresponding resistance component for the pressure, frictional and total resistance on the finest grid and keeping the non-dimensional regularisation parameter at $M = 12000$. The total resistance and its components are in Newton.

| $V$ (m/s) | $R_P$ | $U_{it}^P$ | $U_d^P$ | $R_F$ | $U_{it}^F$ | $U_d^F$ | $R_T$ | $U_{it}^T$ | $U_d^T$ |
|---|---|---|---|---|---|---|---|---|---|
| Mud_10 | | | | | | | | | |
| 0.27 | 2.5 | 1.4 | 6.5 | 17.2 | 0.0 | 0.6 | 19.7 | 0.1 | 1.1 |
| 0.52 | 3.6 | 0.0 | 2.6 | 18.0 | 0.0 | 1.7 | 21.6 | 0.0 | 0.9 |
| 0.77 | 5.5 | 0.5 | 0.7 | 18.3 | 0.6 | 2.7 | 23.7 | 0.3 | 2.0 |
| 1.02 | 8.2 | 0.1 | 2.5 | 18.1 | 0.7 | 0.6 | 26.3 | 0.1 | 0.5 |
| Mud_17 | | | | | | | | | |
| 0.27 | 4.1 | 1.7 | 7.1 | 29.6 | 0.0 | 0.1 | 33.7 | 0.2 | 0.8 |
| 0.52 | 5.2 | 0.0 | 1.6 | 31.0 | 0.0 | 1.2 | 36.2 | 0.0 | 1.3 |
| 0.77 | 7.1 | 0.0 | 2.1 | 31.7 | 0.0 | 0.8 | 38.8 | 0.0 | 0.3 |
| 1.02 | 9.7 | 0.3 | 0.8 | 32.2 | 0.2 | 2.6 | 41.9 | 0.1 | 1.9 |
| Mud_23 | | | | | | | | | |
| 0.27 | 5.1 | 3.4 | 13.0 | 37.8 | 0.0 | 0.2 | 42.9 | 0.4 | 1.8 |
| 0.52 | 6.3 | 4.3 | 6.0 | 39.6 | 0.0 | 1.2 | 45.9 | 0.3 | 0.4 |
| 0.77 | 8.1 | 0.0 | 5.1 | 40.8 | 0.0 | 0.7 | 48.9 | 0.0 | 0.3 |
| 1.02 | 10.6 | 0.3 | 0.1 | 41.6 | 1.0 | 0.4 | 52.3 | 0.5 | 0.3 |

It is now convenient to introduce $\epsilon = 1/M$. In order to estimate $U_{reg}$ one needs to know how the solution varies with $\epsilon$. Since this is unknown for the present problem, we have followed the procedure already adopted in Section 4.4.5, i.e. $U_{reg}$ was estimated with the method of Eça and Hoekstra [46] by replacing the grid size with $\epsilon$, as shown in Fig. 5.9.

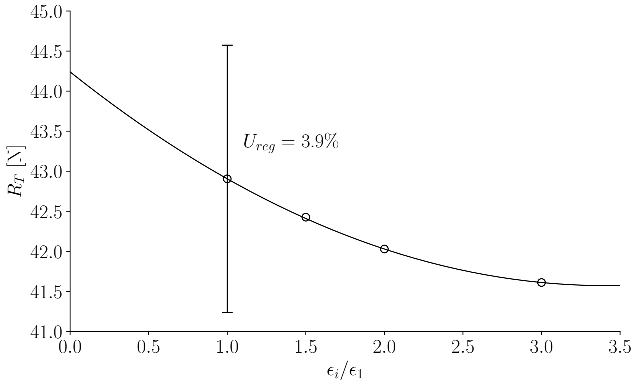

Figure 5.9: Sensitivity of $R_T$ to the inverse of the non-dimensional regularisation parameter $\epsilon = 1/M$ for Mud_23, $V = 0.27$ m/s. The refinement ratios are $\epsilon_i/\epsilon_1 = 1, 1.5, 2, 3$, which correspond to M = 12000, 8000, 6000, 4000, respectively.

The uncertainty estimates are reported in Table 5.5, and they were obtained by varying $M$ between 4000 and 12000. Clearly, the pressure component is (percentage-wise) the most sensitive to the regularisation, especially at low speeds, where $U^P_{reg}$ ranges between 15% and 17.6%. A possible reason for the strong influence of $M$ on $R_P$ is that $M$ affects the viscosity in low shear rate regions, such as near the stagnation points at the front and rear face of the plate where $R_P$ is generated. In these regions, the pressure increases with $M$ (Fig. 5.10). On the other hand, in the high shear

Table 5.5: Regularisation uncertainties in percentage of the corresponding resistance component for the pressure, frictional and total resistance on the finest grid and $M = 12000$.

| $V$ (m/s) | $U^P_{reg}$ | $U^F_{reg}$ | $U^T_{reg}$ | $U^P_{reg}$ | $U^F_{reg}$ | $U^T_{reg}$ | $U^P_{reg}$ | $U^F_{reg}$ | $U^T_{reg}$ |
|---|---|---|---|---|---|---|---|---|---|
| | | Mud_10 | | | Mud_17 | | | Mud_23 | |
| 0.27 | 15.0 | 1.5 | 3.2 | 15.8 | 1.5 | 3.2 | 17.6 | 2.0 | 3.9 |
| 0.52 | 10.4 | 1.5 | 3.0 | 12.7 | 1.7 | 3.2 | 15.1 | 2.0 | 3.8 |
| 0.77 | 6.4 | 1.3 | 2.5 | 9.1 | 1.5 | 2.9 | 10.9 | 1.8 | 3.3 |
| 1.02 | 4.2 | 1.1 | 2.1 | 6.3 | 1.3 | 2.5 | 7.7 | 1.5 | 2.8 |

rate region at the sides of the plate, where the friction component is generated, the viscosity is nearly insensitive to $M$, explaining the lower sensitivity of $R_F$. Fortunately, the pressure contribution is small and so the uncertainties in $R_T$ are within 4%. In conclusion, $M = 12000$ was adopted to mimic the ideal Bingham model.

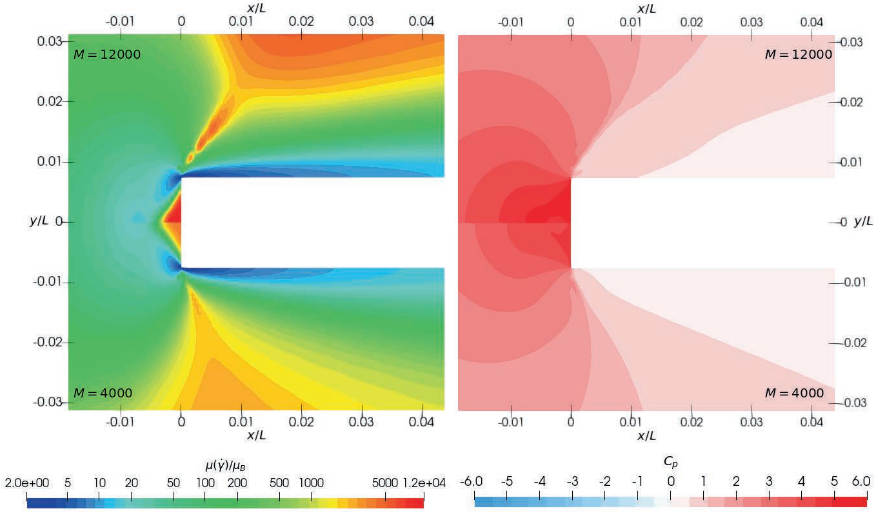

Figure 5.10: Effect of regularisation parameter $M$ on the apparent viscosity (left) and pressure coefficient (right) at the leading face of the plate for Mud_23 and $V = 0.27$ m/s. Viscosity is in logarithmic scale. Flow is from left to right. The cutting plane is at $z/T = -0.5$.

### 5.3.5. INPUT PARAMETERS UNCERTAINTY

Numerical simulations require input parameters that are experimentally determined and that have uncertainties associated with them. The standard input uncertainty, $u_{input}$, can be calculated using the perturbation method, as

$$u^2_{input} = \sum_i \left( \frac{\partial R}{\partial X_i} u_i \right)^2, \tag{5.11}$$

where $R$ is the resistance of the plate, $X_i$ is the i-th input parameter, $u_i$ is its corresponding standard uncertainty, $\partial R / \partial X_i$ is the sensitivity coefficient.

For the present work, the input parameters are the following: plate's draught $T$, carriage's speed $V$ (flow velocity), mud density $\rho$, Bingham yield stress $\tau_B$ and viscosity $\mu_B$. The standard uncertainties associated with the mud properties were reported in Table 5.2. For $T$ and $V$, the standard uncertainty could not be estimated with statistical methods, therefore they were both assumed to be 1%. The sensitivity coefficients could be determined from CFD calculations, however this would lead to an unfeasible number of simulations. It was thus decided to approximate the drag force on the plate by modelling CFD data with the analytical formulas that are discussed in Section 5.5. While there are some discrepancies between these formulas and CFD data, the agreement is deemed sufficient for the purpose of determining the sensitivity coefficients.

The derivation of $\partial R/\partial X_i$ from analytical formulas becomes then a simple yet lengthy task, which was thus carried out with the aid of computer algebra systems. Table 5.6 shows the non-dimensional sensitivity coefficients of each input parameter for Mud_10 and Mud_23.

Table 5.6: Non-dimensional sensitivity coefficients $\partial R_T/\partial X_i\,\overline{X_i}/\overline{R_T}$ for each input parameter $X_i$: plate's draught $T$, carriage's speed $V$, mud density $\rho$, Bingham yield stress $\tau_B$ and viscosity $\mu_B$. $\overline{X_i}$ is the mean input parameter that is used in the CFD simulations whereas $\overline{R_T}$ is the total resistance from the analytical formulas evaluated for $\overline{X_i}$.

| $V$ (m/s) | $\rho$ | $T$ | $V$ | $\tau_B$ | $\mu_B$ | $\rho$ | $T$ | $V$ | $\tau_B$ | $\mu_B$ |
|---|---|---|---|---|---|---|---|---|---|---|
| | | | Mud_10 | | | | | Mud_23 | | |
| 0.27 | 0.04 | 1.00 | 0.10 | 0.94 | 0.02 | 0.02 | 1.00 | 0.04 | 0.97 | 0.01 |
| 0.52 | 0.12 | 1.00 | 0.28 | 0.83 | 0.05 | 0.07 | 1.00 | 0.17 | 0.90 | 0.03 |
| 0.77 | 0.21 | 1.00 | 0.49 | 0.72 | 0.07 | 0.12 | 1.00 | 0.30 | 0.83 | 0.05 |
| 1.02 | 0.30 | 1.00 | 0.70 | 0.61 | 0.09 | 0.18 | 1.00 | 0.43 | 0.75 | 0.07 |

The largest sensitivity coefficient is for the draught $T$. As expected, it is exactly equal to 1 (i.e. linear relation) since both $R_P$ and $R_F$ are proportional to the plate surface, which is in turn a linear function of $T$. For all the other input parameters, the coefficients are less than 1, which means that the input uncertainty for $R_T$ grows less than linearly with an increase of the standard uncertainty. Note, however, that the coefficients in Table 5.6 are calculated for those particular test cases, therefore different values should be expected for other experimental conditions. Furthermore, the coefficients can be considered accurate as long as the resistance of the plate can be well approximated by the analytical formulas discussed in Section 5.5. For example, the linear relation between $R_T$ and $T$ is accurate only for small variations of $T$ and, in any case, as long as the shallow water effects remain negligible.

Assuming a Gaussian error distribution, the final expanded input uncertainties are $U_{input} = 2u_{input}$ (95% confidence) and they are reported in Table 5.7. The largest $U_{input}$ is found for Mud_23 because the latter has the highest uncertainty in $\tau_B$ (see also Table 5.2). Furthermore, $U_{input}$ decreases with $V$, which reflects the behaviour of $\partial R_T/\partial\tau_B$.

Table 5.7: Input parameter uncertainties in percentage of $R_T$ from CFD ($M = 12000$). The input parameters are the: speed $V$, plate draught $T$, mud density $\rho$ and Bingham parameters $\tau_B$ and $\mu_B$.

| $V$ (m/s) | $U^P_{input}$ | $U^F_{input}$ | $U^T_{input}$ | $U^P_{input}$ | $U^F_{input}$ | $U^T_{input}$ | $U^P_{input}$ | $U^F_{input}$ | $U^T_{input}$ |
|---|---|---|---|---|---|---|---|---|---|
| | | Mud_10 | | | Mud_17 | | | Mud_23 | |
| 0.27 | 2.2 | 2.1 | 2.1 | 2.8 | 2.7 | 2.7 | 4.0 | 3.8 | 3.8 |
| 0.52 | 2.3 | 2.2 | 2.2 | 2.7 | 2.6 | 2.6 | 3.5 | 3.7 | 3.7 |
| 0.77 | 2.2 | 2.3 | 2.3 | 2.6 | 2.7 | 2.6 | 3.3 | 3.7 | 3.5 |
| 1.02 | 2.1 | 2.5 | 2.4 | 2.5 | 2.8 | 2.6 | 3.0 | 3.7 | 3.5 |

## 5.4. COMPARISON OF EXPERIMENTAL AND CFD DATA

### 5.4.1. MODELLING ERROR ESTIMATION

According to the validation procedure proposed by ASME [6], the modelling error, $\delta_{model}$, can be estimated by comparing two quantities: the (expanded) validation uncertainty,

$$U_{val} = \sqrt{U^2_{num} + U^2_{exp} + U^2_{input}}, \tag{5.12}$$

and the comparison error,

$$E = S - D, \tag{5.13}$$

where $S$ is the numerical solution value and $D$ is the experimental data. $U_{num}$, $U_{exp}$ and $U_{input}$ are discussed above.

$E$ and $U_{val}$ define an interval within which $\delta_{model}$ falls, i.e.

$$E - U_{val} \leq \delta_{model} \leq E + U_{val}. \tag{5.14}$$

When $|E| >> U_{val}$, the modelling error can be directly estimated as $|\delta_{model}| \approx |E|$. In all other cases, only the upper and lower bounds of $\delta_{model}$ can be determined. If more information about the modelling error is required, the validation uncertainty needs to be reduced.

The estimated $\delta_{model}$, $U_{val}$ and $E$ using the Bingham model with large regularisation parameters ($M = 12000$) are reported in Table 5.8 in percentage of the experimental value.

At intermediate speeds $E$ is close or within $U_{val}$, whereas at the lowest and highest speed $E$ tends to exceed $U_{val}$. In any case, $E$ is never sufficiently larger than $U_{val}$ to allow a direct estimate of $\delta_{model}$. In other words, for all the cases, only the upper bound of the modelling error could be estimated and, for a few cases, also the sign of the error could be determined.

The largest upper bounds of the modelling errors are found at the lowest speed for all three mud conditions, which are also the cases with the largest $E$. The lowest

Table 5.8: Comparison error, validation uncertainty and modelling errors in percentage of the experimental data. In some cases the sign of the modelling errors could be determined and it is reported between parenthesis.

| $V$ (m/s) | $E$ | $U_{val}$ | $\lvert\delta_{model}\rvert \leq$ | $E$ | $U_{val}$ | $\lvert\delta_{model}\rvert \leq$ | $E$ | $U_{val}$ | $\lvert\delta_{model}\rvert \leq$ |
|---|---|---|---|---|---|---|---|---|---|
| | | Mud_10 | | | Mud_17 | | | Mud_23 | |
| 0.27 | 9.7 | 7.6 | 17.3 (+) | 12.3 | 7.8 | 20.1 (+) | 9.4 | 9.2 | 18.5 (+) |
| 0.52 | 5.6 | 6.4 | 12.0 | 5.8 | 7.0 | 12.8 | 2.6 | 8.6 | 11.2 |
| 0.77 | -0.1 | 6.8 | 6.9 | -0.2 | 5.8 | 6.0 | -0.1 | 6.8 | 6.9 |
| 1.02 | -7.1 | 6.0 | 13.1 (-) | -7.2 | 6.7 | 13.9 (-) | -5.3 | 6.6 | 11.8 |

upper bound of the modelling errors is found for $V = 0.77$ m/s because $E$ is very small for all the three mud concentrations. At this speed, there is an intersection of the numerical and experimental data (see Fig. 5.11).

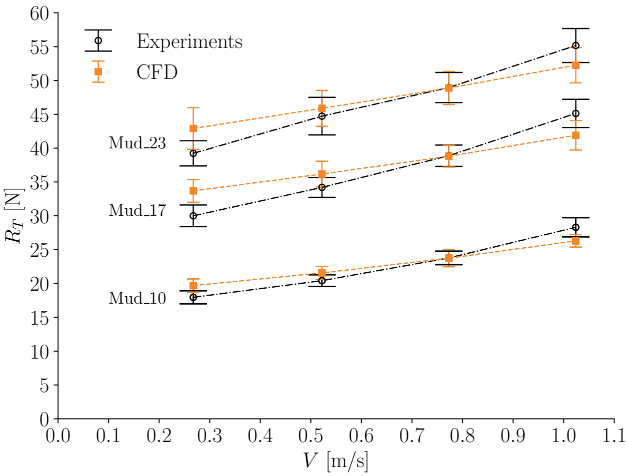

Figure 5.11: Total resistance of the plate moving through mud as a function of the inflow velocity. CFD error bars include numerical and input parameter uncertainties. CFD data were obtained keeping the non-dimensional regularisation parameter at $M = 12000$ (see also Section 5.3.4).

The two main observations from Fig. 5.11 are: i) the variation of resistance due to the changes of mud rheology is well captured by CFD; ii) the slopes of the experimental and CFD curves are visibly different. The first observation suggests that the Bingham model is suitable, at least, to study how $R_T$ changes in response to variations of the mud concentration. About the second observation, CFD tends to overpredict $R_T$ at low speed and to underpredict it at high speed. This trend suggests that $E$ will increase in magnitude for speeds outside the range considered in this work. Some possible causes for this may be the:

- choice of the regularisation parameter
- selected shear rate range for the rheological characterisation of mud
- poor fitting of the Bingham model to the flow curves at low shear rates (see e.g. Fig. 5.3)
- contamination of experimental data by undesired effects

These possible causes are discussed below.

### 5.4.2. EFFECT OF THE REGULARISATION PARAMETER

It was just shown that the largest discrepancies between experiments and CFD are found at the lowest speed for all the three mud conditions. Since lower speeds are related to lower shear rates, a possible explanation for this may be the poor modelling of mud at low shear rates. Experimental evidence (e.g. Dzuy and Boger [45] and Ellwood et al. [56]) suggested that most real fluids do not exhibit an actual yield stress and that regularised models may better capture the behaviour of non-Newtonian materials at low shear rates.

In light of this, it is now questioned whether the rheology of mud may be better described using lower regularisation parameters. A natural choice could be to determine the regularisation parameter, $m$, from the rheological data. Among the many possible choices, three procedures to determine $m$ are considered:

- $M_{down}$: $m$ is chosen such that the regularised curve will intersect the first point (i.e., lowest $\dot{\gamma}$) in the ramp-down flow curve, i.e.

  $$m = -\ln\left(1 + \frac{\mu_B \dot{\gamma}' - \tau'}{\tau_B}\right)\frac{1}{\dot{\gamma}'}, \tag{5.15}$$

  where the prime symbol indicates the first point in the (ramp-down) flow curve. Note that $\tau_B$ and $\mu_B$ do not change as they are determined from the least-square fitting of the ideal Bingham model (see also Section 5.2.3).

- $M_{up}$: $m$ is also obtained from Eq. (5.15) but using the ramp-up curve.

- $M_{fit}$: the triplet $(m, \tau_B, \mu_B)$ is obtained by least-square fitting of

  $$\tau = \tau_B(1 - e^{-m\dot{\gamma}}) + \mu_B \dot{\gamma} \tag{5.16}$$

  to the ramp-down curve.

$M_{down}$ and $M_{up}$ ensure that the regularised Bingham model produces the same apparent viscosity observed in the first point of the ramp-down and ramp-up flow curves, respectively. An alternative procedure similar to $M_{down}$ and $M_{up}$ would be to extrapolate the measured apparent viscosity to $\dot{\gamma} = 0$ and then use the extrapolated value to derive the regularisation parameter. The latter procedure would probably be less susceptible to the noise in the first point of the rheological data.

The Bingham fits obtained using the three procedures above are illustrated in Fig. 5.12, whereas the non-dimensional regularisation parameters are reported in Table 5.9. Note that since $m$ is now determined from the mud rheology, the regularisation uncertainty must be estimated as an input parameter uncertainty,

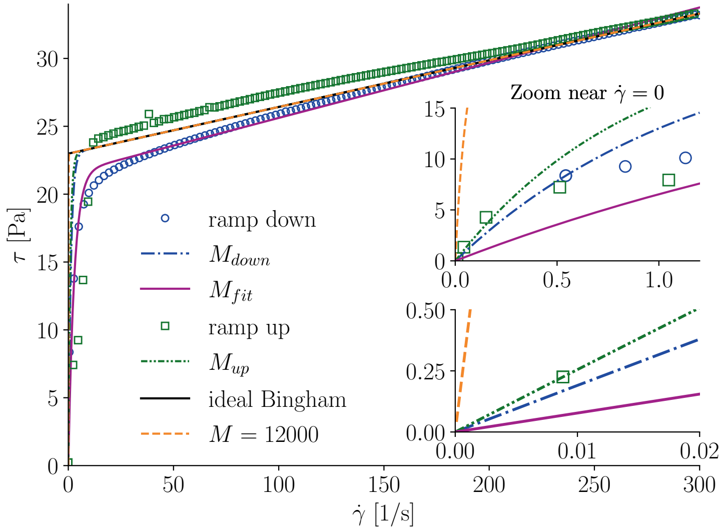

Figure 5.12: Regularised Bingham model using different regularisation parameters: $M = 12000$, $M_{down}$, $M_{up}$ and $M_{fit}$ . The flow curves are for Mud_23.

$$U_{reg} = k\,u_{reg} = k\,\frac{\partial R}{\partial m}u_m\,, \tag{5.17}$$

where $R$ is the resistance. $u_m$ is the standard uncertainty for six repetitions (number of mud samples) and $k = 2.447$ with 95% confidence assuming a Student t-distribution. The derivative in Eq. (5.17) is unknown, thus it was approximated with a second-order accurate finite difference,

$$\frac{\partial R}{\partial m} \approx \frac{R(m + u_m/2) - R(m - u_m/2)}{u_m}\,, \tag{5.18}$$

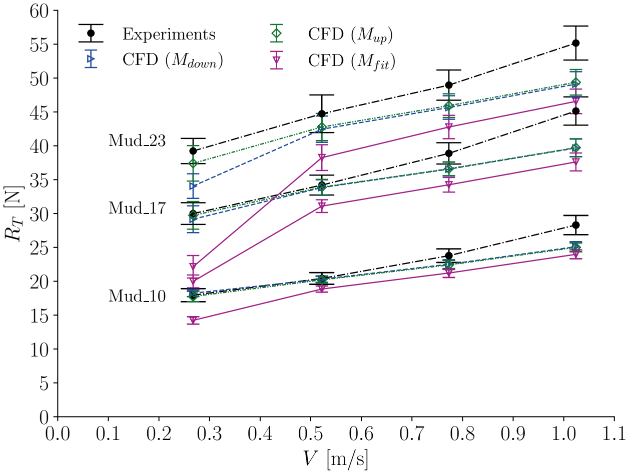

Figure 5.13: Effect of different regularisation parameters on the CFD predictions of the plate resistance.

where the two terms at the numerator were determined from numerical simulations for each mud condition and speed. For most of the test cases, we found that the regularisation uncertainties have been reduced compared to the calculations with $M = 12000$. The closest fit to the ramp-down curve is obtained with $M_{fit}$, whereas

Table 5.9: Mean values (± standard uncertainty) of the non-dimensional regularisation parameters obtained from the rheological data.

| V[m/s] | $M_{up}$ | $M_{down}$ | $M_{fit}$ |
|---|---|---|---|
| Mud_10 | $538 \pm 5.7\%$ | $687 \pm 1.3\%$ | $236 \pm 1.8\%$ |
| Mud_17 | $708 \pm 1.8\%$ | $658 \pm 0.3\%$ | $224 \pm 1.2\%$ |
| Mud_23 | $747 \pm 13.3\%$ | $556 \pm 1.1\%$ | $191 \pm 1.7\%$ |

$M_{up}$ and $M_{down}$ tend to overpredict the shear stress in the low shear rate range (Fig. 5.12). However, these observations are not reflected by the accuracy in the force prediction. Figure 5.13 shows in fact that $M_{fit}$ produces by far the worst agreement to experimental data, whereas $M_{up}$ and $M_{down}$ produce fairly good predictions at the lower speeds. In particular, $M_{up}$ seems to capture very well the trend at low speeds. At $V = 0.27$ m/s, the comparison error, $E$, reduces to 1.1%, 0.9% and 4.9% for Mud_10, Mud_17 and Mud_23, respectively. Except for Mud_23, $M_{down}$ and $M_{up}$ produce nearly the same results.

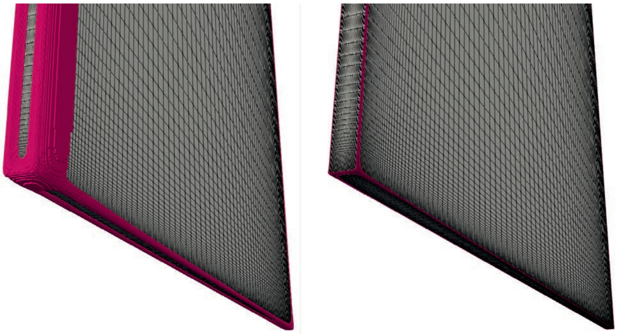

Figure 5.14: Highlighted in magenta are the cells where $\dot{\gamma} \geq 300\ s^{-1}$ for Mud_23 near the leading and bottom edge of the plate. $V = 1.02$ m/s (left); $V = 0.27$ m/s (right).

In conclusion, although the fit using $M_{fit}$ appears closer to the mud flow curves, it gives by far the worst numerical prediction. On the other hand, determining the regularisation parameter based on the first points in the flow curves seems to give good agreement with experimental data at low speed. However, the discrepancies become larger at the higher speeds.

### 5.4.3. EFFECT OF THE SHEAR RATE RANGE FOR THE RHEOLOGY CHARACTERISATION

Despite the improvements observed at low speeds when the regularisation parameter is determined from the mud rheology, the discrepancies at high speed remain large (even larger than the case with $M = 12000$). Since higher speeds are related to higher shear rates, a possible explanation may be sought in the shear rate range considered for the rheological experiments.

Figure 5.14 highlights the fluid regions where the shear rate is above 300 $s^{-1}$, the latter being the maximum shear rate reached in the rheological measurements. These regions are located near the plate edges, where the fluid experiences strong accelerations. As expected, the case at the higher speed has larger fluid regions with $\dot{\gamma} \geq 300\ s^{-1}$. It is possible that fitting the Bingham model to the flow curve up to 300 $s^{-1}$ is insufficient to accurately predict the force at high speeds (shear rates).

Since rheological data for $\dot{\gamma} > 300\ s^{-1}$ are not available, the Bingham parameters corresponding to flow curves with higher $\dot{\gamma}$ have been obtained by extrapolation. Basically, the Bingham parameters were obtained by varying the maximum shear rate[2], $\dot{\gamma}_{max}$, between 200 and 300 $s^{-1}$. Then, the Bingham parameters were linearly[3] extrapolated up to $\dot{\gamma}_{max} = 400s^{-1}$, as illustrated in Fig. 5.15 for $\tau_B$. It was observed that $\tau_B$ increases with $\dot{\gamma}_{max}$, whereas $\mu_B$ decreases (not shown).

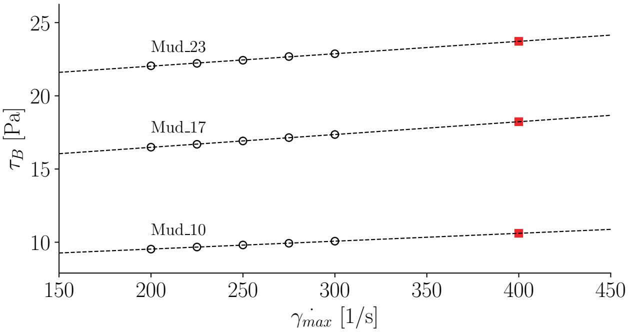

Figure 5.15: Bingham yield stresses, $\tau_B$, obtained using different shear rate intervals having $\dot{\gamma}_{max}$ as maximum (open circles); linear fitting of $\tau_B$ values for $\dot{\gamma}_{max} \leq 300$ $s^{-1}$ (dashed lines); extrapolated $\tau_B$ for $\dot{\gamma}_{max} = 400$ $s^{-1}$ (filled squares).

Numerical simulations were performed for the case $M_{up}$ as an example, which was observed to produce good agreement with experiments at low speed but larger discrepancies at high speed (see Section 5.4.2). Note that the values of $M_{up}$ are not the same as in Table 5.9 because the Bingham parameters have changed.

Figure 5.16 shows that increasing $\dot{\gamma}_{max}$ seems to slightly improve the agreement with experimental data. This is because higher $\dot{\gamma}_{max}$ gives higher $\tau_B$, which shifts up the CFD data. However, the slopes of the CFD curves are still visibly different from the experimental ones. This is because the slopes of the CFD curves are related to $\mu_B$, but the latter has a rather small influence on the resistance (see also Table 5.6).

In conclusion, while increasing the maximum shear rate in the rheological tests leads to slightly better agreement with experimental data, it does not explain the discrepancies at the higher speeds.

### 5.4.4. EFFECT OF USING A MORE COMPLEX RHEOLOGICAL MODEL

Can the CFD predictions become more accurate by simply improving the fit of the rheological model to the flow curves? We showed that $M_{fit}$ gives the closest fit to the ramp-down curve while producing the worst resistance prediction. This is now further investigated using the regularised Tscheuschner rheological model [117],

---

[2] The interval used for the Bingham fitting is [$\dot{\gamma}_{max}$ -100$s^{-1}$,$\dot{\gamma}_{max}$]

[3] It is implicitly assumed that the ramp-down curve will continue up to $\dot{\gamma} = 400s^{-1}$ without major changes.

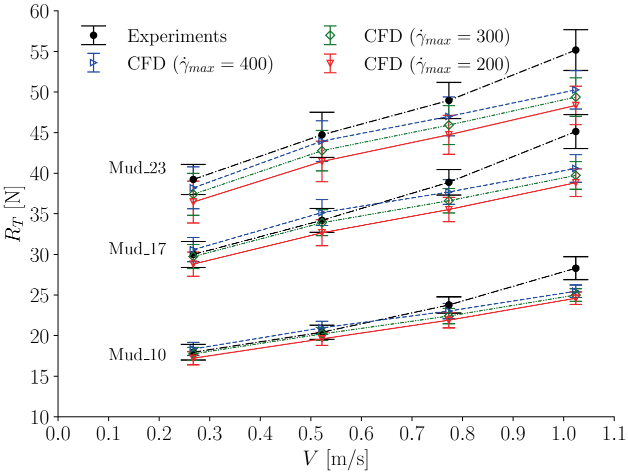

Figure 5.16: Effect of the maximum shear rate in the rheology characterisation on the CFD predictions of the plate resistance.

which can be adjusted to be a virtually perfect fit of the ramp-down flow curves (Fig. 5.17).

This model was originally developed for chocolate and it provides a somewhat mixed behaviour of Bingham and Herschel–Bulkley fluids. For simple shear flows, the model reads

$$\tau = \tau_0\left(1 - e^{-m\dot{\gamma}}\right) + \mu_1\dot{\gamma} + \mu_2\dot{\gamma}^n\,, \tag{5.19}$$

where $\mu_1$ and $\mu_2$ determine the slope of Eq. (5.19) at high and low shear rates, respectively. The quintuplet ($m$, $\tau_0$, $\mu_1$, $\mu_2$, $n$) was obtained by least squares fitting of Eq. (5.19) to the ramp-down curve of the six mud samples, and the mean values (reported in Table 5.10) were fed to the CFD solver.

Table 5.10: Mean values (± standard uncertainty) of the Tscheuschner parameters.

| Mud case | $\tau_0$ ($Pa$) | $m$ ($s$) | $\mu_1$ ($Pa\,s$) | $\mu_2$ ($Pa\,s^n$) | $n$ |
|---|---|---|---|---|---|
| Mud_10 | 3.61 | 0.433 | 0.0146 | 3.97 | 0.103 |
| Mud_17 | 8.07 | 0.372 | 0.0249 | 5.48 | 0.112 |
| Mud_23 | 12.06 | 0.322 | 0.0295 | 6.34 | 0.118 |

In spite of its excellent fit to the flow curves, the Tscheuschner model produces strong underestimations of the resistance (Fig. 5.18), especially at low speed. At

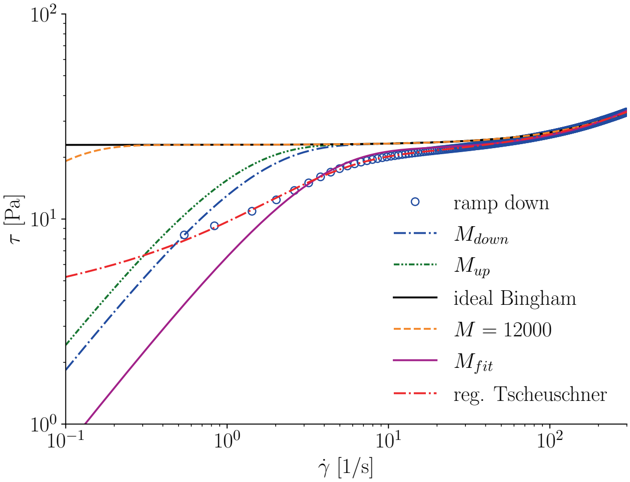

Figure 5.17: Comparison of the Bingham and Tscheuschner models for one (ramp-down) flow curve of Mud_23.

the higher speed, the Tscheuschner model tends to produce the same results as the Bingham model with $M_{up}$. The maximum and minimum comparison errors among all cases are respectively 13% and 25%. The reasons for the poor predictions of the Tscheuschner model despite being an excellent fit of the ramp-down flow curves are not clear. However two possible explanations are given.

First, the protocol used for the rheological experiments may be not accurate enough at low shear rates. Thus, capturing the ramp-down flow curve down to the lowest value of $\dot{\gamma}$ may give worse numerical predictions simply because of inaccuracies in the flow curves. Second, a possible reason can be the thixotropy of mud. Although the mud was heavily mixed prior the experiments, a partial structural recovery has certainly occurred during the tests, thus the ramp-down may not be a very accurate representation of the flow behaviour of mud, in particular at low speeds/shear rates. On the other hand, the Bingham model, which fits the ramp-down flow curve only in the higher shear rate range, seems to be somewhat between the ramp-up and ramp-down curves (see also Fig. 5.12), which may be an acceptable compromise for high-shear flows.

### 5.4.5. EFFECT OF NON-ZERO ANGLES OF ATTACK

Another possible explanation for the discrepancies at high speed could be sought in the experimental data rather than in the rheological model.

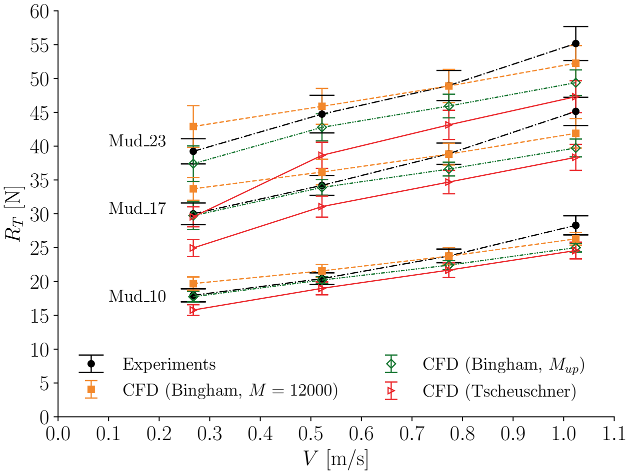

Figure 5.18: Total resistance using the Bingham and Tscheuschner model. The Tscheuschner uncertainty bars are set to 5% as a reference.

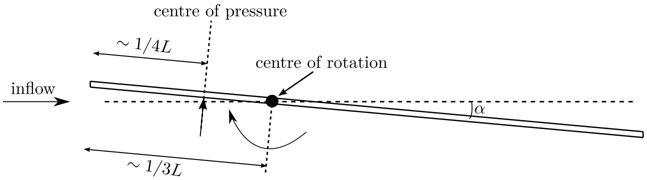

Figure 5.19: Schematic representation of the mechanism responsible for the possible increased rotations of the plate at the higher speeds.

The alignment of the plate with the flow direction is one of the main challenges when performing towing experiments. While the increase in resistance due to small misalignments may be negligible at low speeds, it could become substantial at higher speeds. In fact, increasing the angle of attack mainly increases the pressure resistance, which is proportional to $V^2$. In turn, stronger pressure disturbance can also increase the wave resistance. Furthermore, for the present experiments, the load cell was attached to the plate at about $1/3L$ from the leading edge (Fig. 5.19). But the centre of pressure for flat plates is approximately at $1/4L$ from the leading edge, meaning that an initially small angle of attack could have been amplified at higher speeds. The magnitude of this amplification depends upon the rigidity of the mechanical system formed by the plate and the load cell.

Unfortunately, the angle of attack is not known, thus correcting experimental data for this effect is not possible. Nevertheless, the effect of the plate rotation can be modelled numerically to verify whether the trend of the experimental data can be better captured.

Calculations were thus performed after applying a grid deformation (rotation around the z-axis). Since the rotation of the plate can increase the wave resistance, calculations were performed including the free surface, with the same settings as in Section 5.3.1. Obviously, since the problem is no longer symmetrical, calculations were performed on the full domain instead of half, as shown in Fig. 5.20.

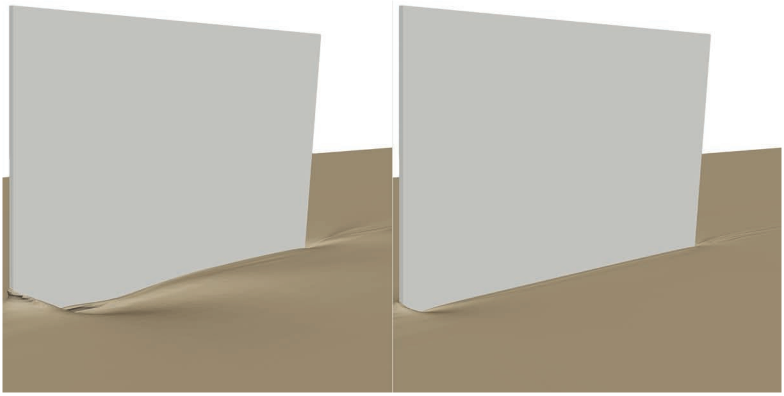

Figure 5.20: Simulated mud free surface for Mud_10 at V=1.02 (left) and 0.52 m/s (right). Both simulations are with an angle of attack of 3 degrees and $M = 12000$. Flow is from left to right.

It is remarked that the uncertainties in the CFD data are no longer known both because the input uncertainties cannot be simply determined from analytical formulas (as was done in Section 5.3.5) and because performing a grid/regularisation refinement study for these computations was deemed outside of the scope of the present study. As reference, the uncertainties from the analogous double-body calculations with zero angle of attack are shown[4].

The effect of an angle of attack of 3 degrees on the resistance is illustrated in Fig. 5.21 for the cases $M_{up}$ and $M = 12000$. Interestingly, the slope of experimental data with respect to $V$ is now well predicted by CFD. In particular, $M_{up}$ almost duplicates the experimental data, whereas the ideal Bingham model ($M = 12000$) captures the trend of the experimental data but it visibly over estimates the resistance.

---

[4] The actual uncertainties are likely larger than those of the double-body calculations because of the additional discretisation errors produced by the volume-fraction equation.

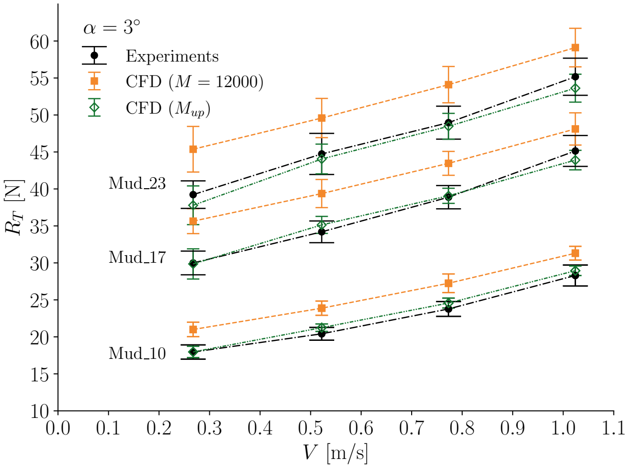

Figure 5.21: Resistance of the plate moving through mud. CFD data are obtained with an angle of attack of 3 degrees and including the effect of the free surface. CFD uncertainties are relative to the analogous double-body calculations with zero angle of attack.

It is thus inferred that experimental data at the highest speeds are likely contaminated by a rotation of the plate. This also suggests that lower regularisation parameters (e.g. $M_{up}$) produce better prediction than the ideal Bingham model, which tends to over-estimate the total resistance.

The difference in the predictions between $M_{up}$ (low regularisation parameter) and $M = 12000$ (very high regularisation parameter) is mainly due to the pressure component. In particular, this appears to be related to the larger viscosity in the low deformation regions (i.e where the regularisation is activated), as for example at the rear stagnation point (Fig. 5.22, left panel). For $M = 12000$, such high viscosity leads to higher pressure on the right surface (pressure side) and to lower pressure on the left surface (suction side) compared to $M_{up}$ (Fig. 5.22, right panel). Similar observations were also made above when analysing the regularisation uncertainty.

### 5.4.6. FINAL REMARKS ON THE REGULARISATION PARAMETER AND PROPOSED RULE OF THUMB

We recall that the general rule when using regularisation methods is to use the highest possible regularisation parameter in order to mimic the ideal model as closely as possible. This approach, however, can lead not only to larger discrepancies with experimental data (see Section 5.4.2) but also to numerical difficulties, such as stagnating

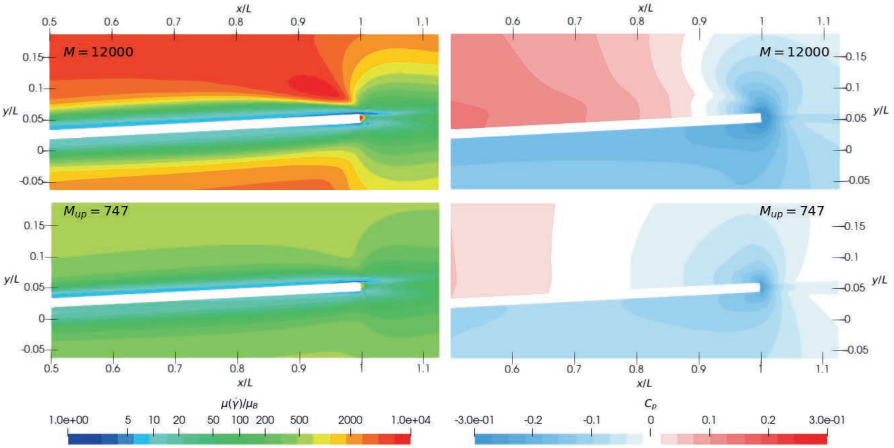

Figure 5.22: Contour diagram at the rear part of the plate with an angle of attack of 3 degrees. Apparent viscosity (left); hydrodynamic pressure coefficient (right). The cutting plane is at $z/T = -0.5$ ($T$ is the plate's draught) and the test case is Mud_23, $V = 1.02$ m/s.

or even diverging residuals in the iterative solver (see, for example, Section 4.4.6).

It was shown that these issues can be mitigated by using lower regularisation parameters based on the first point in the flow curves. Although this procedure is purely empirical and no physical explanations were provided, a general rule of thumb could be devised. In fact, for all the mud conditions considered in this work, the non-dimensional regularisation parameters obtained from the first point in either the ramp-up ($M_{up}$) or ramp-down ($M_{down}$) were between 538 and 747. A reasonable rule of thumb to choose the regularisation parameter is thus $M = m\tau_B/\mu_B \approx 800$. This means that the mud apparent viscosity in low-deformation regions is about 800 times the viscosity of mud in the high shear rate regions (e.g. boundary layers). Further research is needed to verify the applicability of such an empirical approach to other test cases.

## 5.5. COMPARISON OF CFD DATA WITH ANALYTICAL FORMULAS

### 5.5.1. FRICTIONAL RESISTANCE

The frictional component of the total resistance, $R_F$, originates from the shear stress acting on the side surfaces of the plate. These surfaces can be approximated as flat plates. A friction coefficient for laminar Bingham flows over flat plates was derived by Chhabra and Richardson [30] using a third degree polynomial approximation for the velocity profile:

$$C_{RF} \equiv \frac{R_F}{1/2\rho V^2 S} = \frac{1.292}{\sqrt{Re}} + Bn, \tag{5.20}$$

where $Re = \rho VL/\mu_B$ is the Reynolds number, $Bn = \tau_B/(1/2\rho V^2)$ is another definition of the Bingham number (cf. with Eq. (4.3)) and $S$ is the surface of the flat plate that, for the present work, is $2LT$. Equation (5.20) is identical to its Newtonian counterpart when $Bn = 0$. Therefore, we propose a slightly different version that reduces to the well-known Blasius formula when $Bn = 0$, i.e.

$$C'_{RF} = \frac{1.328}{\sqrt{Re}} + Bn. \tag{5.21}$$

The comparison of Eq. (5.21) with CFD data is plotted in Fig. 5.23. At the lower speeds, the agreement is excellent, with an average difference of about 2% relative to CFD. On the other hand, the agreement seems to deteriorate at higher speeds. In particular, the numerical predictions appear to decrease with speed, which may be surprising. However, this can be explained by the presence of a recirculation region near the leading edge (Fig. 5.24). In this region, the velocity is relatively low, leading to lower shear rate (and consequently shear stress) at the wall. As expected, we found that the recirculation region is larger for Mud_10, which is the least viscous mud.

For the case of a ship moving through mud, Eq. (5.21) shows that (for laminar mud flow) the increase in frictional resistance due to the yield stress is well approximated by $\tau_B S_{mud}$, where $S_{mud}$ is the surface area of the hull in contact with mud.

### 5.5.2. PRESSURE RESISTANCE

The pressure component, $R_P$, originates from the pressure difference acting on the front and rear faces of the plate. For Newtonian fluids it may be reasonable to simply use the stagnation pressure applied over the front surface. However, the yield stress influences the pressure significantly, thus this is a too crude approximation.

A possible alternative would be to use the formula proposed by Nirmalkar et al. [124] for the pressure resistance coefficient, $C_{RP}$, based on CFD simulations of the Bingham laminar flow over a square cylinder:

$$C_{RP} \equiv \frac{R_P}{1/2\rho V^2 S_f} = \frac{27}{Re_*}, \tag{5.22}$$

where $S_f = tT$ is the projected frontal area of the cylinder, $Re_* = Re/(1+Bn*)$ is the modified Reynolds number and $Bn^* = \tau_B L/(\mu_B V)$ is the canonical Bingham number. The conditions of the present work, however, differ from those in Nirmalkar

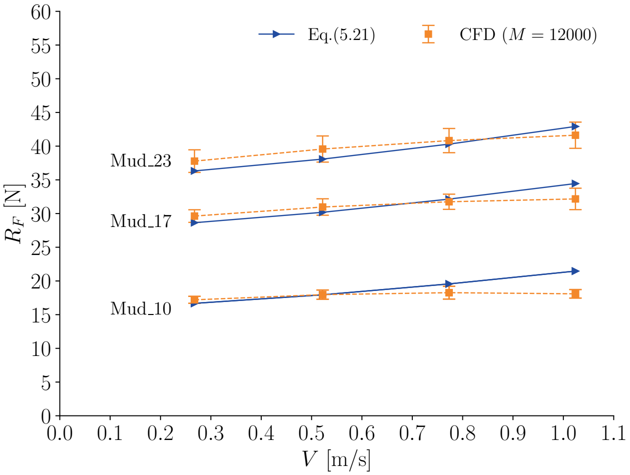

Figure 5.23: Comparison of the frictional resistance obtained with Eq. (5.21) and CFD using large regularisation parameters ($M = 12000$).

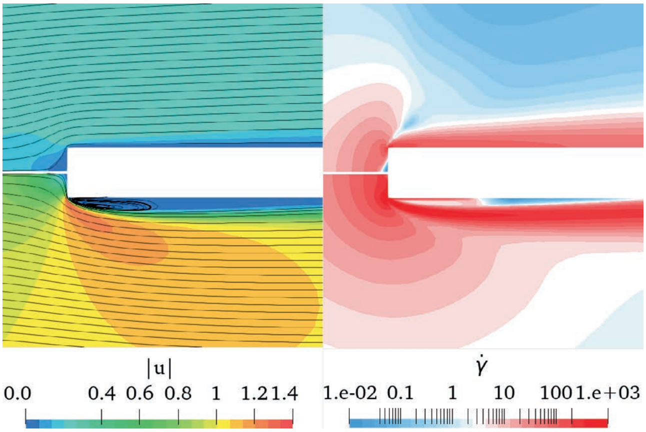

Figure 5.24: Contour diagram of velocity (left) and shear rate (right) near the leading edge for Mud_10 ($M = 12000$). Lowest speed (top); highest speed (bottom). Shear rate is in logarithmic scale.

et al. [124]. First, Eq. (5.22) was derived for $0.1 < Re < 40$, whereas for our test cases $7500 < Re < 56000$. Second, the plate has an aspect ratio of about 66.7 instead of 1. In order to account for these different conditions, Eq. (5.22) was modified by changing its numerator and by replacing $Re_*$ with $Re_*^a$, where $a$ is a fitting parameter. However, the new formula still showed substantial discrepancies at high $Re_*$. Eventually, a good fit was instead obtained using the following cubic relation in logarithmic scale:

$$\begin{aligned} \log_{10}(C_{RP}) = &\log_{10}(k_1) + k_2 \log_{10} Re_* + k_3 (\log_{10} Re_*)^2 \\ &+ k_4 (\log_{10} Re_*)^3 , \end{aligned} \tag{5.23}$$

where $k_1 = 41.58$, $k_2 = -1.132$, $k_3 = 0.1148$ and $k_4 = 0.0313$ are the fitting parameters obtained by least-square fitting of Eq. (5.23) to the present CFD data ($M = 12000$) for $C_{RP}$. Equation (5.23) corresponds, in linear scale, to

$$C_{RP} = k_1 Re_*^{k_2 + k_3 \log_{10} Re_* + k_4 (\log_{10} Re_*)^2} . \tag{5.24}$$

5

Figure 5.25 confirms that Eq. (5.24) is an excellent fit of the CFD data, with a maximum difference of 0.42%. Furthermore, while Eq. (5.22) may still be acceptably accurate for low $Re_*$ (low speed, high mud concentration), it is not adequate at higher $Re_*$, where even the simple stagnation pressure applied to the front face of the plate ($C_{RP} = 1$) appears to be closer to CFD data.

### 5.5.3. TOTAL RESISTANCE

The total resistance obtained combining Eqs. (5.21) and (5.24) agrees well with CFD data (see Fig. 5.26), with larger discrepancies at higher speeds stemming from the frictional component. In conclusion, the analytical formulas provide reasonably good estimates of $R_T$, with average and maximum difference of 3.6% and 12.4%, respectively, relative to CFD. Since the trend of the CFD data is reasonably well captured, Eqs. (5.21) and (5.24) have been used to determine the sensitivity coefficients for the input parameter uncertainties (see Section 5.3.5).

## 5.6. CONCLUSIONS, LIMITATIONS AND FINAL REMARKS

### 5.6.1. CONCLUSIONS

We have investigated the accuracy of the Bingham model for CFD applications concerned with marine vessels sailing through fluid mud. As a simplified case, the laminar flow over a plate was considered in order to primarily investigate the influence of the mud properties on the frictional part of the resistance.

The comparison with experimental data showed that the ideal Bingham model ($M = 12000$) well captures the relative increase in the resistance due to the increase

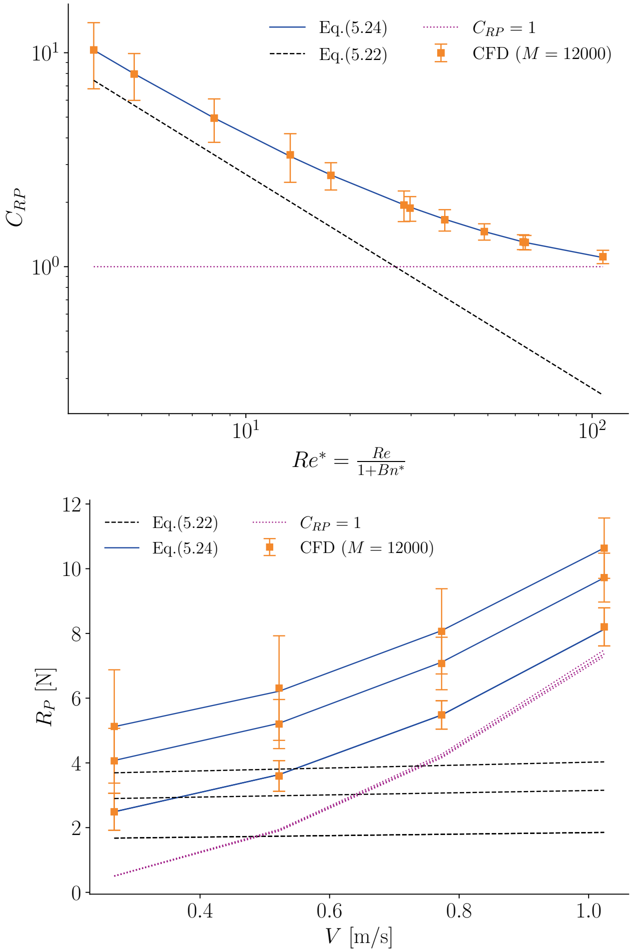

Figure 5.25: Pressure resistance coefficients versus the modified Reynolds number (top) and pressure resistance versus speed (bottom).

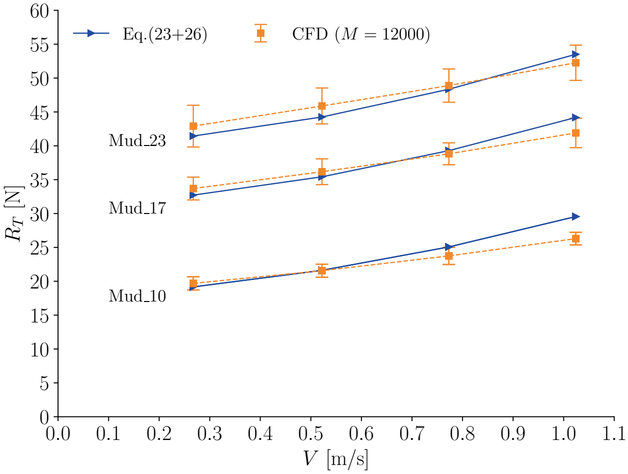

Figure 5.26: Comparison of the total resistance predicted by analytical formulas and CFD data.

in the mud concentration. On the other hand, at low speed (i.e. low shear), the ideal Bingham model tends to overpredict the resistance. Better predictions at low speed were achieved by using lower regularisation parameters ($500 < M < 800$), determined from the first points in the mud flow curves.

It was observed that the Tscheuschner model, which is a virtually perfect fit of the ramp-down flow curves of mud, produced strong underpredictions of the resistance, especially at low speed. The reasons might be the thixotropy of mud and possible inaccuracies of the rheological protocol at low shear rates. The main message is that improving the fit of the ramp-down curve does not necessarily lead to better numerical predictions of the plate resistance. Possible causes for this may be sought in the adopted rheometry techniques or in the constitutive equations. In this regard, it is possible that including thixotropy would improve the numerical predictions.

In addition, it was observed that the computed forces can be fairly well approximated by analytical formulas, especially the friction component. This allowed to quantify the influence on the resistance of each input parameter.

We found indications that experimental data at high speed have been affected by unwanted non-zero angles of attack of the plate. When an angle of attack of 3 degrees was included in the CFD calculations, the trend of the experimental data was very well captured. Therefore, the experimental results need to be interpreted with due caution. Further work is recommended to provide new experimental data with higher rigidity and a better alignment of the plate. Nonetheless, the following observations were made:

- The ideal Bingham model ($M = 12000$) tends to overpredict the experimental data, with an average and maximum comparison error of 13 and 19%, respectively. Nevertheless, the model appears suitable, at least, to investigate how the resistance changes in response to changes in the mud properties.

- Using lower regularisation parameters ($500 < M < 800$) produce better predictions, with comparison errors that are within or close to the validation uncertainties.

### 5.6.2. LIMITATIONS

The generalisation of these results is subject to a number of limitations related to the mud. First, towing tank experiments were conducted on dilutions of the natural mud collected in the harbour area. However, diluted and natural mud can exhibit different rheological characteristics (Shakeel et al. [148]). Second, this study was limited to three mud conditions, thus our findings cannot be extrapolated to all types of mud. Future studies with other mud conditions would be interesting.

### 5.6.3. FINAL REMARKS

In this work we have investigated the performance of the Bingham model for predicting the frictional resistance. However, as mentioned in Chapter 1, ships can experience a strong increase in the wave-making resistance associated with the mud-water undulation that can occur even without contact between the hull and mud. Future investigations might focus on this type of scenarios, keeping in mind that in such cases the maximum shear rate will be rather small (at least smaller than for object moving through mud), hence the Herschel–Bulkley model may be more suitable than Bingham.

Furthermore, the best predictions were achieved using a regularisation parameter such that the simulated mud exhibits the same apparent viscosity of the real mud in the first point of the ramp-up flow curve. Note however that the Bingham yield stress and viscosity were determined from the ramp-down curve, so the simulated mud contained information of both the ramp-up and ramp-down flow curves. While this is somewhat inconsistent, it could also be a crude way to mimic thixotropy using a non-thixotropic model. In fact, the regularisation parameter determines the flow behaviour at low shear rate, while the Bingham yield stress and viscosity determine the flow behaviour at higher shear rates. Thus, with the adopted choice of parameters, the low deformation regions (e.g. near the stagnation points or far from the plate) will follow more the ramp-up curve. On the surface of the plate, where the particle bonds are broken by the high shear rate, the fluid elements will obey to the ramp-down curve. Indications that experimental data may have been affected by deflections of the plate prevent, however, from drawing definitive conclusions.

Lastly, as the flow was assumed to be laminar, it can be argued that this study is only relevant for CFD simulations of ships moving very slowly through mud (e.g. while docking). However, as will be discussed in Section 6.8, CFD simulations of a ship sailing through Mud_23 predicted a laminar boundary layer in the mud region. The work carried out in this chapter appears thus to be relevant also for practical CFD applications.

# 6

# TURBULENCE MODELLING OF WALL-BOUNDED HERSCHEL–BULKLEY FLOWS

*...in which three eddy-viscosity models for Newtonian fluids, namely the* $k$*-*$\omega$ *SST,* $k$*-*$\sqrt{k}L$ *and Spalart-Allmaras model, have been tested on turbulent pipe flows of Herschel–Bulkley fluids. Additionally, a new turbulence closure based on the* $k$*-*$\omega$ *SST model for predicting turbulent wall-bounded flows of Herschel–Bulkley fluids is developed. The model has been calibrated with direct numerical simulations (DNS) data for fully-developed pipe flow of shear-thinning and viscoplastic fluids. The new model shows good agreement in the mean velocity, average viscosity, mean shear stress budget and friction factor. The latter compares well also against correlations from the literature for a wide range of Reynolds numbers. The main conclusions are that (i) the new model produces the best prediction; (ii) the standard SST model may be considered for simulations of weakly shear-thinning/viscoplastic fluids at high Reynolds numbers; (iii) the* $k$*-*$\sqrt{k}L$ *and the Spalart-Allmaras models appear to be unsuitable for turbulent Herschel-Bulkley flows. Finally, for a realistic example of a ship sailing through mud, it was observed that all the considered RANS models tend to predict laminar flow in the mud layer.*

---

The work in this chapter is based on the published article “Lovato, S., Keetels, G. H., Toxopeus, S. L., and Settels, J. W. (2022). An eddy-viscosity model for turbulent flows of Herschel–Bulkley fluids. *Journal of Non-Newtonian Fluid Mechanics*, 301, 104729" [98].

## 6.1. INTRODUCTION

When a ship sails through mud (Fig. 6.1), the boundary layer developing in the water part is certainly turbulent. In the mud layer, on the other hand, the situation is more uncertain[1]. In Chapter 5, the validation was carried out in laminar regime, but there are not yet theories that can reliably predict, for realistic scenarios, whether the mud flow along the hull is laminar, transitional or turbulent. Available formulas to determine the flow regime of mud are mainly for open channel (Liu and Mei [97]) and pipe flows (Wilson and Thomas [180]), and their applicability may strongly dependent upon the mud composition.

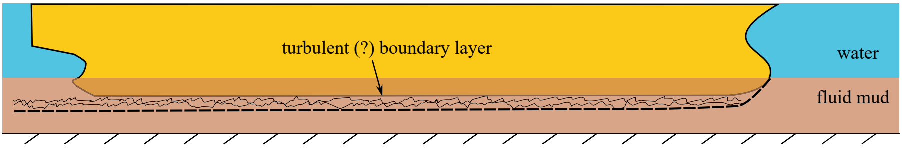

Figure 6.1: Illustration of a ship sailing through fluid mud.

If, with a certain stretch of imagination, the mud layer illustrated in Fig. 6.1 is thought of as an upside-down channel, where the ship bottom corresponds to the sheared channel bottom, then the criterion in Liu and Mei [97] states that the mud flow is turbulent if

$$Re^e > 2000-3000\,. \tag{6.1}$$

$Re^e$ is the effective Reynolds number, which is defined as

$$\frac{1}{Re^e} = \frac{1}{Re^\mu} + \frac{1}{Re^\tau} \equiv \frac{\mu}{4\rho U h} + \frac{\tau_0}{8\rho U^2}\,, \tag{6.2}$$

with $h$ being the thickness of the mud layer and $U$ the average velocity over the channel depth; $\mu$, $\tau_0$ and $\rho$ are the mud plastic viscosity, yield stress and density, respectively. Imagining a ship slowing sailing at 3 m/s ($\approx$ 6 knots) through a fluid layer having the same properties as Mud_23[2] (see Section 5.2.3) and with a thickness of 5 m, $Re^e$ is about 3750, which means that the fluid mud layer will be turbulent according to Eq. (6.1).

However, rather than the wall of a channel the ship's bottom could be more accurately represented by a flat plate. For Newtonian fluids, the boundary layer

---

[1] As mentioned in Section 2.1, the turbulent mixing occurring at the water-mud interface is neglected, thus the turbulent effects considered in this chapter are only those associated to the boundary layer along the hull.

[2] In this case we assume that the rheological properties of Mud_23 are the same also in an hypothetical turbulent regime, although this may not be true [154].

developing at the plate wall is considered turbulent when the (canonical) Reynolds number, $Re = \rho UL/\mu$, exceeds $\sim 5 \cdot 10^5$. For the water part, the Reynolds number of a cargo ship that is 320 metres long and that moves very slowly, say at 2 knots, is already greater than $10^8$, thus the water boundary layers is unquestionably turbulent. There is however not such criterion for a yield-stress fluid.

Nonetheless, let now consider the flow of a fluid having the rheological properties as Mud_23 but with zero yield stress. The corresponding Reynolds number for the same ship and speed would be about $1 \cdot 10^7$. This means that the boundary layer of a "zero-yield-stress version" of Mud_23 would be turbulent. On the other hand, it is not known whether the effect of the yield stress would be sufficiently strong to completely damp the turbulent fluctuations, thus the flow regime of the actual Mud_23 remains uncertain. The only situation in which the flow regime of mud can be determined with a higher degree of confidence is when the Reynolds number of the "zero-yield-stress mud" is below $\sim 5 \cdot 10^5$. In that case, adding the effect of the yield stress would make the mud more viscous, thus further decreasing the Reynolds number.[3]

In spite of the above considerations, in the rest of the chapter it is hypothesised that the boundary layer in the fluid mud part is turbulent since laminar flows were already discussed in Chapters 4 and 5.

### 6.1.1. RESEARCH QUESTIONS AND AIM OF THE CHAPTER

The prohibitive costs of direct numerical simulations (DNS) for predicting turbulent flows makes turbulence modelling the only feasible alternative for most engineering applications as it offers an acceptable compromise between cost and accuracy. The most widespread modelling technique is the so-called Reynolds-averaging, which makes use of the Reynolds-Average Navier-Stokes (RANS) equations. These models are therefore usually referred to as RANS models.

For Newtonian fluids, several RANS models are typically available in general-purpose CFD codes. On the other hand, RANS models for Herschel–Bulkley fluids have not yet received enough recognition in the CFD community, thus CFD practitioners often apply Newtonian RANS models to non-Newtonian fluids, and this continued to happen until very recently (e.g., Gao et al. [62], Kaidi et al. [78], Kelly et al. [80], Busch and Johansen [26], and Mehta et al. [111]). This raises the following questions:

1) Are the standard RANS models for Newtonian fluids suitable also for Herschel–Bulkley fluids?

2) Do dedicated RANS models for Herschel–Bulkley fluids exist in the literature?

---

[3] This was in fact the case for the plate discussed in Chapter 5, where the flow was assumed to be laminar.

3) If not, how can we modify existing Newtonian RANS models to account for non-Newtonian effects?

The two main difficulties concerning the Reynolds-averaged modelling for non-Newtonian fluids are the shear-dependent viscosity and the appearance of extra correlations in the governing equations as a result of the fluctuating viscosity. These correlations are unknown a priori and therefore require a closure.

Significant progress has been made for viscoelastic fluids in the past twenty years Pinho [133], Cruz and Pinho [35], Cruz et al. [36], Pinho et al. [134, 134], Resende et al. [137, 136], Iaccarino et al. [74], and Masoudian et al. [106]. However, fewer studies have dealt with inelastic fluids such as power-law, Bingham and Herschel–Bulkley.

Firsts efforts date back to 1997, when Malin [105, 104] modified the damping function in the eddy viscosity of the $k$-$\epsilon$ model of Lam and Bremhorst [90]. The modification accounted for the shear-thinning rheology and results showed fairly good agreement against experimental data on the friction factor and mean velocity profile of pipe flows. However, apart from the modified damping function, results were obtained with a Newtonian RANS model, hence no turbulence closure was used for the non-Newtonian correlations. A similar approach was adopted by Bartosik [12, 11], who modified the damping function of the $k$-$\epsilon$ model accounting for the yield stress of Bingham and Herschel–Bulkley fluids. Recently, a significant step forward has been made by Gavrilov and Rudyak [64], who proposed a turbulence closure for power-law fluids, using the $k$-$\epsilon$-$v2$-$f$ model of Durbin [44].

This chapter aims at developing a RANS model for Herschel–Bulkley fluids that introduces the minimum amount of complexities while capturing the relevant physics of interest for engineering applications concerned with wall-bounded flows. In this chapter the turbulent closure of Gavrilov and Rudyak [64] for power-law fluids is extended to Herschel–Bulkley fluids and is presented in a general form that can be easily extended to any generalised Newtonian (GN) fluid model. However, instead of using the $k$-$\epsilon$-$v2$-$f$ model, the new model is developed starting from the popular $k$-$\omega$ SST model of Menter et al. [113]. The latter was developed for Newtonian fluids and it was proved to be a robust and accurate model for a large number of applications, including wall-bounded flows with adverse pressure gradient, which makes it suitable for turbulent flows of Newtonian fluids around bluff bodies. Being a blending of the $k$-$\epsilon$ (Launder et al. [92]) and $k$-$\omega$ (Wilcox [178]) models, the SST model inherits their best features, i.e. the insensitivity to free-stream parameters of the $k$-$\epsilon$ and the accuracy in the near-wall region of the $k$-$\omega$ without using damping functions.

The results obtained with the new model are compared against recent DNS of Singh et al. [153, 152, 151] for fully-developed pipe flow and against correlations for the friction factor, covering a wide range of rheological parameters and Reynolds numbers.

In addition, in order to answer question 1), this chapter assesses the accuracy of three Newtonian RANS models when they are applied to turbulent flows of Herschel–Bulkley fluids. The selected RANS models are: the $k$-$\omega$ SST (Menter et al. [113]), the $k$-$\sqrt{k}L$ (Menter et al. [115]) and the Spalart-Allmaras [157] models. These models are very popular for CFD simulations of turbulent flows in the maritime and aeronautical sectors.

## 6.2. GOVERNING EQUATIONS

The incompressible flow is governed by the following continuity and momentum equations (the hat symbol denotes instantaneous quantities):

$$\nabla \cdot \hat{\boldsymbol{u}} = 0\,, \tag{6.3}$$

$$\frac{\partial(\rho\hat{\boldsymbol{u}})}{\partial t} + \nabla\cdot(\rho\hat{\boldsymbol{u}}\,\hat{\boldsymbol{u}}) = \nabla\cdot\hat{\boldsymbol{\tau}} - \nabla\hat{p}\,, \tag{6.4}$$

where $\hat{\boldsymbol{u}}(\boldsymbol{x},t)$ is the velocity vector, $\boldsymbol{x}$ is the position vector, $t$ is time, $\hat{p}$ is pressure, $\rho$ is density, $\hat{\boldsymbol{\tau}}$ is the deviatoric stress tensor that, for GN fluids, reads

$$\hat{\boldsymbol{\tau}} \equiv \hat{\tau}_{ij} = 2\hat{\mu}\hat{\boldsymbol{S}}\,, \qquad \hat{\boldsymbol{S}} \equiv \hat{S}_{ij} = \frac{1}{2}\left(\frac{\partial\hat{u}_i}{\partial x_j} + \frac{\partial\hat{u}_j}{\partial x_i}\right), \tag{6.5}$$

where $\hat{S}_{ij}$ is the deformation rate tensor and $\hat{\mu}$ is the instantaneous apparent viscosity which, for Herschel–Bulkley fluids with the Papanastasiou regularisation, reads

$$\hat{\mu} = \frac{\tau_0(1-e^{-m\dot{\hat{\gamma}}}) + K\,\dot{\hat{\gamma}}^n}{\dot{\hat{\gamma}}}\,, \tag{6.6}$$

where $m$ is the already mentioned regularisation parameter.

### 6.2.1. REYNOLDS-AVERAGED EQUATIONS

Following the procedure originally proposed by Osborne Reynolds (1895), a generic instantaneous flow quantity $\hat{\phi}$ can be expressed as the sum of a mean and a fluctuating part (Reynolds decomposition),

$$\hat{\phi}(\boldsymbol{x},t) = \phi(\boldsymbol{x},t) + \phi'(\boldsymbol{x},t)\,. \tag{6.7}$$

The mean value, $\phi(\boldsymbol{x},t)$, is here obtained from ensemble-averaging[4], hence

$$\phi(\boldsymbol{x},t) \equiv \overline{\hat{\phi}}(\boldsymbol{x},t) \equiv \frac{1}{N}\lim_{N\to\infty}\sum_{n=1}^{N}\hat{\phi}_n(\boldsymbol{x},t)\,, \tag{6.8}$$

---

[4] Contrary to $\phi'(\boldsymbol{x},t)$, the time dependency of $\phi(\boldsymbol{x},t)$ is relative to the nonturbulent unsteadiness of the flow.

with $N$ being the number of repeated observations of $\hat{\phi}_n(\boldsymbol{x}, t)$. This operation is known as Reynolds-averaging and it will be indicated with the overbar.

By applying the Reynolds-averaging to Eq. (6.3) and Eq. (6.4), the Reynolds-averaged continuity and momentum equations for GN fluids are obtained:

$$\nabla \cdot \boldsymbol{u} = 0\,, \tag{6.9}$$

$$\rho \frac{\partial \boldsymbol{u}}{\partial t} + \rho \nabla \cdot (\boldsymbol{u}\,\boldsymbol{u}) = \nabla \cdot \boldsymbol{\tau} - \nabla p - \rho \nabla \cdot (\overline{\boldsymbol{u}'\,\boldsymbol{u}'}) + \nabla \cdot \boldsymbol{\tau}^{nn}\,, \tag{6.10}$$

where $-\rho\overline{\boldsymbol{u}'\,\boldsymbol{u}'}$ is the (unknown) Reynolds stress tensor and $\boldsymbol{\tau} \equiv \tau_{ij} = 2\mu S_{ij}$ is the mean deviatoric stress tensor. As a result of the fluctuating viscosity for non-Newtonian fluids, an additional term appears on the right-hand side of Eq. (6.10),

$$\boldsymbol{\tau}^{nn} \equiv \tau_{ij}^{nn} = 2\overline{\mu' S'_{ij}}\,. \tag{6.11}$$

This term, hereafter referred to as non-Newtonian stress tensor, is *a priori* unknown and it requires turbulent closure.

### 6.2.2. TURBULENCE MODELLING

The turbulence model proposed in this article is based on the two-equation $k$-$\omega$ SST model of Menter et al. [113], which approximates the Reynolds stress tensor using the Boussinesq hypothesis,

$$-\rho\overline{u'_i u'_j} = \mu_t S_{ij} - \frac{2}{3}\rho\delta_{ij}k \tag{6.12}$$

where $\delta_{ij}$ is the Kronecker symbol, $k = \frac{1}{2}\overline{u'_i u'_i}$ is the turbulent kinetic energy (TKE) and $\mu_t$ is the so-called eddy (or turbulent) viscosity. The eddy viscosity is a function of $k$ and $\omega$, the latter being the specific dissipation rate of TKE. The variation of $k$ and $\omega$ in the flow is modelled by two respective transport equations.

The transport equation for $k$ can be derived from the transport equations of the Reynolds stress by summation over the diagonal components (see e.g. Gori and Boghi [66] for the complete derivation), and it has the following expression:

$$\frac{D(\rho k)}{Dt} = P + \Pi + T + \mathscr{D} - \rho\epsilon + \xi^{nn} + \chi^{nn} + \mathscr{D}^{nn}\,. \tag{6.13}$$

The first four terms on the right-hand side are:

- production: $P = -\rho\overline{u'_i u'_j}S_{ij}$

- pressure diffusion: $\Pi = -\dfrac{\partial \overline{p' u'_j}}{\partial x_j}$
- turbulent transport: $T = -\dfrac{\partial \overline{\rho u'_i u'_i u'_j}}{\partial x_j}$
- mean viscous transport: $\mathscr{D} = \dfrac{\partial}{\partial x_j}\left(\mu \dfrac{\partial k}{\partial x_j} + \mu \dfrac{\partial \overline{u'_i u'_j}}{\partial x_i}\right)$
- viscous dissipation: $\rho\epsilon = 2\mu\overline{S'_{ij}S'_{ij}} + 2\overline{\mu' S'_{ij}S'_{ij}}$

The above terms are the same that are found in the equation for Newtonian fluids except for $\epsilon$, that now contains the non-Newtonian contribution due to the fluctuating viscosity. The last three terms in Eq. (6.13) are non-Newtonian contributions and, adopting the terminology of Singh et al. [153], they read:

- mean shear turbulent viscous dissipation:
  $\chi^{nn} = -2\overline{\mu' S'_{ij}}S_{ij}$
- mean shear turbulent viscous transport:
  $\xi^{nn} = \dfrac{\partial (2\overline{\mu' u'_i}S_{ij})}{\partial x_j}$
- turbulent viscous transport:
  $\mathscr{D}^{nn} = \dfrac{\partial}{\partial x_j}\left(\dfrac{1}{2}\overline{\mu' \dfrac{\partial u'_i u'_i}{\partial x_j}} + \overline{\mu' \dfrac{\partial u'_i u'_j}{\partial x_i}}\right)$

Note that all the non-Newtonian contributions contain the fluctuating viscosity $\mu'$, therefore they all vanish when the fluid is Newtonian.

The first five terms of Eq. (6.13) are modelled as in the standard $k-\omega$ SST model (which is reported in Appendix B.1), hence:

$$\frac{D(\rho k)}{Dt} = \overbrace{\tilde{P}_k}^{P} + \overbrace{\nabla\cdot\left[(\mu+\sigma_k\mu_t)\nabla k\right]}^{\mathscr{D}+\Pi+T} - \rho\overbrace{\beta^* k\omega}^{\epsilon} + \xi^{nn} + \chi^{nn} + \mathscr{D}^{nn}. \tag{6.14}$$

$$\tilde{P}_k = \min(\mu_t S^2, 10\beta^* \rho k\omega)$$

where $S^2 = 2S_{ij}S_{ij}$. Eq. (6.14) is thus equal to the equation of the $k-\omega$ SST model except for the shear-dependent viscosity $\mu$ and the non-Newtonian contributions on the right-hand side that need to be modelled.

The exact transport equation of $\omega$ for GN fluids is lengthy and it can be derived from the exact transport equation of $\epsilon$ in Gori and Boghi [66]. Following the approach of Gavrilov and Rudyak [64], in the present work we consider the same empirical equation of the $k-\omega$ SST model, except for an additional (not yet specified) non-Newtonian contribution ($E^{nn}$):

$$\begin{aligned}\frac{D(\rho\omega)}{Dt} = \frac{\rho\alpha}{\mu_t}\tilde{P}_k + \nabla\cdot\left[(\mu+\sigma_\omega\mu_t)\nabla\omega\right] - \beta\rho\omega^2 \\ + 2\rho(1-F_1)\frac{\sigma_{\omega 2}}{\omega}\nabla k\cdot\nabla\omega + E^{nn}\,.\end{aligned} \tag{6.15}$$

In order to solve Eqs. (6.10), (6.14) and (6.15), the unknown non-Newtonian contributions $\tau_{ij}^{nn}$, $\xi^{nn}$, $\chi^{nn}$, $\mathscr{D}^{nn}$, $\epsilon^{nn}$ and $E^{nn}$ require turbulent closure. This is the topic of the next section.

## 6.3. TURBULENCE CLOSURE FOR THE NON-NEWTONIAN TERMS

The closure is derived along the lines of Gavrilov and Rudyak [64]. The main difference is that in this work the closure is derived for the $k$-$\omega$ SST model and in a general form that can be easily extended to any GN model.

### 6.3.1. AVERAGE VISCOSITY MODEL

The average viscosity model proposed in Gavrilov and Rudyak [64] assumes that the average viscosity is a function of the mean shear rate, i.e

$$\overline{\hat{\mu}(\dot{\hat{\gamma}})} \simeq \mu(\overline{\dot{\hat{\gamma}}}) \equiv \mu(\dot{\gamma})\,. \tag{6.16}$$

In turn, the mean shear rate (squared) reads:

$$\dot{\gamma}^2 = 2\overline{\hat{S}_{ij}\hat{S}_{ij}} = 2S_{ij}S_{ij} + 2\overline{S'_{ij}S'_{ij}}\,, \tag{6.17}$$

where the second term on the right-hand side can be estimated from the total viscous dissipation rate of turbulent kinetic energy

$$\rho\epsilon = 2\mu\overline{S'_{ij}S'_{ij}} + 2\overline{\mu' S'_{ij}S'_{ij}}\,. \tag{6.18}$$

Gavrilov and Rudyak [64] assumed that since $\mu'$ can be either positive or negative whereas $S'_{ij}S'_{ij}$ is always positive, the second term in Eq. (6.18) will be small on average and therefore it can be neglected. DNS data of Singh et al. [153] confirm that such assumption is fairly acceptable when $n < 1$. On the other hand, for Bingham fluids ($n = 1$) this assumption seems incorrect. Nevertheless, for lack of knowledge of how to model such term we retain the assumption to be valid also for Bingham fluids. The main message is that larger modelling errors in the average viscosity should be expected for Bingham fluids.

In light on the above consideration, the second term of Eq. (6.17) can be approximated using Eq. (6.18),

$$2\overline{S'_{ij}S'_{ij}} \simeq \frac{\rho\epsilon}{\mu} = \frac{\rho\beta^*\omega k}{\mu}, \tag{6.19}$$

and substituting in Eq. (6.17) gives

$$\dot{\gamma}^2 = 2S_{ij}S_{ij} + \frac{\rho\beta^*\omega k}{\mu}. \tag{6.20}$$

Note that, in Eq. (6.16), $\mu$ is a function of $\dot{\gamma}$, which in turn is now a function of $\mu$ because of Eq. (6.20). In mathematical terms, $\mu = f(\mu)$, where $f(\mu)$ is the function obtained combining Eqs. (6.16) and (6.20). Since the governing equations are solved using iterative solution methods, the mean viscosity can be simply computed at each new outer iteration using $\mu$ from the previous iteration. However, to avoid possible numerical instabilities in the iterative solver due to the highly non-linear nature of $\mu = f(\mu)$, it is advised to perform a few intermediate iterations (e.g., using a simple fixed-point algorithm) before proceeding to the next outer iteration.

### 6.3.2. CLOSURE FOR THE NON-NEWTONIAN STRESS TENSOR

DNS for shear-thinning fluids of Singh et al. [152, 151] showed that $\mu'/\mu$ does not exceed 30%. Thus, assuming small viscosity fluctuations, it is reasonable to relate $\mu'$ to the fluctuations of the deformation rate tensor as

$$\mu' \approx \frac{\partial\mu}{\partial S_{ij}}S'_{ij} = \frac{\partial\mu}{\partial\dot{\gamma}}\frac{\partial\dot{\gamma}}{\partial S_{ij}}S'_{ij} = \frac{\partial\mu}{\partial\dot{\gamma}}\frac{2S_{ij}}{\dot{\gamma}}S'_{ij}, \tag{6.21}$$

whence,

$$\tau^{nn}_{ij} = 2\overline{\mu' S'_{ij}} = 2\frac{\partial\mu}{\partial\dot{\gamma}}\frac{S_{ij}}{\dot{\gamma}}2\overline{S'_{ij}S'_{ij}}, \tag{6.22}$$

and by virtue of Eq. (6.19),

$$\tau^{nn}_{ij} = 2\frac{\partial\mu}{\partial\dot{\gamma}}\frac{S_{ij}}{\dot{\gamma}}\frac{\rho\beta^*\omega k}{\mu}. \tag{6.23}$$

The expression above can be rearranged in a more convenient form:

$$\tau^{nn}_{ij} = 2\mu^{nn}S_{ij}, \quad \mu^{nn} = \frac{\partial\mu}{\partial\dot{\gamma}}\frac{\rho\beta^*\omega k}{\mu\dot{\gamma}}, \tag{6.24}$$

where $\mu^{nn}$ can thus be interpreted as a turbulent non-Newtonian viscosity. For shear-thinning fluids $\mu^{nn}$ is always negative, thus it acts to reduce the turbulent transport of momentum.

## 6.3.3. CLOSURE FOR THE TURBULENCE TRANSPORT EQUATIONS

The remaining terms that need to be modelled are $\chi^{nn}$, $\mathscr{D}^{nn}$, $\xi^{nn}$ and $E^{nn}$.

The first term is easily modelled by virtue of Eq. (6.21) as

$$\chi^{nn} = -2\overline{\mu' S'_{ij}} S_{ij} = -\mu^{nn} S^2 . \tag{6.25}$$

For shear-thinning fluids this term is always positive and therefore it acts as a production term (see also Appendix B.4), even though it originates from the viscous term.

The second term, $\mathscr{D}^{nn}$, can be neglected since it is identical to the mean viscous transport term $\mathscr{D}$ but with the fluctuating viscosity instead of the mean viscosity. The smallness of this term is also confirmed by DNS of Singh et al. [153, 152].

Following the approach in Gavrilov and Rudyak [64], $\xi^{nn}$ is modelled assuming that in the boundary layer the following approximations hold: $|\boldsymbol{u}| \approx u_1$, $S_{ij} \approx S_{12}$ and $k \approx \overline{u_1'^2}/2$, where 1 and 2 indicate the stream and cross-stream directions, respectively. Hence,

$$\begin{aligned}
\xi^{nn} &= \frac{\partial(2\overline{\mu' u'_i} S_{ij})}{\partial x_j} \approx \frac{\partial}{\partial x_j}\left(2\frac{\partial \mu}{\partial \dot\gamma}\frac{2S_{kl}}{\dot\gamma}\overline{S'_{kl} u'_i} S_{ij}\right) \\
&\approx \frac{\partial}{\partial x_2}\left(2\frac{\partial \mu}{\partial \dot\gamma}\frac{2S_{12}^2}{\dot\gamma}\overline{S'_{12} u'_1}\right) = \frac{\partial}{\partial x_2}\left[\frac{\partial \mu}{\partial \dot\gamma}\frac{2S_{12}^2}{\dot\gamma}\overline{\left(u'_1 \frac{\partial u'_1}{\partial x_2} + u'_1 \frac{\partial u'_2}{\partial x_1}\right)}\right] \\
&\approx \frac{\partial}{\partial x_2}\left(\frac{\partial \mu}{\partial \dot\gamma}\frac{2S_{12}^2}{\dot\gamma}\frac{\overline{\partial u'_1 u'_1/2}}{\partial x_2}\right) \approx \frac{\partial}{\partial x_2}\left(\frac{\partial \mu}{\partial \dot\gamma}\frac{2S_{12}^2}{\dot\gamma}\frac{\partial k}{\partial x_2}\right),
\end{aligned} \tag{6.26}$$

and in its general form:

$$\xi^{nn} = \nabla \cdot \left(\frac{\partial \mu}{\partial \dot\gamma}\frac{S^2}{\dot\gamma}\nabla k\right). \tag{6.27}$$

For shear-thinning fluids, the quantity that multiplies $\nabla k$ is negative, thus acting as a reduction of the turbulent diffusion of $k$.

Finally, the last term that needs to be modelled is the non-Newtonian contribution to the transport equation of $\omega$, $E^{nn}$. Since the $\omega$-equation is empirical, this term is simply treated in analogy with the production term of the $\omega$ equation for the SST model, i.e.

$$E^{nn} = \frac{\rho\alpha}{\mu_t}(\xi^{nn} + \chi^{nn}), \tag{6.28}$$

where $\alpha$ is a closure coefficient of the $k$-$\omega$ SST model (see Appendix B.1).

### 6.3.4. FINAL MATHEMATICAL MODEL

The complete mathematical model reads:

$$\nabla \cdot \boldsymbol{u} = 0\,, \tag{6.29}$$

$$\frac{\partial(\rho \boldsymbol{u})}{\partial t} + \nabla \cdot (\rho \boldsymbol{u}\,\boldsymbol{u}) = \nabla \cdot \Big[2(\mu + \mu_t + C_\tau \mu^{nn})\boldsymbol{S}\Big] - \nabla(p + \frac{2}{3}k)\,, \tag{6.30}$$

$$\frac{D(\rho k)}{Dt} = \tilde{P}_k + D - \rho\epsilon + \xi^{nn} + \chi^{nn}\,, \tag{6.31}$$

$$\begin{aligned} \frac{D(\rho\omega)}{Dt} = {} & \frac{\rho\alpha}{\mu_t}\tilde{P}_k + \nabla \cdot \Big[(\mu + \sigma_\omega \mu_t)\nabla\omega\Big] - \beta\rho\omega^2 \\ & + 2\rho(1 - F_1)\frac{\sigma_{\omega 2}}{\omega}\nabla k \cdot \nabla\omega + E^{nn}\,. \end{aligned} \tag{6.32}$$

$$D \equiv \nabla \cdot \Big[(\mu + \sigma_k \mu_t)\nabla k\Big]\,, \tag{6.33}$$

$$\epsilon = \beta^* \omega k\,, \tag{6.34}$$

$$\dot{\gamma}^2 = 2S_{ij}S_{ij} + \frac{\rho C_\beta \epsilon}{\mu}\,, \tag{6.35}$$

$$\mu^{nn} = \frac{\partial\mu}{\partial\dot{\gamma}}\frac{\rho C_\beta \epsilon}{\mu\dot{\gamma}}\,, \tag{6.36}$$

$$\chi^{nn} = -C_\chi \mu^{nn} S^2\,, \tag{6.37}$$

$$\xi^{nn} = C_\xi \nabla \cdot \left(\frac{\partial\mu}{\partial\dot{\gamma}}\frac{S^2}{\dot{\gamma}}\nabla k\right)\,, \tag{6.38}$$

$$E^{nn} = C_E \frac{\rho\alpha}{\mu_t}(\xi^{nn} + \chi^{nn})\,. \tag{6.39}$$

The original SST model and its closure coefficients are reported in Appendix B.1, whereas the closure coefficients relative to the new model ($C_\beta$, $C_\tau$, $C_\chi$, $C_\xi$ and $C_E$) are given in Section 6.7.1.

The quantity $\partial\mu/\partial\dot{\gamma}$ depends on the rheological model at hand. For the Herschel–Bulkley model with the Papanastasiou regularisation it reads:

$$\frac{\partial\mu}{\partial\dot{\gamma}} = \frac{(n-1)K\dot{\gamma}^n - \tau_0(1 - e^{-m\dot{\gamma}}) + m\dot{\gamma}\tau_0 e^{-m\dot{\gamma}}}{\dot{\gamma}^2}\,. \tag{6.40}$$

Finally, for the boundary conditions on perfectly smooth walls, the same conditions of the standard SST model can be applied because all the non-Newtonian contributions ($\mu^{nn}$, $\chi^{nn}$, $\xi^{nn}$ and $E^{nn}$) are zero at the wall (for $\chi^{nn}$ and $\xi^{nn}$, see Appendix B.4).

## 6.4. PIPE FLOW SIMULATIONS: TEST CASES, COMPUTATIONAL DOMAIN AND BOUNDARY CONDITIONS

The new model, hereafter labelled as ‘SST-HB’, has been calibrated on DNS data of Singh et al. [153, 152, 151] for fully-developed flows in smooth pipes of power-law (PL), Bingham (Bn) and Herschel–Bulkley (HB) fluids. Furthermore, as anticipated in the introduction, the performance of three Newtonian eddy-viscosity models is investigated. The selected models are the $k-\omega$ SST [113], the $k$-$\sqrt{k}L$ [115] and the Spalart-Allmaras [157] models. These will be hereafter referred to as SST, KSKL and SA, respectively. Their formulation is reported in Appendices B.1 to B.3.

### 6.4.1. TEST CASES

The definition of the Reynolds number for Herschel–Bulkley fluids is difficult because the choice of the viscosity is not univocal. For pipe flows, a standard choice is to use the wall kinematic viscosity, that for Herschel–Bulkley fluids reads

$$\nu_w = \frac{\tau_w}{\rho}\left(\frac{K}{\tau_w - \tau_0}\right)^{1/n}, \tag{6.41}$$

where $\tau_w$ is the shear stress at the wall. For a pipe having diameter $D = 2R$, with the Cartesian axes at centre of the pipe and with the $z$-axis aligned with the flow, $\tau_w$ is related to the pressure gradient $\partial p/\partial z$ inside the pipe as

$$\tau_w = \frac{R}{2}\frac{\partial p}{\partial z}. \tag{6.42}$$

From the wall viscosity, the Reynolds number can be thus defined as

$$Re_w = \frac{U_b D}{\nu_w}, \tag{6.43}$$

where $U_b$ is the bulk velocity. The problem with this definition is that $Re_w$ cannot be determined *a priori* because either $U_b$ or $\nu_w$ is unknown before the simulation, depending on whether the pressure gradient or the flow rate is imposed. It is thus useful to introduce the friction Reynolds number,

$$Re_\tau = u_\tau R/\nu_w, \tag{6.44}$$

with $u_\tau = \sqrt{\tau_w/\rho}$ being the friction velocity. The latter is also used to define $u^+ = u/u_\tau$, $k^+ = k/u_\tau^2$ and the wall unit $y^+ = (R-r)u_\tau/\nu_w$, with $r = \sqrt{x^2+y^2}$.

The wall viscosity was chosen as $\nu_w = 1/Re_\tau$ and the non-dimensional pressure gradient $(\partial p/\partial z)R/\tau_w$ was set equal to 2. From these non-dimensional parameters the fluid properties for each test case (Table 6.1) can be uniquely determined.

Table 6.1: Summary of the considered test cases. Calculations were performed for each possible combination of rheology, Reynolds number and RANS model listed in the table.

| Case | $n$ | $\tau_0/\tau_w$(%) | $Re_\tau$ | $Re_w$(Nwt) | RANS model |
|---|---|---|---|---|---|
| Nwt | 1.0 | 0 | 323 | ~ 10000 | New model (SST-HB) |
| PL08 | 0.8 | 0 | 500 | ~ 17000 | $k-\omega$ SST-2003 (SST) |
| PL06 | 0.6 | 0 | 750 | ~ 27000 | Spalart-Allmaras (SA) |
| PL04 | 0.4 | 0 | 1000 | ~ 37000 | $k-\sqrt{k}L$ (KSKL) |
| Bn5 | 1.0 | 5 | 1250 | ~ 48000 | |
| Bn10 | 1.0 | 10 | 1500 | ~ 59000 | |
| Bn20 | 1.0 | 20 | 2000 | ~ 82000 | |
| Bn30 | 1.0 | 30 | 2500 | ~ 105000 | |
| HB10 | 0.8 | 10 | | | |

### 6.4.2. COMPUTATIONAL DOMAIN AND BOUNDARY CONDITIONS

The full pipe was discretised using four structured grids (Fig. 6.2) covering a refinement ratio of 2, with the finest grid made of about 86000 cells (232 and 212 cells in the radial and azimuthal direction, respectively). The grid resolution at the pipe wall was chosen such that $y^+ \lesssim 0.1$ for all the considered test cases to ensure low levels of numerical uncertainty (Eça et al. [49]), as shown in Section 6.6.

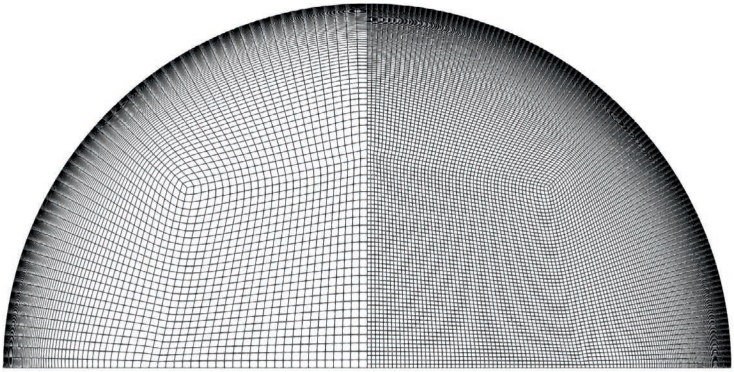

Figure 6.2: One quarter of the coarsest and finest grid.

Since the flow is fully developed, only one layer of cells was considered in the flow direction, and periodic boundary conditions were applied stream-wise. At the pipe wall ($x^2 + y^2 = R^2$), the impermeable/no-slip boundary conditions for the velocity ($\boldsymbol{u} = 0$) and the Neumann condition for pressure ($\partial p/\partial n = 0$) were applied. All the turbulence quantities except $\omega$ are set to zero at the wall. For $\omega$, the following value is imposed at the first cell-centre away from the wall,

$$\omega = \frac{6\mu}{\rho \beta_1 d^2}, \tag{6.45}$$

where $d$ is the distance from the wall and $\beta_1 = 3/40$. The value of $\omega$ at the wall surface is set to ten times the value given by Eq. (6.45), as in the original SST model of Menter [114].

## 6.5. CFD SETUP

The convective fluxes of all transport equations are linearised with the Picard method and discretised with the Harmonic scheme [93].

## 6.6. NUMERICAL UNCERTAINTIES

For a meaningful comparison with data from the literature, it is important to ensure that the numerical errors/uncertainties are sufficiently small.

For statistically steady flows, it is commonly accepted to divide numerical errors in three categories: discretisation, iterative and round-off errors. Round-off errors are due to the finite precision of computers and they can be safely neglected for the present work by using double precision. Iterative errors are due to the use of iterative methods to find the solution of the discretised equations. These can be neglected by reducing residuals to machine accuracy, although less strict criteria are usually sufficient for practical applications. For the present work, calculations were stopped when the $L_2$ norm of the normalised residuals was below $2 \times 10^{-10}$, which was observed to be sufficient to safely neglect the contribution of iterative errors. We have thus assumed that the numerical uncertainties are only due to discretisation errors.

The discretisation uncertainties in the friction factor $f = 2\tau_w/(\rho U_b^2)$ were estimated using the method of Eça and Hoekstra [46] and they are reported in Table 6.2 for the lowest and highest Reynolds numbers considered in this work. Among the three Newtonian eddy-viscosity models, the SST model has clearly the largest uncertainties, confirming the observations made in Eça et al. [49]. Overall, the discretisation uncertainties never exceed 1.4%, and they are only slightly affected by the fluid rheology.

It is anticipated that, for Bingham and Herschel–Bulkley fluids, the Newtonian RANS models incorrectly predict a plug region (see Sections 6.7.2 and 6.7.4), i.e. a region with $\dot{\gamma} = 0$. This means that the regularisation is activated and the choice of the regularisation parameter, $m$, influences the numerical solution. In general, the

Table 6.2: Numerical uncertainty in the friction factor $f$ for the finest grid in percentage of the simulated data.

| | SST-HB | SST | SA | KSKL |
|---|---|---|---|---|
| $Re_\tau = 323$ ($y^+_{\max} = 0.016$) | | | | |
| Nwt | 0.21 | 0.21 | 0.04 | 0.08 |
| PL04 | 0.17 | 0.19 | 0.02 | 0.03 |
| Bn20 | 0.19 | 0.21 | 0.03 | 0.07 |
| HB10 | 0.28 | 0.21 | 0.05 | 0.11 |
| $Re_\tau = 2500$ ($y^+_{\max} = 0.125$) | | | | |
| Nwt | 1.37 | 1.37 | 0.03 | 0.30 |
| PL04 | 1.21 | 1.33 | 0.07 | 0.01 |
| Bn20 | 1.26 | 1.33 | 0.02 | 0.03 |
| HB10 | 1.28 | 1.35 | 0.02 | 0.07 |

regularisation parameter must be chosen large enough to avoid large regularisation errors, but not too large to compromise the convergence of the iterative solver. For the present calculations, the regularisation parameter was chosen such that $M \equiv \tau_0 m/(\rho v_w) \approx 2000$. The sensitivity of the friction factor due to the regularisation parameter was assessed by varying $M$ from 2000 to 500, and the maximum difference in the friction factor among all the test cases never exceeded 0.1%. With the new model, on the other hand, the average shear rate was actually never low enough to activate the regularisation (thanks to the second term in Eq. (6.35)). Therefore, both the solution and the iterative convergence were totally unaffected by the choice of $m$.[5] In summary, it is reasonable to consider the numerical uncertainty to be within 1.4% of the friction factor.

For the mean velocity profiles, only small differences between the solution on the coarsest and finest grids were observed, and mainly in the viscous sublayer at high Reynolds numbers (see Fig. 6.3). Thus, in conclusion, the numerical uncertainties are sufficiently small to allow a meaningful comparison with data from the literature.

## 6.7. RESULTS AND DISCUSSION

### 6.7.1. MODEL CALIBRATION

In order to achieve a wide range of applicability for the new model, the closure coefficients were chosen to provide satisfactory agreement with DNS data of Singh et al. [153, 152, 151], for a total of 10 test cases. Furthermore, little adjustments in the

---

[5] This is true as long as $m$ is sufficiently large; too low values may still influence the solution. Also, for external flows, the region outside the boundary layer is typically undeformed, so the iterative solver may still be affected by the use of large regularisation parameters.

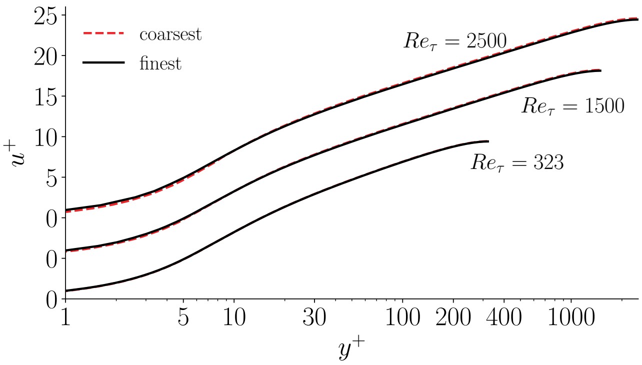

Figure 6.3: Mean velocity profiles on the coarsest and finest grids for Newtonian fluids using the SST model.

closure coefficients were made to improve the agreement with correlations from the literature for the friction factor [2, 3] at higher Reynolds numbers. The final selected closure coefficients are:

- $C_\beta = 0.667$, $C_\tau = 0.6$, $C_\chi = 0.6$, $C_\xi = 0.4$
- $C_E = C_{E1} F_E(n) + C_{E2}(1 - F_E(n))$
- $C_{E1} = 2.5$, $C_{E2} = 1.85$
- $F_E(n) = 0.5 \tanh\left[8(n - 0.75)\right] + 0.5$

Among the large number of combinations of closure coefficients that provided satisfactory agreement with data from the literature, the set with the lower coefficients was favoured. In this way, the modification of the SST model is minimised, and so is the impact of the additional terms on the iterative solver.

It was also decided to use a blending function, $F_E$, such that $C_E$ yields values from $C_{E1}$ to $C_{E2}$ when the flow index $n$ goes from 1 to 0.4. The reason for this is that $C_{E1}$ was observed to be optimal as long as $0.8 \leq n \leq 1$, whereas for $n < 0.8$ the effect of $E^{nn}$ on the numerical solution became excessive, especially at high Reynolds numbers. $F_E$ was thus devised to reduce $E^{nn}$ for $n < 1$. In practice, since $E^{nn} > 0$ for the tested rheologies, $F_E$ reduces the extra production of $\omega$ for low values of the flow index.

It is finally remarked that the blending functions $F_1$ and $F_2$ stemming from the original SST model (see also Appendix B.1) have not been modified for the new model. However, these functions contain the molecular viscosity and, since they were originally designed for Newtonian fluids, they may not always work as intended when using non-Newtonian fluids. For pipe flows, these functions are virtually constant (equal to one) across the pipe section, thus no issues were encountered. On the other hand, further research is needed to verify this on more complex wall-bounded flows, for example with adverse pressure gradient and flow separation.

### 6.7.2. MEAN VELOCITY

The mean velocity profiles for $Re_\tau = 323$ are shown in Fig. 6.4. For Newtonian fluids (Fig. 6.4 top), the SST and SST-HB produce identical results, as expected, and the SA shows the best agreement with DNS, even in the buffer layer ($5 < y^+ < 30$).

For the non-Newtonian cases, the new model produces the best agreement with DNS, although some discrepancies are noticeable around $y^+ = 30$. However, such discrepancies occur also for Newtonian fluids, so they are not strictly related to the non-Newtonian closure.

The Newtonian RANS models KSKL and SA tend to overpredict the mean velocity, meaning higher flow rates and lower friction factors, whereas the SST model seems rather insensitive to the non-Newtonian character of the fluid, which results in an underprediction of the mean velocity profile. Interestingly, for Bingham and Herschel–Bulkley fluids, the Newtonian RANS models incorrectly predict flat velocity profiles near the centreline (especially visible for Bn20 and Bn30), which indicates the presence of an unyielded region, or ‘plug’. This plug is caused by the very large viscosity in the core region (see also Section 6.7.3) and it characterised by zero mean shear rate[6]. Unyielded plugs are typical of laminar flows of yield-stress fluids in pipes and channels. For turbulent flows, both DNS (Rudman and Blackburn [141] and Singh et al. [153]) and experimental data (Peixinho et al. [131] and Güzel et al. [69]) suggest that the solid plug at the core is broken once the flow becomes turbulent. For viscoplastic fluids with truly time-independent rheology, plugs smaller than the Kolmogorov scales may still exist where the instantaneous shear rate is zero.

Unfortunately, DNS data for $Re_\tau > 323$ are only available for power-law fluids. Nevertheless, the agreement of the SST-HB model with the DNS appears to slightly improve for $Re_\tau = 750$ (Fig. 6.5), whereas no discernible improvements are observed for the SST, SA and KSKL models.

### 6.7.3. AVERAGE VISCOSITY

The average viscosity predicted by the SST-HB model compares well with DNS, although the agreement seems to deteriorate for yield stress fluids (see Fig. 6.6). In the core region, the SST-HB clearly outperforms the other models. In particular, the Newtonian turbulence models predict a very large viscosity near the centreline

---

[6] For the present calculations, the mean shear rate is actually close to zero but not exactly zero because of the use of the regularisation.

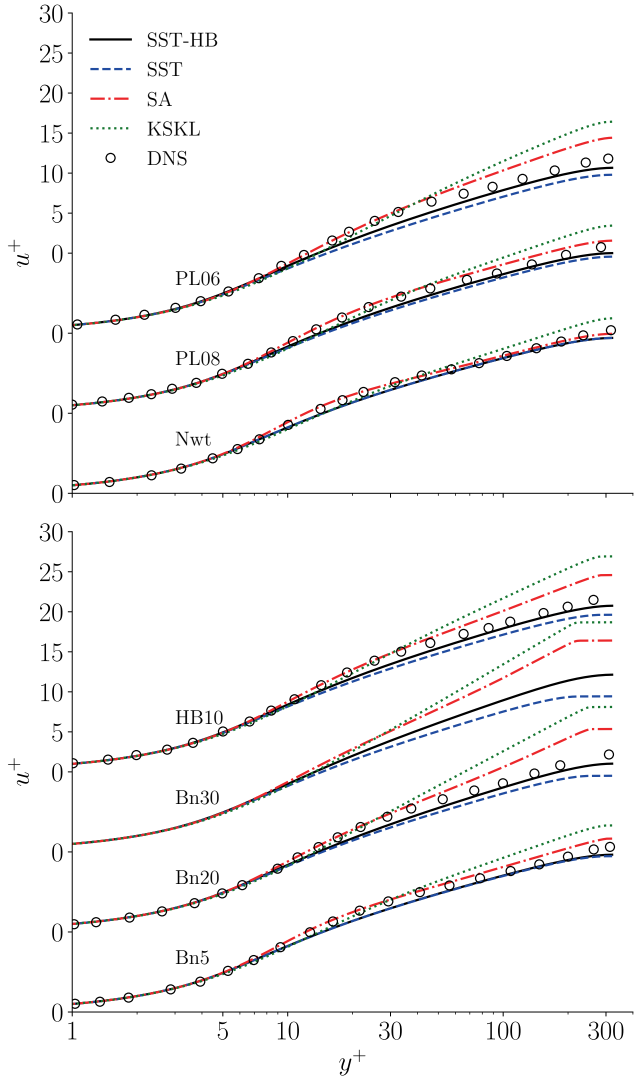

Figure 6.4: Mean velocity profiles for $Re_\tau = 323$. DNS data are from Singh et al. [153] and do not include the case Bn30.

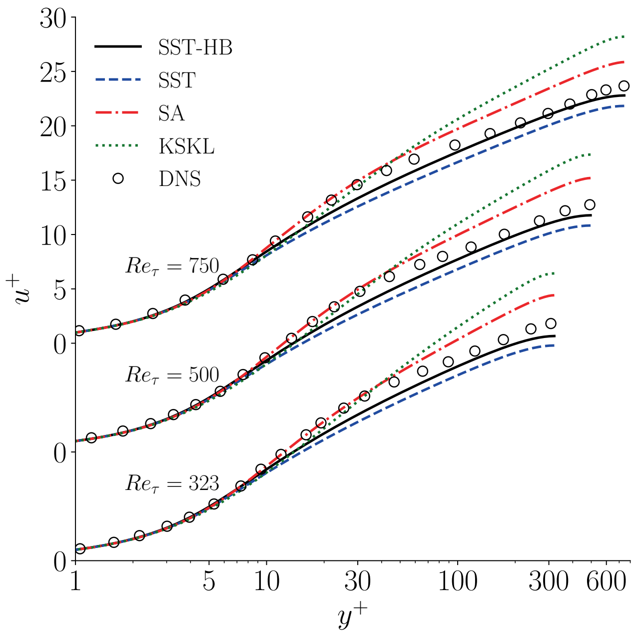

Figure 6.5: Mean velocity profiles for PL06 at $Re_\tau = 323, 500, 750$. DNS data are from Singh et al. [151].

of the pipe, as a result of the (nearly) zero mean shear rate. Remarkably, for Bn20 and $y^+ < 200$, the SA model agrees very well with DNS. However, this seems rather a fortuity since such good agreement is lost for the other test cases.

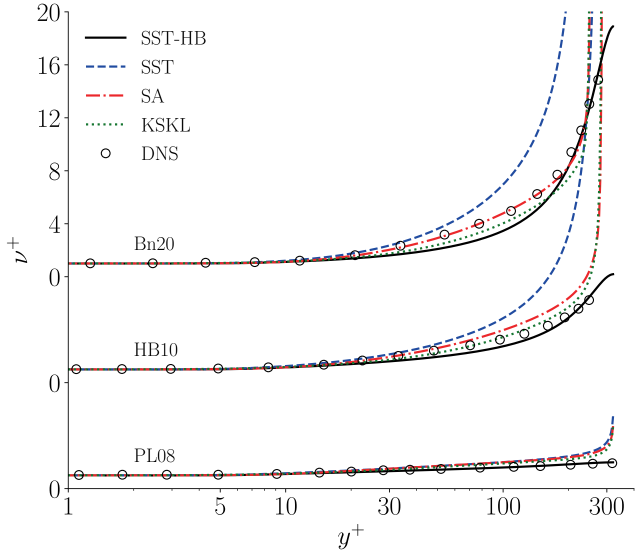

Figure 6.6: Average viscosity for $Re_\tau = 323$. DNS data are from Singh et al. [153].

While the new model produces the best agreement among the considered eddy-viscosity models, a clear discrepancy is noticeable for $20 < y^+ < 200$ for Bn20 and HB10. This could be explained by looking at the two main assumptions underlying the average viscosity model.

The first assumption is Eq. (6.16). From the mathematical standpoint, this assumption is exact when the viscosity is either a constant or a linear function of the instantaneous shear rate $\dot{\hat{\gamma}}$. For power-law fluids, the viscosity is proportional to $\dot{\hat{\gamma}}^{n-1}$, therefore the lower the flow index $n$ the more the assumption becomes weak. In the limit of $n = 0$, the viscosity is proportional to $\dot{\hat{\gamma}}^{-1}$, as for Bingham fluids. This means that for Bingham fluids this assumption is always weaker than for power-law fluids. The second assumption concerns the mean shear rate $\dot{\gamma}^2 = 2S_{ij}S_{ij} + 2\overline{S'_{ij}S'_{ij}}$. The last term was approximated using the mean dissipation rate of TKE, assuming that $\overline{\mu' S'_{ij}S'_{ij}} \approx 0$. DNS of Singh et al. [153] showed that the latter term is not negligible for Bingham fluids, especially for $20 < y^+ < 200$. In light of these considerations, it is plausible that the average viscosity model performs less well for Bingham fluids and

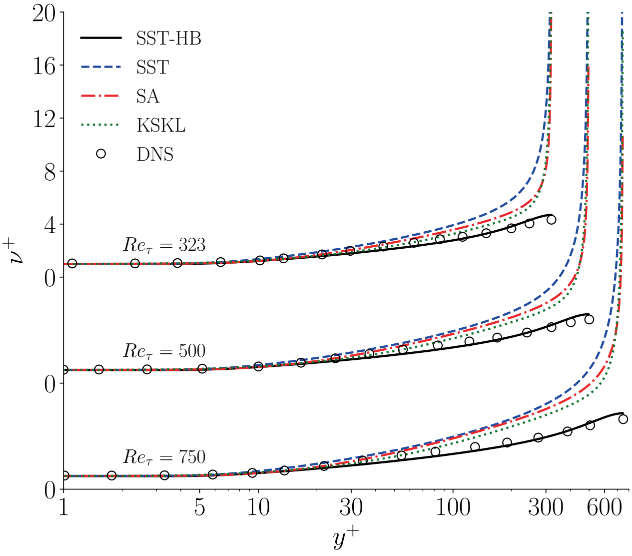

Figure 6.7: Average viscosity for PL06 at different Reynolds numbers. DNS data are from Singh et al. [151].

for $20 < y^+ < 200$.

It is finally remarked that viscosity is especially important near the wall, where the viscous stresses are dominant. Thus, outside the wall region ($y^+ > 10$), the small viscosity errors just mentioned above do not influence the mean velocity profile [154].

Fig. 6.7 shows that, for power-law fluids, the agreement of the SST-HB model with DNS is qualitatively the same for all Reynolds numbers, suggesting that the average viscosity model of Gavrilov and Rudyak [64] may be suitable also for calculations at higher Reynolds numbers.

To summarise, the new SST-HB model well predict the average viscosity for power-law fluids, also at different Reynolds numbers. For Bingham and Herschel–Bulkley fluids, the viscosity predicted by the SST-HB model shows some discrepancies with DNS, but these discrepancies are small and outside the wall region, thus they do not affect the mean flow. The main benefit of the new model is the significant reduction of large viscosity errors in the core region. This prevents the formation of unphysical plugs for yield-stress fluids, with positive effects also on iterative convergence (see Appendix B.5).

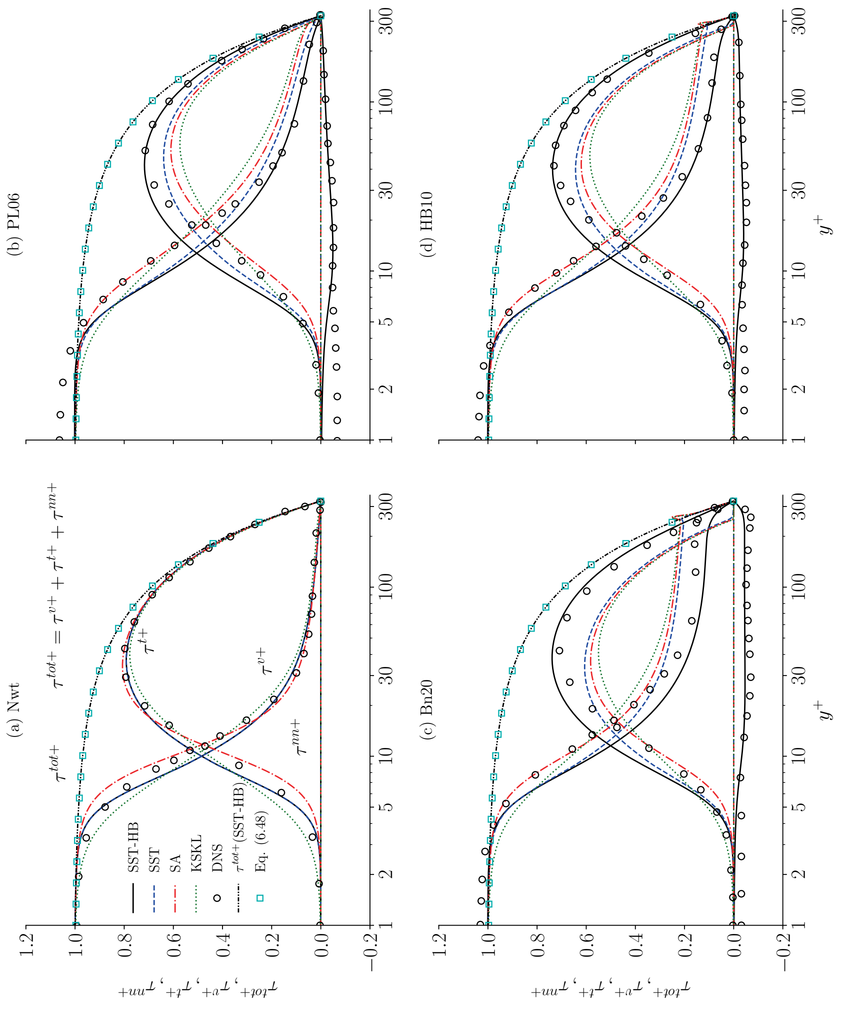

Figure 6.8: Mean shear stress budget at $Re_\tau = 323$ obtained with the four eddy-viscosity models and from DNS of Singh et al. [153, 152]. The total mean shear stress $\tau_{tot}$ is relative to the SST-HB model.

### 6.7.4. MEAN SHEAR STRESS BUDGET

The total mean shear stress written in cylindrical coordinates reads:

$$\tau_{zr}^{tot} = \mu \frac{du_z}{dr} - \overline{u_r' u_z'} + \overline{\mu' S_{zr}'}, \tag{6.46}$$

where $z$ and $r$ indicate the axial and radial direction, respectively, and the terms on the right-hand side are the viscous, turbulent and non-Newtonian stresses. For the SST-HB model, the total mean shear stress is modelled as (subscripts are omitted)

$$\tau^{tot} = \mu \frac{du_z}{dr} + \mu_t \frac{du_z}{dr} + \mu^{nn} \frac{du_z}{dr} \equiv \tau^v + \tau^t + \tau^{nn}, \tag{6.47}$$

whereas for the Newtonian eddy-viscosity models the last component is zero. Integration in the radial direction of the momentum equation in the axial direction and using the non-dimensional wall coordinates leads to

$$\tau^{tot+} = 1 - \frac{y^+}{Re_\tau}. \tag{6.48}$$

This means that the distribution of the mean viscous, turbulent and non-Newtonian shear stresses can be a function of the fluid rheology, but the total shear stress must always vary linearly across the pipe diameter. The total mean shear stress and its components are plotted in Fig. 6.8 for $Re_\tau = 323$.

For Newtonian fluids, all models produce a fairly good prediction of $\tau^v$ and $\tau^t$, with some loss of accuracy in the buffer layer ($5 < y^+ < 30$). For non-Newtonian fluids, the SST, SA and KSKL models poorly predict all the shear stress components. In particular, for Bingham and Herschel–Bulkley fluids, the viscous stress predicted by these models has an unexpected local peak (at $y^+ \approx 250$ for Bn20, see Fig. 6.8 c), which alters the correct linear distribution of the total stress over the pipe diameter. The position of this incorrect peak is in proximity of the plug, where the velocity gradient and the viscosity have a steep variation in a relative short distance, causing large discretisation errors. These errors could be reduced by locally refining the grid around the plug, but note that results would still be physically incorrect.

The SST-HB has clearly the best agreement with DNS for all the shear stress components, and the total stress follows the expected linear behaviour for all test cases. Furthermore, the non-Newtonian shear stresses, $\tau_{ij}^{nn}$, are very well captured by the SST-HB model, except in the viscous sublayer. This is because $\mu^{nn} \propto \omega k$ (see Eq. (6.36)) and the turbulent kinetic energy is set to zero at the wall. In any case, in the viscous sublayer the total stress is completely dominated by the viscous component, therefore the effects of this deficiency on the numerical solution are expected to be small.

### 6.7.5. TURBULENT KINETIC ENERGY

All eddy-viscosity models are clearly unable to accurately predict the distribution of TKE (Fig. 6.9), even for Newtonian fluids[7]. According to DNS for shear-thinning and viscoplastic fluids, the peak of $k$ should increase. However, the SST, SA and KSKL models predict a decrease in $k$. While the new SST-HB is also unable to capture the peak of $k$, it is capable, at least, of maintaining a higher level of turbulent kinetic energy compared to the other turbulence models. This is possible thanks to the $\chi^{nn}$ term in the $k$-equation, which acts as a production of turbulent kinetic energy (see Appendix B.4).

The poor prediction of $k$ is an expected limitation of two-equation turbulence models. In fact, for increasing shear-thinning effects, $k$ increases and $\mu_t$ decreases, whereas two-equation models imply direct proportionality between $\mu_t$ and $k$. Nevertheless, the accurate prediction of $k$ is often not of importance for many engineering applications, which are usually interested in the mean velocity and pressure profiles and in the friction factor.

Finally, the incorrect plug region already discussed in the previous sections is visible also in Fig. 6.9 (c) for the SA and KSKL models, showing zero turbulent kinetic energy for $y^+ \gtrsim 250$. Despite that the plug was predicted also by the SST model, the turbulent kinetic energy is however not zero for this model, which is physically inconsistent.

In summary, the SST-HB always predict a higher level of $k$ among the considered turbulence models, and its accuracy is unsatisfactory yet comparable with that of the SST model when the latter is applied to Newtonian fluids.

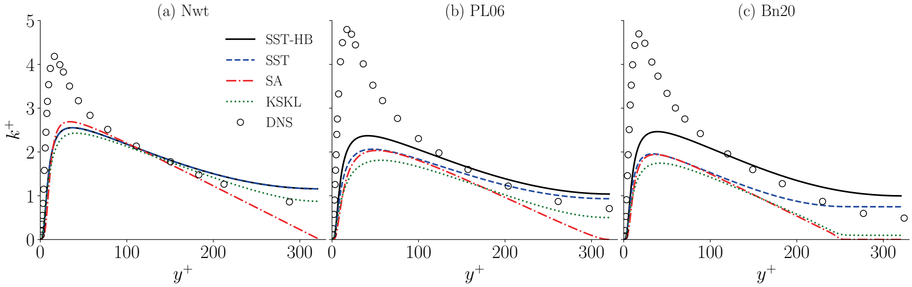

Figure 6.9: Turbulent kinetic energy for $Re_\tau = 323$. DNS data are from Singh et al. [153].

---

[7] This was already observed by Wilcox [179] for the $k-\omega$ model. Despite the poor prediction of $k$ (and $\epsilon$), Wilcox showed that the velocity profile and the skin friction were well predicted for both external and internal flows.

Table 6.3: Friction factor $f = 2\tau_w/(\rho U_b^2)$ from DNS Singh et al. [153, 152, 151] and from eddy-viscosity models of the present work. The difference $\Delta f$ is relative to DNS.

| | | DNS | SST-HB | | SST | | SA | | KSKL | |
|---|---|---|---|---|---|---|---|---|---|---|
| | Case | $f \times 10^3$ | $f \times 10^3$ | $\Delta f$ (%) | $f \times 10^3$ | $\Delta f$ (%) | $f \times 10^3$ | $\Delta f$ (%) | $f \times 10^3$ | $\Delta f$ (%) |
| $Re_\tau = 323$ | Nwt | 7.88 | 8.264 | 4.9 | 8.264 | 4.9 | 7.819 | -0.8 | 7.203 | -8.6 |
| | PL08 | 7.36 | 7.831 | 6.5 | 8.219 | 11.7 | 6.786 | -7.7 | 6.291 | -14.5 |
| | PL06 | 6.74 | 7.422 | 10.2 | 8.134 | 20.7 | 5.734 | -14.9 | 5.227 | -22.4 |
| | PL04 | 5.95 | 6.797 | 14.3 | 7.982 | 34.2 | 4.971 | -16.4 | 4.710 | -20.8 |
| | Bn5 | 7.70 | 8.120 | 5.5 | 8.176 | 6.2 | 7.055 | -8.3 | 6.378 | -17.1 |
| | Bn10 | 7.36 | 7.879 | 7.1 | 8.092 | 10.0 | 6.390 | -13.1 | 5.597 | -23.9 |
| | Bn20 | 6.74 | 7.270 | 7.9 | 7.942 | 17.9 | 5.499 | -18.4 | 4.694 | -30.3 |
| | HB10 | 6.88 | 7.381 | 7.3 | 8.062 | 17.2 | 5.789 | -15.9 | 5.089 | -26.0 |
| $Re_\tau = 500$ | Nwt | 6.89 | 7.108 | 3.2 | 7.108 | 3.2 | 6.889 | 0.0 | 6.279 | -8.8 |
| | PL06 | 5.86 | 6.332 | 8.0 | 6.981 | 19.1 | 4.965 | -15.3 | 4.456 | -24.0 |
| $Re_\tau = 750$ | Nwt | 6.15 | 6.256 | 1.8 | 6.256 | 1.8 | 6.163 | 0.3 | 5.598 | -8.9 |
| | PL06 | 5.28 | 5.553 | 5.3 | 6.122 | 16.0 | 4.443 | -15.8 | 3.941 | -25.3 |

### 6.7.6. FRICTION FACTOR

The friction factor, $f$, is often one or even the only quantity of interest for many engineering applications. It is therefore an important quantity to assess the performance of the new model.

The comparison of the friction factor, $f$, with DNS is reported in Table 6.3. The difference $\Delta f$ reflects the predictions of the mean velocity profiles already observed in Section 6.7.2: SA and KSKL underpredict $f$ ($U_b$ is larger), vice-versa for SST.

The SST-HB model undoubtedly provides the best prediction for all the test cases, especially at the higher Reynolds numbers. While the difference of 14.3% for PL04 is considerable, it is still the smallest among all turbulence models. Such difference could be easily reduced by increasing, for example, the calibration coefficient $C_{E2}$ (see Section 6.7.1) from 1.85 to 2.0. By doing so, however, the accuracy for power-law fluids at higher $Re_\tau$ would deteriorate. It was thus decided to sacrifice some accuracy at $Re_\tau = 323$ in favour of more consistent accuracy for a wide range of Reynolds numbers.

In order to assess the new model also for $Re_\tau > 750$, the friction factor has been compared against correlations from the literature. For power-law fluids, two correlations were considered. The first (Anbarlooei et al. [2]) reads

$$f = \left(0.102 - 0.033n + \frac{0.01}{n}\right) \frac{1}{Re_{MR}^{\frac{1}{2(n+1)}}}, \tag{6.49}$$

where $Re_{MR}$ is the Reynolds number defined by Metzner and Reed [116],

$$Re_{MR} = \frac{8\rho U_b^{2-n} D^n}{K(6+2/n)^n}, \tag{6.50}$$

also called Metzner-Reed Reynolds number. Note that, for a particular rheology, higher $Re_{MR}$ means also higher $Re_\tau$, thus the following discussion is valid for both Reynolds numbers. The second correlation (Anbarlooei et al. [3]) reads

$$f = 0.079\left[\frac{Re_{MR}}{8}(6+2/n)^n\right]^{\frac{-1}{2(n+1)}}. \tag{6.51}$$

Both correlations are plotted in Fig. 6.10, together with DNS (open symbols) and RANS data (filled symbols). The maximum difference between DNS and the correlations is about −3.5%, which can be seen as a coarse indication of the correlation's uncertainty.

The new model (Fig. 6.10 d) well predicts $f$ for power-law fluids also at high Reynolds numbers. At $Re_\tau = 2500$, the maximum difference relative to the first and second correlations is -2.7% and -6.1%, respectively. Compared to SST, the benefits of using the new model are more evident for highly shear-thinning fluids. In fact, the accuracy of SST may be actually considered acceptable for moderate shear-thinning fluids, especially at high Reynolds numbers, where non-Newtonian effects become less important. To some extent, this is also true for the SA model (Fig. 6.10 a), whereas it is clearly not true for the KSKL model (Fig. 6.10 b), which significantly under predicts the friction coefficients for all $Re_{MR}$. Actually, KSKL appears to be rather inaccurate also for Newtonian fluids. This is surprising as KSKL proved to perform well for external wall bounded flows of Newtonian fluids (e.g. Eça and Hoekstra [48] and Pereira et al. [132]). Fig. 6.10 (b) suggests that KSKL may perform better at higher Reynolds numbers.

6

For Bingham fluids, two correlations [1, 3] were considered, both having the following form

$$f = \frac{0.316}{4\sqrt{2}}\sqrt{\sqrt{\frac{He^2}{Re_G^4}+\frac{4}{Re_G}}+\frac{He}{Re_G^2}} - C\frac{He}{Re_G^2}, \tag{6.52}$$

where $Re_G = \rho U_b D/K$ is the generalised Reynolds number and $He = \rho\tau_0 D^2/K^2$, the latter being the Hedstrom number. The correlation reduces to the Blasius formula for $He = 0$, i.e. for zero yield stress.

In the earlier version [1] the coefficient $C$ is equal to 2, whereas the later version [3] does not include the last term ($C = 0$). When these correlations were compared with the DNS data of Singh et al. [153], the maximum difference using $C = 2$ was around +10%, whereas with $C = 0$ the maximum difference was about -10%. We have thus deliberately opted for the middle way, i.e. $C = 1$, which has decreased the maximum difference down to 1.7% (see Table 6.4). This has increased the confidence in the correlation as being a more reliable representation of DNS data, nonetheless the comparison must be interpreted with the due caution.

Table 6.4: Difference $\Delta f(\%)$ of the friction factor relative to Eq. (6.52) with $C = 1$. DNS data are from Singh et al. [153].

| | | DNS | SST-HB | SST | SA | KSKL |
|---|---|---|---|---|---|---|
| $Re_\tau = 323$ | Nwt | 0.5 | 4.7 | 4.7 | -0.2 | -7.1 |
| | Bn5 | 1.7 | 6.7 | 7.3 | -5.9 | -14.0 |
| | Bn10 | 1.0 | 7.5 | 10.2 | -11.1 | -21.2 |
| | Bn20 | -0.1 | 7.4 | 16.8 | -17.5 | -28.8 |
| | Bn30 | - | 6.16 | 24.94 | -19.48 | -28.68 |
| $Re_\tau = 750$ | Nwt | -0.2 | 1.3 | 1.3 | 0.0 | -8.0 |
| | Bn5 | - | 2.5 | 3.4 | -6.3 | -15.7 |
| | Bn10 | - | 2.5 | 5.6 | -13.9 | -25.4 |
| | Bn20 | - | 1.4 | 10.9 | -24.1 | -37.5 |
| | Bn30 | - | -0.78 | 17.45 | -29.10 | -41.11 |
| $Re_\tau = 1500$ | Nwt | - | 1.3 | 1.3 | 1.8 | -6.4 |
| | Bn5 | - | 2.1 | 3.0 | -4.3 | -14.6 |
| | Bn10 | - | 1.8 | 4.9 | -13.4 | -25.8 |
| | Bn20 | - | 0.2 | 9.2 | -26.2 | -40.9 |
| | Bn30 | - | -2.73 | 14.64 | -32.91 | -46.37 |
| $Re_\tau = 2500$ | Nwt | - | 2.3 | 2.3 | 3.9 | -4.2 |
| | Bn5 | - | 2.9 | 3.8 | -1.9 | -12.7 |
| | Bn10 | - | 2.5 | 5.3 | -11.9 | -25.1 |
| | Bn20 | - | 0.5 | 9.1 | -26.5 | -42.0 |
| | Bn30 | - | -2.96 | 13.78 | -34.34 | -48.68 |

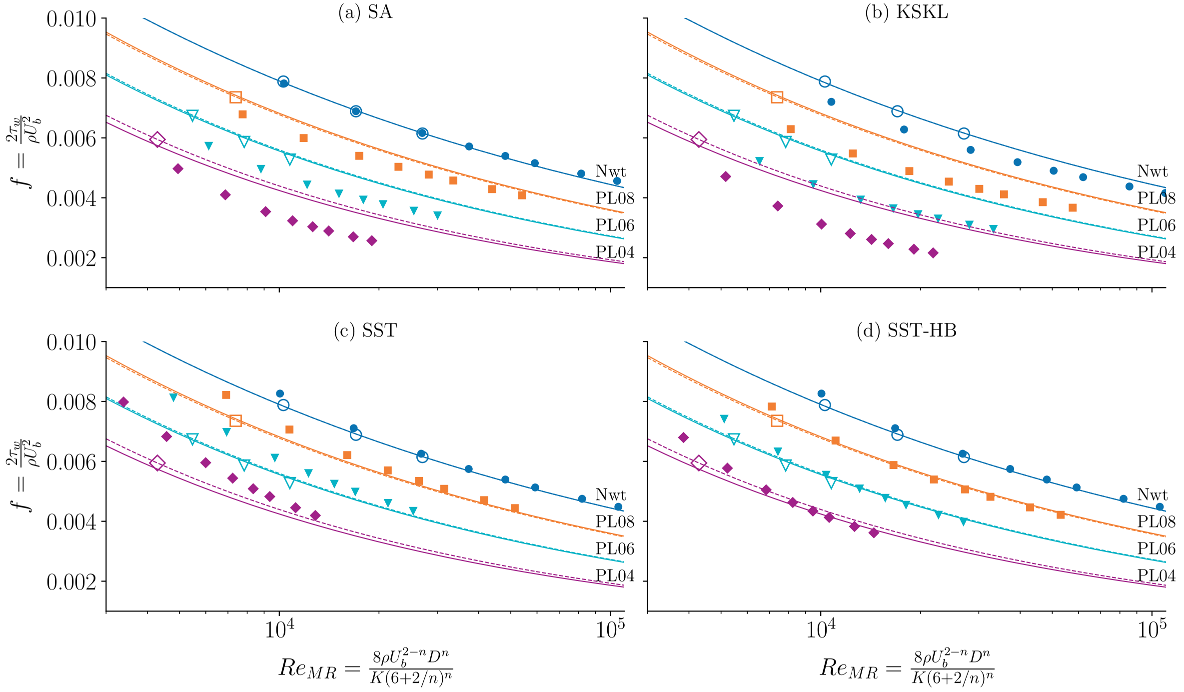

Figure 6.10: Friction factor versus $Re_{MR}$ for power-law fluids from present work (filled symbols), from DNS of Singh et al. [152, 151] (open symbols) and from the correlations of Anbarlooei et al. [2] (solid lines, Eq. (6.49)) and of Anbarlooei et al. [3] (dashed lines, Eq. (6.51)). The 8 points for each rheology correspond to $Re_\tau = 323, 500, 750, 1000, 1250, 1500, 2000, 2500$.

Keeping the above considerations in mind, Table 6.4 shows the comparison of the present results against Eq. (6.52) with $C = 1$. The SST model appears to be suitable for weakly non-Newtonian fluids ($\tau_0/\tau_w = 10\%$) and for high Reynolds numbers, whereas the SA and KSKL models seem to perform poorly for Bingham fluids, at any flow regime.

The new model, on the other hand, seems to well predict $f$ at all Reynolds numbers. However, the important finding here is that, for $Re_\tau > 323$, the new model appear to maintain approximately the same level of accuracy, without any marked change in $\Delta f(\%)$. This suggests that the model may be suitable for viscoplastic flows for a wide range of Reynolds numbers. For a more compelling validation, however, DNS data for Bingham and Herschel–Bulkley fluids at high Reynolds numbers and with higher level of yield stress are needed. This is an important issue for future research.

## 6.8. FINAL CONSIDERATIONS FOR PRACTICAL APPLICATIONS

### 6.8.1. YIELD STRESS LIMIT

This chapter focused on pipe flows because it was the only wall-bounded case for which Herschel–Bulkley DNS data were published in the literature. However, the same near-wall behaviour for the tested RANS models could be expected in boundary-layer flows, such as the flow over a flat plate or around a ship. More specifically, the same accuracy can be expected if the yield stress does not exceed 20% of the wall shear stress, i.e. the limit for which the Newtonian RANS models have been tested ($\tau_0/\tau_w \leq 20\%$) and for which the SST-HB model has been calibrated. Above a certain limit, say above 30%, the accuracy of the turbulence models is unknown.

But what is the typical ratio $\tau_0/\tau_w$ for realistic navigational scenarios? In other terms, what would be the maximum yield stress for which the tested RANS models behave as shown in this chapter? To answer this question, the wall shear stress, $\tau_w$, needs to be estimated for a ship sailing through mud. Note, however, that the wall shear stress in this case is not constant like for pipe flows, but rather it varies along the hull. Thus, the average shear stress over a surface $S$ will be considered instead:

$$\tau_w \approx \overline{\tau_w} = \frac{1}{S}\int_S \tau_w dS = \frac{1}{2}\rho U^2 C_F \tag{6.53}$$

where the overbar represents the average over the surface $S$, which is the portion of the hull in contact with mud; $C_F$ is the frictional resistance coefficient, which can be estimated using existing correlations for a flat plate (shallow water and form effects are neglected for simplicity). Unfortunately, no correlations for turbulent Herschel–Bulkley flows over a flat plate are available. Nonetheless, it is reasonable to assume that for limited amount of yield stress the wall shear stress is only moderately affected. Thus, in a first approximation, correlations for Newtonian fluids can be used. Here, the correlation of Katsui [79] is used, which reads:

$$C_F = \frac{0.0066577}{(\log_{10}(Re) - 4.3762)^a} \tag{6.54}$$

with

$$a = 0.042612 \log_{10}(Re) + 0.56725 \tag{6.55}$$

As an example, let's consider a ship having $L = 320$ m and moving through Mud_10 and Mud_23, which are two of the three fluid mud conditions that were considered in Chapter 5. The estimated ratios $\tau_0/\tau_w$ are reported in Table 6.5.

In the considered conditions, the mud yield stress is within 50% of the average wall shear stress only at rather high speeds (unlikely reachable in confined waters). Above roughly 40-50%, the assumption that the yield stress is not influencing the shear stress becomes quite incorrect, so Eq. (6.54) cannot be reliably used to estimate $\tau_w$. Nevertheless, even if the ratio cannot be reliably estimated at lower speeds, it can be safely stated that $\tau_0/\tau_w$ will keep increasing with decreasing speed. Hence, the main point here is that for sailing speeds in confined areas (typically below 6-8 knots), $\tau_0/\tau_w$ may often be above 20-30%, in which case the accuracy of the considered RANS models remains unknown due to lack of validation data. Ratios $\tau_0/\tau_w$ below 20-30% for typical sailing speeds in the confined waters correspond to yield stresses no larger than 1-3 Pa.

Table 6.5: Estimated ratio $\tau_0/\tau_w$ using Eq. (6.54) for a flat plate moving through Mud_10 and Mud_23 assuming turbulent flow and negligible influence of the yield stress. For the rheological properties of Mud_10 and Mud_23 (see Table 5.2).

| U [Kn] | U [m/s] | $Re$ | $C_F \times 1000$ | $\sim \tau_0/\tau_w$ |
|---|---|---|---|---|
| | | Mud_10 | | |
| 8.0 | 4.12 | 9.0E+07 | 2.098 | 48% |
| 10.0 | 5.14 | 1.1E+08 | 2.037 | 32% |
| 12.0 | 6.17 | 1.3E+08 | 1.989 | 22% |
| | | Mud_23 | | |
| 12.0 | 6.17 | 6.9E+07 | 2.174 | 46% |

### 6.8.2. EDDY VISCOSITY FOR A SHIP SAILING THROUGH MUD

What would actually happen when performing RANS simulations of a large vessel sailing through mud? As an example, Fig. 6.11 shows the ratio $\mu_t/\mu$ in the mud layer (Mud_23) when using SST. Clearly, the eddy viscosity near the hull is negligible compared to the apparent viscosity ($\mu_t/\mu << 1$), hence the SST model actually predicts laminar flow. Analogous observations were made with SA, KSKL and SST-HB. Of course, the results may differ depending on the mud rheology, ship's size and speed, and on the regularisation parameter; nonetheless, this example suggests that for some practical applications the RANS models will tend to predict laminar flow in the mud layer.

It is remarked that these RANS models are not supposed to correctly capture the flow transition. Hence, the fact that they predict laminar flows could be spurious, especially for non-Newtonian fluids. On the other hand, it is realistically plausible that for $\tau_0/\tau_w$ well above 20 – 30% the flow of mud is laminarised due to its high viscosity. If this should be the case, the Newtonian RANS models are then performing correctly without any modifications, at least for the example shown in Fig. 6.11 and for analogous scenarios.

## 6.9. CONCLUSIONS AND LIMITATIONS

### 6.9.1. CONCLUSIONS

A new turbulence model for Herschel–Bulkley fluids (and their special cases, i.e. Bingham and power-law) has been derived by modifying the popular $k-\omega$ SST model. The derivation was carried out along the lines of Gavrilov and Rudyak [64], who developed a turbulence closure for power-law fluids. The calibration coefficients were chosen to ensure satisfactory agreement with DNS data and with correlations for shear-thinning and yield-stress fluids for a wide range of Reynolds numbers. Furthermore, we have assessed three widely-used RANS models for Newtonian fluids, namely the SST, the Spalart-Allmaras (SA) and the $k$-$\sqrt{k}L$ (KSKL) models. The main conclusions of this work are summarised as follows:

- The new model showed good agreement in the mean velocity, average viscosity, mean shear stress budget and friction factors as compared to DNS data. Furthermore, the new model appears to be always more accurate than the standard SST model.

- The new model is inadequate for applications that require accurate predictions of the TKE. Nonetheless, the accuracy of the prediction is comparable to that of the other selected RANS models when applied to Newtonian flows.

- The friction factor predicted by the new model agrees well with both DNS and correlations for power-law and Bingham fluids.

- Among the three Newtonian RANS models, the SST proved to be most suitable for weakly non-Newtonian fluids ($n \geq 0.8$ and $\tau_0/\tau_w \leq 10\%$) and for high Reynolds numbers ($Re_\tau > 750$). The SST model tends to underpredict the

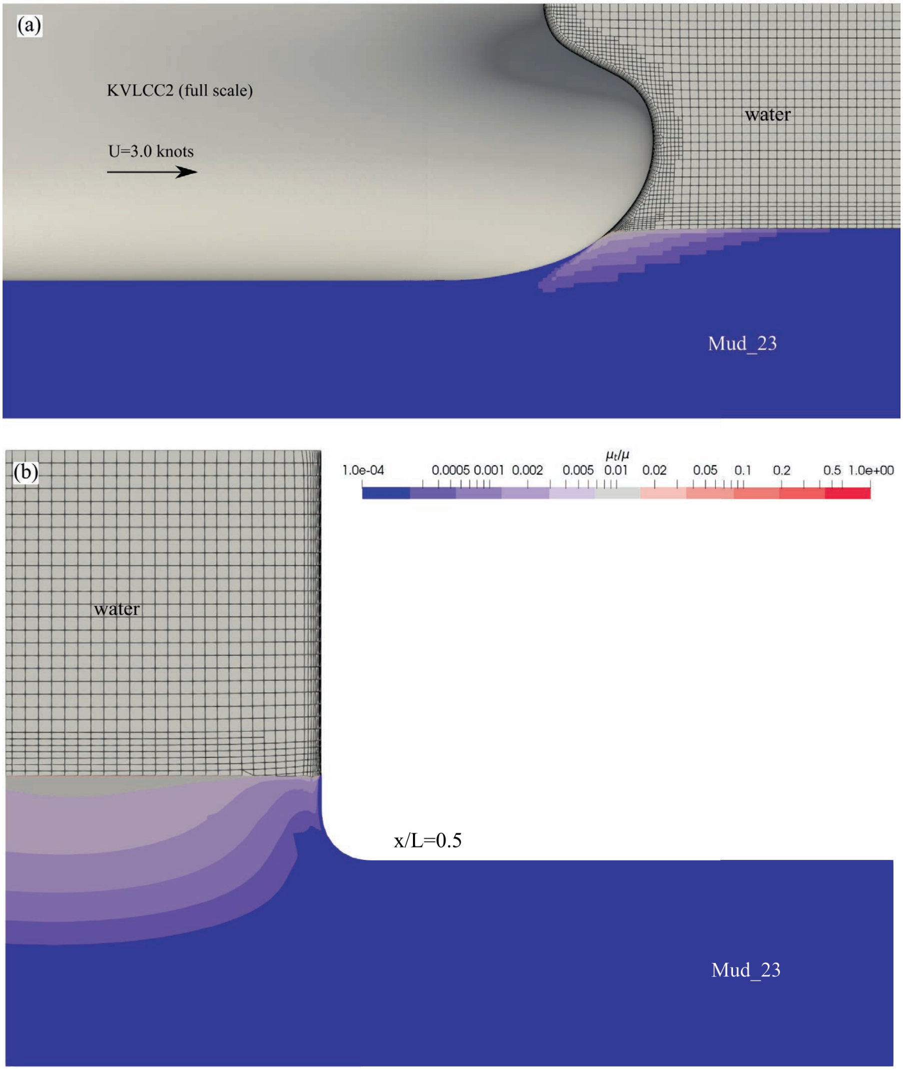

Figure 6.11: Ratio of the eddy-viscosity over the apparent viscosity for the SST model in a Bingham mud layer having the same rheological properties of Mud_23 (see Table 5.2). The ship is a full-scale KVLCC2 tanker [150] sailing at 3 knots with an under-keel clearance of $0.5T$ and $-0.2T$ ($T$ is the ship's draught) with respect to the solid bottom and the mud-water interface, respectively. (a) bow region at the symmetry plane; (b) midship section of half ship.

mean velocity and to overpredict the friction factor. Vice-versa for SA and KSKL, with the latter giving the worst agreement for all test cases.

- For yield-stress fluids, the three Newtonian RANS models incorrectly predict a plug. This is not only physically incorrect, as proved by previous studies, but it may also lead to large discretisation errors and difficult iterative convergence. With the new model, on the other hand, no plugs were predicted and the iterative convergence did not show any difficulty (see Appendix B.5). This last feature can be particularly appreciated for viscoplastic fluids in complex geometries, where the combination of large yield stresses and the slowly converging SIMPLE-like algorithms could easily lead to stagnating/diverging iterative convergence.

- For a ship sailing through mud, $\tau_0/\tau_w$ may often be above 20-30%, in which case the accuracy of the considered RANS models is unknown. Ratios $\tau_0/\tau_w$ below 20-30% for typical sailing speeds in the confined waters correspond to yield stress no larger than 1-3 Pa. On the other hand, when $\tau_0/\tau_w$ is well above 30%, it is possible that the mud boundary layer is laminar because of viscous damping. In this case, the Newtonian RANS models seem to perform correctly without any modifications as they already tend to predict laminar flow ($\mu_t/\mu << 1$) in the mud layer.

### 6.9.2. LIMITATIONS

A number of important limitations need to be considered. First, while only one new empirical function ($F_E(n)$) was needed in the SST-HB model to produce good agreement with DNS for pipe flows, further empirical modifications of the original SST model may still be required for complex applications, such as those with adverse pressure gradient and flow separation both in external and internal flow configurations. In this regard, the applicability of the new model to complex external flows, such as the flow around a ship, still requires further investigations.

Second, the current study was limited to $Re_\tau > 323$, and the accuracy of the new model is expected to decrease at lower Reynolds numbers.

Third, DNS data are also affected by numerical errors/uncertainties which, unfortunately, could not be found. It was thus implicitly assumed that these errors were small compared to the modelling errors. In order to overcome this aspect, it is recommended for future DNS to provide uncertainty estimates.

Fourth, it remains a question whether the new model is suitable for fluids with high yield stress, both because no validation data is available and because the flow may become transitional/laminar in the core of the pipe, especially at lower Reynolds numbers. Further DNS investigations at $Re_\tau > 323$ and with higher yield stress levels will be of great help to develop and improve turbulence models for Herschel–Bulkley fluids. It is remarked that the new RANS model was calibrated and tested for pipe flows only, a relatively simple internal-flow problem. The applicability of the new model to complex external flows, such as the flow around a ship, still requires further investigations.

Finally, although RANS simulations of a ship sailing through Mud_23 predicted laminar flow in the mud layer near the hull, it cannot be conclusively stated that this is physically correct because the tested RANS models are not supposed to capture the flow transition of Newtonian fluids, let alone the flow transition for non-Newtonian fluids. In order to increase the confidence in the force predictions, DNS of the flow over a flat plate will help to elucidate on the actual flow regime in the mud layer for typical navigation scenarios.

# 7

# CONCLUSIONS AND RECOMMENDATIONS

*...in which the main conclusions of the four research steps are summarised. Recommendations for future CFD calculations and developments are provided at the end of the chapter.*

## 7.1. INTRODUCTION

This research project was initiated with the aim to implement, verify and validate non-Newtonian models in REFRESCO in order to predict the influence of muddy seabeds on the navigational performance of ships. The goal is to improve the current understanding of the ship-mud interaction using CFD instead of the more traditional experimental methods. The benefit for society will be the reduction of operational and maintenance costs for ports and waterways, while preserving the required safety for navigation.

ReFRESCO is a CFD code developed for maritime applications and it was originally designed to simulate only Newtonian fluids. Since mud is a non-Newtonian fluid, the first step has been the implementation of non-Newtonian models in REFRESCO. A suitable choice of the rheological model depends, among others, on the required level of accuracy and on the type of mud. In this work, the choice fell on the Herschel-Bulkley model, which was deemed to be a good starting point to describe the shear-thinning and viscoplastic behaviour of mud.

## 7.2. CONCLUSIONS

### 7.2.1. CODE VERIFICATION OF THE HERSCHEL–BULKLEY SOLVER

It is important that the implementation of new features is followed by code verification to ensure that the code is free of mistakes and numerical algorithm deficiencies. The code verification based on the MMS showed that the code performs as intended for both single- and two-phase flows of Herschel–Bulkley fluids. The illustrated procedure can be used to verify the implementation of other rheological model as well. When verifying the correct implementation of a new rheological model, it is important to examine, in addition to the grid convergence of velocity and pressure, also the grid convergence of the apparent viscosity. In this way there are higher chances of identifying coding mistakes pertaining to the implementation of the non-Newtonian model.

### 7.2.2. TESTING THE HERSCHEL–BULKLEY SOLVER ON A BENCHMARK PROBLEM

While code verification ensured that the Herschel–Bulkley model was correctly implemented, obtaining fully-converged solutions for realistic non-Newtonian problems may still be difficult to obtain. This is because, for yield-stress fluids, the viscosity can vary by several order of magnitude within a short distance, making the equations stiffer and thus more difficult to solve. Therefore, the non-Newtonian solver of REFRESCO has been tested on the laminar flow of Herschel-Bulkley fluids around a sphere. The latter is the simplest three-dimensional flow exhibiting features that are somewhat close to those observed in the flow around ships, such as boundary layer development and flow separation.

Some difficulties were encountered when using large regularisation parameters, which led to stagnating residuals and thus large iterative errors. A determining factor turned out to be the choice of the viscosity interpolation scheme. Although obtaining a fully-converged solutions remained challenging, the improved iterative convergence proved to be sufficient to replicate data from the literature with good accuracy despite the high non-linearity introduced by the non-Newtonian viscosity. This provided confidence to employ the CFD code on more practical applications.

### 7.2.3. VALIDATION OF THE BINGHAM MODEL FOR A PLATE MOVING THROUGH MUD

The comparison between experimental and numerical data for a plate moving through mud showed that the ideal Bingham model (large regularisation parameters) well captures the relative increase of the resistance due to the increase of mud concentration. However, at low speed, it tends to overpredict the resistance. If one wants to simulate the flow of an ideal Bingham fluid, (non-dimensional) values of the regularisation parameter above 10000-20000 may be required. For simulations of fluid mud, on the other hand, lower values seem more favourable, both from the numerical (better iterative convergence) and physical perspective (real mud, as used during the experiments, does not exhibit a discontinuity around $\dot{\gamma} = 0$).

This research also revealed that the Tscheuschner model, which was a virtually perfect fit of the ramp-down flow curves of mud, produced strong underpredictions of the resistance, and in general worse prediction than the Bingham model. From this it is concluded that using a more advanced model than Bingham may not necessarily lead to more accurate numerical predictions. Two possible explanations are the neglected thixotropy of mud and/or possible inaccuracies of the rheological protocol at low shear rates. This latter case would support the fact that the use of more advanced rheological models should go hand-by-hand both with more accurate rheological characterisation of mud and with improvements of other components of the mathematical model. If this is not possible, advanced rheological models might perform as good as (or even worse than) simple models like Bingham. This should be kept in mind before considering the implementation of new rheological models in the CFD code.

### 7.2.4. TURBULENCE MODELLING

Although it is not known a priori whether the flow of mud around the ship is turbulent or not (it may depend on the ship's size, speed and on the mud rheology), it was questioned whether RANS models developed for Newtonian fluids can be applied reliably to Herschel-Bulkley flows. This was investigated for turbulent flows inside circular pipes, for which DNS data are available for power-law, Bingham and Herschel-Bulkley fluids.

From this study it was concluded that, among the three tested Newtonian RANS models, the SST model produced the best predictions and it is reasonably accurate for weakly non-Newtonian fluids and at high Reynolds numbers. Overall, the SST model tends to underpredict the mean velocity and to overpredict the friction factor. Vice-versa for the SA and KSKL models, which are not recommended for turbulent non-Newtonian flows.

A new RANS model, labelled SST-HB, has been developed starting from the SST model. The newly developed SST-HB showed good agreement with DNS in the mean velocity, average viscosity, mean shear stress budget and friction factors. The SST-HB correctly predicted a drag reduction when the yield stress was increased.

It should be noted that the accuracy of the tested RANS models for turbulent flows with $\tau_0/\tau_w > 20-30\%$ is still uncertain as validation data for such conditions is not currently available. When tested on some realistic conditions, however, all four

RANS models predicted laminar flow in the mud layer ($\mu_t/\mu << 1$). While it is not possible to assess what would be the actual flow regime in real-life scenarios, it is possible that turbulence is damped by the high viscosity of mud, thus making the flow laminar.

Finally, it is remarked that the new RANS model was calibrated and tested for pipe flows only, a relatively simple internal-flow problem. The applicability of the new model to complex external flows, such as the flow around a ship, still requires further investigations.

## 7.3. RECOMMENDATIONS AND FUTURE DIRECTIONS

### 7.3.1. BEYOND THE BINGHAM/HERSCHEL-BULKLEY MODEL

#### GNF MODELS

Investigating the effects of the Bingham yield stress on the ships' forces is already an important step towards a better understanding of the ship-mud interaction. However, it may turn out in the future that the Herschel-Bulkley model is not sufficiently accurate to describe the rheology of certain types of mud. In this case, possible GNF models are Tscheuschner [117], Worrall-Tuliani [182] and the two-step yielding model of Shakeel et al. [149]. The verification procedure would be straightforward for these models as the same manufactured solutions can be used. One would only need to find the RHS source terms associated with the new constitutive equation.

#### THIXOTROPY

In case thixotropy needs to be modelled, a first step could be to modify the Herschel-Bulkley model by expressing the yield stress as $\tau_0 = \lambda\tau_y$, where $\lambda$ is a scalar between 0 and 1 that indicates the degree of structure in the fluid, whereas $\tau_y$ is the maximum yield stress corresponding to the fully structured fluid ($\lambda = 1$). This type of thixotropic models belongs to the class of 'structural kinetics models', where shear history effects are taken into account by the structural parameter $\lambda$. Thus, at least another additional transport equation for $\lambda$ needs to be implemented. For more advanced models of this type, the one proposed by Houska [73] and Toorman [164] could be considered.

Note that the mud flow curve for these thixotropic models will be bounded by two curves, one upper curve corresponding to the highest degree of structure ($\lambda = 1$), and one lower curve representing a completely 'fluidised' mud ($\lambda = 0$). Thus, a first estimate of the effect of thixotropy could be obtained by performing CFD simulations with two different non-thixotropic mud conditions that follow the upper and lower curve, respectively. It is then reasonable to expect that the results obtained with a thixotropic model would fall in between these two cases. If the difference between these two cases is sufficiently small, thixotropy effects are expected to be small as well. Previous CFD simulations of thixotropic Bingham flows around a cylinder at a fixed Reynolds number of 45 confirmed such expectation (Syrakos et al. [161]), although some exceptions have been observed at higher Reynolds numbers and with low yield stress (Bui and Ho [23]).

The MMS procedure presented in Chapter 3 can also be applied to verify the implementation of thixotropic models, as done in Kim and Park [82]. Note that, in this case, a manufactured solution for $\lambda$ is required. In analogy with the tests on the flow around the sphere presented in Chapter 4, the flow solver could also be tested on the thixotropic flow around the cylinder, with the aim of reproducing the CFD results of Syrakos et al. [161].

Finally, it is remarked that when a ship hull is not in contact with mud (positive UKC), the maximum shear rate in the mud layer is expected to be rather small, at least much smaller than when the ship sails through the mud layer. Thus, in this case, considering the mud layer as a non-thixotropic fully-structured ($\lambda = 1$) fluid that mimic the un-remoulded behaviour may be a reasonable assumption to avoid the use of thixotropic models.

#### PROPERTIES GRADIENT AND IN-SITU DATA

An even further step is to include the variation of the mud properties with depth, thus allowing the simulation of different mud stratifications. It is however reminded that using more complex models may be rendered ineffective without accurate in-situ concentration profiles of the mud layer. Therefore, progress in non-intrusive monitoring techniques (see e.g. Ma et al. [103] and Buisman et al. [24]) to obtain accurate in-situ data will play a key role not only for monitoring the nautical bottom, but also to provide realistic initial and boundary conditions to the flow solver.

### 7.3.2. LAMINAR OR TURBULENT MUD FLOW?

Although RANS simulations of a ship sailing through Mud_23 predicted laminar flow in the mud layer near the hull (Section 6.8), it cannot be conclusively stated that this is physically correct because the tested RANS models are not supposed to capture the flow transition of Newtonian fluids, let alone the flow transition for non-Newtonian fluids. DNS investigations of the turbulent flow of yield-stress fluids over a flat plate for $\tau_B/\tau_w > 20\%$ would be an important step forward to elucidate on the transition from laminar to turbulent regime, beside helping to develop new RANS models. However, as DNS may still be prohibitive in the near future, even for simulating the flow over flat plate, Large-Eddy Simulations (LES) may be a possible step beyond RANS simulations as a trade-off between costs and accuracy (e.g. Molla and Paul [121], Ohta and Miyashita [128], and Basso et al. [13]).

Finally, laminar mud flow implies that, for navigation at low speed with negative UKC, the frictional resistance due to contact with the mud layer can be estimated with Eq. (5.21) or, more roughly, as the product of the yield stress and the surface area of the hull in contact with mud (Appendix C). Note, however, that as the ship's speed increases, the contact area between the hull and the mud layer is expected to reduce according to previous numerical studies [94, 78]. Therefore, such estimation may need to be revised at higher speeds, where the effects of the internal wave can become more important than the mere contact with the mud layer.

### 7.3.3. CHOICE OF THE REGULARISATION PARAMETER

The adoption of regularisation methods allows a straightforward implementation of yield-stress models in existing CFD solver without major modifications. One of the drawbacks of the regularisation approach, however, is that the CFD user is left with the arbitrary choice of the regularisation parameter, $m$, which can have a significant influence on the numerical solution, as it was observed in Chapters 4 and 5. This is especially true for laminar flows. Therefore, how to choose the regularisation parameter when simulating mud? Two possible approaches are identified.

#### IDEAL BINGHAM/HERSCHEL-BULKLEY BEHAVIOUR

One approach is to try to mimic the ideal Herschel-Bulkley model as closely as possible, hence using the largest possible value for $m$. A sensitivity analysis should be performed to ensure that the solution is somewhat $m$-independent, although this is not a trivial task. One issue is that the iterative solver may diverge before a sufficiently large $m$ is reached. The other issue is how to estimate the sensitivity to $m$. For example, one could double the regularisation parameter until negligible differences in the solution is observed. But increasing it by a factor 10 could still lead to substantial differences, so there is not a clear way to verify that the solution is $m$-independent. In absence of rigorous methods, one approach could be to use the same method used to estimate the discretisation uncertainties, as done in Chapters 4 and 5, thus using $1/m$ instead of the grid spacing. Our experience showed that choosing $m$ such that the ratio of maximum-to-minimum viscosity is about 10000-20000 provides a satisfactory approximation of the ideal Herschel-Bulkley behaviour, at least for a target application as depicted in Fig. 2.1.

The advantage of this approach is that the investigation will be more general because, whilst there are infinite possible regularised Bingham/Herschel-Bulkley models, the ideal Bingham/Herschel-Bulkley model is unique. The drawback would be that, since the viscosity of mud at zero shear rate is actually not infinite, the predicted viscous forces will likely be overestimated.

#### REALISTIC MUD BEHAVIOUR

The other approach consists in choosing values of $m$ that better capture the actual flow curve of a particular mud condition. This approach may be more suitable when the investigation concerns specific mud conditions for which the rheological characteristics are known. In this case, the regularisation parameter will most likely be lower than in the first approach, with the advantage that the convergence of the iterative solver will be less problematic. On the other hand, the determination of $m$ from the mud flow curves still leaves room for arbitrariness. Three options were given in Section 5.4.2. If one wants to mimic the behaviour of mud without having information about its flow curves, then selecting $m$ such that the maximum-to-minimum viscosity is around 1000 is a reasonable choice according to the findings in Chapter 5.

Finally, it should be born in mind that the regularisation parameter is not a physical parameter. Hence, if a more accurate description of the flow behaviour at low shear rate is needed, other models such as Tscheuschner [117] and Worrall-Tuliani [182] may be preferable.

### 7.3.4. FUTURE DIRECTIONS

Although numerical studies on ships navigation with muddy bottoms have been increasing in the past few years, there is still a long road ahead. In this dissertation, a bottom-up approach has been followed, where simplified problems have been studied in order to gain insights that can be used for the practical applications. This should now be accompanied by a top-down approach, where the CFD solver is applied to more realistic scenarios to gain insights about what needs to be improved in the CFD model.

#### RESISTANCE, MANOEUVRING COEFFICIENTS, SINKAGE AND TRIM

Even with a simple rheological like Herschel-Bulkley, there are now numerous aspects that are worth investigating at the current state of knowledge. Among them, one of the most compelling question concerns the link between the rheological properties of mud and the hydrodynamic forces acting on ships. This is not only interesting from the theoretical/academic perspective, but it will also provide useful insights for port authorities concerned with finding a trade-off between safe navigation and dredging costs.

Particularly interesting is the influence of the mud yield stress. Investigating the ships' resistance could be a good starting point before considering the full set of manoeuvring coefficients. A wide range of speeds should be studied in order to cover the subcritical, critical and supercritical range with respect to the internal wave. This is important because opposite trends may be observed depending on the range at which the ship is moving.

The ships' trim and sinkage are also important aspects for navigation in confined waters. However, in this case, the ship should be left free to move, thus either deforming or overset grids must be used in the CFD simulations. Note that in this case the air-water free surface cannot be neglected, therefore the computational costs will increase substantially.

### SCALE EFFECTS

Ideally, CFD simulations should be performed with a wall-resolved grid (i.e. without using wall functions) and at full scale. This is because neither the effect of using wall functions in the mud layer nor the scaling effects are yet known. However, the computational power required for these simulations can be onerous, especially for navigation with non-zero drift angles, where the symmetry of the problem can no longer be exploited and the full domain must be modelled. Furthermore, the presence of the mud layer increases the number of parameters to be investigated (e.g. rheological properties, density ratio, layer thickness, etc.), leading to a potentially enormous amount of test cases to be simulated.

It is therefore recommended to study which simplification can be applied to save computational resources. Two very important simplifications are certainly the use of wall functions and the possibility to carry out the numerical simulations at model scale. For the latter, two main research questions are identified: at what scale do the scaling effects become negligible? What are the scaling laws that allow extrapolating the results to full-scale?

The second question will be more difficult to answer as it shall require good knowledge of the underlying physics, especially with respect to the effects of the non-Newtonian rheology on the hydrodynamic forces. The second question will also be interesting for extrapolating results from ship-model tests to full scale. Probably a differentiation must be made between situations at high and low speeds, and between positive and negative UKC. In fact, at low speed with negative UKC, the effect of the rheological properties are expected to dominate, whereas at higher speeds the (densimetric) Froude number associated to the mud undulation is expected to be more influential.

### NEWTONIAN MUD

Another possible simplification concerns the rheological model. Whilst it is possible that more advanced models than Herschel-Bulkley will be required, it is also possible that the non-Newtonian properties of mud are of minor importance in some navigation scenarios. For instance, considering a highly viscous Newtonian mud may be acceptable for the cases where the ship does not directly shear the mud layer, i.e. with positive UKC. In fact, in this cases, the shear rate in the mud is expected to be rather low, as it is just caused by the ship-induced undulations. Limited viscosity variations are thus expected within the flow. But what value should be used for the Newtonian viscosity? A possible candidate is the maximum apparent viscosity of the Bingham model. In case of the Papanastasiou regularisation, the maximum viscosity is $\tau_0 \cdot m$, where $\tau_0$ and $m$ are the yield stress and the regularisation parameter, respectively. While this simplification may be too crude, it could nevertheless be applied to reduce the number of parameters to investigate. After all, the mud layer has already been modelled as a Newtonian fluid in the previous CFD study of Kaidi et al. [78], while also the work Leijs [94] showed a rather limited influence of the mud yield stress on the ship's resistance. This aspect needs to be clarified in future studies.

### PROPELLER-INDUCED TURBULENT MIXING

So far the focus has been on the hydrodynamic forces acting on the hull. However, the ships' controllability and manoeuvrability are the result of the combined action of the hull forces, the propeller and the rudder. Hence, a complete manoeuvring model requires also knowledge about the propeller and the rudder action with muddy bottoms.

An interesting research question to investigate is how the propeller efficiency changes in presence of a mud layer. It is remarked that accurate CFD predictions of the propeller characteristics are already quite challenging in case of water, thus the presence of mud will certainly add extra difficulties. To name one, in case of negative UKC, part of the mud is expected to be sucked by the propeller. Hence, for such cases, mud and water can probably no longer be assumed to be immiscible. A possible step in this direction is to use a mixture model approach (e.g. Goeree et al. [65], Ouda and Toorman [129], and Elerian et al. [55]), in which water and mud can mix and have a non-zero relative velocity.

### VALIDATION DATA

Finally, no matter how advanced a CFD model can be, obtaining reliable experimental data that can validate such model will be one of the major challenges for navigation with muddy bottoms. Experiments with scaled models of ships seem out of reach as ship model basins are reluctant to work with fluids other than water, although this may change in the future. For now, this leaves no other option than considering simplified problems, such as a plate (Chapter 5) or a cylinder [155] moving through mud. Nonetheless, in absence of anything else, even investigations on simplified problems can still provide useful insights for CFD developers.

Full-scale trials are even more challenging to conduct, and obtaining accurate measurements that can be used for validation of CFD simulations is a very difficult. Nevertheless, full-scale trials could shed some light on what to expect from CFD simulations. For instance, the RPM-speed curves could be measured when navigating above or through different types of mud layers. This could not only provide useful insights to pilots on how ships behave, but also confirm or dismiss expected phenomena such as the sharp increase of resistance associated to internal waves.

# BIBLIOGRAPHY

[1] H. R. Anbarlooei, D. O. Cruz, F. Ramos, C. M. Santos, and A. P. Silva Freire. "Phenomenological friction equation for turbulent flow of Bingham fluids". *Physical Review E* 96.2 (2017): 1–6. DOI: `10.1103/PhysRevE.96.023107` (cit. on p. 130).

[2] H. R. Anbarlooei, D. O. Cruz, F. Ramos, and A. P. Silva Freire. "Phenomenological Blasius-type friction equation for turbulent power-law fluid flows". *Physical Review E - Statistical, Nonlinear, and Soft Matter Physics* 92.6 (2015): 5–9. DOI: `10.1103/PhysRevE.92.063006` (cit. on pp. 120, 129, 132).

[3] H. Anbarlooei, D. Cruz, F. Ramos, C. Santos, and A. Silva Freire. "On the connection between Kolmogorov microscales and friction in pipe flows of viscoplastic fluids". *Physica D: Nonlinear Phenomena* 376-377 (2018): 69–77. DOI: `10.1016/j.physd.2017.11.005` (cit. on pp. 120, 130, 132).

[4] R. W. Ansley and T. N. Smith. "Motion of spherical particles in a Bingham plastic". *AIChE Journal* 13.6 (1967): 1193–1196. DOI: `10.1002/aic.690130629` (cit. on p. 46).

[5] A. S. Arabi and R. S. Sanders. "Particle terminal settling velocities in non-Newtonian viscoplastic fluids". *Canadian Journal of Chemical Engineering* 94.6 (2016): 1092–1101. DOI: `10.1002/cjce.22496` (cit. on p. 46).

[6] ASME PTC Committee. "Standard for Verification and Validation in Computational Fluid Dynamics and Heat Transfer: ASME V&V 20". *The American Society of Mechanical Engineers (ASME)* (2009). ISSN: 01604120 (cit. on pp. 61, 84).

[7] D. Atapattu, R. Chhabra, and P. Uhlherr. "Creeping sphere motion in Herschel-Bulkley fluids: flow field and drag". *Journal of Non-Newtonian Fluid Mechanics* 59.2-3 (1995): 245–265. DOI: `10.1016/0377-0257(95)01373-4` (cit. on p. 46).

[8] D. Atapattu, R. Chhabra, and P. Uhlherr. "Wall effect for spheres falling at small reynolds number in a viscoplastic medium". *Journal of Non-Newtonian Fluid Mechanics* 38.1 (1990): 31–42. ISSN: 03770257. DOI: `10.1016/0377-0257(90)85031-S` (cit. on p. 46).

[9] H. A. Barnes and K. Walters. “The yield stress myth?” *Rheologica Acta* 24.4 (1985): 323–326. ISSN: 0035-4511. DOI: `10.1007/BF01333960` (cit. on p. 19).

[10] R. Barth, C. van der Made, L. Bourgonjen, J. van Dijken, M. Vantorre, and J. Verwilligen. “Manoeuvring with negative underkeel clearance: 2nd full scale field test in the port of Delfzijl”. In: *4th MASHCON-International Conference on Ship Manoeuvring in Shallow and Confined Water with Special Focus on Ship Bottom Interaction.* 2016, 262–271 (cit. on p. 8).

[11] A. Bartosik. “Application of Rheological Models in Prediction of Turbulent Slurry Flow”. *Flow, Turbulence and Combustion* 84.2 (2010): 277–293. ISSN: 1386-6184. DOI: `10.1007/s10494-009-9234-y` (cit. on p. 108).

[12] A. Bartosik. “Modelling of a turbulent flow using the Herschel-Bulkley rheological model”. *Chemical and Process Engineering - Inzynieria Chemiczna i Procesowa* (2006). ISSN: 0208-6425 (cit. on p. 108).

[13] F. O. Basso, A. T. Franco, and D. B. Pitz. “Large-eddy simulation of turbulent pipe flow of Herschel-Bulkley fluids - Assessing subgrid-scale models”. *Computers & Fluids* 244.February (2022): 105522. ISSN: 00457930. DOI: `10.1016/j.compfluid.2022.105522` (cit. on p. 143).

[14] M. Beaulne and E. Mitsoulis. “Creeping motion of a sphere in tubes filled with Herschel–Bulkley fluids”. *Journal of Non-Newtonian Fluid Mechanics* 72.1 (1997): 55–71. DOI: `10.1016/S0377-0257(97)00024-4` (cit. on pp. 46, 52).

[15] A. N. Beris, J. A. Tsamopoulos, R. C. Armstrong, and R. A. Brown. “Creeping motion of a sphere through a Bingham plastic”. *Journal of Fluid Mechanics* 158 (1985): 219–244. DOI: `10.1017/S0022112085002622` (cit. on pp. 46, 48, 55, 56, 62).

[16] E. C. Bingham. “An investigation of the laws of plastic flow”. *Bulletin of the Bureau of Standards* 13.2 (1916). ISSN: 0096-8579. DOI: `10.6028/bulletin.304` (cit. on p. 21).

[17] J. Blackery and E. Mitsoulis. “Creeping motion of a sphere in tubes filled with a Bingham plastic material”. *Journal of Non-Newtonian Fluid Mechanics* 70.1-2 (1997): 59–77. DOI: `10.1016/S0377-0257(96)01536-4` (cit. on pp. 46, 52, 56).

[18] B. Blais and F. Bertrand. “On the use of the method of manufactured solutions for the verification of CFD codes for the volume-averaged Navier-Stokes equations”. *Computers & Fluids* 114 (2015): 121–129. DOI: `10.1016/j.compfluid.2015.03.002` (cit. on pp. 26, 42).

[19] G. van Bochove and L. Nederlof. “Vaargedrag van diepstekende schepen in slibrijke gebieden”. *De Ingenieur* 91.30/31 (1978): 525–530 (cit. on p. 8).

[20] B. J. Briscoe, M. Glaese, P. F. Luckham, and S. Ren. “The falling of spheres through Bingham fluids”. *Colloids and Surfaces* 65.1 (1992): 69–75. DOI: `10.1016/0166-6622(92)80176-3` (cit. on p. 46).

[21] C. Brossard, A. Delouis, P. Galichon, J. Granboulan, and P. Monadier. “Navigability in Channels Subject to Siltation Physical Scale Model Experiments”. In: *22nd International Coastal Engineering Conference, Delft, The Netherlands.* American Society of Civil Engineers, 1991, 3088–3101. DOI: `10.1061/9780872627765.236` (cit. on p. 7).

[22] J. Brouwer, J. Tukker, Y. Klinkenberg, and M. van Rijsbergen. “Random uncertainty of statistical moments in testing: Mean”. *Ocean Engineering* 182 (2019): 563–576. DOI: `10.1016/j.oceaneng.2019.04.068` (cit. on p. 72).

[23] C. M. Bui and T. X. Ho. “Numerical study of an unsteady flow of thixotropic liquids past a cylinder”. *AIP Advances* 9.11 (2019): 115002. DOI: `10.1063/1.5125731` (cit. on p. 143).

[24] M. Buisman, E. Martuganova, T. Kiers, D. Draganov, and A. Kirichek. “Continuous monitoring of the depth of the water-mud interface using distributed acoustic sensing”. *Journal of Soils and Sediments* (2022). DOI: `10.1007/s11368-022-03202-2` (cit. on p. 143).

[25] G. R. Burgos, A. N. Alexandrou, and V. Entov. “On the determination of yield surfaces in Herschel–Bulkley fluids”. *Journal of Rheology* 43.3 (1999): 463–483. DOI: `10.1122/1.550992` (cit. on p. 53).

[26] A. Busch and S. T. Johansen. “Cuttings transport: On the effect of drill pipe rotation and lateral motion on the cuttings bed”. *Journal of Petroleum Science and Engineering* (2020). DOI: `10.1016/j.petrol.2020.107136` (cit. on p. 107).

[27] M. Carrozza, M. Hulsen, and P. Anderson. “Benchmark solutions for flows with rheologically complex interfaces”. *Journal of Non-Newtonian Fluid Mechanics* (2020). DOI: `10.1016/j.jnnfm.2020.104436` (cit. on p. 26).

[28] I.-C. Chan and P. L.-F. Liu. “Responses of Bingham-plastic muddy seabed to a surface solitary wave”. *Journal of Fluid Mechanics* 618 (2009): 155–180. DOI: `10.1017/S0022112008004357` (cit. on p. 66).

[29] R. Chhabra. *Bubbles, Drops, and Particles in Non-Newtonian Fluids.* CRC Press, 2006. DOI: `10.1201/9781420015386` (cit. on pp. 46, 64).

[30] R. P. Chhabra and J. F. Richardson. *Non-Newtonian Flow and Applied Rheology.* Elsevier, 2008, 536. DOI: `10.1016/B978-0-7506-8532-0.X0001-7` (cit. on pp. 22, 97).

[31] A. Choudhary, C. J. Roy, J.-F. Dietiker, M. Shahnam, R. Garg, and J. Musser. “Code verification for multiphase flows using the method of manufactured solutions”. *International Journal of Multiphase Flow* 80 (2016): 150–163. DOI: `10.1016/j.ijmultiphaseflow.2015.12.006` (cit. on p. 26).

[32] P. Coussot and J. M. Piau. “On the behavior of fine mud suspensions”. *Rheologica Acta* 33.3 (1994): 175–184. DOI: `10.1007/BF00437302` (cit. on pp. 21, 66).

[33] P. Coussot. *Mudflow Rheology and Dynamics.* Routledge, 2017. DOI: `10.1201/9780203746349` (cit. on p. 18).

[34] K. van Craenenbroeck, M. Vantorre, and P. De Wolf. “Navigation in muddy areas: establishing the navigate depth in the port of Zeebrugge”. In: *CEDA-PIANC Conference.* PIANC. 1992 (cit. on p. 8).

[35] D. Cruz and F. Pinho. “Turbulent pipe flow predictions with a low Reynolds number k–$\epsilon$ model for drag reducing fluids”. *Journal of Non-Newtonian Fluid Mechanics* 114.2-3 (2003): 109–148. DOI: `10.1016/S0377-0257(03)00119-8` (cit. on p. 108).

[36] D. Cruz, F. Pinho, and P. Resende. “Modelling the new stress for improved drag reduction predictions of viscoelastic pipe flow”. *Journal of Non-Newtonian Fluid Mechanics* 121.2-3 (2004): 127–141. DOI: `10.1016/j.jnnfm.2004.05.004` (cit. on p. 108).

[37] G. Dazhi and R. Tanner. “The drag on a sphere in a power-law fluid”. *Journal of Non-Newtonian Fluid Mechanics* 17.1 (1985): 1–12. DOI: `10.1016/0377-0257(85)80001-X` (cit. on p. 46).

[38] G. Delefortrie, M. Vantorre, and K. Eloot. “Modelling navigation in muddy areas through captive model tests”. *Journal of Marine Science and Technology* 10.4 (2005): 188–202. DOI: `10.1007/s00773-005-0210-5` (cit. on p. 7).

[39] G. Delefortrie, M. Vantorre, E. Verzhbitskaya, and K. Seynaeve. “Evaluation of Safety of Navigation in Muddy Areas through Real-Time Maneuvering Simulation”. *Journal of Waterway, Port, Coastal, and Ocean Engineering* 133.2 (2007): 125–135. DOI: `10.1061/(ASCE)0733-950X(2007)133:2(125)` (cit. on p. 12).

[40] *Deltares, Water and Soil Flume.* `https://www.deltares.nl/en/facilities/water-soil-flume` (cit. on p. 67).

[41] S. D. Dhole, R. P. Chhabra, and V. Eswaran. “Flow of power-law fluids past a sphere at intermediate Reynolds numbers”. *Industrial & Engineering Chemistry Research* 45.13 (2006): 4773–4781. DOI: `10.1021/ie0512744` (cit. on pp. 46, 56, 60–62).

[42] L. Doctors. “The influence of a bottom mud layer on the steady-state hydrodynamics of marine vehicles”. In: *21st Symposium on Naval Hydrodynamics*. National Academies Press. 1996, 727–742 (cit. on p. 7).

[43] K. Duraisamy, J. D. Baeder, and J. G. Liu. “Concepts and Application of Time-Limiters to High Resolution Schemes”. *Journal of Scientific Computing* (2003). DOI: `10.1023/A:1025395707090` (cit. on p. 36).

[44] P. A. Durbin. “Separated flow computations with the k-epsilon-v-squared model”. *AIAA Journal* 33.4 (1995): 659–664. DOI: `10.2514/3.12628` (cit. on p. 108).

[45] N. Q. Dzuy and D. V. Boger. “Direct Yield Stress Measurement with the Vane Method”. *Journal of Rheology* 29.3 (1985): 335–347. DOI: `10.1122/1.549794` (cit. on pp. 52, 86).

[46] L. Eça and M. Hoekstra. “A procedure for the estimation of the numerical uncertainty of CFD calculations based on grid refinement studies”. *Journal of Computational Physics* 262 (2014): 104–130. DOI: `10.1016/j.jcp.2014.01.006` (cit. on pp. 49, 50, 79, 81, 118).

[47] L. Eça and M. Hoekstra. “Evaluation of numerical error estimation based on grid refinement studies with the method of the manufactured solutions”. *Computers & Fluids* 38.8 (2009): 1580–1591. ISSN: 00457930. DOI: `10.1016/j.compfluid.2009.01.003` (cit. on pp. 54, 79).

[48] L. Eça and M. Hoekstra. “The numerical friction line”. *Journal of Marine Science and Technology* 13.4 (2008): 328–345. DOI: `10.1007/s00773-008-0018-1` (cit. on p. 130).

[49] L. Eça, F. S. Pereira, and G. Vaz. “Viscous flow simulations at high Reynolds numbers without wall functions: Is $y^+ \simeq 1$ enough for the near-wall cells?” *Computers & Fluids* 170 (2018): 157–175. DOI: `10.1016/j.compfluid.2018.04.035` (cit. on pp. 117, 118).

[50] L. Eça, G. Vaz, S. L. Toxopeus, and M. Hoekstra. “Numerical Errors in Unsteady Flow Simulations”. *Journal of Verification, Validation and Uncertainty Quantification* 4.2 (2019). DOI: `10.1115/1.4043975` (cit. on pp. 27, 29).

[51] L. Eça, C. M. Klaij, G. Vaz, M. Hoekstra, and F. S. Pereira. “On code verification of RANS solvers”. *Journal of Computational Physics* 310 (2016): 418–439. DOI: `10.1016/j.jcp.2016.01.002` (cit. on pp. 26, 28, 29, 31, 33–35, 42).

[52] L. Eça, M. Hoekstra, A. Hay, and D. Pelletier. “Verification of RANS solvers with manufactured solutions”. *Engineering with Computers* 23.4 (2007): 253–270. DOI: `10.1007/s00366-007-0067-9` (cit. on p. 26).

[53] H. Eda, R. Falls, and D. A. Walden. *Ship maneuvering safety studies.* Tech. rep. 1979 (cit. on p. 5).

[54] V. W. Ekman. “On dead water”. *Norwegian North Polar Expedition, 1893-1896* (1904): 1–150 (cit. on p. 6).

[55] M. Elerian, C. van Rhee, and R. Helmons. “Experimental and Numerical Modelling of Deep-Sea-Mining-Generated Turbidity Currents”. *Minerals* 12.5 (2022). DOI: `10.3390/min12050558` (cit. on p. 147).

[56] K. R. J. Ellwood, G. C. Georgiou, T. C. Papanastasiou, and J. O. Wilkes. “Laminar jets of Bingham-plastic liquids”. *Journal of Rheology* 34.6 (1990): 787–812. DOI: `10.1122/1.550144` (cit. on pp. 52, 86).

[57] Eurostat. *International trade in goods by mode of transport.* `https://ec.europa.eu/eurostat/statistics-explained/index.php?title=International_trade_in_goods_by_mode_of_transport` (cit. on p. 2).

[58] L. Ko-Fei and C. C. Mei. “Long waves in shallow water over a layer of bingham-plastic fluid-mud—I. Physical aspects”. *International Journal of Engineering Science* 31.1 (1993): 125–144. DOI: `10.1016/0020-7225(93)90070-B` (cit. on p. 66).

[59] J. H. Ferziger, M. Perić, and R. L. Street. *Computational Methods for Fluid Dynamics.* Springer International Publishing, 2020. ISBN: 978-3-319-99691-2. DOI: `10.1007/978-3-319-99693-6` (cit. on p. 23).

[60] A. Filali, L. Khezzar, and E. Mitsoulis. “Some experiences with the numerical simulation of Newtonian and Bingham fluids in dip coating”. *Computers & Fluids* 82 (2013): 110–121. DOI: `10.1016/j.compfluid.2013.04.024` (cit. on p. 39).

[61] I. A. Frigaard and C. Nouar. “On the usage of viscosity regularisation methods for visco-plastic fluid flow computation”. *Journal of Non-Newtonian Fluid Mechanics* 127.1 (2005): 1–26. DOI: `10.1016/j.jnnfm.2005.01.003` (cit. on p. 53).

[62] Z. Gao, H. Yang, and M. Xie. “Computation of Flow around Wigley Hull in Shallow Water with Muddy Seabed”. *Journal of Coastal Research* 73 (2015): 490–495. DOI: `10.2112/SI73-086.1` (cit. on pp. 9, 11, 21, 66, 107).

[63] A. A. Gavrilov, K. A. Finnikov, and E. V. Podryabinkin. “Modeling of steady Herschel–Bulkley fluid flow over a sphere”. *Journal of Engineering Thermophysics* 26.2 (2017): 197–215. DOI: `10.1134/S1810232817020060` (cit. on pp. 46, 52, 55, 56, 60–62).

[64] A. A. Gavrilov and V. Y. Rudyak. “Reynolds-averaged modeling of turbulent flows of power-law fluids”. *Journal of Non-Newtonian Fluid Mechanics* 227 (2016): 45–55. DOI: `10.1016/j.jnnfm.2015.11.006` (cit. on pp. 108, 112, 114, 125, 135).

[65] J. C. Goeree, G. H. Keetels, E. A. Munts, H. H. Bugdayci, and C. van Rhee. “Concentration and velocity profiles of sediment-water mixtures using the drift flux model”. *The Canadian Journal of Chemical Engineering* 94.6 (2016): 1048–1058. DOI: `10.1002/cjce.22491` (cit. on p. 147).

[66] F. Gori and A. Boghi. “A three dimensional exact equation for the turbulent dissipation rate of Generalised Newtonian Fluids”. *International Communications in Heat and Mass Transfer* 39.4 (2012): 477–485. ISSN: 07351933. DOI: `10.1016/j.icheatmasstransfer.2012.02.010` (cit. on pp. 110, 112).

[67] D. Graham and T. Jones. “Settling and transport of spherical particles in power-law fluids at finite Reynolds number”. *Journal of Non-Newtonian Fluid Mechanics* 54.C (1994): 465–488. DOI: `10.1016/0377-0257(94)80037-5` (cit. on p. 46).

[68] M. Grasinger, S. Overacker, and J. Brigham. “Numerical investigation of the accuracy, stability, and efficiency of lattice Boltzmann methods in simulating non-Newtonian flow”. *Computers & Fluids* 166 (2018): 253–274. DOI: `10.1016/j.compfluid.2018.02.008` (cit. on p. 26).

[69] B. Güzel, T. Burghelea, I. A. Frigaard, and D. M. Martinez. “Observation of laminar–turbulent transition of a yield stress fluid in Hagen–Poiseuille flow”. *Journal of Fluid Mechanics* 627 (2009): 97–128. DOI: `10.1017/S0022112009005813` (cit. on p. 121).

[70] A. Hajivand and S. H. Mousavizadegan. “Virtual maneuvering test in CFD media in presence of free surface”. *International Journal of Naval Architecture and Ocean Engineering* 7.3 (2015): 540–558. DOI: `10.1515/ijnaoe-2015-0039` (cit. on p. 12).

[71] W. H. Herschel and R. Bulkley. “Konsistenzmessungen von Gummi-Benzollösungen”. *Kolloid-Zeitschrift* 39.4 (1926). ISSN: 0303402X. DOI: `10.1007/BF01432034` (cit. on p. 21).

[72] C. Hirt and B. Nichols. “Volume of fluid (VOF) method for the dynamics of free boundaries”. *Journal of Computational Physics* 39.1 (1981): 201–225. DOI: `10.1016/0021-9991(81)90145-5` (cit. on p. 17).

[73] M. Houska. *Engineering Aspects of the Rheology of Thixotrpic Liquids.* PhD Thesis, Czech Technical University of Prague, Prague, Czech Republic, 1981 (cit. on p. 142).

[74] G. Iaccarino, E. S. Shaqfeh, and Y. Dubief. "Reynolds-averaged modeling of polymer drag reduction in turbulent flows". *Journal of Non-Newtonian Fluid Mechanics* 165.7-8 (2010): 376–384. DOI: `10.1016/j.jnnfm.2010.01.013` (cit. on p. 108).

[75] International Organization for Standardization (ISO). Guide to the expression of uncertainty in measurement. 1995 (cit. on p. 72).

[76] F. Irgens. *Rheology and Non-Newtonian Fluids.* Cham: Springer International Publishing, 2014, 1–190. DOI: `10.1007/978-3-319-01053-3` (cit. on p. 22).

[77] F. Jiang and A. J. Mehta. "Some observations on fluid mud response to water waves". In: *Dynamics and exchanges in estuaries and the coastal zone.* 1992, 351–376. URL: `https://agupubs.onlinelibrary.wiley.com/doi/abs/10.1029/CE040p0351` (cit. on p. 66).

[78] S. Kaidi, E. Lefrançois, and H. Smaoui. "Numerical modelling of the muddy layer effect on Ship's resistance and squat". *Ocean Engineering* 199 (2020): 106939. DOI: `10.1016/j.oceaneng.2020.106939` (cit. on pp. 9, 11, 66, 107, 144, 147, 181).

[79] T. Katsui. "The proposal of a new friction line". In: *Fifth Osaka colloquium on advanced CFD applications to ship flow and hull form design, Osaka, Japan.* 2005 (cit. on p. 134).

[80] N. S. Kelly, H. S. Gill, A. N. Cookson, and K. H. Fraser. "Influence of Shear-Thinning Blood Rheology on the Laminar-Turbulent Transition over a Backward Facing Step". *Fluids* 5.2 (2020): 57. DOI: `10.3390/fluids5020057` (cit. on p. 107).

[81] T. van Kessel and C. Blom. "Rheology of cohesive sediments: comparison between a natural and an artificial mud". *Journal of Hydraulic Research* 36.4 (1998): 591–612. DOI: `10.1080/00221689809498611` (cit. on p. 66).

[82] J. Kim and J. D. Park. "The non-homogeneous flow of a thixotropic fluid around a sphere". *Applied Mathematical Modelling* 82 (2020): 848–866. DOI: `10.1016/j.apm.2020.02.009` (cit. on pp. 26, 143).

[83] N. Kim and J. Reddy. "3-D least-squares finite element analysis of flows of generalized Newtonian fluids". *Journal of Non-Newtonian Fluid Mechanics* 266 (2019): 143–159. DOI: `10.1016/j.jnnfm.2019.03.004` (cit. on p. 26).

[84] A. Kirichek, C. Chassagne, H. Winterwerp, and T. Vellinga. "How navigable are fluid mud layers". *Terra et Aqua* 151.Summer (2018): 6–18 (cit. on p. 67).

[85] C. M. Klaij, M. Hoekstra, and G. Vaz. "Design, analysis and verification of a volume-of-fluid model with interface-capturing scheme". *Computers & Fluids* 170 (2018): 324–340. DOI: `10.1016/j.compfluid.2018.05.016` (cit. on pp. 30, 35, 36, 40, 42, 76, 171).

[86] C. M. Klaij and C. Vuik. "SIMPLE-type preconditioners for cell-centered, colocated finite volume discretization of incompressible Reynolds-averaged Navier-Stokes equations". *International Journal for Numerical Methods in Fluids* 71.7 (2013): 830–849. DOI: `10.1002/fld.3686` (cit. on p. 23).

[87] D. Knoch and A. Malcherek. "A numerical model for simulation of fluid mud with different rheological behaviors". *Ocean Dynamics* 61.2-3 (2011): 245–256. DOI: `10.1007/s10236-010-0327-x` (cit. on p. 66).

[88] P. Knupp. *Verification of Computer Codes in Computational Science and Engineering*. Chapman and Hall/CRC, 2002. DOI: `10.1201/9781420035421` (cit. on pp. 26, 31).

[89] K. Koziol and P. Glowacki. "Determination of the free settling parameters of spherical particles in power law fluids". *Chemical Engineering and Processing: Process Intensification* 24.4 (1988): 183–188. DOI: `10.1016/0255-2701(88)85001-3` (cit. on p. 46).

[90] C. K. Lam and K. Bremhorst. "A modified form of the k-$\epsilon$ model for predicting wall turbulence". *Journal of Fluids Engineering, Transactions of the ASME* (1981). DOI: `10.1115/1.3240815` (cit. on p. 108).

[91] L. Larsson and H. C. Raven. *Ship Resistance and Flow*. 2010. ISBN: 978-0-939773-76-3 (cit. on pp. 35, 76).

[92] B. E. Launder, G. J. Reece, and W. Rodi. "Progress in the development of a Reynolds-stress turbulence closure". *Journal of Fluid Mechanics* (1975). DOI: `10.1017/S0022112075001814` (cit. on p. 108).

[93] B. van Leer. "Towards the ultimate conservative difference scheme. V. A second-order sequel to Godunov's method". *Journal of Computational Physics* 32.1 (1979): 101–136. DOI: `10.1016/0021-9991(79)90145-1` (cit. on pp. 30, 118, 171).

[94] K. Leijs. *CFD simulations of the flow around a tanker in shallow water with muddy seabed*. MSc Thesis, Delft University of Technology, Delft, The Netherlands, 2021. URL: `http://resolver.tudelft.nl/uuid:a7c7e1ae-e7f0-4e15-9a03-0901af9e8959` (cit. on pp. 144, 147, 181).

[95] S. Lemaire and M. Klapwijk. *pyTST*. 2021. URL: `https://doi.org/10.5281/zenodo.4428158` (cit. on p. 72).

[96] B. T. Liu, S. J. Muller, and M. M. Denn. “Convergence of a regularization method for creeping flow of a Bingham material about a rigid sphere”. *Journal of Non-Newtonian Fluid Mechanics* 102.2 (2002): 179–191. DOI: `10.1016/S0377-0257(01)00177-X` (cit. on pp. 53, 62).

[97] K. Liu and C. C. Mei. “Effects of wave-induced friction on a muddy seabed modelled as a Bingham-plastic fluid”. *Journal of Coastal Research* 5.4 (1989): 777–789. ISSN: 07490208 (cit. on pp. 66, 106).

[98] S. Lovato, G. H. Keetels, S. L. Toxopeus, and J. W. Settels. “An eddy-viscosity model for turbulent flows of Herschel–Bulkley fluids”. *Journal of Non-Newtonian Fluid Mechanics* 301 (2022): 104729. DOI: `10.1016/j.jnnfm.2021.104729` (cit. on p. 105).

[99] S. Lovato, A. Kirichek, S. L. Toxopeus, J. W. Settels, and G. H. Keetels. “Validation of the resistance of a plate moving through mud: CFD modelling and towing tank experiments”. *Ocean Engineering* 258 (2022): 111632. DOI: `10.1016/j.oceaneng.2022.111632` (cit. on p. 65).

[100] S. Lovato, G. Vaz, S. L. Toxopeus, G. H. Keetels, and J. W. Settels. “Code Verification exercise for 2D Poiseuille flow with non-Newtonian fluid”. In: *Numerical Towing Tank Symposium (NuTTS)*. 2018. URL: `https://research.tudelft.nl/files/71826136/Lovato_2018_Code_Verification_exercise_for_2D_Poiseuille_flow_with_non_Newtonian_fluid.pdf` (cit. on p. 26).

[101] S. Lovato, S. L. Toxopeus, J. W. Settels, G. H. Keetels, and G. Vaz. “Code Verification of Non-Newtonian Fluid Solvers for Single- and Two-Phase Laminar Flows”. *Journal of Verification, Validation and Uncertainty Quantification* 6.2 (2021). DOI: `10.1115/1.4050131` (cit. on pp. 25, 27, 44, 54).

[102] S. Lovato, S. L. Toxopeus, J. W. Settels, and G. H. Keetels. “Application of a maritime CFD code to a benchmark problem for non-Newtonian fluids: the flow around a sphere”. *International Shipbuilding Progress* 70.1 (2022): 1–25. DOI: `10.3233/ISP-220002` (cit. on p. 45).

[103] X. Ma, A. Kirichek, K. Heller, and D. Draganov. “Estimating P- and S-Wave Velocities in Fluid Mud Using Seismic Interferometry”. *Frontiers in Earth Science* 10 (2022). DOI: `10.3389/feart.2022.806721` (cit. on p. 143).

[104] M. R. Malin. “Turbulent pipe flow of Herschel-Bulkley fluids”. *International Communications in Heat and Mass Transfer* (1998). DOI: `10.1016/S0735-1933(98)00019-0` (cit. on p. 108).

[105] M. Malin. “Turbulent pipe flow of power-law fluids”. *International Communications in Heat and Mass Transfer* 24.7 (1997): 977–988. DOI: `10.1016/S0735-1933(97)00083-3` (cit. on p. 108).

[106] M. Masoudian, K. Kim, F. Pinho, and R. Sureshkumar. “A Reynolds stress model for turbulent flow of homogeneous polymer solutions”. *International Journal of Heat and Fluid Flow* 54 (2015): 220–235. DOI: `10.1016/j.ijheatfluidflow.2015.05.017` (cit. on p. 108).

[107] *Maxima, a Computer Algebra System. Version 5.37.2.* http://maxima.sourceforge.net/. URL: `http://maxima.sourceforge.net/` (cit. on p. 27).

[108] W. H. McAnally et al. “Management of Fluid Mud in Estuaries, Bays, and Lakes. II: Measurement, Modeling, and Management”. *Journal of Hydraulic Engineering* 133.1 (2007). ISSN: 0733-9429 (cit. on p. 3).

[109] M. McBride. “Harbour approach channels - Design guidelines”. *PIANC Report No. 121* (2014) (cit. on pp. 2, 66, 67).

[110] A. J. Mehta. *An introduction to hydraulics of fine sediment transport.* Vol. 38. World Scientific Publishing Company, 2013 (cit. on p. 18).

[111] D. Mehta, A. K. Thota Radhakrishnan, J. B. van Lier, and F. H. Clemens. “Assessment of numerical methods for estimating the wall shear stress in turbulent Herschel–Bulkley slurries in circular pipes”. *Journal of Hydraulic Research* (2020): 1–18. DOI: `10.1080/00221686.2020.1744751` (cit. on p. 107).

[112] C. C. Mei and K.-F. Liu. “A Bingham-Plastic Model for a muddy seabed under long waves”. *Journal of Geophysical Research* 92.C13 (1987): 14581. DOI: `10.1029/JC092iC13p14581` (cit. on p. 66).

[113] F. R. Menter, M. Kuntz, and R. Langtry. “Ten Years of Industrial Experience with the SST Turbulence Model Turbulence”. *Turbulence, Heat and Mass Transfer 4* (2003) (cit. on pp. 108–110, 116, 173).

[114] F. R. Menter. “Two-equation eddy-viscosity turbulence models for engineering applications”. *AIAA Journal* 32.8 (1994): 1598–1605. DOI: `10.2514/3.12149` (cit. on p. 118).

[115] F. R. Menter, Y. Egorov, and D. Rusch. “Steady and Unsteady Flow Modelling Using the $k-\sqrt{k}L$ Model”. In: *Proceedings of the International Symposium on Turbulence, Heat and Mass Transfer.* New York: Begellhouse, 2006, 403–406. DOI: `10.1615/ICHMT.2006.TurbulHeatMassTransf.800` (cit. on pp. 109, 116, 174).

[116] A. B. Metzner and J. C. Reed. “Flow of non-newtonian fluids—correlation of the laminar, transition, and turbulent-flow regions”. *AIChE Journal* 1.4 (1955): 434–440. DOI: `10.1002/aic.690010409` (cit. on p. 129).

[117] T. Mezger. *The Rheology Handbook*. Vincentz Network, 2020. DOI: 10.1515/9783748603702 (cit. on pp. 90, 142, 145).

[118] T. F. Miller and F. W. Schmidt. "Use of a pressure-weighted interpolation method for the solution of the incompressible navier-stokes equations on a nonstaggered grid system". *Numerical Heat Transfer* (1988). DOI: 10.1080/10407788808913641 (cit. on pp. 23, 40).

[119] K. A. Missirlis, D. Assimacopoulos, E. Mitsoulis, and R. P. Chhabra. "Wall effects for motion of spheres in power-law fluids". *Journal of Non-Newtonian Fluid Mechanics* 96.3 (2001): 459–471. DOI: 10.1016/S0377-0257(00)00189-0 (cit. on p. 46).

[120] E. Mitsoulis and J. Tsamopoulos. "Numerical simulations of complex yield-stress fluid flows". *Rheologica Acta* 56.3 (2017): 231–258. DOI: 10.1007/s00397-016-0981-0 (cit. on p. 22).

[121] M. M. Molla and M. C. Paul. "LES of non-Newtonian physiological blood flow in a model of arterial stenosis". *Medical Engineering and Physics* 34.8 (2012): 1079–1087. DOI: 10.1016/j.medengphy.2011.11.013 (cit. on p. 143).

[122] F. Moore. "The rheology of ceramic slip and bodies". *Trans. Brit. Ceram. Soc.* 58 (1959): 470–492 (cit. on p. 66).

[123] F. Nansen. *Farthest North: The epic adventure of a visionary explorer*. Skyhorse Publishing Inc., 2008 (cit. on p. 6).

[124] N. Nirmalkar, R. Chhabra, and R. Poole. "Laminar forced convection heat transfer from a heated square cylinder in a Bingham plastic fluid". *International Journal of Heat and Mass Transfer* 56.1-2 (2013): 625–639. DOI: 10.1016/j.ijheatmasstransfer.2012.08.049 (cit. on p. 97).

[125] N. Nirmalkar, R. P. Chhabra, and R. J. Poole. "Effect of Shear-Thinning Behavior on Heat Transfer from a Heated Sphere in Yield-Stress Fluids". *Industrial & Engineering Chemistry Research* 52.37 (2013): 13490–13504. ISSN: 0888-5885. DOI: 10.1021/ie402109k (cit. on pp. 46, 52, 55, 56, 61, 62).

[126] N. Nirmalkar, R. P. Chhabra, and R. J. Poole. "Numerical Predictions of Momentum and Heat Transfer Characteristics from a Heated Sphere in Yield-Stress Fluids". *Industrial & Engineering Chemistry Research* 52.20 (2013): 6848–6861. ISSN: 0888-5885. DOI: 10.1021/ie400703t (cit. on pp. 46, 52, 55, 56, 60–62).

[127] W. L. Oberkampf and C. J. Roy. *Verification and Validation in Scientific Computing*. Cambridge University Press, 2010. ISBN: 9780521113601. DOI: 10.1017/CBO9780511760396 (cit. on pp. 26, 27).

[128] T. Ohta and M. Miyashita. “DNS and LES with an extended Smagorinsky model for wall turbulence in non-Newtonian viscous fluids”. *Journal of Non-Newtonian Fluid Mechanics* 206 (2014): 29–39. DOI: `10.1016/j.jnnfm.2014.02.003` (cit. on p. 143).

[129] M. Ouda and E. A. Toorman. “Development of a new multiphase sediment transport model for free surface flows”. *International Journal of Multiphase Flow* 117 (2019): 81–102. DOI: `10.1016/j.ijmultiphaseflow.2019.04.023` (cit. on p. 147).

[130] T. C. Papanastasiou. “Flows of Materials with Yield”. *Journal of Rheology* 31.5 (1987): 385–404. DOI: `10.1122/1.549926` (cit. on p. 22).

[131] J. Peixinho, C. Nouar, C. Desaubry, and B. Théron. “Laminar transitional and turbulent flow of yield stress fluid in a pipe”. *Journal of Non-Newtonian Fluid Mechanics* 128.2-3 (2005): 172–184. DOI: `10.1016/j.jnnfm.2005.03.008` (cit. on p. 121).

[132] F. Pereira, L. Eça, and G. Vaz. “Verification and Validation exercises for the flow around the KVLCC2 tanker at model and full-scale Reynolds numbers”. *Ocean Engineering* 129.October 2016 (2017): 133–148. ISSN: 00298018. DOI: `10.1016/j.oceaneng.2016.11.005` (cit. on p. 130).

[133] F. Pinho. “A GNF framework for turbulent flow models of drag reducing fluids and proposal for a k–$\epsilon$ type closure”. *Journal of Non-Newtonian Fluid Mechanics* 114.2-3 (2003): 149–184. DOI: `10.1016/S0377-0257(03)00120-4` (cit. on p. 108).

[134] F. T. Pinho, C. F. Li, B. A. Younis, and R. Sureshkumar. “A low Reynolds number turbulence closure for viscoelastic fluids”. *Journal of Non-Newtonian Fluid Mechanics* 154.2-3 (2008): 89–108. DOI: `10.1016/j.jnnfm.2008.02.008` (cit. on p. 108).

[135] S. B. Pope. *Turbulent Flows.* Cambridge University Press, 2000. DOI: `10.1017/CBO9780511840531` (cit. on p. 17).

[136] P. R. Resende, F. T. Pinho, B. A. Younis, K. Kim, and R. Sureshkumar. “Development of a low-Reynolds-number k-$\omega$ model for FENE-P fluids”. *Flow, Turbulence and Combustion* 90.1 (2013): 69–94. DOI: `10.1007/s10494-012-9424-x` (cit. on p. 108).

[137] P. Resende, K. Kim, B. Younis, R. Sureshkumar, and F. Pinho. “A FENE-P k–$\epsilon$ turbulence model for low and intermediate regimes of polymer-induced drag reduction”. *Journal of Non-Newtonian Fluid Mechanics* 166.12-13 (2011): 639–660. DOI: `10.1016/j.jnnfm.2011.02.012` (cit. on p. 108).

[138] P. J. Roache. *Fundamentals of Verification and Validation*. Hermosa Publishers, Albuquerque, New Mexico, 2009 (cit. on p. 28).

[139] P. J. Roache. “Code Verification by the Method of Manufactured Solutions”. *Journal of Fluids Engineering* 124.1 (2002): 4–10. DOI: `10.1115/1.1436090` (cit. on pp. 26, 27, 31).

[140] P. J. Roache. “Verification and Validation in Computational Science and Engineering, Hermosa Publishers, New Mexico” (1998): 107–240 (cit. on p. 26).

[141] M. Rudman and H. Blackburn. “Direct numerical simulation of turbulent non-Newtonian flow using a spectral element method”. *Applied Mathematical Modelling* 30.11 (2006): 1229–1248. DOI: `10.1016/j.apm.2006.03.005` (cit. on p. 121).

[142] K. Salari and P. Knupp. “Code Verification by the Method of Manufactured Solutions”. Technical report.SAND2000-1444 (2000). DOI: `10.2172/759450` (cit. on pp. 31, 42).

[143] M. Sano and Y. Kunitake. “Numerical solution for a ship-wave problem in a two-layer fluid using a double-model linearised interface condition”. *Ships and Offshore Structures* 13.3 (2018): 293–302. DOI: `10.1080/17445302.2017.1371391` (cit. on pp. 9–11, 20, 66).

[144] P. Saramito and A. Wachs. “Progress in numerical simulation of yield stress fluid flows”. *Rheologica Acta* 56.3 (2017): 211–230. DOI: `10.1007/s00397-016-0985-9` (cit. on p. 22).

[145] R. Sellmeijer and G. van Oortmerssen. “The effect of mud on tanker manoeuvres”. *Royal Institution of Naval Architects Transactions* 126 (1984) (cit. on pp. 7–9).

[146] A. Shakeel, A. Kirichek, and C. Chassagne. “Effect of pre-shearing on the steady and dynamic rheological properties of mud sediments”. *Marine and Petroleum Geology* 116 (2020): 104338. DOI: `10.1016/j.marpetgeo.2020.104338` (cit. on pp. 18, 66).

[147] A. Shakeel, A. Kirichek, and C. Chassagne. “Rheological analysis of mud from Port of Hamburg, Germany”. *Journal of Soils and Sediments* 20.6 (2020): 2553–2562. DOI: `10.1007/s11368-019-02448-7` (cit. on p. 66).

[148] A. Shakeel, A. Kirichek, and C. Chassagne. “Rheological analysis of natural and diluted mud suspensions”. *Journal of Non-Newtonian Fluid Mechanics* 286 (2020): 104434. DOI: `10.1016/j.jnnfm.2020.104434` (cit. on p. 102).

[149] A. Shakeel, A. Kirichek, A. Talmon, and C. Chassagne. "Rheological analysis and rheological modelling of mud sediments: What is the best protocol for maintenance of ports and waterways?" *Estuarine, Coastal and Shelf Science* 257 (2021): 107407. DOI: `10.1016/j.ecss.2021.107407` (cit. on pp. 66, 71, 142).

[150] *SIMMAN 2008: Workshop on Verification and Validation of Ship Manoeuvring Simulation Methods.* `http://www.simman2008.dk/kvlcc/KVLCC2/tanker2.html` (cit. on p. 136).

[151] J. Singh, M. Rudman, and H. M. Blackburn. "Reynolds number effects in pipe flow turbulence of generalized Newtonian fluids". *Physical Review Fluids* 3.9 (2018): 094607. DOI: `10.1103/PhysRevFluids.3.094607` (cit. on pp. 108, 113, 116, 119, 123, 125, 129, 132).

[152] J. Singh, M. Rudman, and H. M. Blackburn. "The influence of shear-dependent rheology on turbulent pipe flow". *Journal of Fluid Mechanics* 822 (2017): 848–879. DOI: `10.1017/jfm.2017.296` (cit. on pp. 108, 113, 114, 116, 119, 126, 129, 132).

[153] J. Singh, M. Rudman, and H. Blackburn. "The effect of yield stress on pipe flow turbulence for generalised newtonian fluids". *Journal of Non-Newtonian Fluid Mechanics* 249 (2017): 53–62. DOI: `10.1016/j.jnnfm.2017.09.007` (cit. on pp. 108, 111, 112, 114, 116, 119, 121, 122, 124, 126, 128–131, 175).

[154] J. Singh, M. Rudman, H. M. Blackburn, A. Chryss, L. Pullum, and L. J. Graham. "The importance of rheology characterization in predicting turbulent pipe flow of generalized Newtonian fluids". *Journal of Non-Newtonian Fluid Mechanics* 232 (2016): 11–21. DOI: `10.1016/j.jnnfm.2016.03.013` (cit. on pp. 106, 125).

[155] M. Sotelo, D. Boucetta, P. Doddugollu, E. Toorman, B. Brouwers, G. Delefortrie, and W. van Hoydonck. "Experimental study of a cylinder towed through natural mud". In: *6th MASHCON-International Conference on Ship Manoeuvring in Shallow and Confined Water with Special Focus on Port Manoeuvres.* 2016, 221–231 (cit. on p. 147).

[156] P. R. Souza Mendes and E. S. S. Dutra. "Viscosity Function for Yield-Stress Liquids". *Applied Rheology* 14.6 (2004): 296–302. DOI: `10.1515/arh-2004-0016` (cit. on p. 22).

[157] P. Spalart and S. Allmaras. "A one-equation turbulence model for aerodynamic flows". In: *30th Aerospace Sciences Meeting and Exhibit.* Reston, Virigina: American Institute of Aeronautics and Astronautics, 1992, 23. DOI: `10.2514/6.1992-439` (cit. on pp. 109, 116, 175).

[158] G. G. Stokes. “On the Effect of the Internal Friction of Fluids on the Motion of Pendulums”. In: *Mathematical and Physical Papers*. Cambridge: Cambridge University Press, 2010, 1–10. DOI: `10.1017/CBO9780511702266.002` (cit. on p. 48).

[159] A. Syrakos, G. C. Georgiou, and A. N. Alexandrou. “Performance of the finite volume method in solving regularised Bingham flows: Inertia effects in the lid-driven cavity flow”. *Journal of Non-Newtonian Fluid Mechanics* 208-209 (2014): 88–107. DOI: `10.1016/j.jnnfm.2014.03.004` (cit. on pp. 34, 54).

[160] A. Syrakos, G. C. Georgiou, and A. N. Alexandrou. “Solution of the square lid-driven cavity flow of a Bingham plastic using the finite volume method”. *Journal of Non-Newtonian Fluid Mechanics* 195 (2013): 19–31. DOI: `10.1016/j.jnnfm.2012.12.008` (cit. on p. 54).

[161] A. Syrakos, G. C. Georgiou, and A. N. Alexandrou. “Thixotropic flow past a cylinder”. *Journal of Non-Newtonian Fluid Mechanics* 220 (2015). ISSN: 03770257. DOI: `10.1016/j.jnnfm.2014.08.008` (cit. on p. 143).

[162] A. Syrakos, S. Varchanis, Y. Dimakopoulos, A. Goulas, and J. Tsamopoulos. “A critical analysis of some popular methods for the discretisation of the gradient operator in finite volume methods”. *Physics of Fluids* 29.12 (2017): 127103 (cit. on p. 34).

[163] H. Tabuteau, P. Coussot, and J. R. de Bruyn. “Drag force on a sphere in steady motion through a yield-stress fluid”. *Journal of Rheology* 51.1 (2007): 125–137. DOI: `10.1122/1.2401614` (cit. on p. 46).

[164] E. A. Toorman. “Modelling the thixotropic behaviour of dense cohesive sediment suspensions”. *Rheologica Acta* 36.1 (1997): 56–65. DOI: `10.1007/BF00366724` (cit. on pp. 66, 142).

[165] S. L. Toxopeus. *Practical application of viscous-flow calculations for the simulation of manoeuvring ships*. Ph.D. Thesis, Delft University of Technology, Delft, The Netherlands, 2011. URL: `http://resolver.tudelft.nl/uuid:1226f51d-58bb-4699-9b42-70af62ad49a7` (cit. on p. 12).

[166] A. Tripathi, R. P. Chhabra, and T. Sundararajan. “Power law fluid flow over spheroidal particles”. *Industrial & Engineering Chemistry Fundamentals* 33.2 (1994): 403–410. DOI: `10.1021/ie00026a035` (cit. on pp. 46, 61, 62).

[167] E. Turgeon and D. Pelletier. “Verification and Validation in CFD Using an Adaptive Finite-Element Method”. *Canadian Aeronautics and Space Journal* 48.4 (2002): 219–231. DOI: `10.5589/q02-027` (cit. on p. 26).

[168] L. Valentik and R. L. Whitmore. "The terminal velocity of spheres in Bingham plastics". *British Journal of Applied Physics* 16.8 (1965): 1197–1203. DOI: 10.1088/0508-3443/16/8/320 (cit. on p. 46).

[169] M. Vantorre. "Ship behaviour and control in muddy areas: state of the art". In: *3rd International Conference On Manoeuvring and Control of Marine Craft (MCMC '94), Southampton, UK.* 1994 (cit. on pp. 7, 16).

[170] M. Vantorre, E. Laforce, and G. Delefortrie. "A novel methodology for revision of the nautical bottom". *VLIZ Special Publication* (2006). URL: https://www.vliz.be/imisdocs/publications/ocrd/97151.pdf#page=19 (cit. on p. 4).

[171] M. Vantorre and I. Coen. "On sinkage and trim of vessels navigating above a mud layer". In: *The Royal Society of Flemish Engineers, Harbour Congress.* 1988 (cit. on p. 7).

[172] G. Vaz, F. Jaouen, and M. Hoekstra. "Free-Surface Viscous Flow Computations: Validation of URANS Code FRESCO". In: *Proceedings of OMAE 2009, Honolulu, Hawaii, USA.* 2009, 425–437. DOI: 10.1115/OMAE2009-79398 (cit. on p. 23).

[173] S. P. Veluri, C. J. Roy, and E. A. Luke. "Comprehensive code verification techniques for finite volume CFD codes". *Computers & Fluids* 70 (2012): 59–72. DOI: 10.1016/j.compfluid.2012.04.028 (cit. on pp. 26, 42).

[174] J. Venkatesan and S. Ganesan. "A three-field local projection stabilized formulation for computations of Oldroyd-B viscoelastic fluid flows". *Journal of Non-Newtonian Fluid Mechanics* 247 (2017): 90–106. DOI: 10.1016/j.jnnfm.2017.06.007 (cit. on p. 26).

[175] J. Verwilligen, M. Vantorre, G. Delefortrie, J. Meinsma, and K. van der Made. "Manoeuvrability in proximity of nautical bottom in the harbour of Delfzijl". In: *33rd PIANC World congress.* PIANC. 2014, 1–18 (cit. on p. 8).

[176] P. Wesseling. *Principles of Computational Fluid Dynamics.* Vol. 29. Springer Series in Computational Mathematics. Springer Berlin Heidelberg, 2001, 644. DOI: 10.1007/978-3-642-05146-3. URL: http://link.springer.com/10.1007/978-3-642-05146-3 (cit. on p. 29).

[177] W. H. White. "The Norwegian North Polar Expedition, 1893–6". *Nature* 74.1924 (1906): 485–486. DOI: 10.1038/074485a0 (cit. on p. 6).

[178] D. C. Wilcox. "Reassessment of the scale-determining equation for advanced turbulence models". *AIAA Journal* (1988). DOI: 10.2514/3.10041 (cit. on p. 108).

[179] D. C. Wilcox. *Turbulence Modeling for CFD (Third Edition).* 3rd Edition. DCW Industries, Canada, CA, USA, 2006. ISBN: 1928729088 (cit. on pp. 17, 128).

[180] K. C. Wilson and A. D. Thomas. “Analytic Model of Laminar-Turbulent Transition for Bingham Plastics”. *The Canadian Journal of Chemical Engineering* 84.5 (2008): 520–526. DOI: `10.1002/cjce.5450840502` (cit. on p. 106).

[181] J. Winterwerp, R. d. Graaff, J. Groeneweg, and A. Luijendijk. “Modelling of wave damping at Guyana mud coast”. *Coastal Engineering* 54.3 (2007): 249–261. DOI: `10.1016/j.coastaleng.2006.08.012` (cit. on p. 66).

[182] W. Worrall and S. Tuliani. “Viscosity changes during the ageing of clay-water suspensions”. *Trans. Brit. Ceram. Soc.* 63 (1964): 167–185 (cit. on pp. 66, 142, 145).

[183] V. Wright and R. Krone. “Aggregate structure in hyperconcentrated mud flows”. *Journal of Coastal Research* (1989): 117–125 (cit. on p. 66).

[184] W. Wu, X. Huang, H. Yuan, F. Xu, and J. Ma. “A modified lattice boltzmann method for herschel-bulkley fluids”. *Rheologica Acta* 56.4 (2017): 369–376. DOI: `10.1007/s00397-017-1000-9` (cit. on p. 26).

[185] R. W. Wurpts. “15 years experience with fluid mud: Definition of the nautical bottom with rheological parameters”. *Terra et Aqua* (2005). ISSN: 03766411 (cit. on pp. 21, 66).

[186] R. W. Yeung and T. C. Nguyen. “Waves generated by a moving source in a two-layer ocean of finite depth”. *Journal of Engineering Mathematics* 35.1-2 (1999). DOI: `10.1023/a:1004399917692` (cit. on p. 9).

[187] G. Zilman and T. Miloh. “Hydrodynamics of a body moving over a mud layer - Part I: wave resistance”. *Journal of Ship Research* 39.3 (1995). ISSN: 00224502 (cit. on pp. 6, 7, 9, 66).

# A

# APPENDIX A

## A.1. SENSITIVITY TO CODING MISTAKES IN THE RHEOLOGICAL MODEL

This exercise illustrates the sensitivity of the three test cases discussed in Chapter 3 to coding errors in the implementation of the apparent viscosity. For this purpose, we simulated the presence of bugs in the viscosity by inserting the following command right below the line of code where the apparent viscosity is calculated:

```
mu(:) = mu(:) * (1.0 + err/100.0)
```

where `err` represents the (small) coding error in percentage. This error mimics the presence of coding mistakes in the apparent viscosity that produce a uniform viscosity error equal to `err`.

For Case 1 (Section 3.5), the presence of a coding error is clearly visible from both the observed order of accuracy $p$ (Table A.1) and the convergence of $e_0$ (Fig. A.1) of all quantities.

For Case 2 (Section 3.6), the observed order of accuracy of viscosity appears to be highly sensitive to the small coding error (Table A.2), whereas for velocity, pressure and volume fraction, $p$ is virtually unaffected. Likewise, the extrapolated error $e_0$ (Fig. A.2) shows an alarming trend for the viscosity, whereas for the other variables $e_0$ appears to be the same as in the exercise without the coding error.

For Case 3 (Section 3.7), the presence of an anomaly in the rheological model is suggested by the convergence of the viscosity error, which appears to stagnate instead of decreasing with grid refinement (Fig. A.3). However, as for Case 2, the

Table A.1: Observed order $p$ for the five finest grids of Case 1 with err = 0.01%

| $h_i/h_1$ | $p(L_2[e(\phi)])$ | | | $p(L_\infty[e(\phi)])$ | | |
|---|---|---|---|---|---|---|
| | $u$ | $C_p$ | $\mu$ | $u$ | $C_p$ | $\mu$ |
| 2.00 | 2.01 | -0.11 | 2.32 | 2.05 | 0.96 | 9.21 |
| 1.61 | 2.01 | 2.02 | 2.24 | 2.03 | 0.97 | -0.04 |
| 1.35 | 2.02 | -0.13 | 2.19 | 2.03 | 0.97 | -0.04 |
| 1.14 | 2.04 | -0.10 | 2.14 | 2.07 | 0.97 | 1.05 |
| 1.00 | 2.08 | 0.73 | 2.11 | 2.11 | 0.98 | 1.03 |

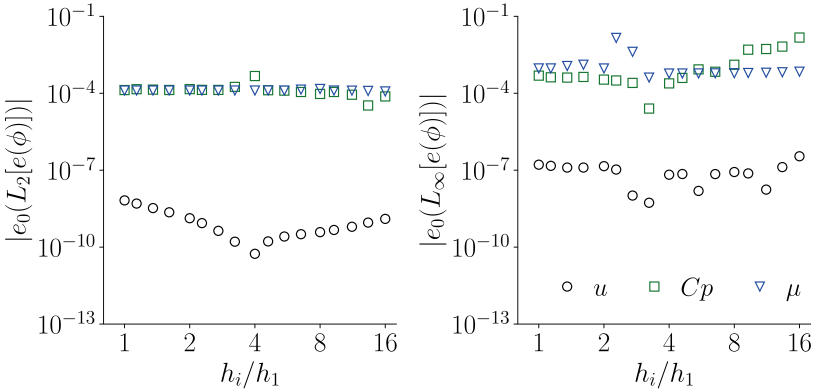

Figure A.1: Extrapolated error $e_0$ for Case 1 with err = 0.01%

Table A.2: Observed order $p$ for the five finest grids of Case 2 with err = 0.01%

| $\lambda_i/\lambda_1$ | $p(L_1[e(\phi)])$ | | | | $p(L_2[e(\phi)])$ | | | |
|---|---|---|---|---|---|---|---|---|
| | $u$ | $C_p$ | $c$ | $\mu$ | $u$ | $C_p$ | $c$ | $\mu$ |
| 2.00 | 2.00 | 2.02 | 2.13 | 5.05 | 2.04 | 2.05 | 2.10 | 2.82 |
| 1.61 | 2.00 | 2.02 | 2.08 | 5.05 | 2.04 | 2.04 | 2.06 | 3.45 |
| 1.35 | 2.00 | 2.02 | 2.06 | 9.09 | 2.03 | 2.03 | 2.05 | 4.10 |
| 1.14 | 2.00 | 2.01 | 2.06 | 9.09 | 2.03 | 2.03 | 2.04 | 5.37 |
| 1.00 | 2.00 | 2.01 | 2.04 | 9.09 | 2.03 | 2.02 | 2.03 | 8.65 |

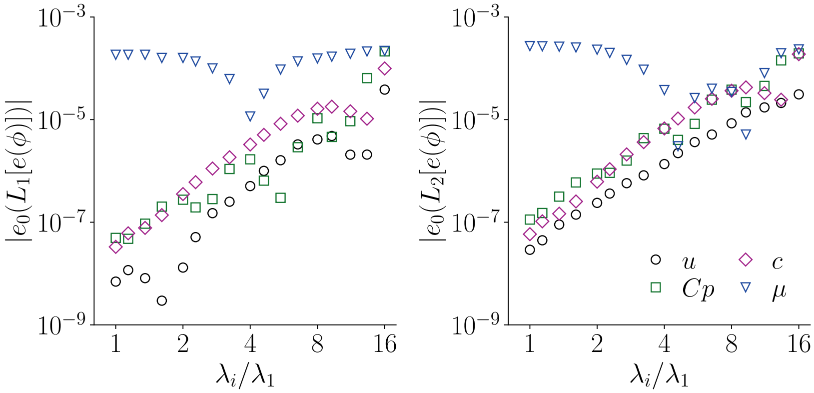

Figure A.2: Extrapolated error $e_0$ for Case 2 with err = 0.01%

grid/time convergence properties of the other variables appear to be unaffected by the coding error.

The insensitivity of the dependent variables to coding mistakes in the viscosity for Case 2 and Case 3 is due to the fact that the diffusion term in the momentum equations is much smaller than the other terms. This is simply due to the nature of the manufactured solution, which represents a gravity wave. Therefore, for Case 2 and Case 3, it is recommended to examine the grid/time convergence properties of the viscosity for detection of bugs in the rheological model.

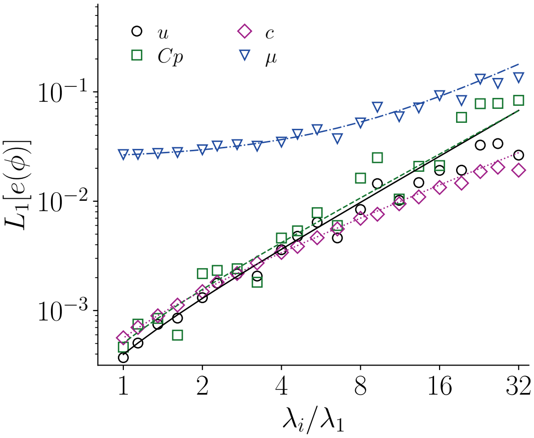

Figure A.3: $L_1$ error norms as function of the refinement factor with err = 1%. Lines are obtained from the best weighted least-square fitting of Eq. (3.8) to data on the 10 finest grids.

## A.2. PARAMETER VALUES USED FOR THE THREE TEST CASES

Table A.3: Parameters used for the three test cases in Chapter 3.

| Parameter | Value |
|---|---|
| Case 1 | |
| Computational domain [m] | $(x, y) \in [0, 0.6] \times [0.1, 0.7]$ |
| Finest grid | $640 \times 640$ |
| Density [kg m$^{-3}$] | $\rho = 1$ |
| Flow index [-] | $n = 0.8$ |
| Consistency parameter [Pa s$^n$] | $k = 0.5$ |
| Yield stress [Pa] | $\tau_0 = 5$ |
| Regularisation parameter [s] | $m = 1$ |
| Convergence tolerance for residuals [-] | $L_\infty$ norm $< 2 \times 10^{-14}$ |
| Case 2 | |
| Computational domain [m] | $(x, z) \in [0, 1] \times [-0.75, 0.25]$ |
| Finest grid and time step | $640 \times 640$, $\tau_1 = T/4800$ |
| Wave speed [m s$^{-1}$] | $c = 1.25$ |
| Wave amplitude [m] | $A = 0.02$ |
| Gravity [m s$^{-2}$] | $g = 9.81$ |
| Steepening coefficient [m$^{-1}$] | $b = 12$ |
| Wave length [m] and period [ s] | $\lambda = 1$, $T = 0.8$ |
| Molecular viscosity fluid 2 [Pa s] | $\mu_2 = 0.001$ |
| Consistency parameter fluid 1 [Pa s$^n$] | $k = 0.002$ |
| Flow index fluid 1 [-] | $n = 0.8$ |
| Yield stress fluid 1 [Pa] | $\tau_0 = 0.002$ |
| Regularisation parameter fluid 1 [s] | $m = 4$ |
| Density [kg m$^{-3}$] | $\rho_1 = 1200$, $\rho_2 = 1000$ |
| Convergence tolerance for residuals [-] | $L_\infty$ norm $< 10^{-10}$ |
| Convection scheme volume-fraction equation | TVD Harmonic [93] |
| Case 3 (other parameters are as Case 2) | |
| Steepening coefficient [m$^{-1}$] | $b = 1200$ |
| Molecular viscosity fluid 2 [Pa s] | $\mu_2 = 2 \times 10^{-5}$ |
| Density fluid 2 [kg m$^{-3}$] | $\rho_2 = 1$ |
| Convection scheme volume-fraction equation | ReFRICS [85] |

# B

# APPENDIX B

This appendix reports the details of the three turbulence models that were used in Chapter 6, together with the non-Newtonian contributions in the TKE budget and the iterative convergence for some of the test cases considered in Chapter 6.

## B.1. $k-\omega$ SST (2003)

The $k-\omega$ SST model of Menter et al. [113] that is used as a baseline for the derivation of the new SST-HB model (see Sections 6.3.4 and 6.7.1) is reported below.

$$\frac{D(\rho k)}{Dt} = \tilde{P}_k + \nabla\cdot\Big[(\mu+\sigma_k\mu_t)\nabla k\Big] - \rho\overbrace{\beta^* k\omega}^{\epsilon} \tag{B.1}$$

$$\frac{D(\rho\omega)}{Dt} = \frac{\rho\alpha}{\mu_t}\tilde{P}_k + \nabla\cdot\Big[(\mu+\sigma_\omega\mu_t\nabla\omega\Big] - \beta\rho\omega^2 + 2\rho(1-F_1)\frac{\sigma_{\omega 2}}{\omega}\nabla k\cdot\nabla\omega \tag{B.2}$$

$$F_1 = \tanh\left\{\min\left[\max\left(\frac{\sqrt{k}}{\beta^*\omega d},\frac{500\nu}{d^2\omega}\right),\frac{4\rho\sigma_{\omega 2}k}{CD_{k\omega}d^2}\right]^4\right\} \tag{B.3}$$

$d$ is the distance to the wall boundary.

$$CD_{k\omega} = \max\left(2\rho\sigma_{\omega 2}\frac{1}{\omega}\nabla k\cdot\nabla\omega, 10^{-10}\right) \tag{B.4}$$

$$\nu_t = \frac{a_1 k}{\max(a_1\omega, SF_2)}, a_1 = 0.31 \tag{B.5}$$

$$F_2 = \tanh\left\{\left[\max\left(\frac{2\sqrt{k}}{\beta^*\omega d}, \frac{500\nu}{d^2\omega}\right)\right]^2\right\} \tag{B.6}$$

$$\tilde{P_k} = \min(\mu_t S^2, 10\beta^*\rho k\omega)\,,\ \beta^* = 0.09 \tag{B.7}$$

$$\begin{aligned}
\alpha = \alpha_1 F_1 + (1-F_1)\alpha_2, &\quad \beta = \beta_1 F_1 + (1-F_1)\beta_2,\\
\sigma_k = \sigma_{k1} F_1 + (1-F_1)\sigma_{k2}, &\quad \sigma_\omega = \sigma_{\omega 1} F_1 + (1-F_1)\sigma_{\omega 2},\\
\alpha_1 = 5/9, \quad \beta_1 = 3/40, &\quad \sigma_{k1} = 0.85, \quad \sigma_{\omega 1} = 0.5,\\
\alpha_2 = 0.44, \quad \beta_2 = 0.0828, &\quad \sigma_{k2} = 1, \quad \sigma_{\omega 2} = 0.856.
\end{aligned}$$

## B.2. $k$-$\sqrt{k}L$ (KSKL)

The RANS model of Menter et al. [115] is a two-equation model that solves the following transport equations:

$$\frac{D(\rho k)}{Dt} = \mu_t S^2 + \nabla\cdot\left[\left(\mu + \frac{\mu_t}{\sigma_k}\right)\nabla k\right] - c_\mu^{3/4}\rho\frac{k^2}{\Phi} - 2\mu\frac{k}{d^2}\,, \tag{B.8}$$

$$\frac{D(\rho\Phi)}{Dt} = \frac{\Phi}{k}\mu_t S^2\left[\zeta_1 - \zeta_2\left(\frac{L}{L_{vK}}\right)^2\right] + \nabla\cdot\left[(\mu + \frac{\mu_t}{\sigma_\Phi})\nabla\Phi\right] - \zeta_3\rho k - 6\mu\frac{\Phi}{d^2}f_\Phi\,, \tag{B.9}$$

where $d$ is the distance to the wall boundary and

$$L_{vK} = \kappa\left|\frac{U'}{U''}\right|, \quad \Phi = \sqrt{k}L, \quad U' = S = \sqrt{2S_{ij}S_{ij}}, \quad U'' = \sqrt{\sum_i\sum_j\sum_k \frac{\partial^2 u_i}{\partial x_k^2}\frac{\partial^2 u_i}{\partial x_j^2}}\,,$$

$$f_\Phi = \frac{1+4.7\xi}{1+\xi^4} \quad \xi = \frac{\sqrt{0.3k}k}{20\mu}\,, \quad \zeta_1 = 0.8\,, \quad \zeta_2 = 1.47\,, \quad \zeta_3 = 0.0288\,,$$

$$\sigma_k = \sigma_\Phi = 2/3\,, \quad \kappa = 0.41\,.$$

The eddy viscosity reads:

$$\mu_t = \min\left(c_\mu^{1/4}\rho\Phi, \frac{a_1 k}{S}\right), \tag{B.10}$$

where

$$a_1 = 0.32 f_b + 0.577(1-f_b)\,, \quad f_b = \tanh\left[\left(\frac{20c_\mu^{1/4}\Phi + 20\nu}{\kappa^2 S d^2 + 0.01\nu}\right)^2\right]$$

The following limiters are applied to the length scale $L_{vK}$:

$$0.1L < L_{vK} < 1.3\kappa d$$

## B.3. SPALART-ALLMARAS (SA)

The RANS model proposed by Spalart and Allmaras [157] is a one-equation model in which the eddy viscosity is a function of an auxiliary quantity $\tilde{\nu}$,

$$\mu_t = \rho \tilde{\nu} f_{v1} , \tag{B.11}$$

and $\tilde{\nu}$ is obtained by solving the following transport equation:

$$\frac{D(\tilde{\nu})}{Dt} = c_{b1} \tilde{S} \tilde{\nu} + \frac{1}{\sigma_s} \left\{ \nabla \cdot \left[ (\nu + \tilde{\nu}) \nabla \tilde{\nu} \right] + c_{b2} |\nabla \tilde{\nu}|^2 \right\} - c_{w1} f_w \left( \frac{\tilde{\nu}}{d} \right)^2 , \tag{B.12}$$

where $d$ is the distance to the wall boundary. The other quantities are defined below:

$$\nu \equiv \frac{\mu}{\rho}, \quad \tilde{S} \equiv \Omega + \frac{\tilde{\nu}}{\kappa^2 d^2} f_{v2} , \quad \Omega = \sqrt{2 \Omega_{ij} \Omega_{ij}} ,$$
$$\Omega_{ij} = \frac{1}{2} \left( \frac{\partial u_i}{\partial x_j} - \frac{\partial u_j}{\partial x_i} \right), \quad \chi \equiv \frac{\tilde{\nu}}{\nu} ,$$

$$f_{v1} = \frac{\chi^3}{\chi^3 + c_{v1}^3} , \quad f_{v2} = 1 - \frac{\chi}{1 + \chi f_{v1}} , \quad c_{v1} = 7.1 ,$$
$$r \equiv \frac{\tilde{\nu}}{\tilde{S} \kappa^2 d^2} , \quad g = r + c_{w2} (r^6 - r) , \quad f_w = g \left( \frac{1 + c_{w3}^6}{g^3 + c_{w3}^6} \right)^{1/6} ,$$
$$c_{w1} = \frac{c_{b1}}{\kappa^2} + \frac{1 + c_{b2}}{\sigma_s} , \quad c_{w2} = 0.3 , \quad c_{w3} = 2 ,$$
$$c_{b1} = 0.1355 , \quad c_{b2} = 0.622 , \quad \sigma_s = \frac{2}{3} , \quad \kappa = 0.41 .$$

## B.4. NON-NEWTONIAN CONTRIBUTIONS IN THE TKE BUDGET

In order to give an indication of the magnitude of the non-Newtonian contributions $\chi^{nn}$ and $\xi^{nn}$ in the TKE equation, their distribution is plotted in Fig. B.1 together with the production, dissipation and transport terms (see also Eq. (6.31)). For non-Newtonian fluids, the difference between production and dissipation is absorbed by the non-Newtonian contributions, making the transport term $D^+$ nearly insensitive to the fluid rheology, in line with DNS data (Figs. 10 and 15 in [153]). The sum of the non-Newtonian contributions is positive and appears to be larger for power-law fluids.

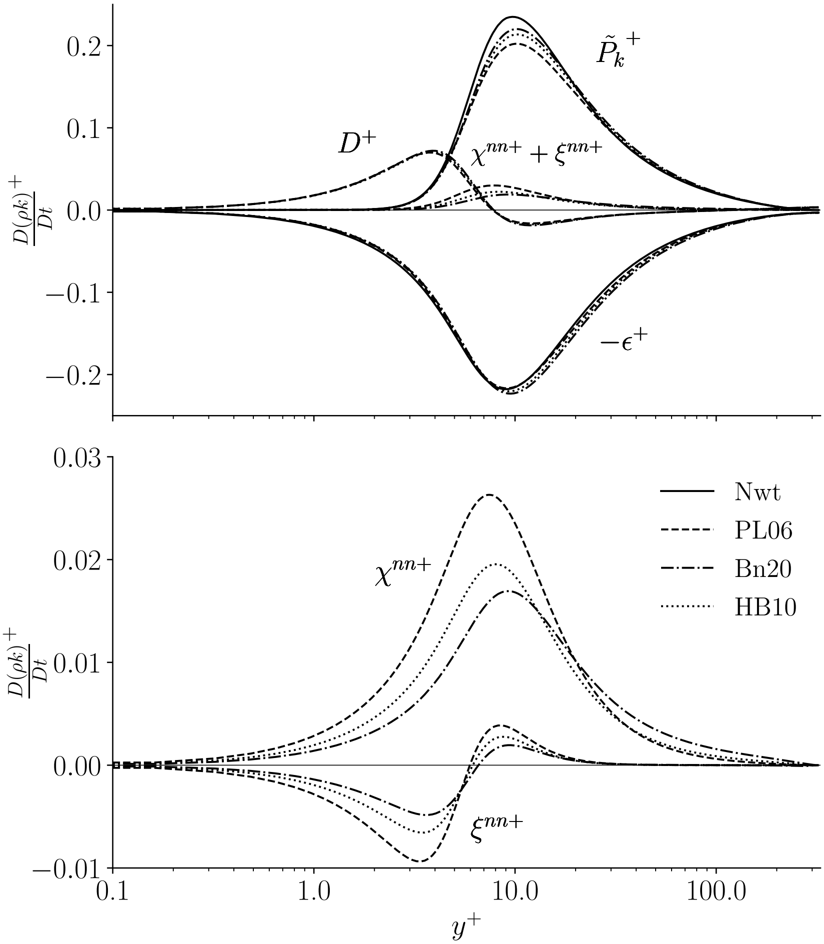

Figure B.1: Production ($\tilde{P_k}^+$), dissipation ($\epsilon^+$) and transport ($D^+$) of TKE (top) and non-Newtonian contributions (bottom) ($Re_\tau = 323$). The non-dimensional terms were obtained by dividing the dimensional terms by $\rho u_\tau^4/\nu_w$.

## B.5. ITERATIVE CONVERGENCE

Fig. B.2 shows the iterative convergence of the residuals (top graph) with the new SST-HB and the standard SST model for Bn30 (most difficult case for iterative convergence), together with the estimated iterative error for the wall shear stress (bottom graph). The latter can be estimated since the pressure gradient is imposed and thus the exact wall shear stress is known. The wall shear stress requires about 7000 iterations to converge with the new model, whereas the standard SST (similarly for the SA and KSKL model) requires about 30000 SIMPLE iterations. The better iterative convergence of the new model is simply due to the fact that the viscosity does not reach very large values in the core of the pipe, contrary to the other selected RANS models, which show an incorrect asymptote in the viscosity typical of laminar flows (see also Section 6.7.3).

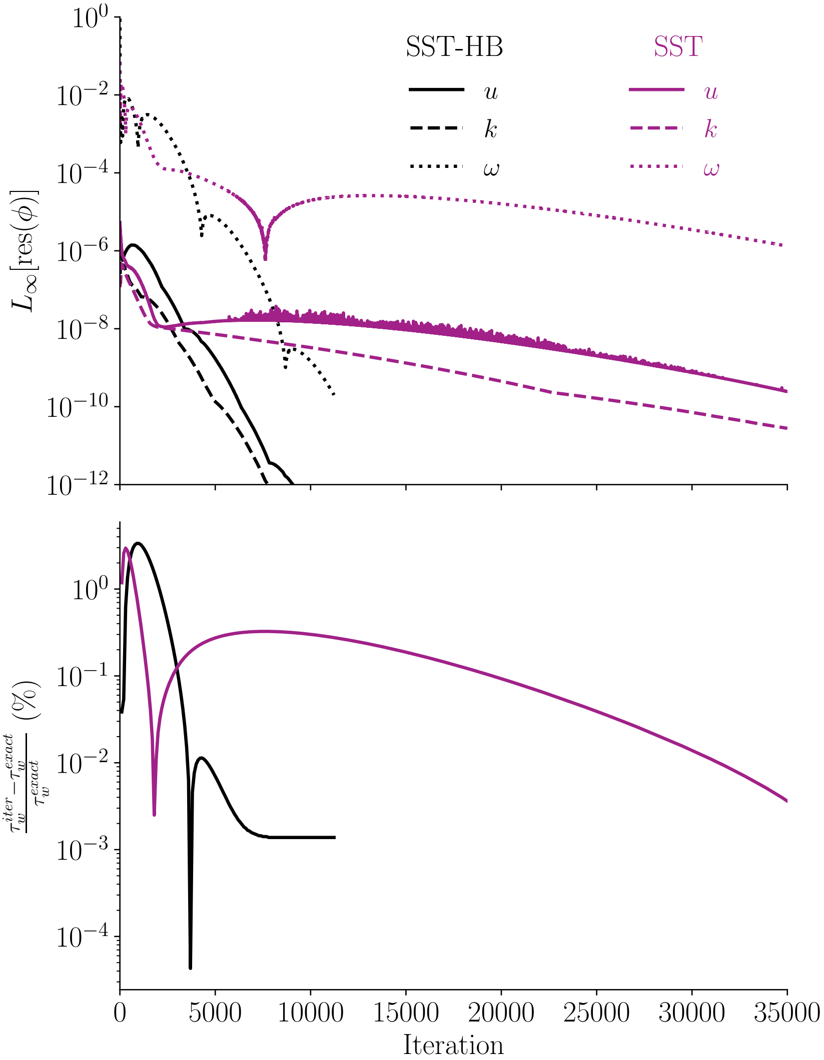

Figure B.2: Iterative convergence of the $L_\infty$ norm of the residuals (top) and wall shear stress error in percentage (bottom) for the case $Re_\tau = 323$, Bn30.

# C

# APPENDIX C

In this appendix the frictional resistance due to the contact with Mud_10 and Mud_23 is estimated assuming laminar flow in light of the considerations made in Section 6.8.

## C.1. ESTIMATION OF THE FRICTIONAL RESISTANCE FOR LAMINAR FLOW

For laminar flows, the correlation for Bingham fluids (Eq. (5.21)) can be used to estimate the average wall shear stress on the portion of the hull in contact with mud. In this case, the wall shear stress is almost completely dominated by the yield stress, which leads in fact to ratios $\tau_0/\tau_w$ close to 100%, as shown in Table C.1. The total frictional resistance due to the contact with mud can thus be well approximated by $\tau_0 \cdot S_{mud}$, where $S_{mud}$ is the hull surface area wetted by mud. Indeed, for the simulation illustrated in Fig. 6.11, the component in the flow direction of the wall shear stress averaged over the hull surface in contact with mud ($c_{mud} < 0.5$) is 23.05 Pa, which is virtually identical to the yield stress of Mud_23. This also further confirms that boundary layer in the mud region predicted by the RANS models is indeed laminar. Hence, as long as the mud rheology is well described by the Bingham model, $\tau_0 \cdot S_{mud}$ is a good estimate of the frictional resistance due to contact with the mud layer.

For a quick estimation of $S_{mud}$, one could approximate it as $[(L \cdot B)+2 \cdot T_{mud} \cdot L] \cdot C_B$, where $L$, $B$ and $C_B$ are the ship's length, beam and block coefficient, respectively, whereas $T_{mud}$ is the draught with respect to the undisturbed mud level. For the test case shown in Fig. 6.11, this approximation leads to an overestimation of 10%

Table C.1: Estimated ratio $\tau_0/\tau_w$ and wall shear rate for a flat plate moving through Mud_10 and Mud_23 at different speeds. The flow regime is assumed to be laminar and the average shear stress is estimated with the modified Blasius' formula (Eq. (5.21)). For the rheological properties of Mud_10 and Mud_23 see Table 5.2.

| U [Kn] | U [m/s] | $Re$ | $Bn$ | $C_F \times 1000$ | $\sim \tau_0/\tau_w$ | $\sim \dot{\gamma}_w$ [s$^{-1}$] |
|---|---|---|---|---|---|---|
| | | | Mud_10 | | | |
| 1.0 | 0.51 | 1.1E+07 | 6.4E-02 | 64.67 | 99% | 4 |
| 2.0 | 1.03 | 2.2E+07 | 1.6E-02 | 16.35 | 98% | 10 |
| 4.0 | 2.06 | 4.5E+07 | 4.0E-03 | 4.216 | 95% | 29 |
| 6.0 | 3.09 | 6.7E+07 | 1.8E-03 | 1.947 | 92% | 53 |
| 8.0 | 4.12 | 9.0E+07 | 1.0E-03 | 1.145 | 88% | 81 |
| 10.0 | 5.14 | 1.1E+08 | 6.4E-04 | 0.7682 | 84% | 113 |
| 12.0 | 6.17 | 1.3E+08 | 4.5E-04 | 0.5609 | 80% | 149 |
| | | | Mud_23 | | | |
| 1.0 | 0.51 | 5.7E+06 | 1.4E-01 | 145.4 | 100% | 3 |
| 2.0 | 1.03 | 1.1E+07 | 3.6E-02 | 36.60 | 99% | 7 |
| 4.0 | 2.06 | 2.3E+07 | 9.1E-03 | 9.330 | 97% | 20 |
| 6.0 | 3.09 | 3.4E+07 | 4.0E-03 | 4.250 | 95% | 38 |
| 8.0 | 4.12 | 4.6E+07 | 2.3E-03 | 2.459 | 92% | 58 |
| 10.0 | 5.14 | 5.7E+07 | 1.4E-03 | 1.624 | 89% | 81 |
| 12.0 | 6.17 | 6.9E+07 | 1.0E-03 | 1.166 | 86% | 106 |

with respect to the computed $S_{mud}$, which is generally acceptable when lacking of more detailed geometrical information about the hull. However, the accuracy of this approximation is expected to quickly drop at higher speeds as the water will flow underneath the hull, even with negative UKC, thereby reducing actual surface area in contact with mud. This sort of ‘water lubrication’ has been observed in the numerical studies of Leijs [94] (see Fig. 6.16 therein) and of Kaidi et al. [78] (see Fig. 23 therein).

Finally, still under the assumption of laminar flow in the mud layer, Table C.1 shows also the average shear rate on a flat plate having $L = 320$ m. Interestingly, the shear rate does not exceed 150 $\mathrm{s}^{-1}$ even with Mud_10 and at 12 knots. This suggests that, if the flow is laminar, standard protocols to determine the mud flow curves (for which the maximum shear rate cannot be too large for practical reasons) could be reliably used for ’sailing-through-mud’ applications.

# CURRICULUM VITÆ

**Stefano LOVATO**

| | |
|---|---|
| 12-01-1991 | Born in Turin, Italy. |

## EDUCATION

| | |
|---|---|
| 2005-2010 | Nautical institute San Giorgio, Genoa, Italy |
| 2010-2014 | Bachelor in Marine Engineering and Naval Architecture<br>University of Genoa, Italy |
| 2014-2017 | Master of Science in Marine Engineering and Naval Architecture<br>University of Genoa, Italy |
| 2017-2023 | Ph.D. researcher at TU Delft<br>Faculty of Mechanical, Maritime and Materials Engineering<br>Department of Maritime & Transport Technology<br>Section Offshore and Dredging Engineering |

## WORK EXPERIENCE

| | |
|---|---|
| 2017-2023 | Visiting researcher at MARIN<br>Department of Research & Development<br>Team of CFD developments |
| 2022-2023 | Postdoctoral researcher at TU Delft<br>Faculty of Civil Engineering and Geosciences<br>Department of Hydraulic Engineering<br>Section Rivers, Ports, Waterways and Dredging Engineering |
| 2023-current | Project manager at MARIN<br>Department of Maritime Operations<br>Team of Nautical Operations |

## AWARDS

| | |
|---|---|
| 2010 | San Giorgio Award |

# LIST OF PUBLICATIONS

## JOURNAL PUBLICATIONS (PEER REVIEWED)

4. **S. Lovato**, S.L. Toxopeus, J.W. Settels, G.H. Keetels, *Application of a maritime CFD code to a benchmark problem for non-Newtonian fluids: the flow around a sphere*, International Shipbuilding Progress, 1-25 (2022).

3. **S. Lovato**, A. Kirichek, S.L. Toxopeus, J.W. Settels, G.H. Keetels, *Validation of the resistance of a plate moving through mud: CFD modelling and towing tank experiments*, Ocean Engineering, 258, 111632 (2022).

2. **S. Lovato**, G.H. Keetels, S.L. Toxopeus, J.W. Settels, *An eddy-viscosity model for turbulent flows of Herschel–Bulkley fluids*, Journal of Non-Newtonian Fluid Mechanics, 301, 104729 (2022).

1. **S. Lovato**, S.L. Toxopeus, J.W. Settels, G.H. Keetels, G. Vaz, *Code verification of non-Newtonian fluid solvers for single-and two-phase laminar flows*, Journal of Verification, Validation and Uncertainty Quantification, 6(2) (2021).

## CONFERENCE PAPERS

2. **S. Lovato**, A. Kirichek, S.L. Toxopeus, J.W. Settels, A.M. Talmon, G.H. Keetels, *The resistance of a plate moving through mud: experiments and simulations*, NuTTS 2021: 23rd Numerical Towing Tank Symposium, Duisburg, Germany.

1. **S. Lovato**, G. Vaz, S.L. Toxopeus, J.W. Settels, G.H. Keetels, *Code Verification exercise for 2D Poiseuille flow with non-Newtonian fluid*, NuTTS 2018: 21st Numerical Towing Tank Symposium, Cortona, Italy (2018.

## ORAL AND POSTER PRESENTATIONS

2. **S. Lovato**, G.H. Keetels, J.W. Settels, S.L. Toxopeus *A turbulence model for Herschel-Bulkley flows*, 1st Mudnet conference (2021), online.

1. **S. Lovato**, G. Vaz, S.L. Toxopeus, G.H. Keetels, J.W. Settels, *Verification and Validation of CFD simulations of non-Newtonian laminar flows on canonical test cases*, 19th International Workshop on Numerical Methods for Non-Newtonian Flows (2019), Peso da Régua, Portugal.

## SUPERVISED MSC THESIS

2. A. Goda, *Rheological and plate's hydrodynamic resistance in fluid mud measurements for the nautical bottom applications*, Master thesis (2021), Delft University of Technology.
1. K. Leijs, *CFD simulations of the flow around a tanker in shallow water with muddy seabed*, Master thesis (2021), Delft University of Technology.

# ACKNOWLEDGEMENTS

The time has come and I would like to start by to express my gratitude to my promotors and supervisors for their guidance, support, and encouragement throughout my PhD. Thank you Geert for having given me the possibility to start this project in the first place. Beside your fantastic technical knowledge and scientific curiosity, I really appreciated your ability to resolve difficult situations with calm and cold mind, sometimes even with your distinctive sense of humor. Thank you Cees for your support throughout the PhD; obstacles that look very big became suddenly easy to overcome after talking to you. I also enjoyed the entertaining anecdotes you told during our lunches. Thank you Serge for your expertise and invaluable feedback, for always returning the drafts of my articles with tons of useful comments that were crucial to improve my work. Thank you Just for always finding the time to help me when I needed, and for your crucial inputs to improve my work and to keep me on the right track. Special thanks to my former supervisor, Guilherme, for pushing and motivating me during the first years of my PhD. I will not forget the support that you gave me even after you were no longer my supervisor.

I wish to thank my colleagues at TUD for the stimulating discussions and valuable inputs that have helped me with my research, and even with my life in the Netherlands. In particular I want to thank Edwin, Xiuhan, Jian, Rudy, Antonio, Bas, Dave and Frans. Special thanks go to my office mates, Mohamed and Thijs, with whom I had many interesting and funny conversations about racing, food, geopolitics, imminent catastrophes and (sometimes) CFD. I believe I can finally trust that you will never eat pineapple pizza.

I would also like to extend my sincere thanks to the MUDNET group for the support, it has been a pleasure to share my work with you and to learn from the many talented people that are part of it. Thank you Claire and Ahmad for helping me with the rheological part and for the many laughs we had. Special thanks to Alex, for its incredible support and guidance both during and after my PhD.

I want to thank the Quantum Warriors, the best football team that ever played at TU Delft. In particular, I very much enjoyed sharing the pitch (and the kart race track) with Chris, Francesco, Gustavo, Alberto, Maarten, Sjoerd, Thijs, Jorge, Michael, Mark and Valentin. Thank you also for never discriminating me for being the only engineer amid quantum physicists :).

I want to thank my friends Alessandro, Danilo, Davide, Elena C., Elena S., Gian, Simone e Valeria for being part of my life. I want to thank Riccardo, with whom I always enjoy spending time both inside and outside MARIN. Thank you Irene for the fun we had and the amazing Genovese food you supplied. I also want to thank Stefano for making me laugh since the first year of high school and still today. I want to thank Claudio, my long-time friend that I wish I could see more often.

I want thank my parents for their unwavering and unconditional support and encouragement during the most challenging times. Lastly, I would like to thank Sonia for your (huge amount of) patience, understanding, support and encouragement during the most challenging times. Your constant encouragement and belief in me have been my source of strength throughout this journey. Part of the PhD belongs rightfully to you.